UNIVERSITY OF LEEDS

The Impacts of Tropical Forest Loss on Local Climate

Callum Smith

Submitted in accordance with the requirements for the degree of Doctor of Philosophy

The University of Leeds

School of Earth and Environment

June 2023

Intellectual property

The candidate confirms that the work submitted is his own, except where work which has formed part of jointly authored publications has been included. The contribution of the candidate and the other authors to this work has been explicitly indicated below. The candidate confirms that appropriate credit has been given within the thesis where reference has been made to the work of others.

Chapter 3 consists of the following manuscript in preparation:

Smith, C., Baker, J.C.A. & Spracklen, D.V. Driver of deforestation impacts temperature changes due to tropical forest loss (*in prep*.).

All authors developed the concept of the study, and contributed to experimental design, interpretation of results and writing of the manuscript. C.S. and J.C.A.B. contributed to the analysis.

Chapter 4 consists of the following publication:

Smith, C., Baker, J.C.A. & Spracklen, D.V. Tropical deforestation causes large reductions in observed precipitation. *Nature* **615**, 270–275 (2023). https://doi.org/10.1038/s41586-022-05690-1

All authors developed the concept of the study, and contributed to experimental design, interpretation of results and writing of the manuscript. C.S. and J.C.A.B. contributed to the analysis.

Chapter 5 consists of the following publication:

Smith, C., Baker, J.C.A, Robertson, E., Chadwick, R., Kelley, D.I., Argles, A.P.K., Coelho, C.A.S., de Souza, D.C., Kubota, P.Y., Talamoni, I.L. and Spracklen, D.V. Observed and simulated local climate responses to tropical deforestation. *Environ. Res. Lett.* **18**, (2023). https://doi.org/10.1088/1748-9326/acf0da

JB downloaded and processed CMIP6 model data. JB and CS downloaded and processed MODIS observational data. CS downloaded and processed precipitation datasets. CS and JB analysed the data and designed and produced figures. All authors contributed to the design and editing of the manuscript.

Author contributions

Callum Smith (CS), Jessica C. A. Baker (JCAB) and Dominick V. Spracklen (DVS) all contributed to the design, development and editing of the studies in this thesis. CS completed the data acquisition, processing, analysis and presentation of results with significant help from JCAB. CS drafted and edited this thesis with oversight and editing from DVS. Figures in this thesis are produced by CS, else are cited.

Acknowledgements

Firstly, and most importantly I would like to thank my supervisors Dom and Jess. It is fair to say your perpetual optimism, flexibility and kindness has pushed me to achieve beyond what I thought would be possible. It was hard to imagine getting to the end at some points, but looking back to where it started, volunteering at Hardknott, it is clear how far I've come. Thank you for providing the opportunities to try new things and build confidence, from teaching undergrads about the wonders of temperate rainforests in Pembroke to watching Amazonian sunsets, riverside, beer in hand. It would be hard to imagine a better team to guide me through my PhD experience.

I'd like to thank anyone who reads this thesis or the papers within. I hope it proves fruitful in inspiring action to promote not only tropical forests, but those of the world. Thanks to my funders, the European Research Council and the Newton Fund, for making this and many other important studies possible. Thanks also to the people who have gone before me who have laid the path for my study, providing knowledge, coding climate models, designing satellites and making datasets. Without you, the world really wouldn't go round!

During my PhD I've been fortunate to be surrounded by some incredible, inspiring and welcoming people, namely everyone in the Biosphere and Atmosphere Group (BAG). In particular I would like to thank Cat, Carly, Ailish and Ben who provided a great amount of PhD and life support, and not forgetting entertainment! Through the last few months, a small but crucial group of jacket potato devotees has brought excitement and nourishment to my life, thank you to the "*Lunch Boiiis*" for your company and council. A big shout out to everyone I've lived with over the last few years, who have in no small part brought joy, given me confidence and provided many great mems; Olivia, Kempy, Chloe, Iain, Ben, Chris, Hamish, Olly, Will, Izzy, Sam, Ash and Katie.

A large part of my PhD involved getting to grips with python and computing and this would not have been possible without the help of Ben, Richard Rigby, Luke Conibear and Jess. Richard in particular, helped us seamlessly navigate the confusing and daunting world of quality control implementation, something that proved crucial for nearly everything I did in my PhD. I'd also like to give special thanks to the Leeds IT system and Duo for pushing me to learn more about computing so I could find my own solutions in a bid to be free of its terror. No, but seriously, I've benefited hugely from the generosity of friends and colleagues who have given their time and knowledge freely to me.

Lastly and most importantly I'd like to thank my family, Julie, Mike, Angus, Rufus, Amy, Sonia, Rosie, Pips, Debbie, John and Olivia who have all put up with a lot(!) over the years and will definitely benefit from me handing in! Thank you for your never-ending support, motivation and so much more. I dedicate this thesis to you all.

Abstract

Tropical forests play a crucial and diverse role in the Earth's climate. Not only do they sustain human life and ecosystems, but they sustain themselves. As forests are lost around the tropics, they become less resilient to further changes, threatening to destabilise climate systems. Largely, tropical forest loss historically occurred in the Amazon, with the "arc of deforestation" in the south-eastern Amazon being the epicentre of change. In recent decades, not only has this forest loss become ubiquitous throughout the Amazon but has spread to the other tropical forest regions of the Congo Basin and Southeast Asia. During the 21st century it has been clear that politics plays a substantial role in the proliferation or lack of deforestation. Forest loss in the Amazon had been decreasing however changes to governance reversed this trend and we now see increasing rates. In the central African countries, a scramble to industrialise has spawned pervasive forest loss, whilst in Southeast Asia cash crops such as oil palm have driven significant forest clearance. These land cover changes will bring about important changes to climate.

Satellite data provide tools to empirically assess the climate impacts of land cover change. For the last two decades, large numbers of studies have shown observationally that forest loss can impact the local climate. The studies show that tropical forest loss can on average reduce rainfall and increase temperatures, through modifying the land surface processes and fluxes. However, forest loss can manifest in many different ways, with differing patterns and scales. We show that the driver of deforestation can have a large impact on the response of temperature to forest loss. Across the tropics we show that commodity driven forest loss results in ~0.65 K warming, more than triple the warming attributed to forest loss driven by shifting agriculture (~0.2 K). We find that most forest loss in the Congo is driven by shifting agriculture and correspondingly it has the least warming attributed to forest loss (~0.2 K). Projections show that deforestation in the Congo is likely to become more industrialised in the future. If the Congo shifts from small scale heterogenous forest loss to large scale commercial agriculture, we expect the local warming response to increase.

Whilst the temperature response to forest loss has commonly been observed, the response of precipitation has been more difficult to pin down. Ground-based case studies have shown that reductions and increases in precipitation occur when tropical forest is lost. Remotely

sensed and ground-based studies consider different mechanisms and impacts due to their differing methodology. Here we examine land cover change at a range of spatial scales, finding large reductions in observed rainfall over regions of forest loss across the tropics. Over the observed period, 2003 - 2017, we analyse 18 precipitation datasets, providing clear evidence that forest loss caused reduced local precipitation. The largest reductions occurred alongside the largest scales of deforestation, with 0.25 mm/month per percentage point of forest loss occurring at the 200 km forest loss scale. Using a land cover change model, we estimate that future deforestation is likely to result in large decreases in precipitation associated with forest loss. In the Congo, where forest loss is projected to be most severe, precipitation by the end of this century will have decreased by 8-10%.

To understand how land cover change can affect climate, researchers use climate models, however the impacts presented vary greatly between models. To recognise why there is large uncertainty, we evaluated the local land surface temperature and precipitation responses to forest loss in 24 CMIP6 models, using observations as a benchmark. The local land surface temperature warms as a result of tropical forest loss, both in the observations and models. Over their historical period, most CMIP6 models represented this change well, finding a warming of 0.017 K per percentage point of forest loss (K/%), compared to 0.018 K/% in the observations. The models were less skilful at simulating the precipitation response to forest loss, simulating an increase in wet season precipitation. Inter-model variability was substantial, with diverging responses occurring across all model scales (from ~0.5 to ~3 degrees). We related changes in temperature and precipitation to changes in albedo, finding those simulated changes depended on the surface albedo response to forest loss. Models with less warming and less drying had greater increases in surface albedo due to forest loss. Alongside improved knowledge of our climate system, this research provides insight for climate model developers looking to improve their model's representation of land surface and climate processes.

Throughout the tropics, forest loss continues apace, bringing with it, increased temperatures and reduced precipitation as shown by the three analysis chapters in this thesis. The consequences of these changes are wide ranging and include negative impacts to agriculture, air quality, carbon storage, biodiversity and neighbouring forests and importantly occur in addition to rapidly occurring climate change, further strengthening the case for forest conservation.

List of Figures

List of Tables

Chapter 1

1. Introduction

1.1 Motivation

Tropical deforestation is an issue of increasing importance within the context of our changing climate (Bonan, 2008). Tropical forests provide a range of key benefits to people and the environment, from regulating local and regional climate to controlling the energy and water transfer between the land surface and atmosphere (Baker and Spracklen 2019; Lawrence et al., 2022). Tropical forest loss has taken place in earnest since the 1950s (Rudel 1997), with the highest rates of loss traditionally in the south-eastern Amazon. Several studies assessing the climate impacts of tropical forest loss have focussed on the Amazon (Gash and Nobre, 1997; Alves et al., 2017; Baker and Spracklen, 2019), though given differences in background climate (Malhi and Wright, 2004; Esquivel-Muelbert et al., 2019), biogeography and drivers of forest loss (Lambin and Geist, 2003; Austin et al., 2017; Curtis et al., 2018; Pendrill et al., 2022), the climate impacts are unlikely to be uniform across tropical continents. In recent decades, tropical deforestation has extended beyond the Amazon into the previously less developed southern and central Amazon as well as the Congo basin (Tegegne et al., 2016) and Southeast Asia (Seymour and Harris 2019). There are substantial differences between the three main tropical forest regions and correspondingly the climate impacts across the tropics will vary.

With the proliferation of tropical forest loss and increased media interest, greater numbers of people than ever before are aware and concerned with deforestation and the compounding impact it could have on climate change. To a large extent, the public are concerned with the impacts on biodiversity and the reduction of carbon storage, however of at least equal importance, is the impact on local temperature and rainfall. Assessing the impacts of deforestation on local climate is critical to better inform the public and policy makers so that effective action and legislation can be integrated to mitigate and remediate impacts. This project aims to bring together existing knowledge of how forests affect climate and broaden our understanding of the climate response to deforestation in tropics at local scales in both the present and future. In this introductory chapter I will explore historic and present tropical land cover change, how vegetation interacts and impacts its environment and lastly how we can sense and model these impacts.

1.1.1 Contemporary Tropical Land Cover Change

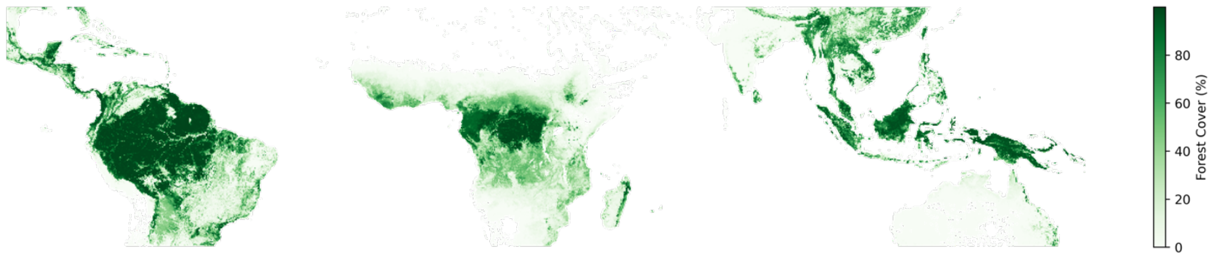

Figure 1.1. *Tropical forest cover in 2003 using satellite data from Hansen et al. (2013). Area is constrained by latitudes of 30^o N-S. Forest cover is shown in 2003 as this is the start year of the analysis of climate impacts in Chapter 4.*

Forests covering boreal, temperate and tropical lands amount to around 42 million km^2 (Bonan, 2008), providing wide ranging habitats and ecosystem services from carbon storage and sequestration to improving social wellbeing. Tropical forests cover only 7% of the land surface, however, they contain two thirds of the Earth's floral and faunal diversity (DeFries et al., 2005; Estoque et al., 2019). Figure 1.1 shows the extent and percent coverage of tropical forests in 2003, with darker greens showing areas of high forest cover. There are three discrete regions of moist tropical forest which are distinguished by their dark green colour in Figure 1.1, the Amazon basin, the Congo Basin and Southeast Asia (SEA).

Table 1.1 describes the forest extent in Brazil, the Democratic Republic of Congo (DRC) and Indonesia, which are the largest countries by area in each of the three main tropical forest regions. In 2020, Brazil has by far the largest total forest extent. As a percentage of country area however, the DRC has the highest forest cover, followed closely by Indonesia then Brazil.

Table 1.1. *Forest area in 1990, 2020 and forest area change over time in hectares (ha), for each of the three main tropical forest countries (FAO, 2022). The DRC refers to the Democratic Republic of Congo.*

Country	Forest Cover in 1990 (ha)	Forest Cover in 2020 (ha)	Forest Change (ha)
Brazil	588,898,000	496,619,600	-92,278,400
DRC	150,629,000	126,155,240	-24,473,760
Indonesia	118,545,000	92,133,200	-26,411,800

Humans have dramatically changed the global land surface (Ramankutty et al., 2008), replacing once abundant natural forest with agriculture which now covers large tracts of the ice-free land (Ramankutty et al., 2008). The mid-latitudes and tropics were once covered in forests however agricultural intensification has meant that 12 million km^2 of forests and woodlands have been removed globally since 1700 AD (Mahmood et al., 2014) and an estimated 18 million km^2 (11% of global land surface) is currently farmed. Tropical forest loss in the 21st century, shown in Figure 1.2, is pervasive, however there are particular hotspots where strong land cover change has occurred in recent decades. These are the south-eastern Amazon, Sumatra and coastal Borneo.

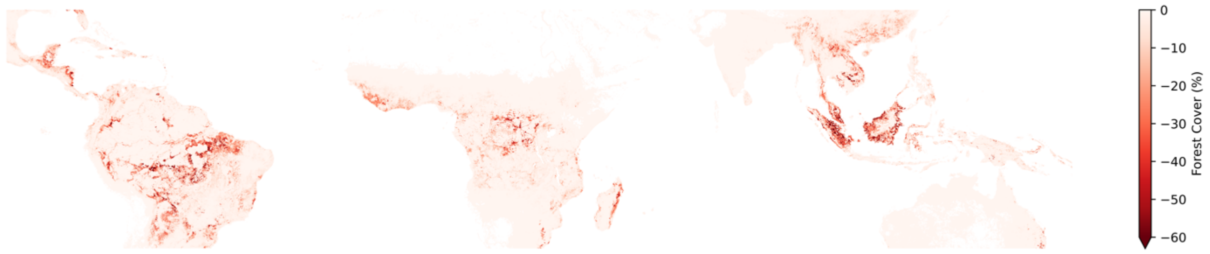

Figure 1.2. *Reductions in tropical forest cover between 2003 and 2020 (Hansen et al., 2013).*

The rate of tropical deforestation, as opposed to mid-latitude deforestation, increased sharply through the 20th century (Rosa et al., 2016). Presently, the highest rates of forest loss are in the tropics (Hansen et al., 2013), where agricultural expansion is a primary driver of land cover change as population increases demand more space for crops and cattle (Curtis et al., 2018). In particular, tropical forest loss has been enhanced by large-scale land acquisitions for intensive agriculture (Davis et al., 2020). Deforestation is a vague term and fails to capture the nuance of land use change. In recent years, researchers have sought to better represent the changes that forests undergo, classifying the forest loss by the dominant driver. Curtis et al. (2018) ascribe forest loss to classes such as commodity-driven deforestation (CA), shifting agriculture (SA), forestry, wildfire and urbanisation. These classes, observed through satellite imagery and sorted by machine learning algorithms attempt to bring nuance to the broad definition of deforestation. Across the tropics, forest loss ubiquitously results from CA and SA with less, but localised, pressure arising from forestry, urbanisation and wildfire. Commodity driven deforestation is dominated by commodity agriculture but also includes forest loss associated with mining and industry. Commodity agriculture is typified by large scale, intensive and long term or permanent conversion of forest to crops or pasture. CA is commonly found in the heavily deforested arc of deforestation in the Amazon and Sumatra, where soybeans and rubber are the principal crops (Jamaludin et al., 2022). SA is defined by conversion to agricultural land that is later abandoned followed by forest regrowth (Curtis et al., 2018). This type of forest clearance is dominant in the Congo basin and some parts of Southeast Asia and the Amazon. Both Curtis et al. (2018) and Pendrill et al. (2022) highlight difficulties with defining land as cleared by SA, including outlining the period of time land is allowed to take to regenerate. SA produces a heterogenous landscape of mixed small-scale fields, forest patches and regeneration, common across much of the Congo basin (Curtis et al., 2018; Fritz et al., 2022). Of the deforested land, only 45-65% becomes agriculturally productive, with the remaining land either allowed to regenerate, or transition to other non-agriculture, non-forest land uses (Pendrill et al., 2022) and regrowth. Shifting agriculture may be declining globally replaced by more CA (Heinimann et al., 2017; Tyukavina et al., 2017) with potential implications for climate.

Rates of tropical forest loss have historically been the highest in the Amazon, however as Amazonian deforestation rates started to decrease at the start of the 21st century, rates of deforestation in SEA overtook those in South America (Rosa et al., 2016). Table 1.1 illustrates that Indonesia has seen the greatest relative losses in forest cover over the period 1990 to 2020, with losses of 22.2%. This is followed by the DRC with 16.2% and Brazil with 15.6%, despite having the highest absolute losses in forest cover.

Ensuring the maintenance of a complete forest structure is integral for the resilience of the forest and the life systems it sustains (Watson et al., 2018). Preserving these intact areas in officially protected areas (PA) can be effective in reducing deforestation. Bebber and Butt (2017) find that PAs have reduced deforestation related carbon emissions by 29% (2000-2012) when compared to expected deforestation rates. Protected tropical forests in the Americas account for a 368.8 TgC y^{-1} reduction in carbon emissions, whilst in SEA and the Congo they account for 25.0 TgC y^{-1} and 12.7 TgC y^{-1} respectively (Bebber and Butt, 2017). These PAs have varying effectiveness across the tropics, with those in SEA proving ineffective at reducing deforestation (Spracklen et al., 2015). Their effectiveness is driven to a large extent by individual local factors rather than poor legislature or governance (Bebber and Butt, 2017).

Tropical forests have huge benefits for local and global ecosystems, people and climate (Baker and Spracklen, 2019). Observing how these areas change is a crucial part in understanding land cover change (LCC) in the tropics (Turubanova et al., 2018). The patterns, mechanisms and drivers of LCC vary greatly across the tropics, consequently, the impacts of LCC on climate and the atmosphere are expected to differ.

Here, I summarise the impacts of LCC across the tropics, focussing on the three main tropical forest regions, the Amazon Basin, the Congo Basin and SEA.

The Amazon

The Amazon biome is 7 million km^2 with tropical humid forests covering 5.3 million km^2 (Marengo et al., 2018) – this represents 40% of the Earth's tropical forests. Figure 1.3 shows the amount of forest cover within the Amazon biome, showing there are large areas of high forest cover interspersed with lower forest cover along river and road tributaries. Herein the "Amazon" refers to the Amazon biome, however the Brazilian Legal Amazon is frequently used in other studies. It is estimated that between 150 and 200 Gt C are stored in the Amazon (Malhi et al., 2006), equivalent to 1.5 decades of global anthropogenic carbon emissions (Soares-Filho et al., 2006).

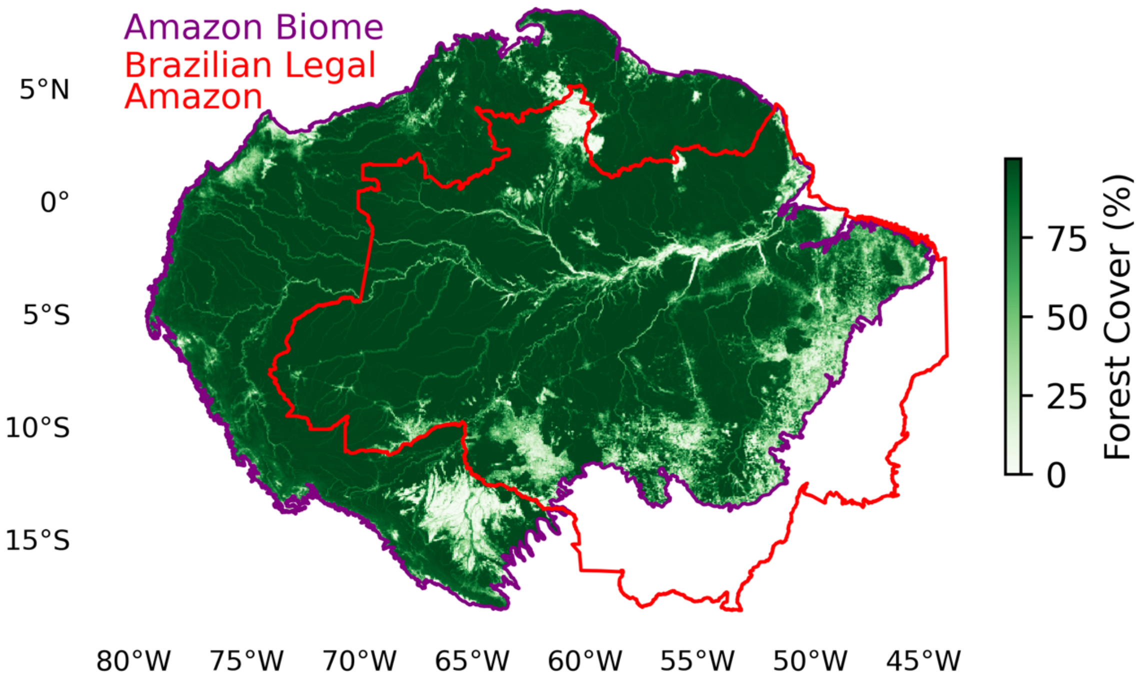

Figure 1.3. *Map showing forest cover in the Amazon biome in 2003. The Amazon biome (purple) and Brazilian Legal Amazon (red) boundaries shown to demonstrate the different definitions of often used by studies considering land cover in the Amazon (source: http://terrabrasilis.dpi.inpe.br/en/download-2/). Forest cover data from Hansen et al., (2013).*

The Amazon has a long history of degradation and exploitation (Fearnside, 2005), which began to accelerate during the 1970s when the Transamazon Highway was created, increasing the accessibility of previously remote areas of forest. With the road access, farmers migrate and settle on these lands, their clearances creating stratified strips of cropland perpendicular to the roads, referred to as ‘fish-bone’ deforestation (Pedlowski et al., 1997). Once crop yields start to fall, the farmers often convert the degraded land to pasture, eventually leaving or selling the land to companies who consolidate the land. Since the 1970s, Amazon development has increased, with the most substantial deforestation along the ‘arc of deforestation’ in the southern Brazilian Amazon (Davidson et al., 2012), which can be seen in Figure 1.2. Through the 1980s and 1990s, agricultural expansion continued unabated with greater than 55% of deforestation happening to intact forests (Gibbs et al., 2010). As of 2003, around 20% of the original forest has been deforested (Soares-Filho et al., 2006; Davidson et al., 2012; Spracklen and Garcia-Carreras, 2015), with a business-as-usual projection of 40% by 2050. In Brazil, 1% of the population own 81% of the productive land (Armenteras et al., 2019). The remaining land is either unproductive or prohibitively expensive, which means that those wishing to purchase, or lease land are faced with either financial burden or acquiring land illegally. Deforesting intact or degraded land is therefore an attractive option for many rural people.

The start of the 21st century saw Amazonian deforestation slow, in part due to tighter internal legislation controlling LCC and pressure from foreign nations (Nepstad et al., 2014; Rosa et al., 2016; Turubanova et al., 2018). Following a period of several years where deforestation rates remained relatively stable (Bebber and Butt, 2017), recent evidence suggests Brazilian deforestation rates are now starting to rise again (FAO, 2022). 2019 saw unprecedented numbers and extent of fires associated with land clearance (Escobar, 2019), which echoes the shift to small-scale, patchy deforestation reported by Kalamandeen et al. (2018). The authors show that the number of large forest clearings (>50 ha) has been significantly reduced (46%, 2001-2014), which is likely due to enhanced monitoring through satellite observations leading to more effective policy implementation. However, Kalamandeen et al (2018) show that small-scale clearings (<1 ha) have increased in number and geographic extent (34% rise from 2001–2007 to 2008–2014). The shift to small-scale agricultural clearings may be attributed to the government’s encouragement of remote settlement and a lack of enforcement of the Forest Code (Schons et al., 2019).

The Congo Basin

The Congo Basin contains the second largest humid tropical forest (Table 1.1) after the Amazon (Tyukavina et al., 2018). The rate and amount of deforestation is less here than in the Amazon (FAO, 2022), however in relative terms compared to total forest area, the amount of forest loss is similar (Table 1.1).

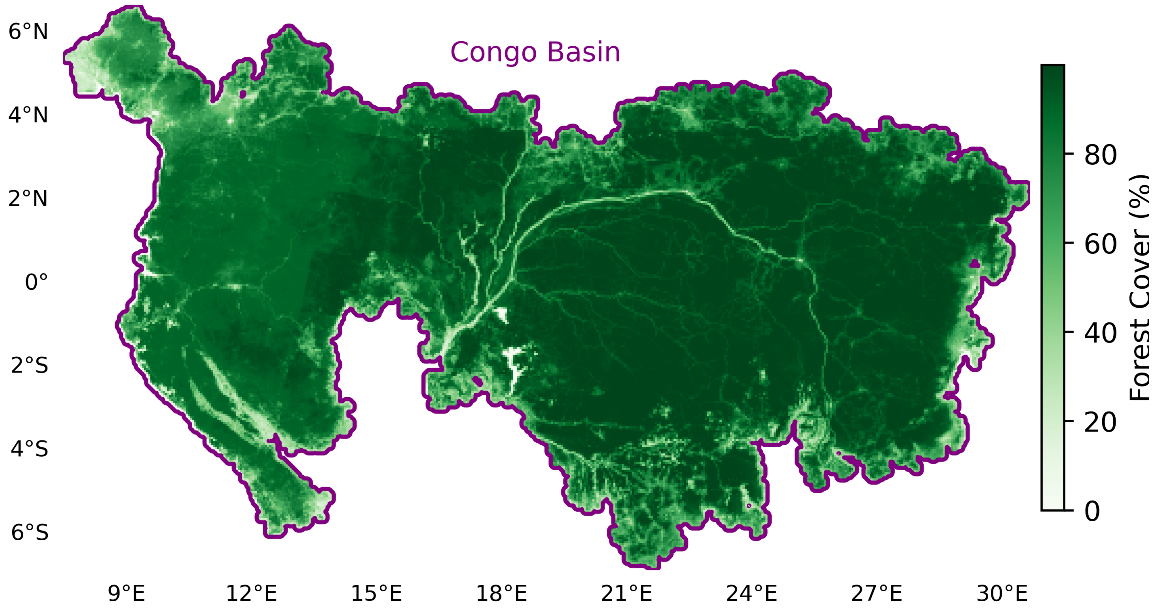

Figure 1.4. *Map showing forest cover in the Congo Basin (outlined in purple) in 2003. Forest cover data from Hansen et al., (2013).*

The Democratic Republic of Congo (DRC) contains around a third of the Congo Rainforest with 1.9 million km^2 of forest cover (Hansen et al., 2013), a map of which is shown in Figure 1.4. The highest forest cover is focussed away from major population hubs in the south and east. The other Central African countries that contain tropical forest are Cameroon, Central African Republic, Equatorial Guinea, Gabon and the Republic of Congo. In many of these countries, deforestation is largely driven by subsistence agriculture, in part because this is the only revenue option for much of the population (Rudel, 2013). Countries that export oil such as Gabon and Equatorial Guinea can afford to import some of their food, reducing the amount of land needed for industrial agriculture, and therefore allowing them to preserve more of their primary forest. The economies in these countries are more developed, driving rapid urbanisation, which also reduces small-scale rural deforestation (Rudel, 2013). For decades, foreign investment has been an economic cornerstone in central Africa, often in return for agro-industrial plantations, and the extraction of timber or minerals, all of which drive deforestation (Feintrenie, 2014; Tegegne et al., 2016; Tyukavina et al., 2018).

Southeast Asia

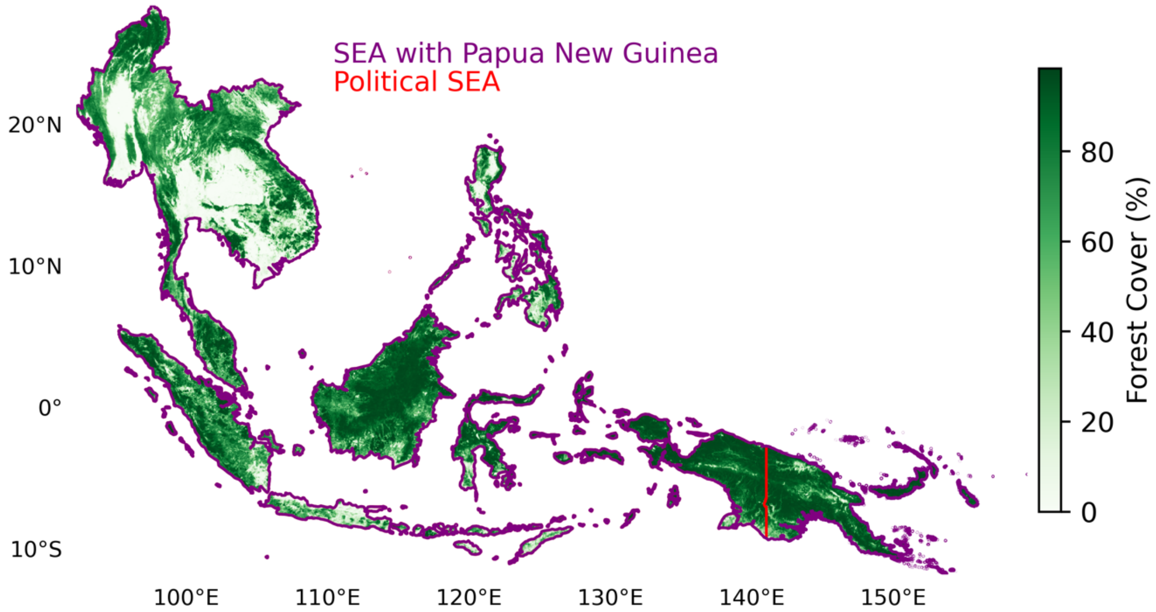

Figure 1.5. *Map of forest cover in SEA in 2003. SEA is outlined by two definitions, Southeast Asia including Papua New Guinea (purple) and the Political definition of Southeast Asia (red), which excludes Papua New Guinea. Our analysis utilises the former, including Papua New Guinea (shapefile source: https://www.marineregions.org/gazetteer.php?p=details&id=18092).*

Southeast Asia (SEA) contains 15% of the Earth's tropical forest (Sodhi, Posa, et al., 2010; Stibig et al., 2014; Estoque et al., 2019). Figure 1.5 shows the spatial coverage of forest in SEA, showing densely forest covered land in the interior of Borneo and West Papua, with patchier forest cover on Sumatra and the coast of Borneo. We chose to use a modified geographical definition of SEA, including Papua New Guinea, rather than the more common political definition (Figure 1.5). The present rate of tropical forest loss in Indonesia is the fastest among the three regions (Hansen et al., 2013), with the majority of the deforestation occurring in humid and low-land forests (Figure 1.2). This loss carries severe impacts for the ecosystems dependent on forests (Zeng et al., 2018). Lowland agriculture in SEA is a primary driver of deforestation, however Zeng et al. (2018) find that deforestation rates in the highlands have previously been underestimated and contribute significantly. Critically, agricultural expansion in the highlands often takes places at the expense of primary or recovering secondary forests. In the study by Estoque et al., (2019), it was shown that between 2005 - 2015, SEA lost 80 Mha of forest, 62% of which was in Indonesia, 16.6% in Malaysia, 5.3 % in Myanmar and 5% in Cambodia. In Borneo alone, 18.7 Mha of old growth forest was lost over the period 1973 - 2015 (Gaveau et al., 2016). However, there was only 9.1 Mha of industrial plantation expansion indicating a lag between LCC and plantation creation (Gaveau et al., 2016). This complicates the attribution of cause and limits the scope of policy to mitigate deforestation. Up to 2014, oil palm plantation was the leading driver of deforestation in Indonesia, accounting for two fifths of the deforestation (Austin et al., 2019). Since 2016 however, oil palm and pulpwood plantations have accounted for <15% of the total new deforestation (Seymour and Harris, 2019). Between 2014 and 2015 small-scale farming accounted for a quarter of all deforestation (Seymour and Harris, 2019), whilst in 2015, the fires are attributed to 20% of the years forest loss (Seymour and Harris, 2019). In 2016 (Austin et al., 2019) and 2019 (Normile, 2019), considerable fire activity was again responsible for burning large swathes of forest.

1.2 Land Surface Vegetation Properties and Fluxes

Land surface properties and fluxes play a substantial role in shaping our climate system. There are many vegetation types covering the land surface, all of which have different properties and fluxes. I describe here, the dynamic interplay between vegetation, the land surface and the atmosphere.

1.2.1 Vegetation Impacts on Land Surface Properties

Land surface properties are strongly affected by the presence or absence of vegetation, and by vegetation type (Lawrence and Vandecar (2015) and references therein). Here I examine the major properties that can be modified by vegetation. The Amazon, Congo and SEA all have different LCC transitions and this will modify the land surface properties in different ways.

Table 1.2. *Key surface property values for tropical forests and pasture. Data from Spracklen et al., (2018), adapted from Gash and Nobre (1997).*

Property	Tropical Forest	Pasture
Vegetation Height	30 m	0.5 m
Canopy Cover	100%	85%
Leaf Area Index	5.2 m^2 m^{-2}	1-2.7 m^2 m^{-2}
Albedo	0.13	0.18

Table 1.2 provides an overview of the differences in key surface properties for tropical forest and pasture land cover types. Tropical forests have a very dense closed canopy structure which provides 100% canopy cover, whilst pasture, with its lower vegetation height, provides 85% canopy cover. The 15% decrease in canopy cover from tropical forest to pasture corresponds to a decrease in leaf area index of between 2.5 and 4.2 m^2m^{-2}. This reflects the difference in density, arrangement and size of leaves. Connected to this, the amount of radiation reflected by the surface (albedo) of pasture is greater than that of tropical forests.

Figure 1.6 summarises the key differences in surface properties between tropical forests and crops or grassland. Forests have greater rooting depths than crops and grasses meaning they can access deep soil moisture, providing resilience in times of drought. Forests also have higher aerodynamic roughness due to their varied vertical structure, meaning their surface generates more turbulence as wind passes across the land than pasture and crops (Spracklen et al., 2018). The amount of incident solar radiation absorbed by forests is greater as they are darker in colour and they have rougher surfaces, scattering more radiation than pasture and crops (Scott et al., 2018). Forests therefore have higher net radiations than pasture and crops.

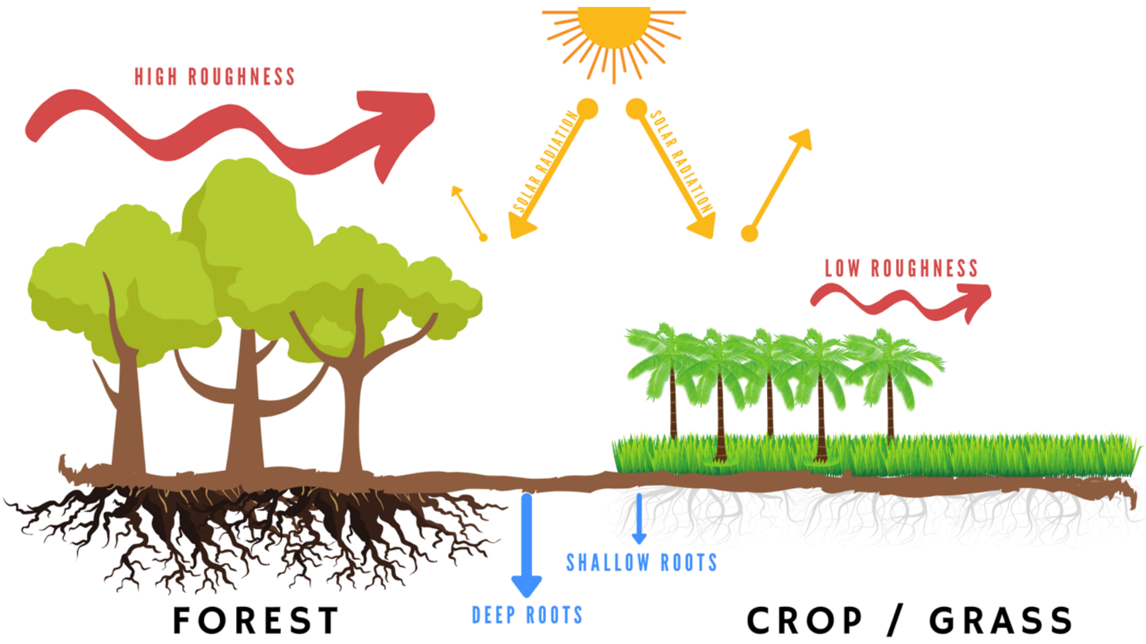

Figure 1.6. *Surface properties of tropical forest and crop (e.g., Oil palm)/ grassland (e.g., pasture). Forests have darker and rougher surfaces than crop and grass land covers. They also have lower aerodynamic roughness and have deeper root systems.*

The process of LCC can take place over many years (Mahmood et al., 2014) and at a variety of length scales from sub-kilometre to hundreds of kilometres. Forest often follows a complex and non-linear path to other vegetation types, such as pasture, grassland, after which, if abandoned, there is the potential for degraded land to return to forest. When left to reforest, the "secondary forest" can mature to have similar properties to undisturbed forest (Giambelluca et al., 1997; Spracklen et al., 2018; Wang et al., 2020). Quantifying the changing impacts of vegetation of surface properties is therefore complicated and case dependent. Below I outline in more detail, the broad impacts that vegetation has on surface properties.

Albedo

Albedo is a dimensionless quantity representing the fraction of incident solar radiation that is reflected by a surface. Figure 1.6 diagrammatically shows more incident radiation being reflected by the “brighter” cropland than the “darker” forests. Since vegetation can change the albedo of a surface, it has an important role in maintaining or modifying the surface energy budget (Gash and Shuttleworth, 1991). Albedo can be driven by phenology (the seasonal change in vegetation), however the impacts in tropical regions are far less important than in higher latitude forests. As shown in Table 1.2, the albedo of forest is generally lower, due to their dark colour and irregular surface, than the albedo of pasture (Gash and Nobre, 1997; von Randow et al., 2004; Spracklen et al., 2018). Similarly, the albedo of crops and desiccated soils are greater than forests due in part to their more uniform surface. It follows that LCC from forest to pasture or cropland leads to an increase in surface albedo. Due to non-linear LCC, changes to albedo are often complex over regional scales (Kirschbaum et al., 2011) and indeed, recovering secondary forests can return to primary forest albedo values within 15 years (Giambelluca et al., 1997).

Leaf Area Index

Leaf area index (LAI) measures the leaf surface area per unit ground area (m^2m^{-2}). It can be estimated from below the canopy at ground level using apparatus to examine the percentage canopy cover. It can also be estimated from remote sensing satellite data using algorithms (Kim et al., 2012; Ramoelo et al., 2014; Wan, 2014). Tropical forests typically have a LAI of ~5.2 m^2m^{-2}, substantially higher than pastures with 1-2.7 m^2m^{-2} (Table 1.2). Vegetation surface area controls LAI, determining the amount of area available for evaporation and gas exchange (Bruijnzeel et al., 2011). Pielke et al. (2007) explain that when LAI and therefore interception is reduced, runoff is increased meaning less water is retained locally, which can have a direct impact on the amount of vegetation that can survive in the environment. Therefore, when forests are deforested, there can be lower water availability leading to increased vulnerability of vegetation including adjected forests to environmental stress (Laurance and Williamson, 2001).

Surface Roughness

As air passes over land, the surface interacts with the air flow. If the surface is heterogeneous, turbulent eddies can form which deflect the flow, creating circulations. Forests are a varied land type and as such have a rough surface due to their vertical structure and LAI (Table 1.2), whereas crops and pasture have relatively smooth surfaces. This increased roughness can effectively transfer heat away from the surface having a cooling effect (Spracklen et al., 2018). This cooling effect can be of equal or greater magnitude than the warming effect of albedo in the tropics (Davin and de Noblet-Ducoudre, 2010; Winckler et al., 2019; Lawrence et al., 2022). Where forest has been deforested, the surface becomes smoother which reduces the magnitude and speed of turbulent heat exchange, resulting in the surface maintaining heat (Spracklen et al., 2018) and a less well mixed boundary layer (BL). At local scales, a complex mosaic of forest patches and areas of degradation may have higher surface roughness than undisturbed forest (Spracklen et al., 2018). Over intermediate scales (tens of kilometres), deforestation leaves rough forest edges divided by open expanses. This can form larger, mesoscale circulations which induce the formation of precipitation (Garcia-Carreras et al., 2010; Khanna and Medvigy, 2014) and in this way influence regional climate.

Rooting Depth

Tropical rainforests can have far deeper roots and greater access to soil moisture than pasture, shrubs and grasses. From observations, trees have the greatest rooting depths, followed by shrubs and herbaceous species (7.0 ± 1.2 m, 5.1 ± 0.8 m and 2.6 ± 0.1 m respectively) (Canadell et al., 1996). As access to soil moisture diminishes through the dry season, the ability of the system to maintain a moist environment decreases. Forests in this way are more resilient than pasture because their deep roots can access deeper ground water, allowing them to grow and transpire longer into the dry season (Nepstad et al., 1994; Kleidon and Heimann, 2000).

1.2.2 Impact of Vegetation on Land Surface Fluxes

Forests can modify the exchange of water, energy and gases (Salati et al., 1979; Silva Dias et al., 2002; Lovejoy and Nobre, 2018; Spracklen et al., 2018; Baker and Spracklen, 2019) between the surface and the atmosphere. Following LCC, these fluxes change, which influence the local and regional climate (Nobre et al., 1991; Gash and Nobre, 1997; D'Almeida et al., 2007; Grace et al., 2014; Lawrence and Vandecar, 2015; Conte et al., 2019), typically resulting in warmer and drier conditions (Bright et al., 2017; Conte et al., 2019). Figure 1.7 explores the impact that land cover can have on surfaces fluxes. Each of the main fluxes, evapotranspiration, energy, gases and aerosols will be explored in the following sections.

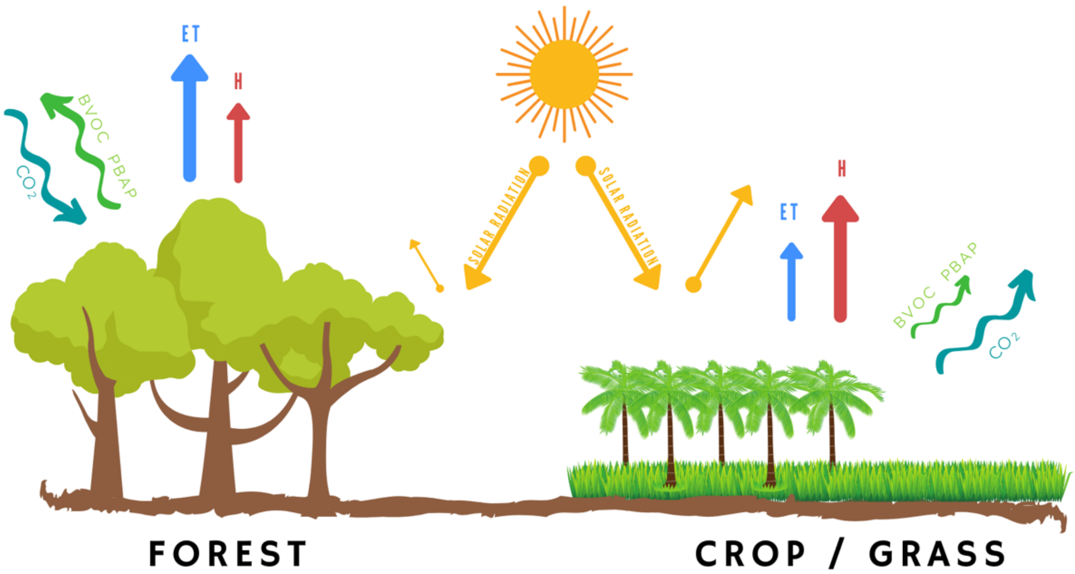

Figure 1.7. *Surface fluxes in a tropical forest and crop or grassland. Compared to agricultural land, forests have lower albedo, higher aerodynamic roughness and greater access to soil moisture. Forests have higher evapotranspiration (ET) and latent heat flux and lower sensible heat flux (H). Conversion of forest to crops or grass leads to an increased in emissions of CO_2 and reduced biogenic emissions (biogenic volatile organic compounds (BVOC), primary biological aerosol particles (PBAP)).*

Evapotranspiration

Evapotranspiration (ET) is a two-part process that describes the transfer of water from the land to the atmosphere. It comprises the physical evaporation and the biological transpiration of water from vegetation (including soil). Rooting depth, and therefore the availability of soil moisture to the system, is a strong control on the ET flux, since transpiration is the uptake of soil moisture through the roots and efflux through the stomata during photosynthesis (Seneviratne et al., 2010). ET can also be controlled by available surface energy, whereby reductions in precipitation and therefore cloud increase incident solar radiation and therefore in ET (Baker et al., 2021).

The rates of forest ET are generally higher than for other tropical land covers (Jipp et al., 1998; Zhang et al., 2010) due to a combination of factors including high LAI, deep soil moisture access, low albedo and high roughness. Due to high LAI, forests can intercept more precipitation allowing for greater rates of evaporation, as well as providing a large surface area for transpiration. The ability to access moisture from deep in the soil is part of the reason that rainforests can maintain a year-round moist environment. Comparing different vegetation types in the Southwest Amazon, von Randow et al. (2004) show that ET over forested areas is 20% and 40% greater in the wet and dry season respectively when compared to pasture. Critically, Kunert et al., (2017) find that the largest trees are disproportionately responsible for ET in the amazon, contributing 70% of the ET in dry months. During the dry season, there is less rainfall, therefore transpiration is almost entirely responsible for ET (Kunert et al., 2017). These findings outline the importance of old-growth and primary forest and the detriment that selective logging of the largest trees can have on the regional ET flux.

Giambelluca et al. (2003) observe the effects of meteorological processes on a small tropical forest patch to show that transpiration at the forest edge is enhanced by micrometeorological effects. In the same way, high aerodynamic roughness, as found in forest land types, enhances evaporative fluxes compared with non-forest. Deforestation across the tropics is increasing fragmentation of the forest landscape. The patches of forest that remain are decreasing in size (Brinck et al., 2017) which has important consequences for habitats, tree mortality and surface fluxes. Brinck et al. (2017) find that 19% of tropical forests sit within 100 m of the forest edge, providing evidence that forest edge effects are of significance. These perimeter zones have greater vulnerability to higher wind speeds and water stresses as well as exposure to harsher temperature variability. Giambelluca et al. (2003) propose that higher rates of ET, due to forest edge effects, could compensate partly for the reduction in ET from deforestation.

Energy

Figure 1.7 shows that incoming (incident) solar radiation is absorbed and reflected in different amounts for different land covers. Radiation can be split into sensible (H) (heating of the lower atmosphere) and latent heat fluxes. Latent heat flux is described as the energy required to change the phase of water from liquid to gas during ET (Giambelluca et al., 2000). The ratio between the latent and sensible heat fluxes is known as the Bowen ratio (Bowen, 1926) and can be described as sensible divided by latent heat. The properties of the land surface determine the partitioning of surface net radiation. Forests, with high ET fluxes and rough surfaces, convert a greater portion of net radiation into latent energy (lower Bowen ratio) than pasture (shown in Figure 1.7), where the partition favours sensible heating (Giambelluca et al., 2000; Roy and Avissar, 2002; Restrepo-Coupe et al., 2013). Roy and Avissar (2002) present flux tower measurements from the Amazon, finding a Bowen ratio of 0.28 and 1.25 over rainforest and pasture respectively. These results outline the large differences in the partitioning in energy for different land cover types. Lee et al., (2011) explain that the relationship between the Bowen ratio and aerodynamic resistance can be expressed as the energy redistribution factor, f which better describes how land cover types interact with their environment. With high aerodynamic resistance, forests both cool the atmosphere through efficiently dissipating sensible heat and releasing latent heat (ET) (Sy et al., 2017).

Lower albedo leads to higher net surface radiation, resulting in a warmer forest surface compared with pasture, whereas the effect of higher latent heating (ET) and greater aerodynamic turbulence of forests cools the surface (Baldi et al., 2008; Garcia-Carreras et al., 2011). ET and turbulence combine to produce the dominant effect in tropical forests, hence forests have an overall cooling effect (Davin and de Noblet-Ducoudre, 2010; Spracklen et al., 2018).

Gases and Aerosols

A few important sources and sinks of gases and aerosols in the tropical forest environment are outlined in Figure 1.7. Forests sequester atmospheric carbon, storing more biomass than pasture and cropland, deforestation is therefore a source of CO_2. Until the 1930s, LCC was a greater source of CO_2 to the atmosphere than fossil fuels, wherein it was overtaken (Li et al., 2017). In the years 1990 to 2010, tropical LCC accounted for around 15% of anthropogenic carbon emissions, or 1.4 PgC y^{-1} (Houghton, 2013) emitted to the atmosphere.

In tropical forests, the number and mass concentrations of aerosol tend to be small, but there is a high organic mass fraction (Martin et al., 2010). Figure 1.7 shows the flux of biogenic volatile organic compounds (BVOC) and primary biological aerosol particles (PBAP) which oxidise to form secondary organic aerosol (SOA) (Spracklen et al., 2018; Rap et al., 2018). The emissions of BVOCs also respond readily to changes in temperature levels of CO_2 (Rap, et al., 2018). SOA changes the radiative balance at the surface directly through scattering and absorbing radiation and indirectly through altering cloud properties (Scott et al., 2014; Rap et al., 2018). Scott et al. (2014) find that overall, SOA likely produces a negative radiative effect, further indicating the role forests play in cooling the surface. Recently, Rap et al. (2018) show that SOA produces a radiation fertilisation effect by diffusing radiation, in this way forest canopies naturally alter the amount of energy they receive, providing more energy to grow.

Fire is an often used mechanism of forest clearance and generates high aerosol mass and number concentrations through the burning of biomass (Martin et al., 2010). Similar to SOA, black and organic carbon produced from fires scatter and absorb incoming radiation, reducing surface and increasing atmospheric temperature (Tosca et al., 2013; Tosca et al., 2014; Kolusu et al., 2015; Tosca et al., 2015). Through the indirect effect, aerosol form cloud condensation nuclei (CCN), the precursors to cloud formation. Where high aerosol concentrations prevail, high numbers of CCN increase cloud albedo (Tosca et al., 2014) thereby causing clouds to reflect more incident radiation and cool the surface. Both direct and indirect effects work to stabilise the lower atmosphere, which lead to decreases in regional precipitation (Boers et al., 2017). Precipitation can be decreased when high CCN from smoke particles contribute to high cloud drop numbers which are then too small to precipitate (Rosenfeld, 1999; Pielke et al., 2007; Tosca et al., 2014). Aerosol from smoke can also inhibit convection (Tosca et al., 2014; Tosca et al., 2015) which limits cloud fraction. This can form a positive feedback whereby increased concentration of smoke particles inhibit upward lift, which reduces cloud fraction, which warms and dries the surface, resulting in favourable conditions for increased fire activity.

1.3 Vegetation Impacts on Temperature and Precipitation

The analysis in Chapters 3 to 5 explores the impacts of vegetation on temperature and precipitation. Here I describe how the differences in surface properties and fluxes between different land cover types can alter the land surface temperature (LST) and precipitation. LST and precipitation responses to LCC are often interconnected so I describe their impacts simultaneously.

Vegetation type and coverage affects the local and regional land surface temperatures (Bonan, 2008). At the local scale, due to their high rates of evapotranspiration, tropical forests can be cooler than surrounding croplands and grass through latent heating (Ellison et al. (2017) and references therein). In the tropics, individual trees evaporate and transpire 100s of litres per day, which translates to a cooling equivalent to 70 kWh for every 100 L (Ellison et al., 2017). This equates to the same power as 2 household central air-conditioning units per day. Utilising their deep roots, trees can maintain this functioning throughout the year, even during periods of high stress such as drought (Teuling et al., 2010; Ellison et al., 2017). Contrastingly, tropical forests have lower albedo than crops and grass, resulting in higher sensible heating and a warmer surface (Lee et al., 2011; Li et al., 2015). In the tropics these are the two main processes controlling land surface temperature, with ET being dominant and therefore controlling land surface temperature, meaning forests are relatively cool.

Forests can generate low-level clouds (Teuling et al., 2017; Duveiller et al., 2021) through convection of their relatively moisture rich environment as well as through the emissions of BVOCs (Spracklen et al., 2008; Scott et al., 2014). This increased low-level cloud can increase the amount of incident radiation being reflected, therefore cooling the surface (Ban-Weiss et al., 2011; Heiblum et al., 2014). This process is tempered by the trapping of long wave radiation below the cloud layer.

The scale, distribution and fragmentation of trees can influence the potential cooling ability of the forest (Arroyo-Rodríguez et al., 2017). The cooling benefits of forests are known and appreciated by the people living in those regions (Sodhi, Lee, et al., 2010; Meijaard et al., 2013), who can notice the local scale micro-climates caused by deforestation and degraded forests. Using the example of protected forests, Xu et al., (2022) show that these forest refuges can buffer against warming air temperatures from LCC, particularly mitigating extreme heating events. Extremes in temperature are likely to occur more frequently with climate change (Ellison et al., 2017) and preserving forests can be a crucial mitigator of risk (Staal et al., 2018; Alves de Oliveira et al., 2021), which can avoid inhospitable environments for people and ecosystems (Masuda et al., 2020).

Vegetation can have a large effect on the amount of precipitation a region receives and generates. Observations and modelling studies have comprehensively shown that tropical deforestation can influence surface fluxes (Baker and Spracklen, 2019) which drive atmospheric motion in the boundary layer (Weaver and Avissar, 2001; D'Almeida et al., 2007; Scott et al., 2018; Conte et al., 2019), precipitation and the formation of clouds (Sud and Smith, 1985; McGuffie et al., 1995; Costa and Foley, 2000; Pielke, 2001; Lawton et al., 2001; Cutrim et al., 2002; Silva Dias et al., 2002; Durieux et al., 2003; Fisch et al., 2004; Ray et al., 2006; Wang et al., 2009; Tosca et al., 2011; Spracklen and Garcia-Carreras, 2015; Quesada et al., 2017), however the nature and magnitude of the forcing has been disputed. Studies find a range of possible climate impacts due to tropical deforestation, arising from using a wealth of different methodologies, different observed mechanisms and scales and different climate and land use change datasets. Precipitation has been observed to increase by studies which examine small scale deforestation (Chagnon and Bras, 2005; Khanna et al., 2017). The mechanisms that drive these increase, such as the vegetation breeze mechanisms (Figure 1.8) can be very different to the dominant drivers at larger spatial scales. At these larger scales, rainfall can decline as a result of reduced precipitation recycling and changes to large scale circulations (Lawrence and Vandecar, 2015; Leite-Filho et al., 2021). These different estimates produce an inconsistent and confusing picture when considering the overall impact forest loss can have on local and regional climate and lead to a need for a unifying narrative.

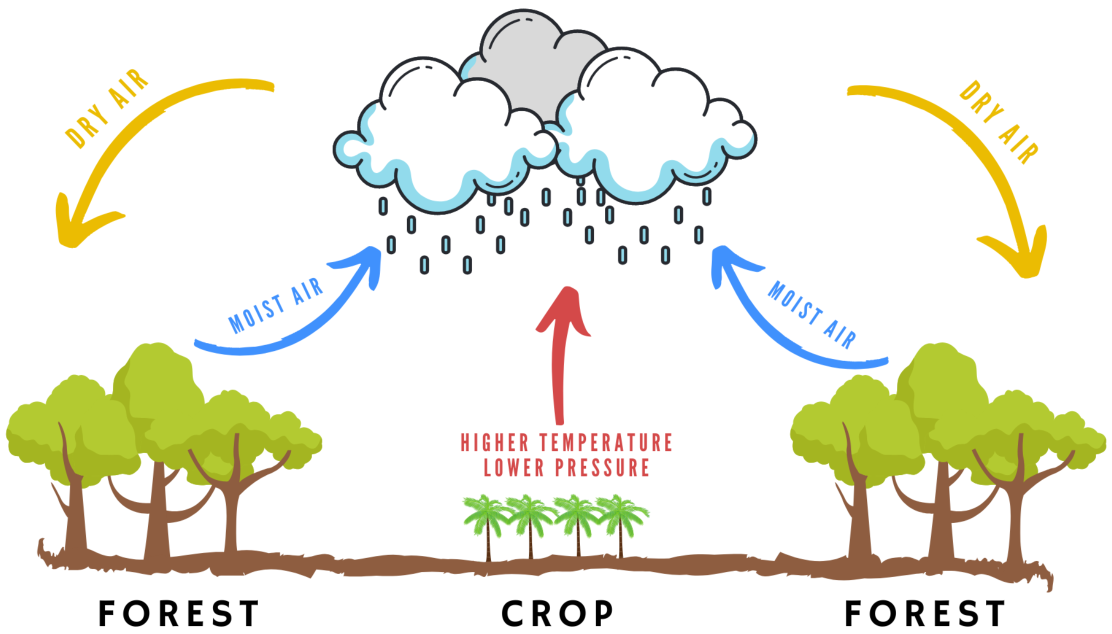

Figure 1.8. *The vegetation breeze mechanism which originates from temperature gradients in land cover types. Moist cool air can be drawn from forests towards areas of low pressure (higher temperature), thus creating a breeze and potentially forming precipitation over deforested land. The subsiding dry may act to suppress precipitation over the forest.*

The surface and BL temperatures of tropical forests are generally cooler than deforested land. Alkama and Cescatti (2016) show the magnitude of the cooling can be up to 2 K (mean annual maximum surface temperature). Through non-radiative processes, eight out of nine common LCC scenarios can lead to large increases in surface temperature, with tropical LCC accounting for (up to) 75% of all surface warming in recent times (1950-2010, (Bright et al., 2017)). As a result of warmer surfaces, the BL over pasture is deeper, warmer and drier than the BL over forests (Silva Dias et al., 2002). This effect is exacerbated in the dry season (Silva Dias et al., 2002) when forests retain the ability to access deep soil moisture, allowing them to maintain a cool and moist surface. The difference in temperature between two different land types can initiate local circulations known as vegetation breezes (Pielke, 2001). Garcia-Carreras et al. (2010) directly observe this effect in their West African field campaign showing that the temperature gradient can determine the strength of the breeze. Models too predict the existence of deforestation induced vegetation breezes occurring at transitions in land cover the Amazon (Baidya Roy et al., 2003; da Silva and Avissar, 2006; Roy, 2009; Saad et al., 2010) and West Africa (Garcia-Carreras et al., 2011; Garcia-Carreras and Parker, 2011). Figure 1.8 outlines the principal characteristics of this situation; warm rising air over pasture generating low pressure, which then draws in moist cool air from forests. The convergence of this moist air can lead to cloud formation (Garcia-Carreras et al., 2011) and precipitation (Wang et al., 2000; Chagnon and Bras, 2005; Roy, 2009; Garcia-Carreras and Parker, 2011; Funatsu et al., 2012; Negri and Adler, 2018) over pasture and cropland. Evidence exists that the opposite response occurs over the forest, whereby the subsiding dry air suppresses precipitation (Garcia-Carreras et al., 2011; Garcia-Carreras and Parker, 2011) for tens of kilometres into the forest.

As the scales of deforestation increase to >10 km, thermally driven circulation may be superseded (Patton et al., 2005) by the impact of reductions in roughness (Khanna and Medvigy, 2014) which combines with lower ET and higher sensible heating to drive mesoscale circulation. These circulations are dependent on the magnitude on the depth of the atmospheric boundary layer and the turbulent sensible heat flux (Pielke, 2001). High sensible heat flux over deforested patches induces vigorous boundary layer development and convergent lift provides the mechanical energy necessary for parcels to reach level of free convection (Knox et al., 2011).

Figure 1.9 shows the movement of atmospheric moisture inland across a tropical rainforest (adapted from (Eltahir and Bras, 1996; Spracklen et al., 2018), principally through mesoscale circulations. Moisture is retained within a system through a series of cycles occurring downwind of one another (Fig. 1.9). At a global scale, 70 % of land evaporation rains down over land (Tuinenburg et al., 2020). Salati et al. (1979) showed that in the Amazon, as air passes from the Atlantic to the West of the basin, moisture is recycled 5 - 6 times. Up to 40% of terrestrial precipitation can be sourced from terrestrial ET (Van Der Ent et al., 2010), though this could be as much as 70% in the southwestern Amazon (50% in Congo basin (Sorí et al., 2017)). These estimates do have uncertainties with the rate of vertical mixing of moisture in the atmosphere being the largest source of error (Tuinenburg and Staal, 2020). Where there is a large enough break in forest cover, the evaporative flux is diminished, and the cycle is muted with less moisture being carried downwind. This can alter the amount of precipitation on scales ranging from one to hundreds of kilometres. Using atmospheric back trajectory modelling it has been shown that deforestation is likely to strengthen the effects of drought downwind of deforested regions throughout the Amazon (Spracklen et al., 2012; Bagley et al., 2013). Forests are dependent on this recycling functionality (Zemp et al., 2017; Staal et al., 2018); which creates a delicate system whereby removing vegetation decreases the moisture availability for the remaining forest and increases the forest's vulnerability to drought (Van Der Ent et al., 2010; Gimeno et al., 2012; Zemp et al., 2017). Further exacerbating forest loss potential, positive feedbacks between deforestation and drought have been identified in the Amazon (Staal et al., 2015; Staal et al., 2020).

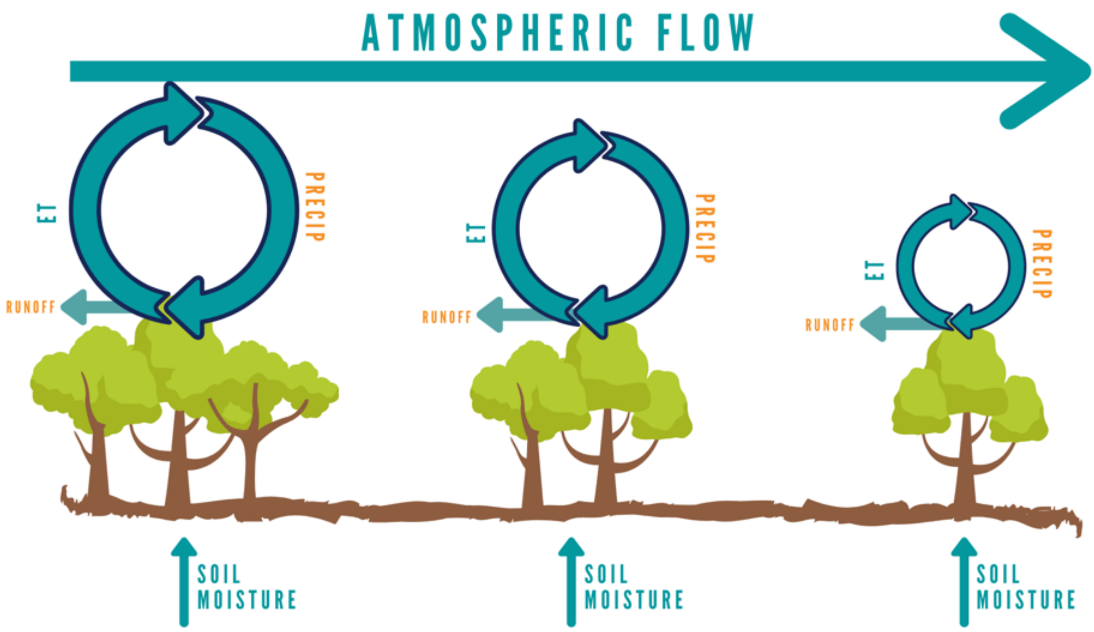

Figure 1.9. *Precipitation recycling effect of vegetation. Moist air passes inland, where water precipitates (P), forests transpire and re-evaporate (ET), and moist air passes downwind. Where there is deforestation, more water is lost as runoff and there is less ET, reducing the total amount of water recycled.*

Spracklen and Garcia-Carreras (2015) conducted a meta-analysis of regional and global climate models to observe the impacts of tropical deforestation on precipitation. They found that using a business-as-usual deforestation regime, precipitation in the Amazon will decrease by 8.1 ±1.4% by 2050. Similarly, Spracklen et al., (2012) estimated a decrease of 12% and 21% in wet and dry season precipitation respectively by 2050. This outlines the increased susceptibility of the dry season to climatic changes and the importance of vegetation in maintaining the ET flux which feeds precipitation.

SEA and other maritime environments are potentially less vulnerable to a reduction in moisture recycling due to their proximity to water sources (Takahashi et al., 2017), whereas the continental Congo and Amazon basins, which rely more heavily on moisture recycling for rainfall could be strongly affected. In the event of decreasing ET flux, the maritime tropical forests can import moisture directly via the land-sea breeze circulation (Takahashi et al., 2017) to compensate for reductions in ET. On larger scales, the intensity and duration of the monsoons of countries such as India may be affected by deforestation (Paul et al., 2016) as reduced evapotranspiration and decreased surface roughness decreases the rain recycling and the amount of available precipitable water (Chadwick et al., 2019).

1.4 Observing Changes

A key way in which scientists view our earth system is to use observations. These can come from a variety of sources and using a variety of techniques. Until the 1960s much of our observational data was from individual site recordings of weather, climate, and the environment. These ground-based observations provide detailed information about a point in space, having good spatial coverage in the mid-latitudes but poorly representing the more remote areas of the world, especially the tropics. They are particularly useful for understanding and comparing mean trends in weather and climate but are more limited for enabling us to understand spatial heterogeneity, for example evaluating climate changes over different land cover types. Alongside ground-based observations, field and air-craft campaigns have increased our knowledge of specific regions over short time periods. They provide useful case studies from which to understand specific conditions in detail, however lack the basin scale data to make comprehensive conclusions. A key role that ground-based observations play is to provide data to validate satellite and model datasets, in a process known as "ground truthing" (Mu et al., 2011; Kim et al., 2012; Ramoelo et al., 2014; Bright et al., 2017). Many of the remotely sensed datasets used in this thesis, which are described in Chapter 2, use this technique.

In the human context, a satellite is a machine that humanity has put in space to orbit around an object or body, usually the Earth. Since 1957 when Sputnik 1 was launched into space, we have launched 1000s of satellites, around a 1000 of which have been or are currently used for earth observation. Satellites often orbit in trains or groups, one such grouping is the "A-Train" or afternoon constellation (Figure 1.10).

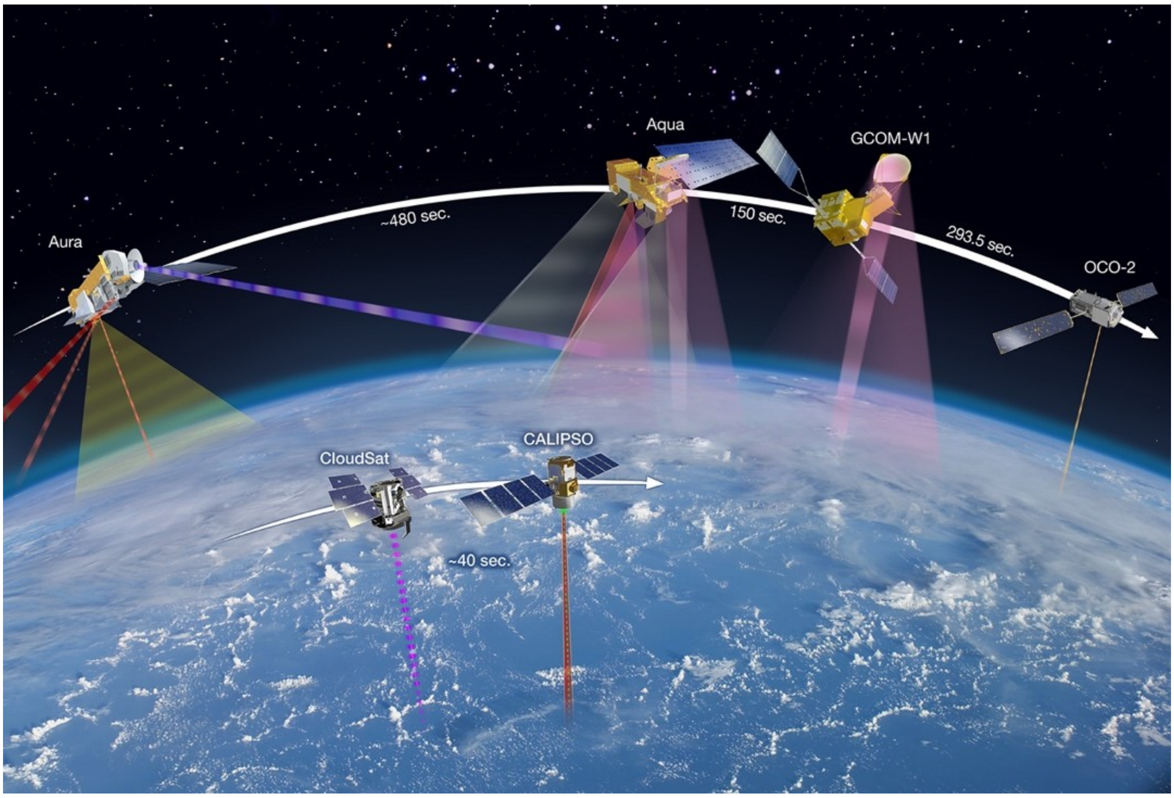

Figure 1.10. *Schematic showing the international "afternoon constellation" which includes the A (OCO-2, GCOM-W1, Aqua, and Aura) and C (CALIPSO and CloudSat) trains in 2019, where Aqua is still present in the constellation (source: https://atrain.nasa.gov/).*

Three common types of satellite orbit are, geostationary which are very high altitude, polar orbiting and non-polar orbiting both of which are low earth orbiting. Near-polar sun synchronous orbital satellites, are very common for earth observations as they can provide daily near global coverage, including observations of the polar regions. They pass the same point on the planet at the same mean solar time allowing for consistent observations of physical changes. Typically sun synchronous satellites are at an altitude of 700 - 800 km above the earth's surface and take around 100 minutes to complete a cycle around the planet, travelling north-south from pole to pole and taking 1-2 days to scan the entire Earth's surface. Alternatively, some satellites such as the Global Precipitation Measurement (GPM) core observatory, are non-polar low earth orbit satellites, providing cover over a partial range of latitudes.

Satellites are vehicles for instruments that carry sensors which detect radiation from a wide range of the electromagnetic spectrum. Everything on Earth absorbs and reflects or emits radiation, each at a distinct wavelength and frequency, providing a fingerprint, or spectral signal by which it can be identified. Satellites scan the Earth's surface in "swaths", where the size can range from 100s to 1000s km. Instruments can be either passive or active, either detecting radiation that reaches them from the earth's atmosphere or surface (passive), or by detecting the reflection of an emitted pulse of radiation (active). The different wavelengths, or bands of radiation can provide different information about the earth's atmosphere, surface, oceans and sub-surface. At short wavelengths, visible light is sensed which can be used for mapping and monitoring of features. Slightly longer wavelengths in the near-infrared range capture living plant materials well, whereas thermal infrared, which have longer wavelengths still, can sense temperature and can be used for climate and weather detection. Microwaves and radio waves have long wavelengths making them well suited to detecting forest structure as well as rainfall and clouds. Passive sensors tend to utilise the shorter wavelengths of energy, from microwave to visible, specialising in measuring quantities such as sea surface temperature and vegetation properties. Dense cloud cover can limit passive satellite retrievals as these wavelengths cannot pass through, meaning passive satellites often have poor spatial coverage in the cloudy tropical regions. Active sensors, alternatively use longer wavelengths, from microwave to radio, giving them the skill to sense vertical atmospheric profiles, precipitation, topography and forest structure.

1.5 Modelling Changes

Alongside observations, climate models are a primary way in which scientists can understand our past and future climate. There are a great number of climate models, each with different aims and capabilities. In general models aim to simulate processes, interactions and conditions within a region or the world to allow us to understand more about how climate might change in the future. Models represent these processes with equations that describe our understanding of the physical, biological and chemical processes that happen across the world. The equations range from fundamental principles such as the first law of thermodynamics to the complex and unresolved Navier-Stokes equations of fluid motion. Within the models, these equations are often referred to as being numerically solved, meaning they are too complex to be explicitly implemented and their solutions are approximated.

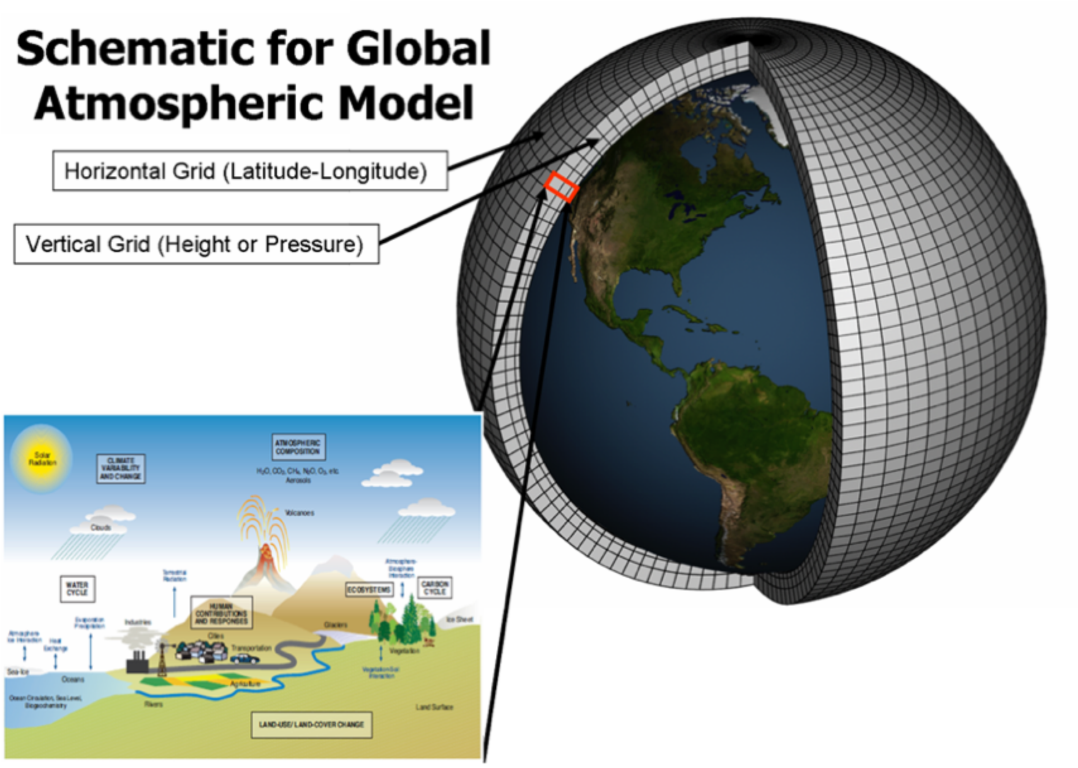

Figure 1.11. *A representation of a climate model, showing the Earth covered in the grid cells used by climate models. The inset diagram shows the climatic processes that the model will calculate for each cell (https://www.gfdl.noaa.gov/climate-modeling/).*

Since their inception in the 1950s, climate models have become more complex as scientists have taken advantage of our greater scientific understanding of processes and increased computing power. However, we lack the computational power to model absolutely all processes and at the highest resolutions, so climate models divide the world into grid cells. Figure 1.11 shows how models split the Earth into a 3D array of grid cells, in which calculations about the climate system are made. The spatial resolution of models can range from very high resolutions which focus on simulating shorter time scales and smaller domains to coarse resolutions (100s km) where simulating global responses for a long time period are important. The balance struck can largely depend on the available computing resources. To overcome representing complex processes at very high resolutions, most climate models use approximations or parametrisations to estimate processes that happen at sub-grid scales, such as convection. At every time step, the average or range of values for climate or land surface variables are represented by code rather than being calculated, hence saving resources. Since we do not know the exact values for every parameter, calibration takes place by running the model with a range of possible parameter values to test for the most reasonable outcome. In Chapter 5, I discuss how albedo and evapotranspiration may need additional tuning to bring the modelled values closer in line with observations. This process of calibration is a constantly operating process, designed to optimise model performance.

To simulate future scenarios, climate models move forward in time, taking information about the climate system from the past and present and extrapolating to the next time step. As with spatial resolution, finding the correct temporal resolution is a balance between accuracy and computational power, with climate models often simulating with a 30-minute time step.

Climate models through time have become more advanced and their ability to combine more strands of the earth system have evolved. Climate models can now simulate changes globally in 3D space, combing strands of models such as atmosphere and ocean, through coupling, into one unified model. Latterly, earth system models, such as UKESM1, have been developed to build upon the physical core of global climate models, adding the ability to simulate carbon, chemistry, ecology and land-use change. Some earth system models include Dynamic Global Vegetation Models (DGVMs), which simulate the dynamic behaviour and interactions of vegetation and land surface processes with the atmosphere. This leads some models to have more skill at simulating climate impacts of land cover change than others. DGVMs simulate vegetation dynamics, land surface processes and carbon and biogeochemical cycling. Importantly this can include simulating photosynthesis and respiration, energy and water fluxes, nutrient cycling, phenology and vegetation-climate interactions and feedbacks.

Climate models are driven by the past and present data that we pass them. To simulate the future, we give models socio-economic scenarios on which to base their predictions. Historically, the scenarios used were called Representative Concentration Pathways (RCPs) however for the latest IPCC AR6 report, new scenarios were developed called Shared Socioeconomic Pathways (SSPs), which range from low to high emission scenarios and span a range of likely futures. SSPs are assigned numbers which can be approximately interpreted as low (SSP1-2.6), medium-low (SSP2-4.5), medium-high (SSP3-7.0) and high (SSP5-8.5) radiative-forcing levels by 2100 (O'Neill et al., 2017). In terms of land-use change, the SSP3-7.0 scenario has the largest reduction in forest cover over the next century, SSP5-8.5 scenario has relatively little change, and forest cover increases in the future under the SSP1-2.6 and SSP2-4.5 scenarios (Lawrence et al., 2016). We expect the models to produce differing outcomes due to differences in each model's representation of the land surface and their parameterisations of sub-grid processes (Bell et al., 2015; Crowhurst et al., 2020). Using these pathways enables us to gain insight about the impacts a range of socio-economic decisions would bring.

There are hundreds of climate models from groups of scientists around the world, each outputting thousands of variables including temperatures, precipitation, cloud cover height, radiation and wind speeds. The models are used to run experiments to test future scenarios such as a doubling of atmospheric CO_2, from which these outputs can be used to analyse and evaluate changes. Each model will produce different results from an experiment due to its differing setup. In order to produce a consensus between models, we can run each model using the same experiments to create a model ensemble, providing a better idea of the mean change, but also the strengths and weaknesses of each. The Coupled Model Intercomparison Project (CMIP) is a collection of model atmosphere-ocean coupled model experiments, combining multiple different models and experiments (Eyring et al., 2016). The current iteration of CMIP is CMIP6, involving up to 49 modelling centres from around the world producing around 100 distinct models. These prescribed experiments include historical runs, future warming scenarios, Atmospheric Model Intercomparison Project (AMIP) experiments, abrupt 4x CO_2, 1% CO_2, paleoclimate and control runs where climate is kept constant. The analysis in chapters 4 and 5 utilises historical and future warming scenarios from CMIP. Historical runs span from the pre-industrial period in 1850 to near present day, using the best concentrations estimates of CO_2, CH_4, N_2O, radiation input and outputs, land-use change and many other factors. They don't replicate the climate exactly as they aren't constrained by real temperature and rainfall observations, rather they rely on model physics to represent the historical period. These runs provide insight into model performance are an important way in which we can validate the historical simulations against observations to assess skill. Similarly, when models are unable to correctly simulate processes or familiar climate features, often due to parametrisations simplifying processes, we can use bias correction. This can involve nudging the simulation back to reality and is important for short term improvements, however ultimately developments to parametrisations need to take place for long term improvements (Maraun et al., 2017).

In contrast, future warming scenarios take SSPs and simulate climate up to and sometimes beyond 2100. The SSPs contain differing radiative forcings, leading to differing projections of climate over the next century. These range from scenarios where severe emissions reductions practices are implemented to business as usual or increased emissions practices. In relation to temperature, over the period 1880 – 2100, SSPs forecast a wide range of increases in mean temperature of between 1.4 K (SSP1 - 1.9) and 5 K (SSP5-8.5) (Hausfather, 2019).

Climate models allow us to observe and understand the impacts that changes to our earth system can have. Each model will have a different representation of the land surface and therefore a different climate response due to a change in the earth system (Boisier et al., 2015; Boysen et al., 2020; Baker, De Souza, et al., 2021; Luo et al., 2022; De Hertog et al., 2022). Alongside providing information about the magnitude and sign of the climate change, the model differences can provide insights for model improvement by identifying the important parameters driving the change. Climate models largely agree that tropical forest loss leads to increases in temperature, albeit with disagreement in magnitude (Winckler et al., 2019; Boysen et al., 2020), however as with observations, changes to precipitation are less well agreed upon (Spracklen and Garcia-Carreras, 2015). A recent study from Luo et al. (2022) found by simulating idealised deforestation, there was a multi-model mean reduction in rainfall of -2.2% due to forest loss, but there was a substantial range in estimates (-5.5% - 0.1% change across 11 models). Existing model assessments have evaluated changes in temperature against satellite observations Li et al., 2015; Alkama and Cescatti, 2016; Duveiller, Hooker, et al., 2018) or in-situ measurements (Lee et al., 2011), yet similar analysis for precipitation is lacking. The disparity and lack of assessments highlights the challenges in arriving at an agreed upon estimate and the need to constrain the model parameters to allow simulations to converge on a consistent result.

1.6 Research Objectives

Understanding and quantifying the impacts of tropical forest loss on climate is critical for both creating mitigative climate policy and for simulating future changes in climate. Previously, studies have assessed changes using a variety of methods and data, from modelling idealised deforestation to ground-based case studies. This thesis aims to bring together and build upon our knowledge of the impacts that tropical forest loss has on local climate. To do this, I aim to use satellite observations, ground-based observations, climate reanalysis and climate models from a wide range of sources, providing both a robust value for the climate impacts of forest loss and the ability to contrast each dataset's resulting climate impact. This will provide a strengthened understanding of climate-land interactions and additionally insight for product efficacy and improvements.

Impacts of the Driver of Forest Loss on Climate

There is a well-established link between tropical forest loss, decreases in ET and increases in LST, as described throughout Chapter 1. The driver of forest loss is an emerging categorisation which describes the characteristics and longevity of forest loss. The differing characteristics provide a yet un-explored opportunity to assess how the climate response to forest loss may vary given different physical circumstances. In this research I aim to unpack how the driver of tropical forest loss can modify the local climate response and how this varies across the three tropical forest regions. To do this I will:

- Establish the drivers of forest loss across the tropics and between regions.
- Understand what LCC traits the drivers of forest loss exhibit.
- Use remotely sensed satellite LST to assess the impact of forest loss.
- Quantify the effect that different drivers of forest loss have on local climate.
- Identify the different regional responses.
- Correlate changes in LST to changes in land surface and climate properties.

Impacts of Forest Loss on Precipitation

The impacts of tropical forest loss on precipitation have been well studied using climate models and ground-based case studies. These analyses have found conflicting results, showing that tropical forest loss can both reduce and increase rainfall. Previously studies using satellite datasets have been unable to replicate and confirm these findings. In this research I will use satellite datasets and a novel approach to untangle the precipitation response to tropical forest loss. To do this I will:

- Unify multiple satellite, ground-based and reanalysis precipitation datasets.
- Regrid the datasets to a range of spatial scales, spanning high to coarse resolutions.
- Evaluate the impact of forest loss on precipitation over a range of spatial scales and for each category of precipitation dataset.
- Understand how the precipitation response to forest loss varies regionally.
- Explore the influence of season on the precipitation response to forest loss.
- Use a LCC model to project future precipitation changes due to forest loss.

Evaluating Simulated Climate Impacts of Forest Loss

Climate models and observations have jointly shown that tropical forest loss can impact local climate. Simulations often produce diverging or uncertain results with respect to temperature and precipitation. The reasons for this disagreement range from analysis methodology to climate model parametrisations. There is an opportunity to present a first analysis of both the simulated temperature and precipitation impacts due forest loss across the entire CMIP6 model range. This research will tie together our new observational understanding of the climate impacts of forest loss and evaluate the ability of the CMIP6 models to represent these changes. I will explore the reasons for the differences in simulated climate responses and assess the changes that could be made in order to provide a more consistent understanding. To do this I will:

- Re-evaluate the observed impact of forest loss on LST and precipitation.
- Assess using observations the simulated historical temperature response to forest loss.
- Assess using observations the simulated historical precipitation response to forest loss.
- Understand the reasons for simulated and observed discrepancies in the climate response to forest loss.
- Pin-point specific areas for model improvements that can realistically be implemented.

Following this introduction, in Chapter 2, I will describe the datasets used in this thesis and provide an overview of the key methods used to analyse them. Chapters 3 to 5 contain analysis which is either published, submitted or in advanced draft form, with supplementary material provided in Appendix A, B and C respectively. Lastly, Chapter 6 contains a synthesis of the main findings from the analysis, a discussion of the limitations and uncertainties in this analysis and finally, proposals for future directions this research could take.

References

Alkama, R. and Cescatti, A. 2016. Biophysical climate impacts of recent changes in global forest cover. *Science*. **351**(6273), pp.600–604.

Alves de Oliveira, B.F., Bottino, M.J., Nobre, P. and Nobre, C.A. 2021. Deforestation and climate change are projected to increase heat stress risk in the Brazilian Amazon. *Communications Earth and Environment*. **2**(1), pp.1–8.

Alves, L.M., Marengo, J.A., Fu, R. and Bombardi, R.J. 2017. Sensitivity of Amazon Regional Climate to Deforestation. *American Journal of Climate Change*. **06**(1), pp.75–98.

Armenteras, D., Negret, P., Melgarejo, L.F., Lakes, T.M., Londoño, M.C., García, J., Krueger, T., Baumann, M. and Davalos, L.M. 2019. Curb land grabbing to save the Amazon. *Nature Ecology & Evolution*. **3**(1), p.1497.

Arroyo-Rodríguez, V., Saldaña-Vázquez, R.A., Fahrig, L. and Santos, B.A. 2017. Does forest fragmentation cause an increase in forest temperature? *Ecological Research*. **32**, pp.81–88.

Austin, K.G., González-Roglich, M., Schaffer-Smith, D., Schwantes, A.M. and Swenson, J.J. 2017. Trends in size of tropical deforestation events signal increasing dominance of industrial-scale drivers. *Environmental Research Letters*. **12**(5).

Austin, K.G., Schwantes, A., Gu, Y. and Kasibhatla, P.S. 2019. What causes deforestation in Indonesia? *Environmental Research Letters*. **14**(2).

Bagley, J.E., Foley, J.A., Desai, A.R., Snyder, P.K. and Harding, K.J. 2013. Drought and Deforestation: Has Land Cover Change Influenced Recent Precipitation Extremes in the Amazon? *Journal of Climate*. **27**(1), pp.345–361.

Baidya Roy, S., Weaver, C.P., Nolan, D.S. and Avissar, R. 2003. A preferred scale for landscape forced mesoscale circulations? *Journal of Geophysical Research D: Atmospheres*. **108**(22), pp.1–11.

Baker, J.C.A., Garcia-Carreras, L., Buermann, W., Castilho De Souza, D., Marsham, J.H., Kubota, P.Y., Gloor, M., Coelho, C.A.S. and Spracklen, D. V. 2021. Robust Amazon precipitation projections in climate models that capture realistic land-atmosphere interactions. *Environmental Research Letters*. **16**(7).

Baker, J.C.A. and Spracklen, D. V 2019. Climate Benefits of Intact Amazon Forests and the Biophysical Consequences of Disturbance. *Frontiers in Forests and Global Change*. **2**, pp.1–13.

Baldi, M., Dalu, G.A. and Pielke, R.A. 2008. Vertical velocities and available potential energy generated by landscape variability - Theory. *Journal of Applied Meteorology and Climatology*. **47**(2), pp.397–410.

Ban-Weiss, G.A., Bala, G., Cao, L., Pongratz, J. and Caldeira, K. 2011. Climate forcing and response to idealized changes in surface latent and sensible heat. *Environmental Research Letters*. **6**(3).

Bebber, D.P. and Butt, N. 2017. Tropical protected areas reduced deforestation carbon emissions by one third from 2000-2012. *Scientific Reports*. **7**(1), pp.1–7.

Bell, J.P., Tompkins, A.M., Bouka-Biona, C. and Sanda, I.S. 2015. A process-based investigation into the impact of the Congo basin deforestation on surface climate. *Journal of Geophysical Research*. **120**(12), pp.5721–5739.

Boers, N., Marwan, N., Barbosa, H.M.J. and Kurths, J. 2017. A deforestation-induced tipping point for the South American monsoon system. *Scientific Reports*. **7**(41489), pp.1–9.

Bonan, G.B. 2008. Forests and climate change: Forcings, feedbacks, and the climate benefits of forests. *Science*. **320**(5882), pp.1444–1449.

Bowen, I.S. 1926. The Ratio of Heat Losses by Conduction and by Evaporation from any Water Surface. *Physical Review*. **27**(1), pp.779–787.

Bright, R.M., Davin, E., O'Halloran, T., Pongratz, J., Zhao, K. and Cescatti, A. 2017. Local temperature response to land cover and management change driven by non-radiative processes. *Nature Climate Change*. **7**(4), pp.296–302.

Brinck, K., Fischer, R., Groeneveld, J., Lehmann, S., Dantas De Paula, M., Pütz, S., Sexton, J.O., Song, D. and Huth, A. 2017. High resolution analysis of tropical forest fragmentation and its impact on the global carbon cycle. *Nature Communications*. **8**(14855), pp.1–6.

Bruijnzeel, L.A., Mulligan, M. and Scatena, F.N. 2011. Hydrometeorology of tropical montane cloud forests: Emerging patterns. *Hydrological Processes*. **25**(3), pp.465–498.

Canadell, J.G., Jackson, R.B., Ehleringer, J.R., Mooney, H.A., Sala, O.E. and Schulze, E.D. 1996. Maximum rooting depth of different vegetation types. *Oceologia*. **108**(4), pp.583–595.

Chadwick, R., Ackerley, D., Ogura, T. and Dommenget, D. 2019. Separating the Influences of Land Warming, the Direct CO2 Effect, the Plant Physiological Effect, and SST Warming on Regional Precipitation Changes. *Journal of Geophysical Research: Atmospheres*. **124**(2), pp.624–640.

Chagnon, F.J.F. and Bras, R.L. 2005. Contemporary climate change in the Amazon. *Geophysical Research Letters*. **32**(13), pp.1–4.

Conte, L., Renner, M., Brando, P., Oliveira dos Santos, C., Silvério, D., Kolle, O., Trumbore, S.E. and Kleidon, A. 2019. Effects of Tropical Deforestation on Surface Energy Balance Partitioning in Southeastern Amazonia Estimated From Maximum Convective Power. *Geophysical Research Letters*. **46**(8), pp.4396–4403.

Costa, M.H. and Foley, J.A. 2000. Combined effects of deforestation and doubled atmospheric CO2 concentrations on the climate of Amazonia. *Journal of Climate*. **13**(1), pp.18–34.

Crowhurst, D.M., Dadson, S.J. and Washington, R. 2020. Evaluation of Evaporation Climatology for the Congo Basin Wet Seasons in 11 Global Climate Models. *Journal of Geophysical Research: Atmospheres*. **125**(6), pp.1–16.

Curtis, P.G., Slay, C.M., Harris, N.L., Tyukavina, A. and Hansen, M.C. 2018. Classifying drivers of global forest loss. *Science*. **361**(6407), pp.1108–1111.

Cutrim, E., Martin, D.W. and Rabin, R. 2002. Enhancement of Cumulus Clouds over Deforested Lands in Amazonia. *Bulletin of the American Meteorological Society*. **76**(10), pp.1801–1805.

D'Almeida, C., Vörösmarty, C.J., Hurtt, G.C., Marengo, J.A., Dingman, S.L. and Keim, B.D. 2007. The effects of deforestation on the hydrological cycle in Amazonia: a review on scale and resolution. *International Journal of Climatology*. **27**(5), pp.633–647.

Davidson, E.A., De Araüjo, A.C., Artaxo, P., Balch, J.K., Brown, I.F., Mercedes, M.M., Coe, M.T., Defries, R.S., Keller, M., Longo, M., Munger, J.W., Schroeder, W., Soares-Filho, B.S., Souza, C.M. and Wofsy, S.C. 2012. The Amazon basin in transition. *Nature*. **481**(7381), pp.321–328.

Davin, E.L. and de Noblet-Ducoudre, N. 2010. Climatic impact of global-scale Deforestation: Radiative versus nonradiative processes. *Journal of Climate*. **23**(1), pp.97–112.

DeFries, R., Hansen, A., Newton, A.C. and Hansen, M.C. 2005. Increasing isolation of protected areas in tropical forests over the past twenty years. *Ecological Applications*. **15**(1), pp.19–26.

Durieux, L., Toledo Machado, L.A. and Laurent, H. 2003. The impact of deforestation on cloud cover over the Amazon arc of deforestation. *Remote Sensing of Environment*. **86**(1), pp.132–140.

Duveiller, G., Filipponi, F., Ceglar, A., Bojanowski, J., Alkama, R. and Cescatti, A. 2021. Revealing the widespread potential of forests to increase low level cloud cover. *Nature Communications*. **12**(1), pp.1–15.

Ellison, D., Morris, C.E., Murdiyarso, D., Gutierrez, V., Verbist, B., Cohen, J., Teuling, A.J., Ilstedt, U., Springgay, E., Sugandi, Y., Gaveau, D., Muys, B., Noordwijk, M. van, Sands, D.C., Spracklen, D. V., Sullivan, C.A., Locatelli, B., Sheil, D., Creed, I.F., Pokorny, J. and Tobella, A.B. 2017. Trees, forests and water: Cool insights for a hot world. *Global Environmental Change*. **43**, pp.51–61.

Eltahir, E.A.B. and Bras, R.L. 1996. Precipitation and Recycling. *Reviews of Geophysics*. **34**(3), pp.367–378.

Van Der Ent, R.J., Savenije, H.H.G., Schaefli, B. and Steele-Dunne, S.C. 2010. Origin and fate of atmospheric moisture over continents. *Water Resources Research*. **46**(9), pp.1–12.

Escobar, H. 2019. Amazon fires clearly linked to deforestation, scientists say. *Science*. **365**(6456), pp.853–853.

Esquivel-Muelbert, A., Baker, T.R., Dexter, K.G., Lewis, S.L., Brienen, R.J.W., Feldpausch, T.R., Lloyd, J., Monteagudo-Mendoza, A., Arroyo, L., Álvarez-Dávila, E., Higuchi, N., Marimon, B.S., Marimon-Junior, B.H., Silveira, M., Vilanova, E., Gloor, E., Malhi, Y., Chave, J., Barlow, J., Bonal, D., Davila Cardozo, N., Erwin, T., Fauset, S., Hérault, B., Laurance, S., Poorter, L., Qie, L., Stahl, C., Sullivan, M.J.P., ter Steege, H., Vos, V.A., Zuidema, P.A., Almeida, E., Almeida de Oliveira, E., Andrade, A., Vieira, S.A., Aragão, L., Araujo-Murakami, A., Arets, E., Aymard C, G.A., Baraloto, C., Camargo, P.B., Barroso, J.G., Bongers, F., Boot, R., Camargo, J.L., Castro, W., Chama Moscoso, V., Comiskey, J., Cornejo Valverde, F., Lola da Costa, A.C., del Aguila Pasquel, J., Di Fiore, A., Fernanda Duque, L., Elias, F., Engel, J., Flores Llampazo, G., Galbraith, D., Herrera Fernández, R., Honorio Coronado, E., Hubau, W., Jimenez-Rojas, E., Lima, A.J.N., Umetsu, R.K., Laurance, W., Lopez-Gonzalez, G., Lovejoy, T., Aurelio Melo Cruz, O., Morandi, P.S., Neill, D., Núñez Vargas, P., Pallqui Camacho, N.C., Parada Gutierrez, A., Pardo, G., Peacock, J., Peña-Claros, M., Peñuela-Mora, M.C., Petronelli, P., Pickavance, G.C., Pitman, N., Prieto, A., Quesada, C., Ramírez-Angulo, H., Réjou-Méchain, M., Restrepo Correa, Z., Roopsind, A., Rudas, A., Salomão, R., Silva, N., Silva Espejo, J., Singh, J., Stropp, J., Terborgh, J., Thomas, R., Toledo, M., Torres-Lezama, A., Valenzuela Gamarra, L., van de Meer, P.J., van der Heijden, G., van der Hout, P., Vasquez Martinez, R., Vela, C., Vieira, I.C.G. and Phillips, O.L. 2019. Compositional response of Amazon forests to climate change. *Global Change Biology*. **25**(1), pp.39–56.

Estoque, R.C., Ooba, M., Avitabile, V., Hijioka, Y., DasGupta, R., Togawa, T. and Murayama, Y. 2019. The future of Southeast Asia's forests. *Nature Communications*. **10**(1), pp.1–12.

FAO 2022. *The State of the World's Forests 2022*. Rome, FAO.

Fearnside, P.M. 2005. Deforestation in Brazilian Amazonia - history, rates, and consequences. *Conservation Biology*. **19**(3), pp.680–688.

Feintrenie, L. 2014. Agro-industrial plantations in Central Africa, risks and opportunities. *Biodiversity and Conservation*. **23**(6), pp.1577–1589.

Fisch, G., Tota, J., Machado, L.A.T., Silva Dias, M.A.F., da, R.F., Nobre, C.A., Dolman, A.J. and Gash, J.H.C. 2004. The convective boundary layer over pasture and forest in Amazonia. *Theoretical and Applied Climatology*. **78**(1–3), pp.47–59.

Fritz, S., Laso Bayas, J.C., See, L., Schepaschenko, D., Hofhansl, F., Jung, M., Dürauer, M., Georgieva, I., Danylo, O., Lesiv, M. and McCallum, I. 2022. A Continental Assessment of the Drivers of Tropical Deforestation With a Focus on Protected Areas. Frontiers in Conservation Science. 3(February), pp.1–12.

Funatsu, B.M., Dubreuil, V., Claud, C., Arvor, D. and Gan, M.A. 2012. Convective activity in Mato Grosso state (Brazil) from microwave satellite observations: Comparisons between AMSU and TRMM data sets. *Journal of Geophysical Research Atmospheres*. **117**(16), pp.1–16.

Garcia-Carreras, L. and Parker, D.J. 2011. How does local tropical deforestation affect rainfall? *Geophysical Research Letters*. **38**(19), pp.1–6.

Garcia-Carreras, L., Parker, D.J. and Marsham, J.H. 2011. What is the mechanism for the modification of convective cloud distributions by land surface-induced flows? *Journal of the Atmospheric Sciences*. **68**(3), pp.619–634.

Garcia-Carreras, L., Parker, D.J., Taylor, C.M., Reeves, C.E. and Murphy, J.G. 2010. Impact of mesoscale vegetation heterogeneities on the dynamical and thermodynamic properties of the planetary boundary layer. *Journal of Geophysical Research Atmospheres*. **115**(3), pp.1–12.

Gash, J.H.C. and Nobre, C.A. 1997. Climatic Effects of Amazonian Deforestation: Some Results from ABRACOS. *Bulletin of the American Meteorological Society*. **78**(5), pp.823–830.

Gash, J.H.C. and Shuttleworth, W.J. 1991. Tropical deforestation: Albedo and the surface-energy balance. *Climatic Change*. **19**(1–2), pp.123–133.

Gaveau, D.L.A., Sheil, D., Husnayaen, Salim, M.A., Arjasakusuma, S., Ancrenaz, M., Pacheco, P. and Meijaard, E. 2016. Rapid conversions and avoided deforestation: Examining four decades of industrial plantation expansion in Borneo. *Scientific Reports*. **6**(October 2015), pp.1–13.

Giambelluca, T.W., Hölscher, D., Bastos, T.X., Frazão, R.R., Nullet, M.A. and Ziegler, A.D. 1997. Observations of albedo and radiation balance over postforest land surfaces in the eastern Amazon Basin. *Journal of Climate*. **10**(5), pp.919–928.

Giambelluca, T.W., Nullet, M.A., Ziegler, A.D. and Tran, L. 2000. Latent and sensible energy flux over deforested land surfaces in the eastern Amazon and northern Thailand. *Singapore Journal of Tropical Geography*. **21**(2), pp.107–130.

Giambelluca, T.W., Ziegler, A.D., Nullet, M.A., Truong, D.M. and Tran, L.T. 2003. Transpiration in a small tropical forest patch. *Agricultural and Forest Meteorology*. **117**(1–2), pp.1–22.

Gibbs, H.K., Ruesch, A.S., Achard, F., Clayton, M.K., Holmgren, P., Ramankutty, N. and Foley, J.A. 2010. Tropical forests were the primary sources of new agricultural land in the 1980s and 1990s. *Proceedings of the National Academy of Sciences of the United States of America*. **107**(38), pp.16732–16737.

Gimeno, L., Stohl, A., Trigo, R.M., Dominguez, F., Yoshimura, K., Yu, L., Drumond, A., Durn-Quesada, A.M. and Nieto, R. 2012. Oceanic and terrestrial sources of continental precipitation. *Reviews of Geophysics*. **50**(4), pp.1–41.

Grace, J., Mitchard, E. and Gloor, E. 2014. Perturbations in the carbon budget of the tropics. *Global Change Biology*. **20**(10), pp.3238–3255.

Hansen, M.C., Potapov, P. V., Moore, R., Hancher, M., Turubanova, S.A., Tyukavina, A., Thau, D., Stehman, S. V., Goetz, S.J., Loveland, T.R., Kommareddy, A., Egorov, A., Chini, L., Justice, C.O. and Townshend, J.R.G. 2013. High-Resolution Global Maps of 21st-Century Forest Cover Change. *Science*. **342**(6160), pp.850–853.

Heiblum, R.H., Koren, I. and Feingold, G. 2014. On the link between Amazonian forest properties and shallow cumulus cloud fields. *Atmospheric Chemistry and Physics*. **14**(12), pp.6063–6074.

Heinimann, A., Mertz, O., Frolking, S., Christensen, A.E., Hurni, K., Sedano, F., Chini, L.P., Sahajpal, R., Hansen, M. and Hurtt, G. 2017. A global view of shifting cultivation: Recent, current, and future extent. PLoS ONE. 12(9), pp.1–21.

Houghton, R.A. 2013. The emissions of carbon from deforestation and degradation in the tropics: Past trends and future potential. *Carbon Management*. **4**(5), pp.539–546.

Jamaludin, J., De Alban, J.D.T., Carrasco, L.R. and Webb, E.L. 2022. Spatiotemporal analysis of deforestation patterns and drivers reveals emergent threats to tropical forest landscapes. Environmental Research Letters. 17(5), pp.1–15.

Jipp, P.H., Nepstad, D.C., Cassel, D.K. and Reis De Carvalho, C. 1998. Deep soil moisture storage and transpiration in forests and pastures of seasonally-dry Amazonia. *Climatic Change*. **39**(2–3), pp.395–412.

Kalamandeen, M., Gloor, E., Mitchard, E., Quincey, D., Ziv, G., Spracklen, D., Spracklen, B., Adami, M., Aragaõ, L.E.O.C., Galbraith, D., Spracklen, B., Mitchard, E., Galbraith, D., Kalamandeen, M., Gloor, E., Aragão, L.E.O.C., Spracklen, D. and Ziv, G. 2018. Pervasive Rise of Small-scale Deforestation in Amazonia. *Scientific Reports*. **8**(1), pp.1–10.

Khanna, J. and Medvigy, D. 2014. Strong control of surface roughness variations control the regional atmospheric response to contemporary scale deforestation in Rondônia, Brazil. *Journal of Geophysical Research: Atmospheres*. **119**, pp.13067–13078.

Kim, H.W., Hwang, K., Mu, Q., Lee, S.O. and Choi, M. 2012. Validation of MODIS 16 global terrestrial evapotranspiration products in various climates and land cover types in Asia. *KSCE Journal of Civil Engineering*. **16**(2), pp.229–238.

Kirschbaum, M.U.F., Whitehead, D., Dean, S.M., Beets, P.N., Shepherd, J.D. and Ausseil, A.G.E. 2011. Implications of albedo changes following afforestation on the benefits of forests as carbon sinks. *Biogeosciences*. **8**(12), pp.3687–3696.

Kleidon, A. and Heimann, M. 2000. Assessing the role of deep rooted vegetation in the climate system with model simulations: Mechanism, comparison to observations and implications for Amazonian deforestation. *Climate Dynamics*. **16**(2–3), pp.183–199.

Knox, R., Bisht, G., Wang, J. and Bras, R. 2011. Precipitation variability over the forest-to-nonforest transition in Southwestern Amazonia. *Journal of Climate*. **24**(9), pp.2368–2377.

Kolusu, S.R., Marsham, J.H., Mulcahy, J., Johnson, B., Dunning, C., Bush, M. and Spracklen, D. V. 2015. Impacts of Amazonia biomass burning aerosols assessed from short-range weather forecasts. *Atmospheric Chemistry and Physics*. **15**(21), pp.12251–12266.

Kunert, N., Aparecido, L.M.T., Wolff, S., Higuchi, N., Santos, J. dos, Araujo, A.C. de and Trumbore, S. 2017. A revised hydrological model for the Central Amazon: The importance of emergent canopy trees in the forest water budget. *Agricultural and Forest Meteorology*. **239**, pp.47–57.

Lambin, E.F. and Geist, H.J. 2003. Regional Differences in Tropical Deforestation. *Environment*. **45**(6), pp.22–36.

Laurance, W.F. and Bruce Williamson, G. 2001. Positive feedbacks among forest fragmentation, drought, and climate change in the Amazon. *Conservation Biology*. **15**(6), pp.1529–1535.

Lawrence, D., Coe, M., Walker, W., Verchot, L. and Vandecar, K. 2022. The Unseen Effects of Deforestation: Biophysical Effects on Climate. *Frontiers in Forests and Global Change*. **5**, pp.1–13.

Lawrence, D. and Vandecar, K. 2015. Effects of tropical deforestation on climate and agriculture. *Nature Climate Change*. **5**(1), pp.27–36.

Lawrence, D.M., Hurtt, G.C., Arneth, A., Brovkin, V., Calvin, K. V., Jones, A.D., Jones, C.D., Lawrence, P.J., Noblet-Ducoudré, N. De, Pongratz, J., Seneviratne, S.I. and Shevliakova, E. 2016. The Land Use Model Intercomparison Project (LUMIP) contribution to CMIP6: Rationale and experimental design. *Geoscientific Model Development*. **9**(9), pp.2973–2998.

Lawton, R.O., Nair, U.S., Pielke R.A., S. and Welch, R.M. 2001. Climatic impact of tropical lowland deforestation on nearby montane cloud forests. *Science*. **294**(5542), pp.584–587.

Lee, X., Goulden, M.L., Hollinger, D.Y., Barr, A., Black, T.A., Bohrer, G., Bracho, R., Drake, B., Goldstein, A., Gu, L., Katul, G., Kolb, T., Law, B.E., Margolis, H., Meyers, T., Monson, R., Munger, W., Oren, R., Paw U, K.T., Richardson, A.D., Schmid, H.P., Staebler, R., Wofsy, S. and Zhao, L. 2011. Observed increase in local cooling effect of deforestation at higher latitudes. *Nature*. **479**, pp.384–387.

Li, W., Ciais, P., Peng, S., Yue, C., Wang, Y., Thurner, M., Saatchi, S.S., Arneth, A., Avitabile, V., Carvalhais, N., Harper, A.B., Kato, E., Koven, C., Liu, Y.Y., Nabel, J.E.M.S., Pan, Y., Pongratz, J., Poulter, B., Pugh, T.A.M., Santoro, M., Sitch, S., Stocker, B.D., Viovy, N., Wiltshire, A., Yousefpour, R. and Zaehle, S. 2017. Land-use and land-cover change carbon emissions between 1901 and 2012 constrained by biomass observations. *Biogeosciences*. **14**(22), pp.5053–5067.

Lovejoy, T.E. and Nobre, C. 2018. Amazon Tipping Point. *Science Advances*. **4**(2), p.1.

Mahmood, R., Pielke, R.A., Hubbard, K.G., Niyogi, D., Dirmeyer, P.A., Mcalpine, C., Carleton, A.M., Hale, R., Gameda, S., Beltrán-Przekurat, A., Baker, B., Mcnider, R., Legates, D.R., Shepherd, M., Du, J., Blanken, P.D., Frauenfeld, O.W., Nair, U.S. and Fall, S. 2014. Land cover changes and their biogeophysical effects on climate. *International Journal of Climatology*. **34**(4), pp.929–953.

Malhi, Y., Wood, D., Baker, T.R., Wright, J., Phillips, O.L., Cochrane, T., Meir, P., Chave, J., Almeida, S., Arroyo, L., Higuchi, N., Killeen, T.J., Laurance, S.G., Laurance, W.F., Lewis, S.L., Monteagudo, A., Neill, D.A., Vargas, P.N., Pitman, N.C.A., Quesada, C.A., Salomão, R., Silva, J.N.M., Lezama, A.T., Terborgh, J., Martínez, R.V. and Vinceti, B. 2006. The regional variation of aboveground live biomass in old-growth Amazonian forests. *Global Change Biology*. **12**(7), pp.1107–1138.

Malhi, Y. and Wright, J. 2004. Spatial patterns and recent trends in the climate of tropical rainforest regions. *Philosophical Transactions of the Royal Society B: Biological Sciences*. **359**(1443), pp.311–329.

Marengo, J.A., Souza, C.M., Thonicke, K., Burton, C., Halladay, K., Betts, R.A., Alves, L.M. and Soares, W.R. 2018. Changes in Climate and Land Use Over the Amazon Region: Current and Future Variability and Trends. *Frontiers in Earth Science*. **6**(228), pp.1–21.

Martin, S.T., Andreae, M.O., Artaxo, P., Baumgardner, D., Chen, Q., Goldstein, A.H., Guenther, A., Heald, C.L., Mayol-Bracero, O.L., McMurry, P.H., Pauliquevis, T., Pöschl, U., Prather, K.A., Roberts, G.C., Saleska, S.R., Dias, M.A.S., Spracklen, D. V., Swietlicki, E. and Trebs, I. 2010. Sources and Properties of Amazonian Aerosol Particles. *Reviews of Geophysics*. **48**, pp.714–725.

Masuda, Y.J., Garg, T., Anggraeni, I., Wolff, N.H., Ebi, K., Game, E.T., Krenz, J. and Spector, J.T. 2020. Heat exposure from tropical deforestation decreases cognitive performance of rural workers: An experimental study. *Environmental Research Letters*. **15**, pp.1–12.

McGuffie, K., Henderson-Sellers, A., Zhang, H., Durbidge, T.B. and Pitman, A.J. 1995. Global climate sensitivity to tropical deforestation. *Global and Planetary Change*. **10**, pp.97–128.

Meijaard, E., Abram, N.K., Wells, J.A., Pellier, A.S., Ancrenaz, M., Gaveau, D.L.A., Runting, R.K. and Mengersen, K. 2013. People's Perceptions about the Importance of Forests on Borneo. *PLoS ONE*. **8**(9), pp.1–14.

Mu, Q., Zhao, M. and Running, S.W. 2011. Improvements to a MODIS global terrestrial evapotranspiration algorithm. *Remote Sensing of Environment*. **115**(8), pp.1781–1800.

Negri, A. and Adler, R. 2018. The Impact of Amazonian Deforestation on Dry Season Rainfall. *Journal of Climate*. **17**(2001), pp.1306–1319.

Nepstad, D., Mcgrath, D., Stickler, C., Alencar, A., Azevedo, A., Swette, B., Bezerra, T., Digiano, M., Shimada, J., Seroa, R., Armijo, E., Castello, L., Brando, P., Hansen, M.C., Mcgrath-horn, M., Carvalho, O. and Hess, L. 2014. Slowing Amazon deforestation through public policy and interventions in beef and soy supply chains. *Science*. **344**(6188), pp.1118–1123.

Nepstad, D.C., Carvalhot, C.R. De, Davidson, E.A., Jlpp, P.H., Lefebvre, P.A., Negrelros, G.H., Sllvat, E.D., Stone, T.A. and Trumbore, S.E. 1994. The role of deep roots in the hydrological and carbon cycles of Amazonian forests and pastures. *Nature*. **372**, pp.666–669.

Nobre, C.A., Sellers, P.J. and Shukla, J. 1991. Amazonian Deforestation and Regional Climate Change. *Journal of Climate*. **4**(10), pp.957–988.

O'Neill, B.C., Kriegler, E., Ebi, K.L., Kemp-Benedict, E., Riahi, K., Rothman, D.S., van Ruijven, B.J., van Vuuren, D.P., Birkmann, J., Kok, K., Levy, M. and Solecki, W. 2017. The roads ahead: Narratives for shared socioeconomic pathways describing world futures in the 21st century. *Global Environmental Change*. **42**, pp.169–180.

Patton, E.G., Sullivan, P.P. and Moeng, C.H. 2005. The influence of idealized heterogeneity on wet and dry planetary boundary layers coupled to the land surface. *Journal of the Atmospheric Sciences*. **62**(7), pp.2078–2097.

Paul, S., Ghosh, S., Oglesby, R., Pathak, A., Chandrasekharan, A. and Ramsankaran, R. 2016. Weakening of Indian Summer Monsoon Rainfall due to Changes in Land Use Land Cover. *Scientific Reports*. **6**, pp.1–10.

Pedlowski, M.A., Dale, V.H., Matricardi, E.A.T. and Pereira, E. 1997. Patterns and impacts of deforestation in Rondonia, Brazil. *Landscape and Urban Planning*. **38**, pp.149–157.

Pendrill, F., Gardner, T.A., Meyfroidt, P., Persson, U.M., Adams, J., Azevedo, T., Lima, M.G.B., Baumann, M., Curtis, P.G., Sy, V. De, Garrett, R., Godar, J., Goldman, E.D., Hansen, M.C., Heilmayr, R., Herold, M., Kuemmerle, T., Lathuillière, M.J., Ribeiro, V., Tyukavina, A., Weisse, M.J. and West, C. 2022. Disentangling the numbers behind agriculture-driven tropical deforestation. *Science*. **377**(1168), pp.1–11.

Pielke, R.A. 2001. Influence of The Spatial Distribution of Vegetation and Soils On The Predicition of Cumulus Convective Rainfall. *Reviews of Geophysics*. **39**(2), pp.151–178.

Pielke, R.A., Adegoke, J., Beltrán-Przekurat, A., Hiemstra, C.A., Lin, J., Nair, U.S., Niyogi, D. and Nobis, T.E. 2007. An overview of regional land-use and land-cover impacts on rainfall. *Tellus, Series B: Chemical and Physical Meteorology*. **59**(3), pp.587–601.

Quesada, B., Arneth, A. and De Noblet-Ducoudré, N. 2017. Atmospheric, radiative, and hydrologic effects of future land use and land cover changes: A global and multimodel climate picture. *Journal of Geophysical Research*. **122**(10), pp.5113–5131.

Ramankutty, N., Evan, A.T., Monfreda, C. and Foley, J.A. 2008. Farming the planet: 1. Geographic distribution of global agricultural lands in the year 2000. *Global Biogeochemical Cycles*. **22**(1), pp.1–19.

Ramoelo, A., Majozi, N., Mathieu, R., Jovanovic, N., Nickless, A. and Dzikiti, S. 2014. Validation of global evapotranspiration product (MOD16) using flux tower data in the African savanna, South Africa. *Remote Sensing*. **6**(8), pp.7406–7423.

von Randow, C., Manzi, A.O., Kruijt, B., de Oliveira, P.J., Zanchi, F.B., Silva, R.L., Hodnett, M.G., Gash, J.H.C., Elbers, J.A., Waterloo, M.J., Cardoso, F.L. and Kabat, P. 2004. Comparative measurements and seasonal variations in energy and carbon exchange over forest and pasture in South West Amazonia. *Theoretical and Applied Climatology*. **78**, pp.5–26.

Rap, A., Scott, C.E., Reddington, C.L., Mercado, L., Ellis, R.J., Garraway, S., Evans, M.J., Beerling, D.J., MacKenzie, A.R., Hewitt, C.N. and Spracklen, D. V. 2018. Enhanced global primary production by biogenic aerosol via diffuse radiation fertilization. *Nature Geoscience*. **11**(9), pp.640–644.

Ray, D.K., Nair, U.S., Lawton, R.O., Welch, R.M. and Pielke, R.A. 2006. Impact of land use on Costa Rican tropical montane cloud forests: Sensitivity of orographic cloud formation to deforestation in the plains. *Journal of Geophysical Research Atmospheres*. **111**(2), pp.1–16.

Restrepo-Coupe, N., da Rocha, H.R., Hutyra, L.R., da Araujo, A.C., Borma, L.S., Christoffersen, B., Cabral, O.M.R., de Camargo, P.B., Cardoso, F.L., da Costa, A.C.L., Fitzjarrald, D.R., Goulden, M.L., Kruijt, B., Maia, J.M.F., Malhi, Y.S., Manzi, A.O., Miller, S.D., Nobre, A.D., von Randow, C., Sá, L.D.A., Sakai, R.K., Tota, J., Wofsy, S.C., Zanchi, F.B. and Saleska, S.R. 2013. What drives the seasonality of photosynthesis across the Amazon basin? A cross-site analysis of eddy flux tower measurements from the Brasil flux network. *Agricultural and Forest Meteorology*. **182–183**, pp.128–144.

Rosa, I.M.D., Smith, M.J., Wearn, O.R., Purves, D. and Ewers, R.M. 2016. The Environmental Legacy of Modern Tropical Deforestation. *Current Biology*. **26**(16), pp.2161–2166.

Rosenfeld, D. 1999. TRMM observed first direct evidence of smoke from forest fires inhibiting rainfall. *Geophysical Research Letters*. **26**(20), pp.3105–3108.

Roy, S.B. 2009. Mesoscale vegetation-atmosphere feedbacks in Amazonia. *Journal of Geophysical Research*. **114**, pp.1–7.

Roy, S.B. and Avissar, R. 2002. Impact of land use/land cover change on regional hydrometeorology in Amazonia. *Journal of Geophysical Research D: Atmospheres*. **107**(20), pp.1–12.

Rudel, T.K. 2013. The national determinants of deforestation in sub-Saharan Africa. *Philosophical Transactions of the Royal Society B: Biological Sciences*. **368**(1625), pp.1–7.

Saad, S.I., Da Rocha, H.R., Silva Dias, M.A.F. and Rosolem, R. 2010. Can the deforestation breeze change the rainfall in Amazonia? A case study for the BR-163 highway region. *Earth Interactions*. **14**(18), pp.1–25.

Salati, E., Dall'Olio, A., Matsui, E. and Gat, J.R. 1979. Recycling of water in the Amazon Basin: An isotopic study. *Water Resources Research*. **15**(5), pp.1250–1258.

Schons, S.Z., Lima, E., Amacher, G.S. and Merry, F. 2019. Smallholder land clearing and the Forest Code in the Brazilian Amazon. *Environment and Development Economics*. **24**(2), pp.157–179.

Scott, C.E., Monks, S.A., Spracklen, D. V., Arnold, S.R., Forster, P.M., Rap, A., Äijälä, M., Artaxo, P., Carslaw, K.S., Chipperfield, M.P., Ehn, M., Gilardoni, S., Heikkinen, L., Kulmala, M., Petäjä, T., Reddington, C.L.S., Rizzo, L. V., Swietlicki, E., Vignati, E. and Wilson, C. 2018. Impact on short-lived climate forcers increases projected warming due to deforestation. *Nature Communications*. **9**(1), pp.1–9.

Scott, C.E., Rap, A., Spracklen, D. V., Forster, P.M., Carslaw, K.S., Mann, G.W., Pringle, K.J., Kivekäs, N., Kulmala, M., Lihavainen, H. and Tunved, P. 2014. The direct and indirect radiative effects of biogenic secondary organic aerosol. *Atmospheric Chemistry and Physics*. **14**(1), pp.447–470.

Seneviratne, S.I., Corti, T., Davin, E.L., Hirschi, M., Jaeger, E.B., Lehner, I., Orlowsky, B. and Teuling, A.J. 2010. Investigating soil moisture-climate interactions in a changing climate: A review. *Earth-Science Reviews*. **99**(3–4), pp.125–161.

Seymour, F. and Harris, N.L. 2019. Reducing tropical deforestation. *Science*. **365**(6455), pp.756–757.

Silva Dias, M.A.F., Rutledge, S., Kabat, P., Silva Dias, P.L., Nobre, C., Fisch, G., Dolman, A.J., Zipser, E., Garstang, M., Manzi, A.O., Fuentes, J.D., Rocha, H.R., Marengo, J., Plana-Fattori, A., Sá, L.D.A., Alvalá, R.C.S., Andrcae, M.O., Artaxo, P., Gielow, R. and Gatti, L. 2002. Cloud and rain processes in a biosphere-atmosphere interaction context in the Amazon Region. *Journal of Geophysical Research D: Atmospheres*. **107**(20), pp.1–18.

da Silva, R.R. and Avissar, R. 2006. The hydrometeorology of a deforested region of the amazon basin. *Journal of Hydrometeorology*. **7**(5), pp.1028–1042.

Soares-Filho, B.S., Nepstad, D.C., Curran, L.M., Cerqueira, G.C., Garcia, R.A., Ramos, C.A., Voll, E., McDonald, A., Lefebvre, P. and Schlesinger, P. 2006. Modelling conservation in the Amazon basin. *Nature*. **440**(7083), pp.520–523.

Sodhi, N.S., Lee, T.M., Sekercioglu, C.H., Webb, E.L., Prawiradilaga, D.M., Lohman, D.J., Pierce, N.E., Diesmos, A.C., Rao, M. and Ehrlich, P.R. 2010. Local people value environmental services provided by forested parks. *Biodiversity and Conservation*. **19**(4), pp.1175–1188.

Sodhi, N.S., Posa, M.R.C., Lee, T.M., Bickford, D., Koh, L.P. and Brook, B.W. 2010. The state and conservation of Southeast Asian biodiversity. *Biodiversity and Conservation*. **19**(2), pp.317–328.

Sorí, R., Nieto, R., Vicente-Serrano, S.M., Drumond, A. and Gimeno, L. 2017. A Lagrangian perspective of the hydrological cycle in the Congo River basin. *Earth System Dynamics*. **8**(3), pp.653–675.

Spracklen, B.D., Kalamandeen, M., Galbraith, D., Gloor, E. and Spracklen, D. V. 2015. A global analysis of deforestation in moist tropical forest protected areas. *PLoS ONE*. **10**(12), pp.1–16.

Spracklen, D. V., Arnold, S.R. and Taylor, C.M. 2012. Observations of increased tropical rainfall preceded by air passage over forests. *Nature*. **489**, pp.282–285.

Spracklen, D. V., Bonn, B. and Carslaw, K.S. 2008. Boreal forests, aerosols and the impacts on clouds and climate. *Philosophical Transactions of the Royal Society A: Mathematical, Physical and Engineering Sciences*. **366**(1885), pp.4613–4626.

Spracklen, D. V. and Garcia-Carreras, L. 2015. The impact of Amazonian deforestation on Amazon basin rainfall. *Geophysical Research Letters*. **42**(21), pp.9546–9552.

Spracklen, D.V., Baker, J.C.A., Garcia-Carreras, L. and Marsham, J.H. 2018. The Effects of Tropical Vegetation on Rainfall. *Annual Review of Environment and Resources*. **43**(1), pp.193–218.

Staal, A., Dekker, S.C., Hirota, M. and van Nes, E.H. 2015. Synergistic effects of drought and deforestation on the resilience of the south-eastern Amazon rainforest. *Ecological Complexity*. **22**, pp.65–75.

Staal, A., Flores, B.M., Aguiar, A.P.D., Bosmans, J.H.C., Fetzer, I. and Tuinenburg, O.A. 2020. Feedback between drought and deforestation in the Amazon. *Environmental Research Letters*. **15**(4).

Staal, A., Tuinenburg, O.A., Bosmans, J.H.C., Holmgren, M., Van Nes, E.H., Scheffer, M., Zemp, D.C. and Dekker, S.C. 2018. Forest-rainfall cascades buffer against drought across the Amazon. *Nature Climate Change*. **8**(6), pp.539–543.

Stibig, H.J., Achard, F., Carboni, S., Raši, R. and Miettinen, J. 2014. Change in tropical forest cover of Southeast Asia from 1990 to 2010. *Biogeosciences*. **11**(2), pp.247–258.

Sud, Y.C. and Smith, W.E. 1985. Influence of local land-surface processes on the Indian Monsoon: a numerical study. *Journal of Climate & Applied Meteorology*. **24**(10), pp.1015–1036.

Sy, S., de Noblet-Ducoudré, N., Quesada, B., Sy, I., Dieye, A.M., Gaye, A.T. and Sultan, B. 2017. Land-surface characteristics and climate in West Africa: Models' biases and impacts of historical anthropogenically-induced deforestation. *Sustainability (Switzerland)*. **9**(10), pp.1–24.

Takahashi, A., Kumagai, T., Kanamori, H., Fujinami, H., Hiyama, T. and Hara, M. 2017. Impact of tropical deforestation and forest degradation on precipitation over Borneo Island. *Journal of Hydrometeorology*. **18**(11), pp.2907–2922.

Tegegne, Y.T., Lindner, M., Fobissie, K. and Kanninen, M. 2016. Evolution of drivers of deforestation and forest degradation in the Congo Basin forests: Exploring possible policy options to address forest loss. *Land Use Policy*. **51**, pp.312–324.

Teuling, A.J., Seneviratne, S.I., Stöckli, R., Reichstein, M., Moors, E., Ciais, P., Luyssaert, S., Van Den Hurk, B., Ammann, C., Bernhofer, C., Dellwik, E., Gianelle, D., Gielen, B., Grünwald, T., Klumpp, K., Montagnani, L., Moureaux, C., Sottocornola, M. and Wohlfahrt, G. 2010. Contrasting response of European forest and grassland energy exchange to heatwaves. *Nature Geoscience*. **3**(10), pp.722–727.

Teuling, A.J., Taylor, C.M., Meirink, J.F., Melsen, L.A., Miralles, D.G., Van Heerwaarden, C.C., Vautard, R., Stegehuis, A.I., Nabuurs, G.J. and De Arellano, J.V.G. 2017. Observational evidence for cloud cover enhancement over western European forests. *Nature Communications*. **8**, pp.1–7.

Tosca, M.G., Diner, D.J., Garay, M.J. and Kalashnikova, O. V. 2015. Human-caused fires limit convection in tropical Africa: First temporal observations and attribution. *Geophysical Research Letters*. **42**(15), pp.6492–6501.

Tosca, M.G., Diner, D.J., Garay, M.J. and Kalashnikova, O. V 2014. Observational evidence of fire-driven reduction of cloud. *Journal of Geophysical Research: Atmospheres*. **119**, pp.8418–8432.

Tosca, M.G., Randerson, J.T. and Zender, C.S. 2013. Global impact of smoke aerosols from landscape fires on climate and the Hadley circulation. *Atmospheric Chemistry and Physics*. **13**(10), pp.5227–5241.

Tosca, M.G., Randerson, J.T., Zender, C.S., Nelson, D.L., Diner, D.J. and Logan, J.A. 2011. Dynamics of fire plumes and smoke clouds associated with peat and deforestation fires in Indonesia. *Journal of Geophysical Research Atmospheres*. **116**(8), pp.1–14.

Tuinenburg, O.A. and Staal, A. 2020. Tracking the global flows of atmospheric moisture and associated uncertainties. *Hydrology and Earth System Sciences*. **24**(5), pp.2419–2435.

Tuinenburg, O.A., Theeuwen, J.J.E. and Staal, A. 2020. High-resolution global atmospheric moisture connections from evaporation to precipitation. *Earth System Science Data*. **12**(4), pp.3177–3188.

Turubanova, S., Potapov, P. V., Tyukavina, A. and Hansen, M.C. 2018. Ongoing primary forest loss in Brazil, Democratic Republic of the Congo, and Indonesia. *Environmental Research Letters*. **13**, pp.1–15.

Tyukavina, A., Hansen, M.C., Potapov, P., Parker, D., Okpa, C., Stehman, S. V., Kommareddy, I. and Turubanova, S. 2018. Congo Basin forest loss dominated by increasing smallholder clearing. *Science Advances*. **4**(11), pp.1–12.

Wan, Z. 2014. New refinements and validation of the collection-6 MODIS land-surface temperature/emissivity product. *Remote Sensing of Environment*. **140**, pp.36–45.

Wang, J., Bras, R.L. and Eltahir, E.A.B. 2000. The Impact of Observed Deforestation on the Mesoscale Distribution of Rainfall and Clouds in Amazonia. *Journal of Hydrometeorology*. **1**(3), pp.267–286.

Wang, J., Chagnon, F.J.F., Williams, E.R., Betts, A.K., Renno, N.O., Machado, L.A.T., Bisht, G., Knox, R. and Bras, R.L. 2009. Impact of deforestation in the Amazon basin on cloud climatology. *Proceedings of the National Academy of Sciences of the United States of America*. **106**(10), pp.3670–3674.

Wang, Y., Ziv, G., Adami, M., Almeida, C.A. de, Antunes, J.F.G., Coutinho, A.C., Esquerdo, J.C.D.M., Gomes, A.R. and Galbraith, D. 2020. Upturn in secondary forest clearing buffers primary forest loss in the Brazilian Amazon. *Nature Sustainability*. **3**, pp.290–295.

Watson, J.E.M., Evans, T., Venter, O., Williams, B., Tulloch, A., Stewart, C., Thompson, I., Ray, J.C., Murray, K., Salazar, A., McAlpine, C., Potapov, P., Walston, J., Robinson, J.G., Painter, M., Wilkie, D., Filardi, C., Laurance, W.F., Houghton, R.A., Maxwell, S., Grantham, H., Samper, C., Wang, S., Laestadius, L., Runting, R.K., Silva-Chávez, G.A., Ervin, J. and Lindenmayer, D. 2018. The exceptional value of intact forest ecosystems. *Nature Ecology and Evolution*. **2**(4), pp.599–610.

Weaver, C.P. and Avissar, R. 2001. Atmospheric disturbances caused by human modification of the landscape. *Bulletin of the American Meteorological Society*. **82**(2), pp.269–281.

Winckler, J., Reick, C.H., Bright, R.M. and Pongratz, J. 2019. Importance of Surface Roughness for the Local Biogeophysical Effects of Deforestation. *Journal of Geophysical Research: Atmospheres*. **124**(15), pp.8605–8618.

Zemp, D.C., Schleussner, C.F., Barbosa, H.M.J., Hirota, M., Montade, V., Sampaio, G., Staal, A., Wang-Erlandsson, L. and Rammig, A. 2017. Self-amplified Amazon forest loss due to vegetation-atmosphere feedbacks. *Nature Communications*. **8**, pp.1–10.

Zeng, Z., Estes, L., Ziegler, A.D., Chen, A., Searchinger, T., Hua, F., Guan, K., Jintrawet, A. and F. Wood, E. 2018. Highland cropland expansion and forest loss in Southeast Asia in the twenty-first century. *Nature Geoscience*. **11**(8), pp.556–562.

Zhang, K., Kimball, J.S., Nemani, R.R. and Running, S.W. 2010. A continuous satellite-derived global record of land surface evapotranspiration from 1983 to 2006. *Water Resources Research*. **46**(9), pp.1–21.

Chapter 2

2 Data and Methodology

In this Chapter I will outline the data and methods used in the analysis chapters (3-6) of this thesis. Firstly, I will examine and detail the important features and inputs of each of the remotely sensed, ground-based and model datasets. Then I will describe the core methods used to analyse the datasets, adding more detail and discussion than is covered in the individual analysis Chapters.

2.1 Data

This thesis relies on the data collected and produced by others. We use a variety of data such as land surface temperature and precipitation, from a variety of sources, ranging from satellite remotely sensed, ground-based observations, model-observation hybrids (reanalysis) and climate models. It is important when analysing the datasets, to understand the types, origins, limitations and differences between them. As such I describe the information pertinent to this in turn, summarising the key information in Table 2.1.

Table 2.1. *Observational datasets used in the analysis in Chapter 3-6, listing their temporal availability (date range), native resolution, categorisation, and their reference. The categorisation refers to the three main observational categories used in this thesis of satellite, station (referring to ground-based observations) and reanalysis. Present refers to the dataset being available at least up to the start of 2023.*

Dataset	Date Range	Native Res.	Category	Reference
MCD43A3	2001 - present	500 m	Satellite	Schaaf and Wang, 2021
MOD16A2GF	2001 - present	500 m	Satellite	Running et al., 2021
MOD15A2H	2001 - present	500 m	Satellite	Myneni et al., 2021
MOD11A2	2001 - present	0.01	Satellite	Wan et al., 2021b

MYD11A2	2003 - present	0.01	Satellite	Wan et al., 2021a
MCD12Q1	2001- present	0.05	Satellite	Friedl and Sulla-Menashe, 2022
Forest Loss, Global Forest Change (GFC) v1.9	2000-2022	30 m x 30 m, annual	Satellite	Hansen et al., 2013
Driver	2001-2019	10 km x 10 km	Satellite	Curtis et al., 2018
CHIRPS v2.0	1981 – present	0.05	Satellite	Funk et al., 2015
CMORPH	1998 – present	0.25	Satellite	Xie et al., 2019
CPC	1979 – present	0.5	Station	Xie et al., 2007
CRU TS v4.06	1901 – present	0.5	Station	Harris et al., 2020
ERA5-Land	1950 – present	0.1	Reanalysis	Hersbach et al., 2020
GPCC v2022	1891 – present	0.25	Station	Schneider et al., 2022
GPCP v3.2	1996 -2020	0.5	Satellite	Huffman et al., 2022
GPM v0.6	2000 – present	0.1	Satellite	Hou et al., 2014
JRA v7.0	1979 – present	0.5625	Reanalysis	Kobayashi et al., 2015
MERRA-2	1980 – present	0.5x0.625	Reanalysis	Gelaro et al., 2017
PERSIANN-CCS	2003 – present	0.04	Satellite	Nguyen et al., 2019
PERSIANN-CDR	1983 – present	0.25	Satellite	Ashouri et al., 2015
PERSIANN-CCSCDR	2003 – present	0.04	Satellite	Sadeghi et al., 2021)
PERSIANN_NOW	2000 – present	0.04	Satellite	Nguyen et al., 2020
PERSIANN	2000 – present	0.25	Satellite	Nguyen et al., 2019
TRMM v3B43	1998 – 2019	0.25	Satellite	Huffman et al., 2007
UDEL v5.01	1990 – 2017	0.5	Station	Matsuura and Willmott, 2018)

2.1.1 Satellite Data

Satellite data forms a large portion of the data used in this thesis. Satellite remote sensing is introduced in Chapter 1, the specifics of the satellites used are detailed and contrasted here. We utilise data from two main satellite series, Landsat and the MODIS (Moderate Resolution Imaging Spectroradiometer) carrying satellites Terra and Aqua. These are two of the primary sources of remote land surface and climate observations, however in 2023 there are several alternatives, notably including from the European Space Agency (ESA) that are not detailed here.

Landsat

Landsat is a collection of 9 near-polar orbiting satellites, the first, Landsat 1 being launched in July 1972 and the latest, Landsat 9 being launched in September 2021 (Landsat Science Outreach, 2023). The data produced by the Landsat satellite series is one of the primary sources of data used in this thesis. The next generation of earth observing satellites, Landsat Next is due to be launched in 2029 and will measure a far greater number of spectral bands than previous generations (25 compared to Landsat 8/9's 11 bands). Currently only Landsat 8 and 9 remain in operation, however in total Landsat has produced continuous earth observations for over 40 years, providing a crucial record of land surface and atmospheric observations. Landsat 8 and 9 both carry two sensors, the Operational Land Imager (OLI) and the Thermal InfraRed Sensor (TIRS) which sense wavelengths from 0.435 – 12.51 µm in 11 bands, with resolutions of 15-30 m (Landsat Science Outreach, 2023). The OLI receives radiation in the visible and infrared spectrum using a 'push-broom' sensor to capture panchromatic images at 15 m spatial resolution and multi-spectral images at 30 m resolution (Landsat Science Outreach, 2023). This allows for the detection of small-scale land use and land cover changes, essential for capturing emergent disturbances (Almeida et al., 2008). The TIRS measures two thermal bands, recording information about the Earth's thermal energy using Quantum Wll Infrared Photodetectors. These sensors detect longer wavelengths, called thermal infrared, and are newer low-cost alternatives to previous infrared technology on-board previous Landsat satellites (Landsat Science Outreach, 2023). The sensors used on different Landsat iterations have advanced over time causing discontinuity, the limitations for our analysis are discussed in Chapter 6. Compared to other satellite instruments, the time it takes Landsat to image the entire Earth's surface is longer than Terra and Aqua, at 16 days, however Landsat can capture very high spatial resolution data.

Two examples of datasets used in this thesis that are based upon remotely sensed data from Landsat are Global Forest Change and the drivers of forest loss datasets.

Global Forest Change

This product provides information of forest cover change over time and is a Landsat satellite-based time series analysis. The dataset was developed by Hansen et al. (2013) in the Global Land Analysis and Discovery (GLAD) lab at the University of Maryland. The dataset provides annual global forest extent in 2000 and forest loss and gain (up to 2012) from 2001-present at 30 m spatial resolution. We do not use forest gain in this thesis due to data only being available until 2012, as such it's methodology will not be discussed.

The dataset has a wide range of applications and has been extremely popular for analysing and comparing trends in forest decline, particularly across the tropics (Li et al., 2016; Baker and Spracklen, 2019; Vancutsem et al., 2021; Pendrill et al., 2022; Smith et al., 2023 and many more). For all land cover datasets, the definition of vegetation is integral and poignant as this can affect the values reported greatly (García-Álvarez et al., 2022). Here trees are defined as vegetation taller than 5 m. Tree cover change was measured in terms of crown cover, with forest loss being a transition from >50% crown cover to ~0%. Forest cover was observed during the growing season, using remotely sensed data originally from Landsat 7's Enhanced Thematic Mapper Plus, but latterly Landsat 8's Operational Land Imager, a transition which is discussed in more detail in the uncertainty and limitations section of Chapter 6. Images were classified using existing tree cover maps (Hansen et al., 2011), MODIS percent tree cover (Hansen et al., 2003) and image interpretation to delineate forest cover, loss and gain. These classified images were fed into a bagged decision tree model to predict changes over unseen images. The processing and modelling was made possible by using the large resources of Google Earth Engine. The result is a freely available, very high resolution annual global forest change dataset.

Drivers of Forest Loss

This dataset provides information about the driver of forest loss for each cell of tree cover loss across the world and was published in 2018 by Curtis et al. (2018). The dataset is produced for 2001 - 2019 at 10 km resolution, classifying forest loss into one of five categories. These categories are commodity driven deforestation, shifting agriculture, forestry, wildfire, and urbanisation. This dataset is particularly useful for identifying the location and proliferation of the distinct drivers of global forest loss and providing insight for researchers and governments.

The dataset is produced by using a model which has been trained on 4699 training samples taken from Google Earth. These samples were categorised into five distinct disturbance classes based on the dominant visible activity occurring within tree cover loss in each cell. This process was iterative, adding more training data for each class until enough “good” examples were attained (Curtis et al., 2018). Areas of forest loss were determined using the GFC dataset (Hansen et al., 2013).

For each cell, a visual inspection using Google’s time series imagery was conducted, assessing the primary driver of forest loss in each cell. Regional models were created to allow for the possibility that the same driver may present differently in different world regions. Commodity driven forest loss was classified by signs of existing agriculture including oil palm plantations, pasture, or mining as well as zero or minimal regrowth in the years post-deforestation. Shifting agriculture was classed as clearings of agriculture or pasture as well as historical clearings containing secondary forest or shrubland regrowth. The forestry class includes general plantations including wood-fibre as well as processes such as selective cutting. Cells were categorised as wildfire if there was strong evidence of a loss event driven by fire, however this did not include areas cleared for agriculture. Lastly urbanisation was classed as visible urban expansion or intensification.

The training images, alongside the following datasets: tree cover extent (GFC, (Hansen et al., 2013)), active fires (MODIS), land cover (Tuanmu and Jetz, 2014) and population count (CIESIN, 2018) were inputted to a decision tree model to predict the most likely driver or tree cover loss for unobserved cells. The model assigned each cell 5 values representing the likelihood of each driver being dominant. If a cell had no single class with >50% likelihood, it was assigned the value of its neighbour. Model validation was carried out using 1565 predicted cells on the training data to assess the model skill.

Curtis et al. (2018) note that no distinction is made between natural and anthropogenic disturbances, and their classes are not labelled as such. They argue that separating human from completely natural events such as wildfire is not easy as the two commonly inextricably linked. In addition to this, due to the relatively coarse scale, compared to other land classification datasets, there may be multiple drivers contributing to loss in each cell. Therefore, cell to cell comparison is unadvisable, instead basin wide insights should be prioritised.

Terra and Aqua carrying MODIS

MODIS is a remote sensing instrument on board the Aqua and Terra satellites operated by the National Aeronautics and Space Administration (NASA). Terra and Aqua are sun-synchronous satellites, meaning they pass overhead with the sun in the same position every day. Terra was designed to sense the land surface and was launched in 1999, beginning data collection in February 2000. It was followed by Aqua which launched in 2002 and was designed primarily to sense water (Smith, 2022). Terra has an equatorial overpass time of 10:30am whilst aqua has an overpass time of 1:30pm. The overpass time has implications for sensing some land surface and climate quantities, in effect providing a morning and afternoon reading. TERRA and Aqua orbit at an altitude of 705 km, giving an orbital period of 98.8 minutes, completing approximately 14.5 orbits per day. The time taken to revisit the same ground track is 233 orbits (16 days) (NASA GSFC, 2023b). For most of its lifetime Aqua had been part of the A train, leaving in Jan 2022 due to fuel limitations.

Terra carries five instruments, with MODIS (Justice et al., 2002) being one, the others being ASTER (Advanced Spaceborne Thermal Emission and Reflection Radiometer) (Hook et al., 2001), CERES (Clouds and the Earth's Radiant Energy System), MISR (Multi-angle Imaging Spectro Radiometer) (Diner et al., 2002) and MOPITT (Measurements of Pollution in the Troposphere) (Drummond et al., 1999; Drummond, 2002). Aqua meanwhile carries 6 instruments including MODIS, of which 4 are fully operational, those being AMSR-E (Advanced Microwave Scanning Radiometer-EOS) (Kawanishi et al., 2003), AMSU-A (Advanced Microwave Sounding Unit) (Mo, 1996) and AIRS (Atmospheric Infrared Sounder) (Aumann et al., 2003) (NASA GSFC, 2023b).

The MODIS instrument can measure 36 spectral bands (groups of wavelengths from 0.4 µm to 14.4 µm), allowing for measurements ranging from distribution of clouds to photosynthetic activity. It has a swath of 2330 km (10 km length pointing directly downwards, "nadir"). MODIS senses at resolutions from 250 m to 1 km depending on the band, with each band having a primary sensing use (Justice et al., 2002). Bands 1-7 (620-2155 nm) sense land, cloud and aerosol boundaries, bands 8-16 (405-877 nm) sense ocean colour, phytoplankton and biogeochemistry, bands 17-19 (890-965 nm) sense atmospheric water vapour, bands 20-23 (3.6-8.1 µm) sense surface and cloud top temperature, bands 24-25 (4.3-4.5 µm) sense atmospheric temperature 26-28 (1.4-7.5 µm) sense cirrus cloud water vapour, band 29 (8.4-8.7 µm) senses cloud properties, band 30 (9.6-9.9 µm) sense ozone, bands 31-32 (10.8-12.3 µm) again sense surface and cloud top temperatures and bands 33-36 (13.2-14.4 µm) sense cloud top height (Justice et al., 2002; NASA GSFC, 2023b). The naming convention for MODIS datasets labels datasets originating from Terra and MODxx, Aqua as MYDxx and a merged product MCDxx.

Overtime, improvements have been made to the algorithms that generate MODIS user products. The datasets used in this thesis are all MODIS collection 6.1, the latest available at time of writing. Collection 6.1 has several technical improvements over collection 6 and is strongly recommended to be preferentially used. Some improvements are advancements in cloud screening, which results in more skilful identification of cloud contaminated pixels which helps reduce errors in products such as land surface temperature. Improvements were made to the atmospheric correction algorithm, taking better account of the absorption and emission in the thermal bands. Additionally, collection 6.1 uses an updated land cover classification which takes advantage of advancements in the estimation of surface emissivity (NASA GSFC, 2023a). The entire available MODIS time series has been reprocessed with the new algorithms, so there are no issues with discontinuity.

Each MODIS dataset comes supplied with a Quality Assurance dataset, applicable to each product with quality control information derived during production or post-production during quality assessment. From this dataset, each pixel is classed on the basis of its existence, calibration quality, cloudiness of the scene and application of additional post-processing. Where applicable when using MODIS products, we have selected pixels that are "cloud free" and have a "good" data quality flag. The datasets used in this thesis, which are the latest versions available to use in 2023 (Collection 6, version 6.1), are described in detail below.

Albedo (MCD43A3)

The albedo of a surface is the ratio of the downwelling radiation incident upon the surface and the upwelling energy scattered from the surface. Albedo is a dimensionless quantity represented by a value between 0 and 1, where values close to 1 represent a highly reflective, light surface and values closer to 0 represent darker, less reflective surfaces (Gash and Shuttleworth, 1991). Broadly, forests have dark surfaces and low albedo values typically around 0.15 (Gash and Shuttleworth, 1991; Bastable et al., 1993; Culf et al., 1995) whilst ice and snow have high albedo values of around 0.6-0.9, dependent largely upon the age of the snow and ice (Lee et al., 2011).

MCD43A3 retrieves both black and white sky albedo at local solar noon for bands 1-7, visible, near infrared and shortwave bands. BSA is the integration of the bi-directional hemispherical reflectance, it assumes the absence of a diffuse component (i.e., cloud), and it is a function of the solar zenith angle. WSA is the integration of directional bi-hemispherical reflection, and it assumes the presence of a diffuse component (Schaaf and Wang, 2021). Whilst MCD43A3 is provided every 16 days, the value presented is a daily aggregate of the total available data. The algorithm uses a semi-empirical model to invert 16 days worth of data into one atmospherically corrected pixel (Schaaf and Wang, 2021). When fewer than 7 days worth of data is available, an inversion isn't possible, and a value is taken from a constantly updating look-up table.

For the analysis in this thesis, we chose to use the combined Terra and Aqua product with a 500 m spatial resolution as combing the sensors allowed for better coverage and a lower incidence of cloud cover. The time of overpass is of lesser importance for sensing albedo than for land surface temperature which changes throughout the day. We analysed both BSA and WSA and found their results to be broadly similar, leading us to present just BSA in the main results. Ito support this, Strahler et al., (1999) outline how albedo is dependent upon the land surface rather than atmosphere and find that either WSA or BSA are suitable for sensing true surface albedo. When comparing albedo from MODIS observations to ground-based or model albedo, Giambelluca et al. (1997) explain that most ground-based observations are retrieved at solar-noon and under cloudless conditions, therefore the retrieval would be dictated by the directional hemispheric reflectance (BSA). Finally, Zhang et al. (2010) find that in comparison to WSA, BSA has smaller seasonal variance, potentially allowing small changes in albedo from land use change to be identified easier.

Evapotranspiration (MOD16A2GF)

Evapotranspiration (ET) is not directly measured, rather it is a derived quantity based on several measurements from different land surface and climate variables and reanalysis from models, a process which is outlined in Figure 2.1. ET is the sum of water vapour fluxes from soil evaporation, wet canopy evaporation and plant transpiration at the dry canopy surface (Mu et al., 2013). It is estimated using the algorithm developed by (Running et al., 2021b) and based on the Penman-Monteith equation (Monteith, 1965). The algorithm, detailed by Mu et al. (2013), incorporates daily meteorological reanalysis and observations leaf area index/ fraction of photosynthetically active radiation (LAI/FPAR), air pressure, temperature, humidity, surface albedo, radiation and land cover data. FPAR dictates the vegetation cover fraction, allowing for the partitioning of net radiation between soil and vegetation. MODIS Albedo, alongside reanalysis radiation and air temperature are used for the calculation of net surface radiation and the soil heat flux. Stomatal conductance, aerodynamic resistance, wet canopy and soil heat flux from which transpiration can be inferred, is determined using model air temperature, vapour pressure deficit, relative humidity and MODIS LAI (Running et al., 2021b). MODIS land cover provides the specific biome type, from which biome dependant constant values are found from the Biome-Property-Lookup-Table. These ET values are largely driven by MODIS GPP and water use efficiency from ground-based eddy flux towers. MOD16 products are verified using ET measured by ground-based eddy flux towers from 232 watersheds.

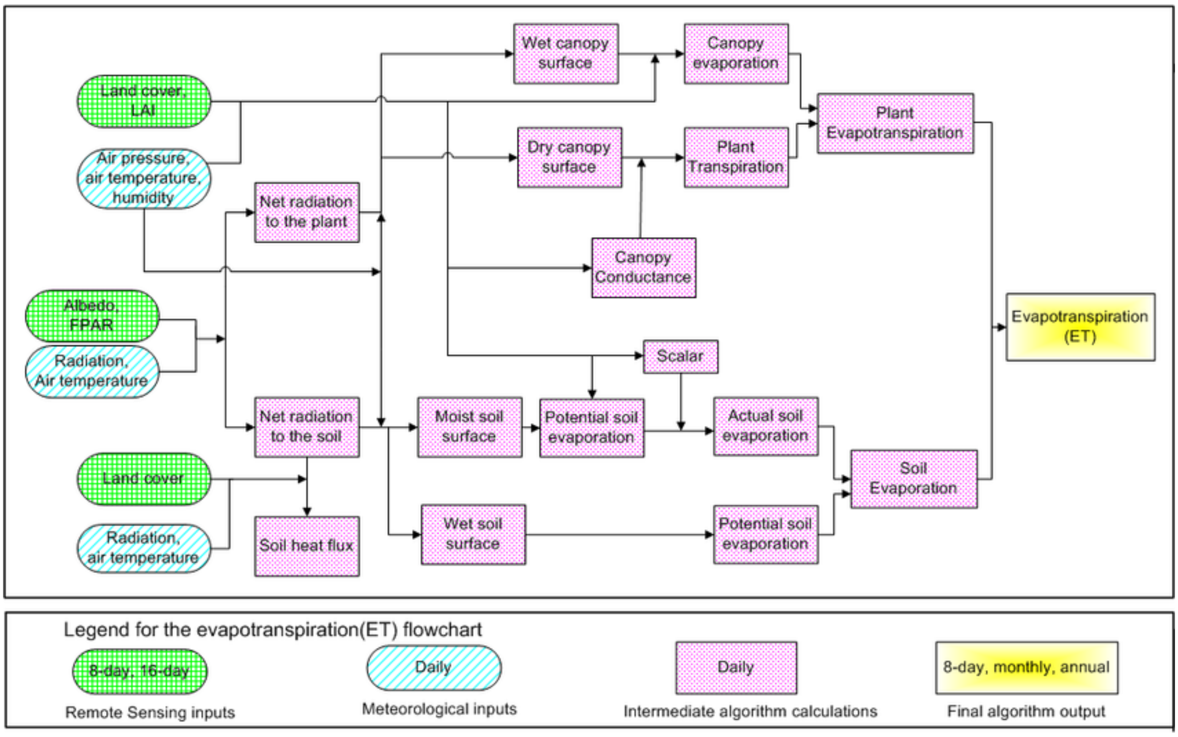

Figure 2.1. *Flowchart of the MOD16A2GF (ET) algorithm (Running et al., 2021b). The algorithm combines several inputs ranging from LAI to land cover to provide an estimate of evapotranspiration.*

In the tropics, retrievals of MODIS LAI and albedo are hampered by high cloud cover, resulting in a greatly reduced number of ET tiles being produced. To counter this, MODIS uses a year-end (completed and supplied at the end of the year) gap filling process, whereby average of the best LAI/FPAR and albedo from the previous 5 years fills the gaps presented by 'poor quality' LAI/FPAR and albedo (Running et al., 2021b). Poor quality is calculated though linear interpolation, examining the previous and next period's value to determine whether the ET value is anomalous (Zhao et al., 2005; Mu et al., 2007). A 5-year period is chosen to span interannual global fluctuations such as ENSO which will alter biosphere characteristics (Keeling et al., 1995), with longer periods being unrealistic as vegetation greenness alongside land use changes over time (Mildrexler et al., 2009; Song et al., 2018). Quality control filtering had already been applied in the production of the ET tiles; thus no further filtering was necessary. The limitations of this methodology are discussed in detail in Chapter 6.

Leaf Area Index (MOD15A2H)

Leaf area index per unit ground area (LAI, dimensionless, m^2/m^2) is estimated based on an algorithm using information from up to 7 spectral bands of surface reflectance (Knyazikhin et al., 1999; Myneni et al., 2021). For broadleaf forests such as those in the tropics, it is defined as the one-sided green LAI, whereas in coniferous forests, it is one-half the total needle surface area per unit ground area. Alongside LAI, FPAR is often used as a quantity to investigate vegetation changes. FPAR is defined as the fraction of incident photosynthetically active radiation (400−700 nm) absorbed by the green elements of a vegetation canopy (Knyazikhin et al., 1999).

The algorithm which generates LAI combines several streams of information, including near infrared and red radiation, MODIS surface reflectance, Normalised Difference Vegetation Index (NDVI) and MODIS land cover (providing a range of typical vegetation structural type for the biome). These are entered into a look-up-table which provides LAI (Knyazikhin et al., 1999). LAI saturates with dense canopy covers, such that it is weakly sensitive to canopy cover properties, in these cases, the algorithm defaults to using vegetation indices rather than spectral information (Fang et al., 2019). We used the quality-control (QC) data layers accompanying the LAI to mask cloud-contaminated grid cells and grid cells where the quality was not ranked at least 'good'.

Land Surface Temperature (MOD11A, MYD11A2)

Land surface temperature (LST) is a very useful quantity for assessing the earth's surface energy balance, climate and land surface changes and hydrological studies, combining surface atmosphere interactions and energy fluxes. MODIS LST provides a long term (2001 to present day) dataset with high spatial resolution (1 km), from which sensible and latent heat fluxes (Vining and Blad, 1992; Kimura and Shimizu, 1994) and soil surface temperature can be derived.

LST is calculated from a combination of the MODIS sensor radiance product, MODIS land-cover products and MODIS cloud masks (Wan, 1999). We used both MOD11 (Terra) and MYD11 (Aqua) products in this thesis. The processes to create the datasets are very similar, so are described as one here. We chose to use 8-day LST as this provides sufficient temporal resolution. It represents an average of the daily MOD11A1 product. LST is provided with both daytime and night time values and associated quality control layers. Using both MOD11 and MYD11 allowed us to compare equatorial morning and afternoon LST due to the difference in overpass time.

Wan (1999) describe the method for producing LST as follows. LST is generated using a split-window algorithm, a radiative transfer equation, which relies on the different thermal infrared spectral bands that are emitted from the Earth's surface (Rozenstein et al., 2014). MODIS uses band 31 (11 µm) and band 32 (12 µm), which are differently sensitive to atmospheric and surface properties. The adsorption, scattering and emission of infrared radiation by the atmosphere are corrected for by using the difference in adsorption properties between atmospheric water vapour and CO_2. In addition to thermal radiation, atmospheric temperature and moisture profiles are required, which can be obtained by ground-based, atmospheric infrared sounder as well as the MODIS instrument. The algorithm assumes uniformity of the surface, estimating a relationship between the bands based on the brightness. The split window algorithm then relates this difference in brightness to LST, whilst considering the atmospheric transmittance and surface emissivity, which can be derived from land cover classifications and look-up-tables. The split window algorithm is applied iteratively to generate an estimate of LST, then computes brightness temperatures based on this, and then adjusts the LST first guess accordingly. Ground-based measurements from eddy-flux towers are used to validate the remotely sensed LST.

In the analysis contained within Chapter 3-6, we chose to use land surface temperature as opposed to near-surface air temperature as LST is globally readily available at suitable temporal and spatial resolutions and is directly applicable to land surface change analysis. Using ground-based studies, air temperature and LST have been closely correlated (Good et al., 2017), justifying our use of satellite-derived land-surface temperature as a suitable metric.

Land Cover Type (MCD12Q1)

Global land cover types are provided at yearly intervals with 500 m spatial resolution. The product is supplied with 13 individual datasets, made up of 8 different classification schemes and 5 quality assurance or masking layers. The classification schemes include the International Geosphere-Biosphere Programme (IGBP) (Belward et al., 1999), University of Maryland (UMD) (Hansen et al., 2000), Leaf Area Index (LAI) (Myneni et al., 2002), BIOME Biogeochemical Cycles (BGC) (Running et al., 2004), Plant Functional Types (PFTs) (Bonan et al., 2002) and a newer three-layer Land Cover Classification System (LCCS) from the Food and Agriculture Organisation (Sulla-Menashe and Friedl, 2022). In this thesis I use the UMD classification system as this is consistent with the GFC data which also originates from the UMD. We use the product to identify areas of evergreen broadleaf forest within the tropical forest regions. Evergreen broadleaf is defined by UMD classification as “dominated by evergreen broadleaf and palmate trees (canopy >2m) with tree cover >60%”. This definition is the same used in the IGBP, LCCS1 and LAI classifications however PFT and BGC classifications use “dominated by evergreen broadleaf and palmate trees (>2m), with tree cover >10%” and “dominated by evergreen broadleaf and palmate trees and shrubs (>1m), with woody vegetation cover >10%” respectively (Sulla-Menashe and Friedl, 2022).

The algorithms take inputs that include MODIS land/ sea mask, reflectance derived from MODIS Albedo (Nadir BRDF-adjusted, bands 1-7), spatial texture (band 1), directional reflectance, MODIS enhanced vegetation index (EVI), snow-cover, MODIS LST and MODIS terrain elevation (Strahler et al., 1999). The product is made using a machine learning technique called Random Forest supervised classification, taking sensed MODIS reflectance data, with training data from the LCCS (Friedl et al., 2010). To reduce the impact of errors causing inter-annual variability, post processing using an algorithm based on Hidden Markov Models is applied which reduces variability (Abercrombie and Friedl, 2016). Despite this process, the product is not recommended for use in land cover change, before and after analysis. The algorithm is verified using a network of test sites with land cover derived from the Advanced Very High Resolution Radiometer (AVHRR) and Landsat satellites to characterise the accuracy of the classification (Strahler et al., 1999).

2.1.2 Precipitation Data

Here I outline the complete list of precipitation datasets used in this thesis, which can be viewed in synthesis in Table 2.1. It isn’t however an exhaustive list of the datasets available as some datasets were excluded from our analysis based on their available spatial or temporal resolution or due to private access. The datasets listed are split into three categories, satellite, ground-based and reanalysis. Most satellite precipitation products used in this analysis are a combination of remote and ground-based data, however below they are categorised by their primary source, either satellite or ground-based. The reanalysis datasets by nature take remotely sensed and ground-based observations to drive their models, however they are categorised separately as reanalysis datasets. Even within classes (satellite, ground-based, reanalysis), the precipitation datasets vary greatly in their construction methodology and spatial resolution. This is explored in detail in the following sections. As a result of these differences, their estimation of rainfall will be variable, and it was therefore important to use a large range of datasets to form an average when conducting the analysis, the impact of land use change on rainfall in Chapter 4.

Satellite Precipitation

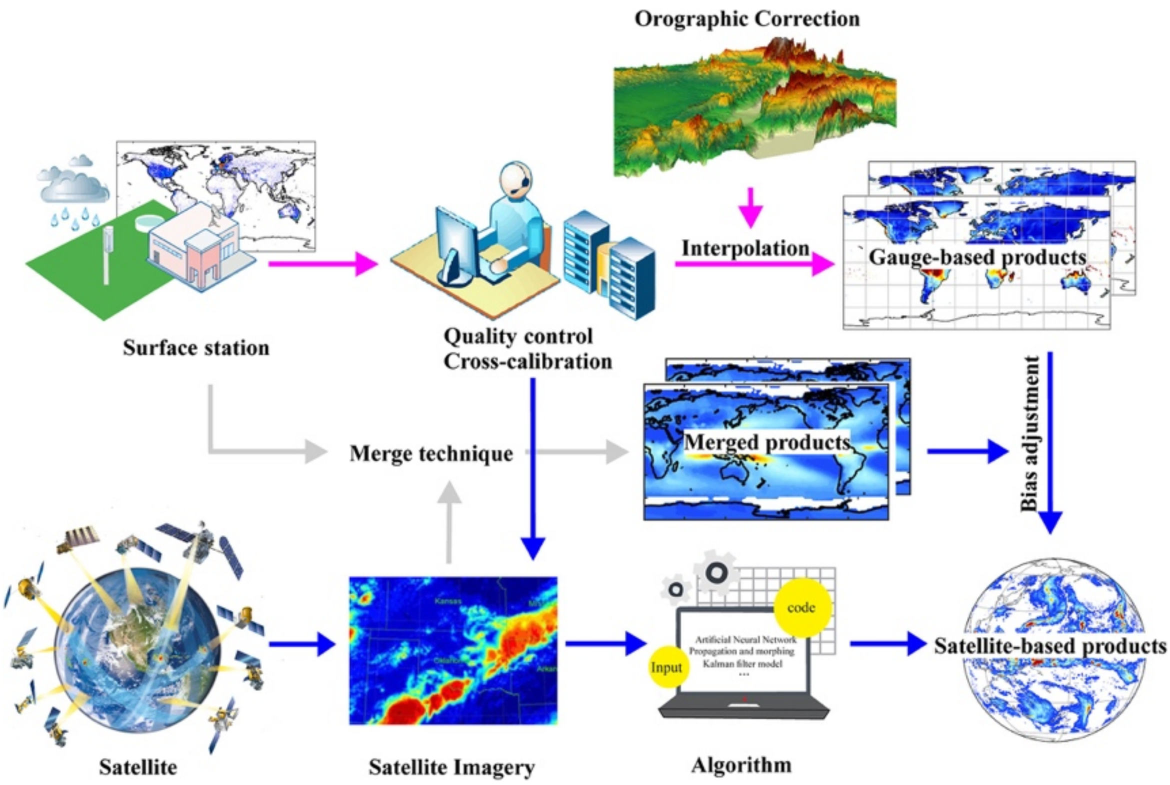

Figure 2.2. *Flowchart for the integration of ground-based and satellite data to make precipitation products. The diagram was created by (Sun et al., 2018) adapted from (Hou et al., 2014).*

Satellite precipitation datasets can estimate rainfall amounts, distributions and variability near globally and with high temporal resolution. Broadly, they sense precipitation by capturing emitted or reflected microwave and infrared radiation and from that inferring rainfall (Sun et al., 2018). Often, satellite measurements are validated using ground-based observations, where there are station data available, a process described by Figure 2.2. The algorithms used to generate rainfall often apply post-processing steps to fill data gaps, remove artifacts and biases or assimilate multiple data streams. Satellite datasets have significant advantages over ground-based estimates as they can sense near globally at very high spatial and temporal resolutions.

CHIRPS

The Climate Hazards Group InfraRed Precipitation with Station data (CHIRPS) precipitation dataset is made by researchers from the USGS (United States Geological Survey) and CHC (Climate Hazards Centre) with additional support from USAID (United States Agency for International Development), NASA (National Aeronautics and Space Administration) and NOAA (National Oceanic and Atmospheric Administration) (Funk et al., 2015). The dataset spans 1981 to the present day, making it one of the longest available satellite precipitation datasets. It has a spatial extent of 50^{o} N-S and produces data gridded to 0.05 degrees, equivalent to around 5 km length at the equator.

CHIRPS was particularly designed for estimating extremes in rainfall with the aim of improving drought early warning systems and environmental monitoring (Funk et al., 2015). It is explicitly designed to help provide low latency (time from data acquisition to publication), high resolution, gridded precipitation data with a long available time series, whilst combing satellite and station data. Other available precipitation datasets often fulfil one of these criteria, for example GPCC and CRU which have long data availability but long latency, and CMORPH and PERSIANN products have low latency but only take satellite data inputs. It allows extreme precipitation events to be put into context using the long time series.

The CHIRPS algorithm has three main parts, the Climate Hazards group precipitation climatology (CHPclim), the satellite only Climate Hazards group Infrared Precipitation (CHIRP) and finally the process by which the satellite data is merged with station data (CHIRPS) (Funk et al., 2015). CHPclim is built from two sources of long-term station-based precipitation means, the first being the Agromet Group of the Food and Agriculture Organisation of the United Nations (FAO) and the second being the Global Historical Climate Network (GHCN) (Peterson and Vose, 1997), which many of the precipitation datasets used in this thesis are also based upon. Together these sources aggregate data from ~50,000 stations globally. In addition to the standardly applied elevation, latitude and longitude, CHPclim takes long term mean monthly data from satellite datasets; the Tropical Rainfall Measuring Mission 2B31 (TRMM 2B31) (Huffman et al., 2007) microwave precipitation estimates, MODIS land surface temperature, infrared brightness temperatures and CMORPH (CPC Morphing) (Joyce et al., 2004) precipitation estimates. In contrast to other precipitation climatologies, CHPclim uses a moving window regression, taking a varying number of inputs dependent on the available station data. CHIRPS precipitation is estimated from a combination CHPclim, a climatology model, remote and ground-based retrievals (Huffman et al., 2007; Funk et al., 2015).

CMORPH

CMORPH (Climate Prediction Center morphing method) is a precipitation product developed by the Climate Prediction Center (CPC) at NOAA (Joyce et al., 2004). The dataset is available at high temporal and spatial resolution, with the product being gridded to 8x8 km and 30-minute time steps between 1998 to present day. The spatial extent is near global, from 60^{o} N-S. In this analysis we used the CMORPH daily product which is available at 0.25 degrees resolution as it was more suitable than sub-hourly for our analysis methods.

The CMORPH product is particularly useful for driving initialisation of numerical weather prediction models as it has high temporal and spatial resolution (Joyce et al., 2004). In remote regions in the world, there are few rain gauges, and fewer with higher than 6 hour temporal resolution, therefore a global remotely sensed dataset is essential to provide accurate information for these areas. The high temporal resolution also allows for disaster mitigation applications as well as longer term climate observation studies.

CMORPH primarily takes polar-orbiting satellite microwave observations from NOAA, DMSP (U.S. Defence Meteorological Satellite Program) and TRMM (Tropical Rainfall Measuring Mission) (Huffman et al., 2007), using the instruments Advanced Microwave Sounding Unit-B (AMSU-B), the Special Sensor Microwave Imager (SSM/I), and the TRMM Microwave Imager (TMI) respectively. The method merges these data to form a single, high-resolution precipitation estimate. The data is processed by the Climate Prediction Center (CPC) using their Morphing Technique (MORPH) (Joyce et al., 2004). Unlike products that average or blend microwave estimates, which are often affected by poor retrievals, CMORPH derives information from high-temporal resolution geostationary infra-red imagery to propagate the precipitation derived from passive microwave radiation.

GPCP

The Global Precipitation Climatology Project (GPCP) is a precipitation product under the umbrella of the World Climate Research Program (WCRP), produced by the Global Water and Energy Exchange (GEWEX). It is a long-term homogenous precipitation product taking data from rain gauges and satellite inputs (Huffman et al., 2022).

GPCP is a daily product and has a spatial extent of 55^{o} N-S and a resolution of 0.5 degrees with data from mid 2000-2020. Since GPCP has satellite and ground based data inputs, it has a wide range of uses, from drought monitoring to disease prediction, however it has daily resolution meaning it cannot be used for sub-daily applications.

The main input for GPCP is taken from the Integrated Multi-satellite Retrievals (IMERG) (Huffman et al., 2020) product for GPM, which is comprised of passive microwave (PMV) and Infra-red (IR) sensors onboard the GPM constellation of satellites. These data are then processed using the Climate Prediction Center (CPC) Morphing-Kalman Filter (CMORPH-KF) quasi-Lagrangian time interpolation procedure (Joyce and Xie, 2011) and the Precipitation Estimation from Remotely Sensed Information using Artificial Neural Networks – Cloud Classification System (PERSIANN-CCS) infrared (IR) recalibration procedure (Sadeghi et al., 2021). These steps merge the PMV and IR datasets. Subsequently, rainfall gauge data from the Deutscher Wetterdienst (DWD) Global Precipitation Climatology Centre monthly gauge analysis (GPCC; (Becker et al., 2013; Schneider et al., 2014; Schneider et al., 2022)) is integrated, producing the final merged product.

GPM

The Global Precipitation Mission (GPM) is a collaboration between NASA and the Japanese Aerospace Exploration Agency (JAXA) providing 30-minute precipitation estimates. Launched In 2014, it is an extension to the Tropical Rainfall Measuring Mission (TRMM), building upon its success in a few key ways. Firstly, GPM provides global data and secondly has enhanced ability to sense light rain, a persistent problem for remotely sensed precipitation products. GPM has coverage over 60^{o} N-S at 0.1 degrees with a 30 minute temporal resolution. Taking advantage of the existing TRMM dataset, GPM continues, providing precipitation estimates from 1998 to present day. As a sub-daily dataset, GPM has uses for improving numerical weather prediction (NWP) models as well as climate studies and resource management (Huffman et al., 2020).

The measurements come primarily from two instruments; the GPM Microwave Imager (GMI) which records 2D spatial patterns and precipitation intensity and the Dual-frequency Precipitation Radar (DPR) which provides 3D structure (Huffman et al., 2020). GMI has 13 microwave bands that observe a range of precipitation types from heavy rain to snow. The unified GPM dataset provides a long precipitation dataset by using the Integrated Multi-satellitE Retrievals for GPM (IMERG) algorithm (Huffman et al., 2020). This takes information from all available satellite instruments to gain a global estimate of precipitation which covers the majority of the Earth's surface.

The IMERG algorithm takes information from The Advanced Microwave Scanning Radiometer-2 (AMSR-2) (Kawanishi et al., 2003), JAXA's Global Change Observation Mission - Water 1 (GCOM-W1) satellite (Shimoda, 2005) and The Advanced Technology Microwave Sounder (ATMS) instrument (Kim et al., 2014) on the Suomi National Polar-orbiting Partnership (SNPP) and NOAA20 satellites. It also takes data from the Sondeur

Atmosphérique du Profil d'Humidité Intertropicale par Radiométrie (SAPHIR) (NOAA NESDIS, 2020) on the Megha-Tropiques satellite launched by the French Centre National D'Etudies Spatiales (CNES) and Indian Space Research Organisation (ISRO), the Microwave Humidity Sounder (MHS) instrument (Bonsignori, 2007) on the NOAA19 satellite, the MHS instruments on the MetOp series of satellites launched by the European Organization for the Exploitation of Meteorological Satellites (EUMETSAT) and lastly the Special Sensor Microwave Imager/Sounder (SSMIS) instruments (NOAA NESDIS, 2020) on U.S. Defence Meteorological Satellite Program (DMSP) satellites. The PMW sensor data is supplemented by IR, from geostationary weather satellites and rain gauge data provided by Global Precipitation Climatology Centre (GPCC) (Schneider et al., 2022). In this way, GPM is able to offer an integration of many precipitation datasets to provide a very high spatial and temporal resolution precipitation estimate.

PERSIANN

Precipitation Estimation from Remotely Sensed Information using Artificial Neural Networks (PERSIANN) is a set of remotely sensed precipitation datasets (Nguyen et al., 2019). Within PERSIANN there are five different products, PERSIANN, PERSIANN-CCS (Cloud Classification System), PERSIANN-CDR (Climate Data Record), PDIR-Now (Dynamic Infrared Rain Rate near real-time), PERSIANN-CCS-CDR (Cloud Classification System, Climate Data Record). Each product has a similar start point, but different algorithms, which are detailed in turn. The datasets are produced by the Center for Hydrometeorology and Remote Sensing (CHRS) at the University of California, Irvine (UCI).

Underpinning all of these datasets is the base PERSIANN algorithm, which uses an artificial neural network, a type of machine learning, to detect and determine relationships between IR sensed cloud-top temperature and rainfall rates. To correct for bias, additional data from passive microwave sensors are used (Nguyen et al., 2019).

PERSIANN

This dataset provides precipitation estimates at 0.25 degrees near globally (60° N-S) and with hourly time steps from March 2000 to present day. It takes geostationary IR radiation (from GOES-8, GOES-10, GMS-5, Metsat-6, and Metsat-7) and daytime visible imagery from low polar orbiting satellites (TRMM, NOAA-15, -16, -17, DMSP F13, F14, F15) and passes this through a neural network to produce the estimates (Nguyen et al., 2019).

PERSIANN-CCS

PERSIANN-Cloud Classification System is a satellite precipitation product with very high near global spatial resolution (4x4 km), providing data from 2003 to present day. The dataset takes the same base methodology as PERSIANN but adds a cloud classification scheme. Using pattern recognition techniques, IR imagery of clouds can be classified to better quantify rainfall estimates. The cloud patterns are classified by features such as cloud height, areal extent, and variability of texture (Nguyen et al., 2019). The patterns are assigned precipitation values based on ground-based radar and TRMM observations. This is thought to improve the detection accuracy when using IR imagery to estimate precipitation. Figure 2.3 outlines the methodology used to produce PERSIANN-CCS, showing how the inputs of IR and PMW are separately treated and combined. The methodology has commonality with the other PERSIANN datasets.

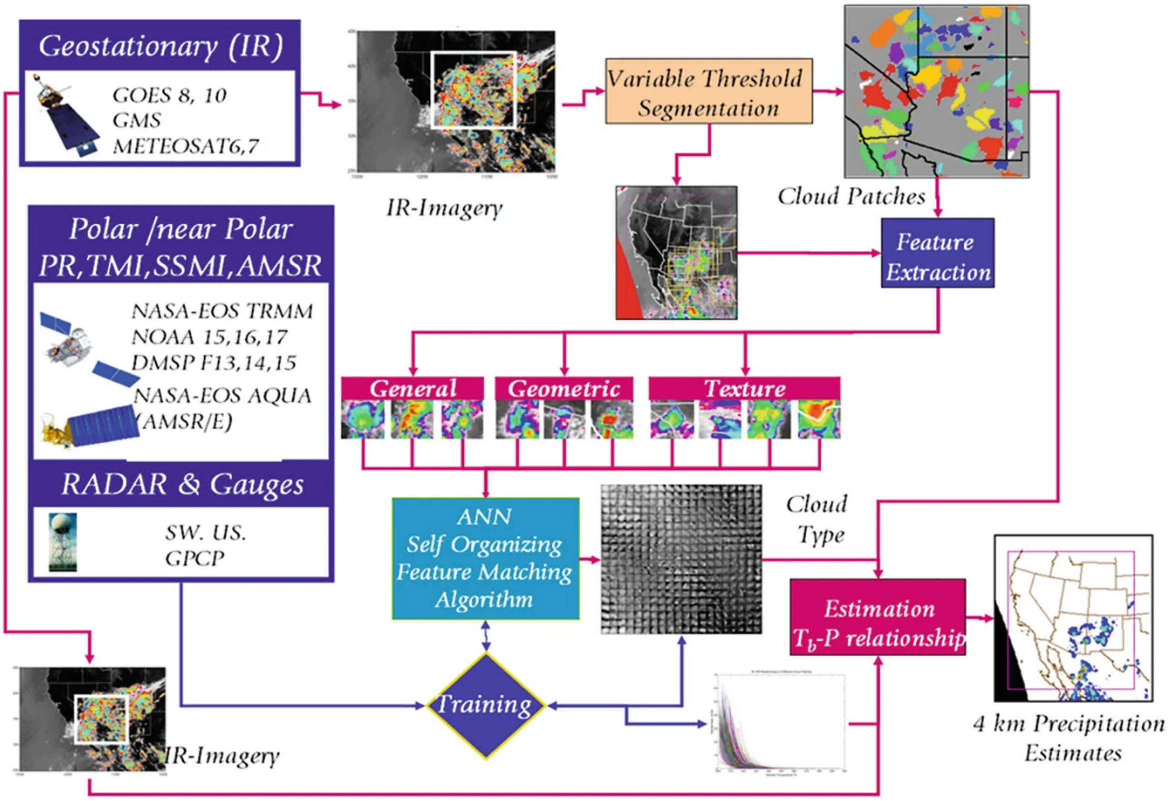

Figure 2.3. *Data processing flow diagram of PERSIANN-CCS (source: https://chrs.web.uci.edu/SP_activities01.php) which takes geostationary and polar satellite observations and combines with radar and rain gauge data.*

PERSIANN-CDR

The Climate Data Record (CDR) dataset builds upon the PERSIANN algorithm but helps to address the need for long-term high spatial resolution precipitation data for climate assessments (Ashouri et al., 2015). This dataset has a spatial resolution of 0.25 degrees and a daily time series starting in 1983 to present day. CDR utilised IR imagery from GridSat-B1 and GPCP PMV precipitation.

PDIR-Now

PDIR-Now is a near real time hourly dataset, providing 4x4 km spatial resolution data with very low latency (15-60 minutes). For this it relies on high frequency IR imagery and can be used in applications such as flood inundation maps where near real time data access is essential. PDIR-Now builds upon the foundation of PERSIANN-CCS, bettering its accuracy in keys areas such as rain/no-rain days and seasonal cycles (Nguyen et al., 2020).

PERSIANN-CCS-CDR

PERSIANN-CCS-CDR combined the long time series of the CDR and the advanced precipitation detection abilities of CCS, providing a high spatial resolution (4x4 km), long (1983 - present), 3-hourly time series (Sadeghi et al., 2021). In addition to the methods used in each separate product, the combined product takes information from NOAA CPC-4km global IR products (Xie et al., 2019).

TRMM

The Tropical Rainfall Measuring Mission (TRMM) was a satellite mission from 1997 - 2015 designed specifically to enhance our understanding of tropical rainfall distribution and intensity (Huffman et al., 2007). It was a joint mission by NASA and JAXA that formed part of the NASA Earth Observing System and aimed to provide high spatially and temporally resolved precipitation data. The product has a spatial resolution of 0.25 degrees and covers 50^{o} N-S. Onboard TRMM were five instruments, the Precipitation Radar (PR), TRMM Microwave Imager (TMI), Visible Infrared Scanner (VIRS), Clouds & Earths Radiant Energy System (CERES) and Lightning Imaging Sensor (LSI) (Huffman et al., 2007). The principal instruments for observing precipitation are the PR and TMI, which contribute to the TRMM Multi-satellite Precipitation Analysis (TMPA), which form the basis of the end user products TMPA 3B43 (monthly) and 3B42 (3-hourly).

TMPA takes microwave data from multiple satellites in the NASA constellation; SSMI, SSMIS, MHS, AMSU-B, AMSR-E and TRMM, with missing data filled in with IR from geostationary satellites (Huffman et al., 2007). The assimilated products are scaled to rain gauge datasets to ensure biases are limited. As with all precipitation datasets that take data from multiple sources, precipitation is at best an estimate, as there will be inconsistencies when data sources are launched and decommissioned.

With its long time series and high spatial resolution, the product is particularly useful for long term analysis of climate change and investigating spatial heterogeneity in precipitation. The TRMM project came to an end in 2017 and was superseded by GPM from NASA. GPM utilises the available data from TRMM, reprocessing historical data with its proprietary algorithm to ensure continuity.

Ground-Based Precipitation

Ground based observations of precipitation are collected predominantly using rain gauges. The data they record represents a snapshot in time and space. In northern mid-latitudes there is good coverage of ground-based stations as shown by Figure 2.4, however in the tropics, there is often poor coverage, especially in the remote tropical forest regions. Radar data do not have the same spatial availability however they are often used for bias correction and quality control of rain gauge measurements (Peterson and Vose, 1997; Chen et al., 2002; Schneider et al., 2022).

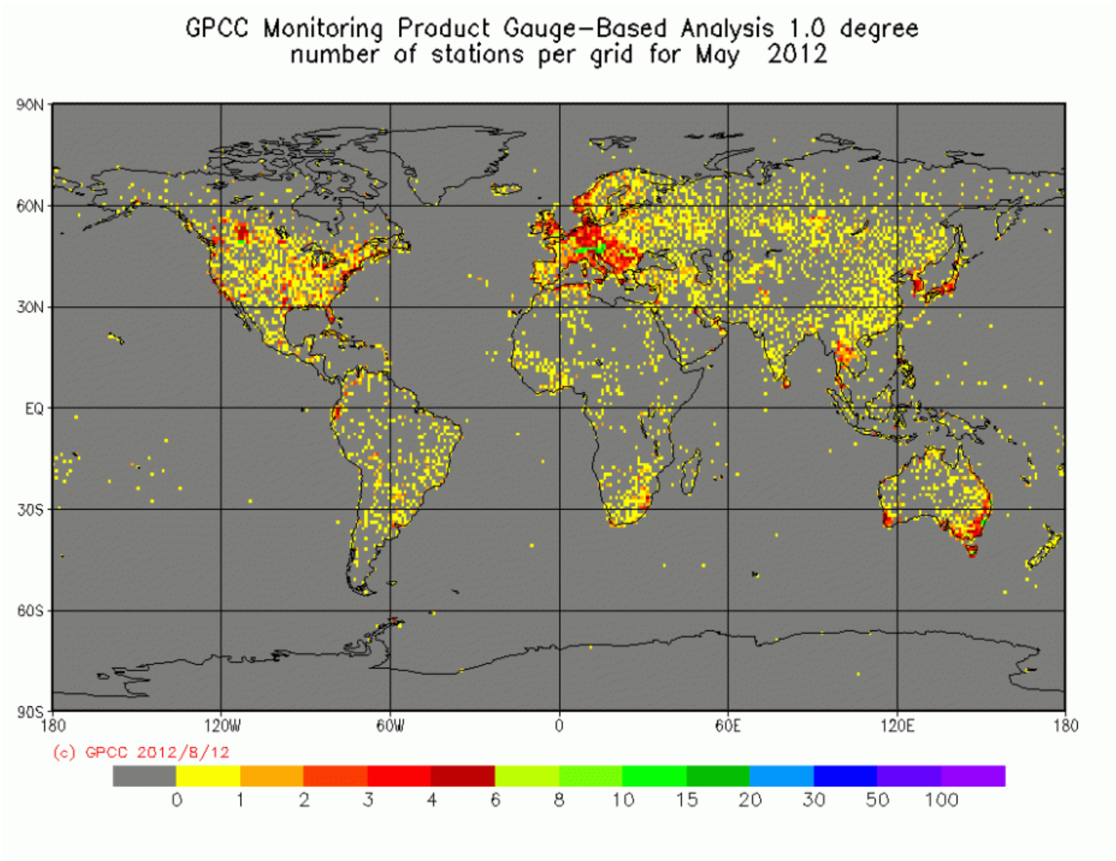

Figure 2.4. *Global map showing the number of stations used as inputs to the GPCC precipitation product in May 2012 (Schneider et al., 2014). Colours represent the number of stations contributing to each grid cell on the map.*

CPC

The Climate Prediction Center (CPC) precipitation dataset is constructed by the NOAA Climate Prediction Centre, taking data from over 30,000 rain gauge stations. CPC is a daily, land only dataset available at 0.5 degrees across the globe for the period 1948 to present day (Xie et al., 2007). The high station density makes this data particularly useful, when compared to other less dense ground-based datasets, for spatial comparison assessments. Whilst it doesn’t have the high resolution of satellite precipitation datasets, it still has applications in observing climate variability and drought assessments.

The rain gauge data originates from a variety of sources, GTS (Global Telecommunication System) (Schneider et al., 2022), COOP (Cooperative Weather Observer Program) (Daly et al., 2007) and other national databases. On each data point, quality control is performed by comparison with historical records, nearby stations, concurrent radar and satellite observations and NWP. Once screened, data are gridded using Optimal Interpolation which can take account of orographic effects (Xie et al., 2007).

CRU

The Climate Research Unit (CRU) is a global gridded weather station dataset, produced and maintained by the UK's Natural Environment Research Council (NERC), the US Department of Energy and the National Centre for Atmospheric Science (NCAS) (Harris et al., 2020). The dataset assimilates data from approximately 4000 weather stations from around the world, producing a dataset continuously running from 1901 to near present day at 0.5 degrees.

CRU can be used to assess global climate and precipitation variability and to derive global drought indices such as Standardised Precipitation Evapotranspiration Index (SPEI) and other extreme metrics (Harris et al., 2020). Data from the weather stations is cleaned by assessing the distance each data point is from the mean and removing data which is >3 standard deviations away. Assimilating the data uses an angular-distance weighting (ADW) interpolation method which takes into account the surrounding amount of anomalous data, weighting differently depending on the quality of data. This produces the 0.5^o globally gridded data. In the recent versions of CRU which use ADW, there is improved traceability between each gridded value and the input observations. This allows greater into to assess how the quality of the data from each station may geographically vary.

GPCC

The Global Precipitation Climatology Centre (GPCC) which gives its name to the precipitation product is the German contribution to the World Climate Research Programme (WCRP). It is the long term assimilation of ~86,000 rain gauges to a global grid (Schneider et al., 2022).

GPCC provides global gridded monthly data at 0.25 degrees from 1891 to present day, making it one of the longest climate time series available. With its long time series and high spatial resolution, this product is suitable for evaluating climate changes over long periods and between land cover types. It also has uses for water balance studies, the calibration/validation of remote sensing based rainfall estimations and the verification of NWP models (Schneider et al., 2014; Schneider et al., 2022). Alongside the full monthly precipitation product used in this thesis, there are separate drought indices and rapidly available precipitation estimates available.

Rain gauge data distributed by the GTS is combined with monthly precipitation totals calculated from synoptic weather reports (SYNOP) and CPC (Schneider et al., 2022). The rain gauges are sourced from CRU, Global Historical Climatology Network (GHCN) (Peterson and Vose, 1997) and a variety of national inventories (Schneider et al., 2014). Precipitation anomalies are calculated for each gauge and these anomalies are then interpolated on the global grid. The product is supplied with error estimates for each data point, so users can determine the error level suitable for their analysis. As with all gridded ground-based datasets, there are major issues for spatial analysis studies as there are regions across the globe with very poor spatial coverage by weather stations and gauges.

UDEL

This gridded precipitation product was developed at the University of Delaware (UDEL). UDEL has global coverage, at 0.5^{o} resolution, with data available from 1900 to 2017 when the project terminated (Matsuura and Willmott, 2018). The dataset wasn't designed for a specific use, rather as a general purpose product. It has been used widely, including uses in numerical climate model validation and economic applications.

UDEL takes inputs from observational station data, largely from the Global Historical Climatology Network dataset (GHCN2) (Peterson and Vose, 1997), the Global Historical Climatology Network Monthly (GHCNM) Version 3 (GHCN3) (Lawrimore et al., 2011), the Daily Global Historical Climatology Network (GHCN-Daily) archive (Menne et al., 2012), and the Global Surface Summary of Day (GSOD). In addition to this, a few individual records were obtained through direct communication with the station owner.

The station data was interpolated across the globe using the spatial interpolation algorithm developed by Shepard (1968), which has been modified by (Willmott et al., 1985) for use on the Earth’s near spherical surface. A digital elevation model (DEM) is incorporated to improve the accuracy of the interpolated values. The values presented are grid point estimates rather than grid averages. Where stations were closer than 2.5 km to each other, a composite was formed of their records. This serves to smooth the data through space and time, also allowing for stations with shorter time series to be included in the full dataset, if their neighbour has a longer available time series.

The product was not corrected at source, taking raw precipitation data from the stations. It should be noted that biases from under or over catch in station datasets can be significant, but difficult to correct for over extensive areas with few nearby data points (Legates and Willmott, 1990). An estimation of the interpolation error was created by finding the interpolated precipitation value for a region or network of stations, removing the central station in the network and calculating the difference between the interpolated and “real” station value. This provided the local or station error.

Reanalysis Precipitation

Reanalysis (retrospective analysis) is the combination of climate models and observations, by data assimilation. It is based upon the method used in numerical weather prediction (NWP) whereby model forecasts are combined with newly available observations to produce a best estimate of the state of the atmosphere and thereby an improved forecast (Kobayashi et al., 2015; Reichle et al., 2017; Hersbach et al., 2020). Similarly, reanalysis combines these elements, but usually at lower resolutions. Reanalysis datasets take in a wide range of current and historical observations and short-range weather forecasts, re-running the forecasts with modern models to create the most accurate assimilated product. Observations that are produced with time lag can be integrated into re-analysis, unlike real-time analysis, therefore a greater pool of observations can be used. This process overcomes the issues generated by sparse and incomplete observations, producing a consistent and complete record through time. These datasets have a range of uses, from analysing changes in climate to education, policy making and industry. The future of reanalysis datasets is to integrate atmosphere and oceanic elements, as currently datasets such as ERA5 are atmosphere only.

ERA5

ERA5 is the successor to ERA-interim, the fifth generation of ECMWF re-analysis (ERA) for climate and weather. The European Center for Medium range Weather Forecasts (ECMWF) reanalysis combined model output with observations to produce a global combined dataset containing a large number of climate and land surface variables. The ERA5-Land dataset is available hourly at 0.1 degrees from 1950 to present day for the entire globe.

Hersbach et al. (2020) detail the full list of satellite and ground-based observations that are assimilated to form the observational component of reanalysis. These data include observations of temperature, humidity, ozone, column water vapour, cloud liquid water, precipitation, ocean surface wind speed, wind vector, land cover, soil moisture and multi-level pressure. Importantly as Duveiller et al. (2022) note, ERA5 uses seasonally static LAI and semi-static land cover representations, both of which can strongly impact the precipitation response to forest loss that the dataset produces. The satellite data originate from US, European and Japanese space agencies whilst the ground-based is from land station, buoys, ships, radiosondes, aircraft and radar precipitation composites (Hersbach et al., 2020). Where observations are limited such as in the tropics, where there are few weather stations and high occurrence of clouds, the data may be insufficient to overcome model biases.

The analysis in chapter 4 uses total precipitation from ERA5-Land, which is the total accumulated liquid and frozen water incident upon the surface. It includes both convective and large-scale precipitation that reach the surface, discounting fog and dew that do not reach the surface.

JRA

JRA-55 is the Japanese Meteorological Agency's (JMA) latest reanalysis product, providing a long time series of climate data integrating 4-D observations with models. Data is assimilated onto a reduced gaussian grid using a semi-lagrangian advection scheme (Kobayashi et al., 2015). Previously the JMA produced JRA-25 which was a 25 year reanalysis dataset spanning 1978 to 2004 and has provided the basis for the improved JRA-55 dataset.

JRA is a 3-hourly data with a spatial resolution of 0.5625 degrees and temporal range from 1958 to present day, coinciding with the start of the global radiosonde record.

Similarly to ERA5, JRA-55 takes observational data from satellite and ground-based sources and assimilates this to drive model reanalysis, producing a long and continuous record of climate since 1958 (Kobayashi et al., 2015). JRA-25 and 55 take the same observational base inputs as ERA-40, which is supplemented JMA archived observations. JRA-55 is known to overestimate tropical precipitation compared to ERA-40 and GPCP, likely due to the 'spin-down' problem associated with deep convection in forecast models (Kobayashi et al., 2015). We don't explore this further in chapter 4, however we conclude that no statistically significant trends are observed using this dataset, possibly because of this phenomenon.

MERRA-2

The Modern-Era Retrospective analysis for Research and Applications, version 2 (MERRA-2) is another example of a global atmosphere only reanalysis product, produced by the NASA Global Modelling and Assimilation Office (GMAO) (Gelaro et al., 2017). Compared to its predecessor, MERRA integrates modern hyperspectral radiance and microwave observations, assimilating the meteorological data with a new assimilation method (Reichle et al., 2017). MERRA-2 is particularly well suited to surface mass balance estimates over ice sheets compared to other reanalysis products.

Compared to other global reanalysis datasets (JRA-55 and ERA5), MERRA-2 has a shorter available time series, from 1980 to present day. Similarly, however it is available at 0.5x0.625^{o} resolution and in 3-hourly steps.

The dataset is driven by the Goddard Earth Observing System Atmospheric Data Assimilation System (GEOS ADAS), which takes the GEOS model as the basis and incorporates the Global Statistical Interpolation (GSI) analysis scheme (Kobayashi et al., 2015). In places around the world where there are few ground-based observations, such as tropical forest interiors, the observations are driven by the satellite-station merged product, CMAP (NOAA CPC Merged Analysis of Precipitation).

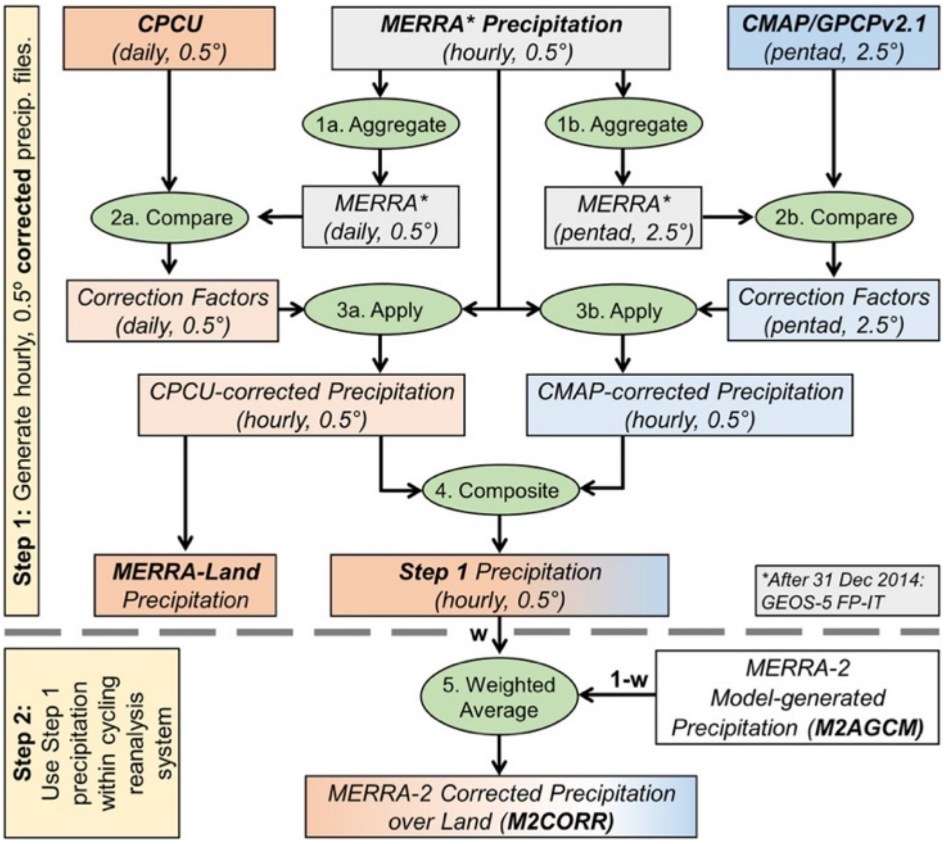

Figure 2.5. *Schematic outlining the bias correction algorithm used in the production of MERRA-2* (Reichle et al., 2017)*. A similar process is utilised by JRA-55 and ERA5 to correct their precipitation using observations.*

One noticeable difference compared with ERA5 and JRA-55 is that 2 m air temperature is not directly assimilated, however a similar array of observations, satellite and ground-based are integrated (Kobayashi et al., 2015). Figure 2.5 outlines the process by which modelled precipitation in MERRA-2 is bias corrected using satellite and ground-based observations. A similar process is used for each variable produced in this reanalysis.

2.1.3 Models

CMIP6

The models used in Chapter 5 to evaluate the impacts of LCC on local climate are listed in Table 2.2. The details of each individual model are described by each modelling institute, accessible via the reference listed in Table 2.2. Here I provide an overview of some key differences between the CMIP6 models used in this thesis.

One of the most important factors differentiating the CMIP6 models is their representation of the land surface. Differences can arise from the spatial location, number and the types of biomes in each region as well as land classifications and their heterogeneity. These factors will influence vegetation phenology, LAI, plant growth, ET, albedo and roughness. Alongside this, the land cover type will influence the carbon cycling ability of the land affecting processes such as photosynthesis and respiration which can in turn impact growth, water, energy and gas fluxes. Interactions between the land surface and the atmosphere, such as evapotranspiration, surface runoff, soil moisture, and heat fluxes can also be strongly affected by the land surface representation. Whilst all models include land surface properties and processes, not all include vegetation that changes with time (Dynamic Global Vegetation Models).

The CMIP6 models have a wide range of spatial resolutions from ~0.5^{o} to ~3^{o}, listed in Table 2.2. Higher resolution models will be able to capture smaller scale features and processes differently to coarser resolutions models, which will result in a different representation of climate and land surface changes due to forest loss. Related to this is the type and number of parametrisations present, with higher resolution models needing fewer approximations than coarser models. The parametrisations themselves are different between modelling groups, therefore each representation of clouds, precipitation and climate processes will be different. All CMIP6 models include atmosphere, ocean and land surface components, however some models additionally model ice sheets, atmospheric chemistry and importantly for this analysis, dynamic vegetation. The more components and processes an earth system model includes, the more computationally expensive and comprehensive the model becomes.

Other factors that are of lesser importance for the analysis of the climate impacts of land cover change are the representation of biogeochemistry, sea ice, permafrost, and aerosol and chemical forcings. These will have less of an impact of the results as we largely consider the local impacts of land use change and over short time scales. Overall, models are constructed differently leading them to have their own biases. The strength of the CMIP6 models is in their numbers, with the ensemble mean of the models providing useful insight in climate and land surface studies.

GCAM

The Global Change Assessment Model (GCAM) is an integrated assessment model (IAM) used for studying global climate change and its interactions with socio-economic systems (JGCRI, 2023). The project is jointly coordinated by the Pacific Northwest National Laboratory and Joint Global Change Research Institute (PNNL, JGCRI) for the USA Environmental Protection Agency. It analyses the effects of various long-term policy and technology choices on greenhouse gas emissions, energy systems, land use, and climate outcomes. GCAM is widely used by researchers, policymakers, and organizations to explore different mitigation scenarios, evaluate the feasibility of climate targets, inform policy decisions, and assess the co-benefits and trade-offs of various strategies related to energy, land use, and climate change (JGCRI, 2023).

To make predictions of future change, GCAM considers a variety of factors such as land use change, economics, energy systems and the climate system. A variety of land surface and climate datasets are integrated to form GCAM, including satellite datasets from MODIS (land cover, land surface and climate variables), and the European Space Agency Climate Change Initiative Land Cover (ESA, 2017). GCAM incorporates land use and agricultural systems to analyse the impact of land use change, deforestation, and land management practices on greenhouse gas emissions, food production, and ecosystem services. Additionally, GCAM includes a representation of the climate system and feedbacks to capture the interactions between greenhouse gas emissions, atmospheric concentrations, land surface and climate changes.

Table 2.2. *Information about the models used in Chapter 4 to evaluate the changes in local climate due to tropical forest loss. Listed is the dataset name, originating institute, resolution the model output is supplied at in terms of latitudinal (lat) and longitudinal (lon) resolution and the appropriate dataset citation.*

Model	Institute	Resolution lon, lat (degrees)	Reference
ACCESS-ESM1-5	CSIRO	1.88 x 1.25	Ziehn et al., 2019
AWI-ESM-1-1-LR	AWI	1.88 x 1.87	Danek et al., 2020
CanESM5	CCCma	2.81 x 2.79	Swart et al., 2019a
CanESM5-CanOE	CCCma	2.81 x 2.79	Swart et al., 2019b
CESM2	NCAR	1.25 x 0.94	Danabasoglu, 2019a
CESM2-FV2	NCAR	2.50 x 1.89	Danabasoglu, 2019b
CESM2-WACCM	NCAR	1.25 x 0.94	Danabasoglu, 2019c
CESM2-WACCM-FV2	NCAR	2.50 x 1.89	Danabasoglu, 2019d
CMCC-CM2-SR5	CMCC	1.25 x 0.94	Lovato and Peano, 2020
CMCC-ESM2	CMCC	1.25 x 0.94	Lovato et al., 2021
CNRM-ESM2-1	CNRM-CERFACS	1.41 x 1.40	Seferian, 2018
EC-Earth3-CC	EC-Earth-Consortium	0.70 x 0.70	EC-Earth-Consortium, 2021
EC-Earth3-Veg	EC-Earth-Consortium	0.70 x 0.70	EC-Earth-Consortium, 2019
EC-Earth3-Veg-LR	EC-Earth-Consortium	1.12 x 1.12	EC-Earth-Consortium, 2020
GISS-E2-1-G	NASA-GISS	2.50 x 2.00	NASA/GISS, 2018

HadGEM3-GC31-LL	MOHC	1.88 x 1.25	Ridley et al., 2019a
HadGEM3-GC31-MM	MOHC	0.83 x 0.56	Ridley et al., 2019b
INM-CM4-8	INM	2.00 x 1.50	Volodin et al., 2019a
INM-CM5-0	INM	2.00 x 1.50	Volodin et al., 2019b
IPSL-CM5A2-INCA	IPSL	3.75 x 1.89	Boucher et al., 2020
IPSL-CM6A-LR	IPSL	2.50 x 1.27	Boucher et al., 2018
MPI-ESM-1-2-HAM	HAMMOZ-Consortium	1.88 x 1.87	Neubauer et al., 2019
MPI-ESM1-2-HR	MPI-M	0.94 x 0.94	Jungclaus et al., 2019
UKESM1-0-LL	MOHC	1.88 x 1.25	Tang et al., 2019
GCAM	PNNL, JGCR	0.05 x 0.05	JGCRI, 2023

2.2 Methodology

In this section I will provide an overview of the methods common or core to the analysis in the Chapters 3 - 5. I will first describe the data acquisition, followed by how I processed the individual datasets. Lastly, I describe and explain the main methods by which I analysed the data and why I chose those methods if there were multiple options available.

2.2.1 Data Acquisition

MODIS

MODIS datasets were downloaded using the NASA Earth Data download portal (https://www.earthdata.nasa.gov/) at their native resolutions for the time periods used in the individual studies. For products with a 500 m spatial resolution, there are approximately 300 tiles comprising one complete global 8-day scene, meaning for a year of data around 13,000 tiles are required. Tiles were downloaded using the command line utility “wget”. For all MODIS datasets, I used 8-day global gridded products in the file format is HDF

(Hierarchical Data Format), allowing us high spatial and temporal data availability at relatively low file sizes.

GFC

Much of the analysis contained within this thesis is underpinned by the Global Forest Change dataset (Hansen et al., 2013). This data can be freely downloaded from Global Forest Watch (GFW) (https://www.globalforestwatch.org), a web portal for viewing and downloading data, built in partnership with the Global Land Analysis and Discovery (GLAD) laboratory at UMD. The data is separated into several classes, '*treecover2000*', '*gain*', '*lossyear*', '*datamask*', '*first*' and '*last*', of which I downloaded and used '*treecover2000*' and '*lossyear*'. Together these provided information about the forest cover extent in 2000 and the year in which forest, if applicable, was lost per 30 m resolution pixel.

Driver of Forest Loss

To classify the drivers of forest loss, I downloaded the drivers of forest loss dataset from the supplementary information of the Curtis et al. (2018) manuscript. Similarly, to GFC, the dataset is also available from the GFW web portal. This dataset is available globally at 10 km spatial resolution from 2001 to 2019.

Precipitation

In Chapters 4 and 5 I analysed changes in precipitation using up to 18 different precipitation datasets (listed in Table 2.1). I downloaded each precipitation dataset from its original source, listed here: CHIRPS from https://data.chc.ucsb.edu/products/?C=M;O=D, CMORPH from https://ftp.cpc.ncep.noaa.gov/precip/CMORPH_RT/GLOBE/data/, CPC from https://psl.noaa.gov/data/gridded/data.cpc.globalprecip.html, CRU from https://crudata.uea.ac.uk/cru/data/hrg/, ERA5 from https://cds.climate.copernicus.eu/cdsapp#!/dataset/reanalysis-era5-single-levels?tab=overview, GPCC from https://opendata.dwd.de/climate_environment/GPCC/html/download_gate.html, GPCP from https://disc.gsfc.nasa.gov/datasets/GPCPMON_3.1/summary?keywords=GPCPMON, GPM from https://gpm1.gesdisc.eosdis.nasa.gov/data/GPM_L3/, JRA from https://climatedataguide.ucar.edu/climate-data/jra-55 https://jra.kishou.go.jp/JRA-55/index_en.html, MERRA-2 from https://disc.gsfc.nasa.gov/datasets?project=MERRA-2, NOAA (PREC/LAND) from https://psl.noaa.gov/data/gridded/data.precl.html, PERSIANN (CCS, CDR, CCS-CDR, PDIR-NOW) from https://chrsdata.eng.uci.edu/, TRMM from https://disc.gsfc.nasa.gov/datasets/TRMM_3B43_7/summary, UDEL from https://psl.noaa.gov/data/gridded/data.UDel_AirT_Precip.html. When downloading, there were often multiple dataset options. Where possible I selected the data closest to mean monthly total precipitation.

CMIP6 Models

To analyse output from the 45 global climate models contributing to CMIP6 (Eyring et al., 2016), I downloaded monthly data from the World Climate Research Program Earth System Grid Federation (https://esgf-node.llnl.gov/projects/cmip6/). To complete the analysis in Chapter 5, I retrieved historical simulations between 1850 - 2014 from models that provided land cover change, evapotranspiration, land surface temperature, albedo and precipitation (n=24 used in this analysis).

GCAM

In Chapter 4, we analysed the impacts of future forest cover change using the Global Change Analysis Model (GCAM) from 2015 to 2100. We chose to use the Shared Socioeconomic Pathway (SSP) - Representative Concentration Pathway (RCP) scenario SSP3 RCP4.5 which represents a middle of the road emissions/ LCC scenario (Chen et al., 2020). The GCAM model output was downloaded at 0.05 degrees from https://doi.org/10.25584/data.2020-07.1357/1644253.

2.2.2 Processing

MODIS

The datasets were processed and quality control measures were applied using the Python packages GDAL (GDAL/OGR Contributors, 2023), Iris (Met Office, 2023) and Xarray (Hoyer and Hamman, 2017). Once I had read in each 8-day raw MODIS tiles, we immediately applied quality control measures, ensuring that no post-processing had taken place before pixels were screened. I selected only pixels with "good" data quality and where the scene was "cloud free". This applied to all MODIS datasets apart from MOD16A2GF (ET) which comes pre-processed due to it being gap-filled. Raw MODIS products are in the sinusoidal projection, so after quality control, tiles were merged and reprojected to the World Geodetic System 1984 (WGS84) projection to allow consistent data analysis with the other available datasets.

Each of these 8-day global scenes were then regridded to the necessary spatial resolutions using the Python package Xesmf (Zhuang, 2022) with either conservative normalised, bilinear or nearest neighbour schemes (further details on spatial regridding provided below). As for all data in this thesis, I analysed data at monthly temporal resolution. The MODIS 8 and 16-day gridded data were temporally resampled to monthly time steps using Xarray and the individual months were concatenated into annual files, ready for data analysis.

GFC

In each analysis chapter we use slightly different time periods to evaluate changes in forest cover, however the process of generating forest cover change is the same. Firstly, I took 'treecover2000' and 'lossyear' data layers from GFC, which provide initial forest cover and the year in which forest cover was lost, respectively. To read in and manipulate these datasets I used the Python packages Xarray and GDAL. To calculate the forest cover extent in each subsequent year, I subtracted areas where forest had been lost from the initial forest extent. To gain forest cover change, I then differenced the forest loss in the particular year, from the initial forest cover. This dataset was then regridded to the appropriate resolution for each analysis by taking the sum of all 30 m complete forest loss pixels within each larger aggregated pixel.

Driver of Forest Loss

The drivers of forest loss dataset came pre-processed by the authors, describing the primary driver of forest loss for the period 2001 - 2019. I regridded the dataset to the appropriate resolution using the spatial regridding Python package Xesmf and the conservative normalised scheme (Zhuang, 2022).

Precipitation

The precipitation datasets used in Chapters 4 and 5 were available at a range of spatial and temporal resolutions, ranging from 4 km to 100 km and 3-hourly to monthly time scales. Some of the precipitation datasets came supplied with quality control layers with flags indicating the quality of the data, whilst some had quality control measures pre-applied. Where possible I screened the data for 'good' quality, mitigating the impact of cloud and poor-quality retrievals, which particularly impact satellite data. I resampled each dataset, using temporal weighting in Xarray to produce monthly means over the analysis time period. We chose to analyse the datasets at a range of spatial scales from 5 km to 200 km spatial resolution, which required each dataset to be spatially regridded to the 6 different grids. The resolutions we chose are standard resolutions (0.05^{o}, 0.1^{o}, 0.25^{o}, 0.5^{o}, 1.0^{o}, 2.0^{o}), that almost sequentially double in spatial scale and match the native resolutions of many precipitation datasets. The precipitation datasets were categorised into satellite (number of datasets, n =10), station (n=4) and reanalysis (n=4) categories for analysis. Each category has fundamental differences and similarities, and categorising allows us to compare these structural differences.

CMIP6

Each CMIP6 model is supplied at a different resolution as listed in Table 2.2. We chose to analyse the model data at their original resolutions, so no spatial regridding took place. We constrained the model data ready for analysis using two constraints. Firstly, we constrained by the tropics (30° N-S) and secondly by where forest cover was greater than 70% at the start of the discrete time periods. We did this to select areas of dense tropical humid forest, that would match well to the evergreen broadleaf biome defined by MODIS land cover type (MCD12Q1) satellite data. We tested using the MODIS evergreen broadleaf biome to constrain the individual models, finding similar pixels were selected and similar results were produced by the analysis in each method. We chose to constrain each individual model by its own 70% forest cover as forest cover in each model will differ depending on the prescribed land cover and dynamics and could produce invalid results if we constrained each by the same area.

To detect simulated changes in local climate due to forest loss we first assessed changes to climate over time. We analysed changes over a 16 year period to match the time period used by the satellite temperature and precipitation datasets. In general, detecting climate changes needs a long time series (Winckler et al., 2017), the longer the time period, the more robust the result will be. To increase robustness, but still maintain the common 16 year time period, I utilised the full available time period of the CMIP6 models, from 1850 - 2014. I chunked the CMIP6 models into ten 16 year time period “chunks”, starting from 1854 and ending in 2014. In Chapter 5 we present the median changes over these 16 year periods in the main text, as well as the individual chunks in the supplementary material.

GCAM

To assess forest cover change over the next century, we used GCAM output, which provides forest cover in 5 year intervals between 2015 and 2100. To find forest loss, we compared each 5 year period to the 2015 baseline. GCAM output is supplied at 0.05 degrees, however we analysed changes in precipitation due to forest loss at 2 degrees, so I spatially regridded the data using Xesmf’s bilinear interpolation scheme.

2.2.3 Spatial Regridding

The datasets used in chapters 3-6 all have different native resolutions, that is, each is gridded using different grid box sizes and shapes. To allow for direct comparisons, these datasets need to be gridded on consistent grid sizes and shapes. To do this I use a process called regridding which takes the original dataset and translates the data onto a new specified grid size and shape. There are many methods that can be used to regrid, from simple linear interpolation to more complex conservative and area weighted. To regrid the datasets used for analysis in this thesis, I primarily use the python package xESMF (Zhuang, 2022). In some instances, to add robustness to the results, I also present results regridding using SciPy (Virtanen et al., 2020) linear interpolation and Iris (Met Office, 2023) area weighted. xESMF is a python interpretation of the Fortran package ESMF (Earth System Modelling Framework, (Balaji et al., 2023)) and offers a wide range of tools packaged in an easy to use, science ready package. It has the advantage over more simplistic applications that it can regrid between regular, rectilinear, and curvilinear grids allowing for accurate regridding of most geospatial datasets. xESMF splits the regridding into two steps, by first creating an array of weights based on the shape of the source and destination grids, then it applies the weights array to the source. The creation of the weights array is expensive, however it can then be quickly (re-)applied to speed up the process of regridding multiple variables or time steps on the same grids. This is particularly useful when regridding very high-resolution data as it can save on memory allocation and allows the process to be run in parallel for vast speed improvements.

There are two main types of datasets used in this thesis, categorical and continuous. The categorical datasets include the drivers of forest loss dataset (Curtis et al., 2018) and the MODIS land cover dataset which both classify land cover into discrete types, for example water and forest types. When regridding we want to conserve these discrete quantities, rather than averaging them, so we use nearest neighbour methods to allocate grid cells based on a weighting of their immediate neighbours. The majority of the geospatial data used in this analysis was continuous data, MODIS LST (MOD11A2) is an example. To modify these grids, we want to take an average of the surrounding grids and return the new grid shape. For highly spatially correlated data such as LST, bilinear interpolation is sufficient, whereby an average is taken of the surrounding cells. For discontinuous variables that are heterogenous spatially and temporally such as 3-hour precipitation, conservative regridding is more appropriate. Lastly for land-only datasets such as land surface temperature, we masked the oceans to stop "bleeding" of *NaN* or zero values into the cells in coastal regions.

2.2.4 Overview of Analytical Methods

All of the observational and simulated datasets were spatially constrained to the tropics region (30^{o} N-S). Spatially constraining had the added benefit of reducing computational load when performing calculations or storing output. Throughout the analysis, we also constrained the observational datasets by the MODIS evergreen broadleaf land cover type (Sulla-Menashe and Friedl, 2022). This spatial constraint was applied by masking by areas that were within the evergreen broadleaf biome at the start of the analysis period (this year differed for the different analyses). The CMIP6 models were constrained by their own forest cover extents, a process described in more detail in the processing section. The third spatial constraint applied to all datasets in Chapters 3 and 4 was the regional shapefiles, denoting the Amazon Basin, the Congo Basin and Southeast Asia, the shapes of which can be seen in Chapter 1. These areas were defined by shapefiles and applied to the datasets using the Python package Rioxarray (Hoyer and Hamman, 2017).

Moving window

To analyse the changes in local climate due to forest loss, I calculated the changes in climate over time and used a moving-window nearest neighbour approach, developed by (Baker and Spracklen, 2019) to understand how deforestation can modify the climate. To calculate changes over time, I took multi-year averages at the start and end of the analysis period to compensate for the effect of inter-annual variabilities, such as anomalously hot or dry years. When calculating the changes over time, I tested the sensitivity of the analysis to the number of averaged years (3 or 5 years) and the total length of analysis period. Broadly the results presented (Extended Data Figure B.3) were insensitive to changes in average time and total time period length.

The moving window analysis method takes the information about how the climate or land-surface has changed over time from deforested regions and pairs this to information from nearby forested regions. This pairing is essential for isolating the local impacts from the background climate and the differences due to geographical features such as elevation. Figure 2.6 shows a diagram of the 5x5 (number of pixels) window used to select “deforested” and nearby “forested” pixels, with the pixel and window size and differing depending on the analysis. To add robustness and to test the impacts of window size on our results, chapters 3 and 4 compare this effect, finding similar results are produced when using either 3x3 or 5x5 window sizes (Extended Data Figure B.3).

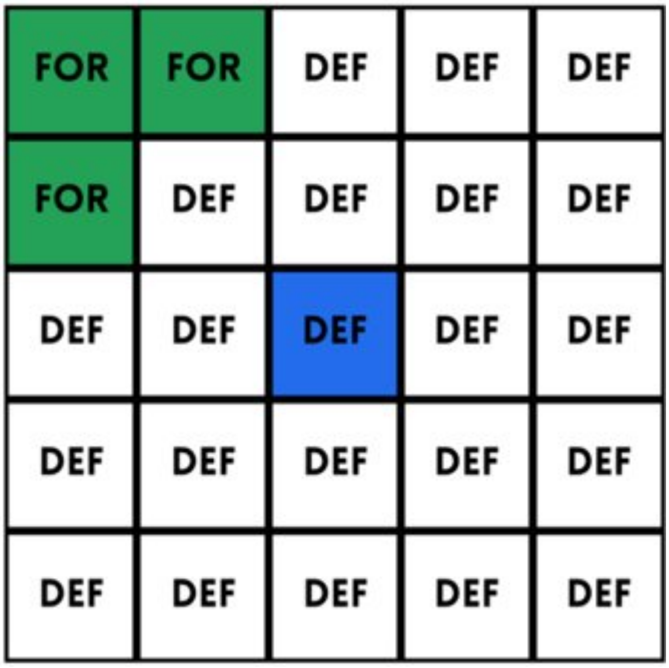

Figure 2.6. *A diagram showing the 5x5 nearest neighbour moving window.*

In Chapter 3, we used two different nearest neighbour moving window methods. The first method involved discretely defining forest and deforested categories of land cover using the GFC data. Here the transition between forest and deforested was calculated in what we termed a “threshold” analysis. The second method calculates forest loss of deforested areas relative to forest loss in neighbouring areas with less forest loss (control), producing a difference between the deforested and forest in terms of a percentage point coverage. This difference is subtle, with the second method allowing for a broader comparison of the impacts of forest loss on local climate. In both methods the deforested pixel is compared to the mean of the control pixels within the moving window, where there must be at least one control pixel per window.

The threshold approach defines “forest” areas by having greater than 90% forest cover at the start of the analysis period and maintaining greater than 90% throughout the analysis. “Deforested” areas are categorised by having greater than 90% forest cover at the start of the period and less than 70% forest cover at the end of the analysis. This categorical method is presented in published work by (Baker and Spracklen, 2019). To test the sensitivity of the results to changes in these thresholds, further thresholds were defined, with the results presented in the Supplementary Figure A.2, showing the results to be broadly insensitive to this change.

The per percentage point method doesn’t define thresholds of forest change, however it still utilises the moving window nearest neighbour approach. Rather, the method compares all deforested areas with nearby areas of forest that have lost less forest. Hence comparing the two regions, we can present changes in climate and land surface as a function of forest loss. In addition, we specified that deforested pixels must have lost more than 0.1 percentage points of forest loss than their paired controls. We calculated the change in the variable, for example precipitation, of the deforested pixel relative to the change in precipitation of the control pixel as the precipitation change of the deforested pixel over the analysis period (e.g., 20xx to 20xx) minus the precipitation change over the control pixel. For precipitation, we reported precipitation changes (ΔP) as a function of forest loss in units of mm month^{-1} %$^{-1}$. To further mitigate the impact of background climate on the analysis, in Chapter 4, we tested additionally constraining deforested and control pixels, requiring them to have less than 10% difference between mean monthly precipitations. We showed that the results were insensitive to this test (Supp. Figure B.7). This method has the advantage of including more pixels in the analysis than the threshold approach, overcoming the issue whereby some tropical regions in the threshold analysis had too few pixels to retrieve a change value. In addition to reporting the absolute changes in precipitation, we also report the changes relative to the background precipitation levels, in terms of %/% (ΔP/P) (an example of which is shown in Supplementary Figure B.2).

Seasonal Analysis

In all analysis chapters, we explored the climate impacts of forest loss in the different seasons. The seasons we chose to analyse were the wet, dry and transition seasons, defined as the wettest/driest 3 months of the year and the remaining 6 months respectively. The wettest and driest 3 months of the year were calculated for each individual pixel and each year, using the satellite datasets in each analysis chapter to find the climatology. For the CMIP6 models, we derived the seasonal pattern using the model's own precipitation values as this could substantially vary between models. The impact of selecting the wet and dry seasons per pixel meant that adjacent pixels could have different months selected for each season and these could change year to year. This ensured that the wettest and driest pixels were being selected each year, however years with anomalous precipitation patterns could increase the interannual heterogeneity of this spatial pattern. This effect is likely mitigated by using multiple satellite precipitation datasets to calculate the climatology. An alternative approach could be to select the mean wettest/driest 3 months over all analysed years, however if the wet and dry seasons change spatially over time, this could skew the results of the analysis.

Statistical Analysis

To assess the statistical significance of our results, we compared the changes in each variable populations control and deforested pixels, first finding their distribution. We tested whether the changes over deforested regions were statistically different from changes over control regions. To do this we used either the Student's t-test, Mann-Whitney U and Wilcoxon signed-rank test, each having specific attributes making it more suitable to a specific case. The Student's t-test was used on populations that were normally distributed and the variances of the groups were approximately equal. The Mann-Whiteney U and Wilcoxon test were used in cases when the data wasn't normally distributed or had a skewness.

To visualise the error associated with the populations of data, standard error of the mean was used to plot error bars on the figures throughout, unless stated. This provided a consistent measure of uncertainty throughout the analysis in the thesis.

References

Abercrombie, S.P. and Friedl, M.A. 2016. Improving the Consistency of Multitemporal Land Cover Maps Using a Hidden Markov Model. *IEEE Transactions on Geoscience and Remote Sensing*. **54**(2), pp.703–713.

Almeida, C.A. De, Coutinho, A.C., César, J., Mora, D., Adami, M., Venturieri, A., Diniz, C.G., Dessay, N., Durieux, L. and Gomes, A.R. 2008. High spatial resolution land use and land cover mapping of the Brazilian Legal Amazon in 2008 using Landsat-5 / TM and MODIS data. *Acta Amazonica*. **46**(3), pp.291–302.

Ashouri, H., Hsu, K.L., Sorooshian, S., Braithwaite, D.K., Knapp, K.R., Cecil, L.D., Nelson, B.R. and Prat, O.P. 2015. PERSIANN-CDR: Daily precipitation climate data record from multisatellite observations for hydrological and climate studies. *Bulletin of the American Meteorological Society*. **96**(1), pp.69–83.

Aumann, H.H., Chahine, M.T., Gautier, C., Goldberg, M.D., Kalnay, E., McMillin, L.M., Revercomb, H., Rosenkranz, P.W., Smith, W.L., Staelin, D.H., Strow, L.L. and Susskind, J. 2003. AIRS/AMSU/HSB on the aqua mission: Design, science objectives, data products, and processing systems. *IEEE Transactions on Geoscience and Remote Sensing*. **41**(2), pp.253–263.

Baker, J.C.A. and Spracklen, D. V 2019. Climate Benefits of Intact Amazon Forests and the Biophysical Consequences of Disturbance. *Frontiers in Forests and Global Change*. **2**, pp.1–13.

Balaji, V., Boville, B., Cheung, S., Clune, T., Collins, N., Craig, T., Cruz, C., Silva, A. da, DeLuca, C., Fainchtein, R. de, Dunlap, R., Eaton, B., Goldhaber, S., Hallberg, B., Henderson, T., Hill, C., Iredell, M., Jacob, J., Jacob, R., Jones, P., Kauffman, B., Kluzek, E., Koziol, B., Larson, J., Li, P., Liu, F., Michalakes, J., Montuoro, R., Murphy, S., Neckels, D., Kuinghttons, R.O., Oehmke, B., Panaccione, C., Rosen, D., Rosinski, J., Rothstein, M., Sacks, B., Saint, K., Sawyer, W., Schwab, E., Smithline, S., Spector, W., Stark, D., Suarez, M., Swift, S., Theurich, G., Trayanov, A., Vasquez, S., Wolfe, J., Yang, W., Young, M. and Zaslavsky, L. 2023. ESMF Reference Manual for Fortran. Available from: https://earthsystemmodeling.org/docs/release/latest/ESMF_refdoc/.

Bastable, H.G., Shuttleworth, W.J., Dallarosa, R.L.G., Fisch, G. and Nobre, C.A. 1993. Observations of Climate, Albedo, and Surface Radiation Over Cleared and Undisturbed Amazonian Forest. *International Journal of Climatology*. **13**(7), pp.783–796.

Becker, A., Finger, P., Meyer-Christoffer, A., Rudolf, B., Schamm, K., Schneider, U. and Ziese, M. 2013. A description of the global land-surface precipitation data products of the Global

Precipitation Climatology Centre with sample applications including centennial (trend) analysis from 1901-present. *Earth System Science Data*. **5**(1), pp.71–99.

Belward, A.S., Estes, J.E. and Kline, K.D. 1999. The IGBP-DIS global 1-km land-cover data set DISCover: A project overview. *Photogrammetric Engineering and Remote Sensing*. **65**(9), pp.1013–1020.

Bonan, G.B., Levis, S., Kergoat, L. and Oleson, K.W. 2002. Landscapes as patches of plant functional types: An integrating concept for climate and ecosystem models. *Global Biogeochemical Cycles*. **16**(2), pp.5-1-5–23.

Bonsignori, R. 2007. The Microwave Humidity Sounder (MHS): in-orbit performance assessment. *Sensors, Systems, and Next-Generation Satellites XI*. **6744**, pp.1–12.

Boucher, O., Denvil, S., Levavasseur, G., Cozic, A., Caubel, A., Foujols, M.-A., Meurdesoif, Y., Balkanski, Y., Checa-Garcia, R., Hauglustaine, D., Bekki, S. and Marchand, M. 2020. IPSL IPSL-CM5A2-INCA model output prepared for CMIP6 CMIP historical. *Earth System Grid Federation*. [Online]. Available from: https://doi.org/10.22033/ESGF/CMIP6.13661.

Boucher, O., Denvil, S., Levavasseur, G., Cozic, A., Caubel, A., Foujols, M.-A., Meurdesoif, Y., Cadule, P., Devilliers, M., Ghattas, J., Lebas, N., Lurton, T., Mellul, L., Musat, I. and Migno, F. 2018. IPSL IPSL-CM6A-LR model output prepared for CMIP6 CMIP historical. *Earth System Grid Federation*. [Online]. Available from: https://doi.org/10.22033/ESGF/CMIP6.5195.

Chen, M., Xie, P. and Janowiak, J.E. 2002. Global land precipitation: A 50-yr monthly analysis based on gauge observations. *Journal of Hydrometeorology*. **3**(3), pp.249–266.

CIESIN 2018. *Gridded Population of the World, Version 4.11 (GPWv4): Population Count*.

Culf, A.D., Fisch, G. and Hodnett, M.G. 1995. The Albedo of Amazonian Forest and Ranch Land. *Journal of Climate*. **9**, pp.1544–1554.

Curtis, P.G., Slay, C.M., Harris, N.L., Tyukavina, A. and Hansen, M.C. 2018. Classifying drivers of global forest loss. *Science*. **361**(6407), pp.1108–1111.

Daly, C., Gibson, W.P., Taylor, G.H., Doggett, M. and Smith, J.I. 2007. Observer Bias in Daily Precipitation Measurements at United States Cooperative Network Stations. *Bulletin of the American Meteorological Society*. **88**(6), pp.899–912.

Danabasoglu, G. 2019a. NCAR CESM2 model output prepared for CMIP6 CMIP historical. *Earth System Grid Federation*. [Online]. Available from: https://doi.org/10.22033/ESGF/CMIP6.10023.

Danabasoglu, G. 2019b. NCAR CESM2-FV2 model output prepared for CMIP6 CMIP historical. *Earth System Grid Federation*. [Online]. Available from: https://doi.org/10.22033/ESGF/CMIP6.11281.

Danabasoglu, G. 2019c. NCAR CESM2-WACCM model output prepared for CMIP6 CMIP historical. *Earth System Grid Federation*. [Online]. Available from: https://doi.org/10.22033/ESGF/CMIP6.10023.

Danabasoglu, G. 2019d. NCAR CESM2-WACCM-FV2 model output prepared for CMIP6 CMIP historical. *Earth System Grid Federation*. [Online]. Available from: https://doi.org/10.22033/ESGF/CMIP6.11282.

Danek, C., Shi, X., Stepanek, C., Yang, H., Barbi, D., Hegewald, J. and Lohmann, G. 2020. AWI AWI-ESM1.1LR model output prepared for CMIP6 CMIP historical. *Earth System Grid Federation*. [Online]. Available from: https://doi.org/10.22033/ESGF/CMIP6.9301.

Diner, D.J., Beckert, J.C., Bothwell, G.W. and Rodriguez, J.I. 2002. Performance of the MISR instrument during its first 20 months in earth orbit. *IEEE Transactions on Geoscience and Remote Sensing*. **40**(7), pp.1449–1466.

Drummond, J.R. 2002. MOPITT: 12 years of planning and 2.5 years of operations. *International Geoscience and Remote Sensing Symposium (IGARSS)*. **2**(416), pp.1085–1087.

Drummond, J.R., Bailey, P.L., Brasseur, G., Davis, G.R., Gille, J.C., Peskett, G.D., Reichle, Jr., H.K., Roulet, N., Mand, G.S. and McConnell, J.C. 1999. Early mission planning for the MOPITT instrument. *Optical Spectroscopic Techniques and Instrumentation for Atmospheric and Space Research III*. **3756**, pp.396–402.

Duveiller, G., Pickering, M., Muñoz-sabater, J., Caporaso, L., Boussetta, S., Balsamo, G. and Cescatti, A. 2022. Getting the leaves right matters for estimating temperature extremes. *Geoscientific Model Development Discussions*. (November), pp.1–25.

EC-Earth-Consortium 2021. EC-Earth-Consortium EC-Earth-3-CC model output prepared for CMIP6 CMIP historical. *Earth System Grid Federation*. [Online]. Available from: https://doi.org/10.22033/ESGF/CMIP6.4702.

EC-Earth-Consortium 2019. EC-Earth-Consortium EC-Earth3-Veg model output prepared for CMIP6 CMIP historical. *Earth System Grid Federation*. [Online]. Available from: https://doi.org/10.22033/ESGF/CMIP6.692.

EC-Earth-Consortium 2020. EC-Earth-Consortium EC-Earth3-Veg-LR model output prepared for CMIP6 CMIP historical. *Earth System Grid Federation*. [Online]. Available from: https://doi.org/10.22033/ESGF/CMIP6.643.

ESA 2017. *Land Cover CCI Product User Guide Version 2. Technical Report* [Online]. Available from: maps.elie.ucl.ac.be/CCI/viewer/download/ESACCI-LC-Ph2-PUGv2_2.0.pdf.

Fang, H., Baret, F., Plummer, S. and Schaepman-Strub, G. 2019. An Overview of Global Leaf Area Index (LAI): Methods, Products, Validation, and Applications. *Reviews of Geophysics*. **57**(3), pp.739–799.

Friedl, M. and Sulla-Menashe, D. 2022. MODIS/Terra+Aqua Land Cover Type Yearly L3 Global 500m SIN Grid V061 [Data set]. *NASA EOSDIS Land Processes DAAC*. [Online]. [Accessed 1 January 2022]. Available from: https://doi.org/10.5067/MODIS/MCD12Q1.061.

Friedl, M.A., Sulla-Menashe, D., Tan, B., Schneider, A., Ramankutty, N., Sibley, A. and Huang, X. 2010. MODIS Collection 5 global land cover: Algorithm refinements and characterization of new datasets. *Remote Sensing of Environment*. **114**(1), pp.168–182.

Funk, C., Peterson, P., Landsfeld, M., Pedreros, D., Verdin, J., Shukla, S., Husak, G., Rowland, J., Harrison, L., Hoell, A. and Michaelsen, J. 2015. The climate hazards infrared precipitation with stations - A new environmental record for monitoring extremes. *Scientific Data*. **2**, pp.1–21.

García-Álvarez, D., Teresa, M. and Olmedo, C. 2022. *Land Use Cover Datasets and Validation Tools*. Springer Cham.

Gash, J.H.C. and Shuttleworth, W.J. 1991. Tropical deforestation: Albedo and the surface-energy balance. *Climatic Change*. **19**(1–2), pp.123–133.

GDAL/OGR Contributors 2023. GDAL/OGR Geospatial Data Abstraction software Library. Open Source Geospatial Foundation. *Open Source Geospatial Foundation*. [Online]. Available from: https://gdal.org.

Gelaro, R., McCarty, W., Suárez, M.J., Todling, R., Molod, A., Takacs, L., Randles, C.A., Darmenov, A., Bosilovich, M.G., Reichle, R., Wargan, K., Coy, L., Cullather, R., Draper, C., Akella, S., Buchard, V., Conaty, A., da Silva, A.M., Gu, W., Kim, G.K., Koster, R., Lucchesi, R., Merkova, D., Nielsen, J.E., Partyka, G., Pawson, S., Putman, W., Rienecker, M., Schubert, S.D., Sienkiewicz, M. and Zhao, B. 2017. The modern-era retrospective analysis for research and applications, version 2 (MERRA-2). *Journal of Climate*. **30**(14), pp.5419–5454.

Giambelluca, T.W., Hölscher, D., Bastos, T.X., Frazão, R.R., Nullet, M.A. and Ziegler, A.D. 1997. Observations of albedo and radiation balance over postforest land surfaces in the eastern Amazon Basin. *Journal of Climate*. **10**(5), pp.919–928.

Good, E.J., Ghent, D.J., Bulgin, C.E. and Remedios, J.J. 2017. A spatiotemporal analysis of the relationship between near-surface air temperature and satellite land surface temperatures using 17 years of data from the ATSR series. *Journal of Geophysical Research: Atmospheres*. **122**(17), pp.9185–9210.

Hansen, M.C., DeFries, R.S., Townshend, J.R.G., Carroll, M., Dimiceli, C. and Sohlberg, R.A. 2003. Global Percent Tree Cover at a Spatial Resolution of 500 Meters: First Results of the MODIS Vegetation Continuous Fields Algorithm. *Earth Interactions*. **7**(10), pp.1–15.

Hansen, M.C., Egorov, A., Roy, D.P., Potapov, P., Ju, J., Turubanova, S., Kommareddy, I. and Loveland, T.R. 2011. Continuous fields of land cover for the conterminous United States using Landsat data: First results from the Web-Enabled Landsat Data (WELD) project. *Remote Sensing Letters*. **2**(4), pp.279–288.

Hansen, M.C., Potapov, P. V., Moore, R., Hancher, M., Turubanova, S.A., Tyukavina, A., Thau, D., Stehman, S. V., Goetz, S.J., Loveland, T.R., Kommareddy, A., Egorov, A., Chini, L., Justice, C.O. and Townshend, J.R.G. 2013. High-Resolution Global Maps of 21st-Century Forest Cover Change. *Science*. **342**(6160), pp.850–853.

Hansen, M.C., Sohlberg, R., Defries, R.S. and Townshend, J.R.G. 2000. Global land cover classification at 1 km spatial resolution using a classification tree approach. *International Journal of Remote Sensing*. **21**(6–7), pp.1331–1364.

Harris, I., Osborn, T.J., Jones, P. and Lister, D. 2020. Version 4 of the CRU TS monthly high-resolution gridded multivariate climate dataset. *Scientific Data*. **7**(1), pp.1–18.

Hersbach, H., Bell, B., Berrisford, P., Hirahara, S., Horányi, A., Muñoz-Sabater, J., Nicolas, J., Peubey, C., Radu, R., Schepers, D., Simmons, A., Soci, C., Abdalla, S., Abellan, X., Balsamo, G., Bechtold, P., Biavati, G., Bidlot, J., Bonavita, M., De Chiara, G., Dahlgren, P., Dee, D., Diamantakis, M., Dragani, R., Flemming, J., Forbes, R., Fuentes, M., Geer, A., Haimberger, L., Healy, S., Hogan, R.J., Hólm, E., Janisková, M., Keeley, S., Laloyaux, P., Lopez, P., Lupu, C., Radnoti, G., de Rosnay, P., Rozum, I., Vamborg, F., Villaume, S. and Thépaut, J.N. 2020. The ERA5 global reanalysis. *Quarterly Journal of the Royal Meteorological Society*. **146**(730), pp.1999–2049.

Hook, S.J., Myers, J.J., Thome, K.J., Fitzgerald, M. and Kahle, A.B. 2001. The MODIS/ASTER airborne simulator (MASTER) - A new instrument for earth science studies. *Remote Sensing of Environment*. **76**(1), pp.93–102.

Hou, A.Y., Kakar, R.K., Neeck, S., Azarbarzin, A.A., Kummerow, C.D., Kojima, M., Oki, R., Nakamura, K. and Iguchi, T. 2014. The global precipitation measurement mission. *Bulletin of the American Meteorological Society*. **95**(5), pp.701–722.

Hoyer, S. and Hamman, J. 2017. xarray: N-D labeled Arrays and Datasets in Python. *Journal of Open Research Software*. **5**(1), p.10.

Huffman, G.J., Adler, R.F., Bolvin, D.T., Gu, G., Nelkin, E.J., Bowman, K.P., Hong, Y., Stocker, E.F. and Wolff, D.B. 2007. The TRMM Multisatellite Precipitation Analysis (TMPA): Quasi-global, multiyear, combined-sensor precipitation estimates at fine scales. *Journal of Hydrometeorology*. **8**(1), pp.38–55.

Huffman, G.J., Bolvin, D.T., Nelkin, E.J. and Tan, J. 2020. *Integrated Multi-satellitE Retrievals for GPM (IMERG) Technical Documentation. NASA/GSFC.* [Online]. Available from: https://gpm.nasa.gov/sites/default/files/document_files/IMERG_doc.pdf.

Huffman, G.J.A., Behrangi, R.F., Adler, D.T., Bolvin, E.J. and Nelkin, G.G. 2022. *Introduction to the New Version 3 GPCP Monthly Global Precipitation Analysis* [Online]. Available from: https://docserver.gesdisc.eosdis.nasa.gov/public/project/MEaSUREs/GPCP/Release_Notes.GPCPV3.2.pdf.

JGCRI 2023. GCAM v7 Documentation: Global Change Analysis Model (GCAM). Available from: https://www.iamcdocumentation.eu/index.php/Model_Documentation_-_GCAM.

Joyce, R.J., Janowiak, J.E., Arkin, P.A. and Xie, P. 2004. CMORPH: A method that produces global precipitation estimates from passive microwave and infrared data at high spatial and temporal resolution. *Journal of Hydrometeorology*. **5**(3), pp.487–503.

Joyce, R.J. and Xie, P. 2011. Kalman filter-based CMORPH. *Journal of Hydrometeorology*. **12**(6), pp.1547–1563.

Jungclaus, J., Bittner, M., Wieners, K.-H., Wachsmann, F., Schupfner, M., Legutke, S., Giorgetta, M., Reick, C., Gayler, V., Haak, H., de Vrese, P., Raddatz, T., Esch, M. and Mauritsen, Thorst, E. 2019. MPI-M MPI-ESM1.2-HR model output prepared for CMIP6 CMIP historical. *Earth System Grid Federation*. [Online]. Available from: https://doi.org/10.22033/ESGF/CMIP6.762.

Justice, C.O., Townshend, J.R.G., Vermote, E.F., Masuoka, E., Wolfe, R.E., Saleous, N., Roy, D.P. and Morisette, J.T. 2002. An overview of MODIS Land data processing and product status. *Remote Sensing of Environment*. **83**(1–2), pp.3–15.

Kawanishi, T., Sezai, T., Ito, Y., Imaoka, K., Takeshima, T., Ishido, Y., Shibata, A., Miura, M., Inahata, H. and Spencer, R.W. 2003. The Advanced Microwave Scanning Radiometer for the Earth Observing System (AMSR-E), NASDA's contribution to the EOS for global energy and water cycle studies. *IEEE Transactions on Geoscience and Remote Sensing*. **41**(2), pp.184–194.

Keeling, C.D., Whorf, T.P., Wahlen, M. and Pllcht, J. van der 1995. Interannual extremes in the rate of rise of atmospheric carbon dioxide since 1980. *Nature*. **375**, pp.666–670.

Kim, E., Lyu, C.-H.J., Anderson, K., Leslie, R.V. and Blackwell, W.J. 2014. S-NPP ATMS instrument prelaunch and on-orbit performance evaluation. *Journal of Geophysical Research: Atmospheres RESEARCH*. **119**(9), pp.5653–5670.

Kimura, F. and Shimizu, Y. 1994. Estimation of Sensible and Latent Heat Fluxes from Soil Surface Temperature Using a Linear Air-Land Heat Transfer Model. *American Meteorological Society*. **33**, pp.477–450.

Knyazikhin, Y., Myneni, R.B., Privette, J.L., Running, S.W., Nemani, R., Zhang, Y., Tian, Y., Wang, Y., Morissette, J.T., Glassy, J. and Votava, P. 1999. *MODIS Leaf Area Index (LAI) and Fraction of Photosynthetically Active Radiation Absorbed by Vegetation (FPAR) Product (MOD15) Algorithm Theoretical Basis Document* [Online]. Available from: http://modis.gsfc.nasa.gov/data/atbd/atbd_mod15.pdf%5Cnhttp://eospso.gsfc.nasa.gov/atbd/modistables.html%5Cn%5CBiblioteca_Digital_SPR%5CMyneni1999_ATBD.pdf.

Kobayashi, S., Ota, Y., Harada, Y., Ebita, A., Moriya, M., Onoda, H., Onogi, K., Kamahori, H., Kobayashi, C., Endo, H., Miyaoka, K. and Kiyotoshi, T. 2015. The JRA-55 reanalysis: General specifications and basic characteristics. *Journal of the Meteorological Society of Japan*. **93**(1), pp.5–48.

Landsat Science Outreach 2023. Landsat Science. *NASA*., https://landsat.gsfc.nasa.gov/.

Lawrimore, J.H., Menne, M.J., Gleason, B.E., Williams, C.N., Wuertz, D.B., Vose, R.S. and Rennie, J. 2011. An overview of the Global Historical Climatology Network monthly mean temperature data set, version 3. *Journal of Geophysical Research Atmospheres*. **116**(19), pp.1–18.

Lee, X., Goulden, M.L., Hollinger, D.Y., Barr, A., Black, T.A., Bohrer, G., Bracho, R., Drake, B., Goldstein, A., Gu, L., Katul, G., Kolb, T., Law, B.E., Margolis, H., Meyers, T., Monson, R., Munger, W., Oren, R., Paw U, K.T., Richardson, A.D., Schmid, H.P., Staebler, R., Wofsy, S. and Zhao, L. 2011. Observed increase in local cooling effect of deforestation at higher latitudes. *Nature*. **479**(7373), pp.384–387.

Legates, D.R. and Willmott, C.J. 1990. Mean seasonal and spatial variability in global surface air temperature. *Theoretical and Applied Climatology*. **41**(1–2), pp.11–21.

Li, Y., Zhao, M., Mildrexler, D.J., Motesharrei, S., Mu, Q., Kalnay, E., Zhao, F., Li, S. and Wang, K. 2016. Potential and actual impacts of deforestation and afforestation on land surface temperature. *Journal of Geophysical Research*. **121**(24), pp.14372–14386.

Lovato, T. and Peano, D. 2020. CMCC CMCC-CM2-SR5 model output prepared for CMIP6 CMIP historical. *Earth System Grid Federation*. [Online]. Available from: https://doi.org/10.22033/ESGF/CMIP6.3825.

Lovato, T., Peano, D. and Butenschön, M. 2021. CMCC CMCC-ESM2 model output prepared for CMIP6 CMIP historical. *Earth System Grid Federation*. [Online]. Available from: https://doi.org/10.22033/ESGF/CMIP6.13164.

Matsuura, K. and Willmott, C.J. 2018. Terrestrial Precipitation: 1900-2017 Gridded Monthly Time Series. *University of Delaware*., http://climate.geog.udel.edu/~climate/html_pages/G.

Menne, M.J., Durre, I., Vose, R.S., Gleason, B.E. and Houston, T.G. 2012. An overview of the global historical climatology network-daily database. *Journal of Atmospheric and Oceanic Technology*. **29**(7), pp.897–910.

Met Office 2023. Iris: A powerful, format-agnostic, and community-driven Python package for analysing and visualising Earth science data. Available from: http://scitools.org.uk/.

Mildrexler, D.J., Zhao, M. and Running, S.W. 2009. Testing a MODIS Global Disturbance Index across North America. *Remote Sensing of Environment*. **113**(10), pp.2103–2117.

Mo, T. 1996. Prelaunch Calibration of the A Microwave Sounding Unit-A for NOAA-K. *Transactions on Microwave Theory and Techniques*. **44**(8), pp.1460–1469.

Monteith, J.L. 1965. Evaporation and Environment. *Symposia of the Society for Experimental Biology*. **19**, pp.205–234.

Mu, Q., Heinsch, F.A., Zhao, M. and Running, S.W. 2007. Development of a global evapotranspiration algorithm based on MODIS and global meteorology data. *Remote Sensing of Environment*. **106**(3), pp.519–536.

Mu, Q., Zhao, M. and Running, S.W. 2013. *MODIS Global Terrestrial Evapotranspiration (ET) Product (NASA MOD16A2/A3) Algorithm Theoretical Basis Document Collection 5* [Online]. Available from: https://lpdaac.usgs.gov/documents/93/MOD16_ATBD.pdf.

Myneni, R., Knyazikhin, Y. and Park, T. 2021. MODIS/Terra Leaf Area Index/FPAR 8-Day L4 Global 500m SIN Grid V061 [Data set]. *NASA EOSDIS Land Processes DAAC.*, https://doi.org/10.5067/MODIS/MOD15A2H.061.

Myneni, R.B., Hoffman, S., Knyazikhin, Y., Privette, J.L., Glassy, J., Tian, Y., Wang, Y., Song, X., Zhang, Y., Smith, G.R., Lotsch, A., Friedl, M., Morisette, J.T., Votava, P., Nemani, R.R. and Running, S.W. 2002. Global products of vegetation leaf area and fraction absorbed PAR from year one of MODIS data. *Remote Sensing of Environment*. **83**(1–2), pp.214–231.

NASA GSFC 2023a. Atmosphere Discipline Team Imager Products. *NASA GSFC.*, https://atmosphere-imager.gsfc.nasa.gov/.

NASA GSFC 2023b. Moderate Resolution Imaging Spectroradiometer. *NASA GSFC.*, https://modis.gsfc.nasa.gov/.

NASA/GISS 2018. NASA-GISS GISS-E2.1G model output prepared for CMIP6 CMIP historical. *Earth System Grid Federation*.

Neubauer, D., Ferrachat, S., Siegenthaler-Le Drian, C., Stoll, J., Folini, D.S., Tegen, I., Wieners, K.-H., Mauritsen, T., Stemmler, I., Barthel, S., Bey, I., Daskalakis, N., Heinold, B. and Kokkola, H, U. 2019. HAMMOZ-Consortium MPI-ESM1.2-HAM model output prepared for CMIP6 CMIP historical. *Earth System Grid Federation*. [Online]. Available from: https://doi.org/10.22033/ESGF/CMIP6.1622.

Nguyen, P., Ombadi, M., Gorooh, V.A., Shearer, E.J., Sadeghi, M., Sorooshian, S., Hsu, K., Bolvin, D. and Ralph, M.F. 2020. Persiann dynamic infrared–rain rate (PDIR-now): A near-real-time, quasi-global satellite precipitation dataset. *Journal of Hydrometeorology*. **21**(12), pp.2893–2906.

Nguyen, P., Shearer, E.J., Tran, H., Ombadi, M., Hayatbini, N., Palacios, T., Huynh, P., Braithwaite, D., Updegraff, G., Hsu, K., Kuligowski, B., Logan, W.S. and Sorooshian, S. 2019. The CHRS data portal, an easily accessible public repository for PERSIANN global satellite precipitation data. *Scientific Data*. **6**, pp.1–10.

NOAA NESDIS 2020. Microwave Integrated Retrieval System (MIRS) - Sensors. *NOAA National Centers for Environmental Information*. [Online]. Available from: https://www.star.nesdis.noaa.gov/mirs/instruments.php.

Pendrill, F., Gardner, T.A., Meyfroidt, P., Persson, U.M., Adams, J., Azevedo, T., Lima, M.G.B., Baumann, M., Curtis, P.G., Sy, V. De, Garrett, R., Godar, J., Goldman, E.D., Hansen, M.C., Heilmayr, R., Herold, M., Kuemmerle, T., Lathuillière, M.J., Ribeiro, V., Tyukavina, A., Weisse, M.J. and West, C. 2022. Disentangling the numbers behind agriculture-driven tropical deforestation. *Science*. **377**(1168), pp.1–11.

Peterson, T.C. and Vose, R.S. 1997. An overview of the Global Historical Climatology Network Temperature Database. *Bulletin of the American Meteorological Society*. **78**(12), pp.2837–2850.

Reichle, R.H., Liu, Q., Koster, R.D., Draper, C.S., Mahanama, S.P.P. and Partyka, G.S. 2017. Land Surface Precipitation in MERRA-2. *Journal of Climate*. **30**(5), pp.1643–1664.

Ridley, J., Menary, M., Kuhlbrodt, T., Andrews, M. and Andrews, T. 2019a. MOHC HadGEM3-GC31-LL model output prepared for CMIP6 CMIP historical. *Earth System Grid Federation*. [Online]. Available from: https://doi.org/10.22033/ESGF/CMIP6.419.

Ridley, J., Menary, M., Kuhlbrodt, T., Andrews, M. and Andrews, T. 2019b. MOHC HadGEM3-GC31-MM model output prepared for CMIP6 CMIP historical. *Earth System Grid Federation*. [Online]. Available from: https://doi.org/10.22033/ESGF/CMIP6.420.

Rozenstein, O., Qin, Z., Derimian, Y. and Karnieli, A. 2014. Derivation of land surface temperature for landsat-8 TIRS using a split window algorithm. *Sensors*. **14**(4), pp.5768–5780.

Running, S., Mu, Q., Zhao, M. and Moreno, A. 2021a. MODIS/Terra Net Evapotranspiration Gap-Filled 8-Day L4 Global 500m SIN Grid V061 [Data set]. *NASA EOSDIS Land Processes DAAC.*, https://doi.org/10.5067/MODIS/MOD16A2GF.061.

Running, S., Mu, Q., Zhao, M. and Moreno, A. 2021b. *User's Guide: MODIS Global Terrestrial Evapotranspiration (ET) Product* [Online]. Available from: https://lpdaac.usgs.gov/documents/931/MOD16_User_Guide_V61.pdf.

Running, S.W., Nemani, R.R., Heinsch, F.A., Zhao, M., Reeves, M. and Hashimoto, H. 2004. A continuous satellite-derived measure of global terrestrial primary production. *BioScience*. **54**(6), pp.547–560.

Sadeghi, M., Nguyen, P., Naeini, M.R., Hsu, K., Braithwaite, D. and Sorooshian, S. 2021. PERSIANN-CCS-CDR, a 3-hourly 0.04° global precipitation climate data record for heavy precipitation studies. *Scientific Data*. **8**(1), pp.1–11.

Schaaf, C. and Wang, Z. 2021. MODIS/Terra+Aqua BRDF/Albedo Daily L3 Global - 500m V061 [Data set]. *NASA EOSDIS Land Processes DAAC.*, https://doi.org/10.5067/MODIS/MCD43A3.061.

Schneider, U., Becker, A., Finger, P., Meyer-Christoffer, A., Ziese, M. and Rudolf, B. 2014. GPCC's new land surface precipitation climatology based on quality-controlled in situ data and its role in quantifying the global water cycle. *Theoretical and Applied Climatology*. **115**(1–2), pp.15–40.

Schneider, U., Elke, R., Hänsel, S., Finger, P. and Ziese, M. 2022. Monthly Land-Surface Precipitation Climatology for Every Month and the Total Year from Rain-Gauges built on GTS-based and Historical Data. *GPCC Climatology Version 2022 at 0.25°*., 10.5676/DWD_GPCC/CLIM_M_V2022_025.

Seferian, R. 2018. CNRM-CERFACS CNRM-ESM2-1 model output prepared for CMIP6 CMIP historical. *Earth System Grid Federation*. [Online]. Available from: https://doi.org/10.22033/ESGF/CMIP6.4068.

Shepard, D. 1968. A two-dimensional interpolation function for irregularly-spaced data. *Proceedings of the 1968 23rd ACM National Conference*., pp.517–524.

Shimoda, H. 2005. GCOM missions. *International Geoscience and Remote Sensing Symposium (IGARSS)*. **6**, pp.4201–4204.

Smith, C., Baker, J.C.A. and Spracklen, D. V 2023. Tropical deforestation causes large reductions in observed precipitation. *Nature*. **615**, pp.270–275.

Smith, J. 2022. Aqua At 20. *NASA Earth Data*. [Online]. Available from: https://www.earthdata.nasa.gov/learn/articles/aqua-at-20.

Song, X.P., Hansen, M.C., Stehman, S. V., Potapov, P. V., Tyukavina, A., Vermote, E.F. and Townshend, J.R. 2018. Global land change from 1982 to 2016. *Nature*. **560**(7720), pp.639–643.

Strahler, A., Gopal, S., Lambin, E. and Moody, A. 1999. *MODIS Land Cover Product Algorithm Theoretical Basis Document (ATBD) MODIS Land Cover and Land-Cover Change* [Online]. Available from: http://modis.gsfc.nasa.gov/data/atbd/atbd_mod12.pdf.

Sulla-Menashe, D. and Friedl, M.A. 2022. *User guide to collection 6 MODIS land cover (MCD12Q1 and MCD12C1) product* [Online]. Available from: https://lpdaac.usgs.gov/documents/1409/MCD12_User_Guide_V61.pdf.

Sun, Q., Miao, C., Duan, Q., Ashouri, H., Sorooshian, S. and Hsu, K.L. 2018. A Review of Global Precipitation Data Sets: Data Sources, Estimation, and Intercomparisons. *Reviews of Geophysics*. **56**(1), pp.79–107.

Swart, N.C., Cole, J.N.S., Kharin, V. V., Lazare, M., Scinocca, J.F., Gillett, N.P., Anstey, J., Arora, V., Christian, J.R., Jiao, Y., Lee, W.G., Majaess, F., Saenko, O.A., Seiler, C. and Seinen, M. 2019a. CCCma CanESM5 model output prepared for CMIP6 CMIP historical. *Earth System Grid Federation*. [Online]. Available from: https://doi.org/10.22033/ESGF/CMIP6.1301.

Swart, N.C., Cole, J.N.S., Kharin, V. V., Lazare, M., Scinocca, J.F., Gillett, N.P., Anstey, J., Arora, V., Christian, J.R., Jiao, Y., Lee, W.G., Majaess, F., Saenko, O.A., Seiler, C. and Seinen, M. 2019b. CCCma CanESM5-CanOE model output prepared for CMIP6 CMIP historical. *Earth System Grid Federation*. [Online]. Available from: https://doi.org/10.22033/ESGF/CMIP6.10205.

Tang, Y., Rumbold, S., Ellis, R., Kelley, D., Mulcahy, J., Sellar, A., Walton, J. and Jones, C. 2019. MOHC UKESM1.0-LL model output prepared for CMIP6 CMIP historical. *Earth System Grid Federation*. [Online]. Available from: https://doi.org/10.22033/ESGF/CMIP6.6113.

Tuanmu, M.N. and Jetz, W. 2014. A global 1-km consensus land-cover product for biodiversity and ecosystem modelling. *Global Ecology and Biogeography*. **23**(9), pp.1031–1045.

Vancutsem, C., Achard, F., Pekel, J.F., Vieilledent, G., Carboni, S., Simonetti, D., Gallego, J., Aragão, L.E.O.C. and Nasi, R. 2021. Long-term (1990–2019) monitoring of forest cover changes in the humid tropics. *Science Advances*. **7**(10), pp.1–22.

Vining, R.C. and Blad, B.L. 1992. Estimation of sensible heat flux from remotely sensed canopy temperatures. *Journal of Geophysical Research*. **97**(17), pp.1984–1987.

Virtanen, P., Gommers, R., Oliphant, T.E., Haberland, M., Reddy, T., Cournapeau, D., Burovski, E., Peterson, P., Weckesser, W., Bright, J., van der Walt, S.J., Brett, M., Wilson, J., Millman, K.J., Mayorov, N., Nelson, A.R.J., Jones, E., Kern, R., Larson, E., Carey, C.J., Polat, \.Ilhan, Feng, Y., Moore, E.W., VanderPlas, J., Laxalde, D., Perktold, J., Cimrman, R., Henriksen, I., Quintero, E.A., Harris, C.R., Archibald, A.M., Ribeiro, A.H., Pedregosa, F., van Mulbregt, P. and SciPy 1.0 Contributors 2020. {SciPy} 1.0: Fundamental Algorithms for Scientific Computing in Python. *Nature Methods*. **17**, pp.261–272.

Volodin, E., Mortikov, E., Gritsun, A., Lykossov, V., Galin, V., Diansky, N., Gusev, A., Kostrykin, S., Iakovlev, N., Shestakova, A. and Emelina, S. 2019a. NM INM-CM4-8 model output prepared for CMIP6 CMIP historical. *Earth System Grid Federation*. [Online]. Available from: https://doi.org/10.22033/ESGF/CMIP6.1422.

Volodin, E., Mortikov, E., Gritsun, A., Lykossov, V., Galin, V., Diansky, N., Gusev, A., Kostrykin, S., Iakovlev, N., Shestakova, A. and Emelina, S. 2019b. NM INM-CM5-0 model output prepared for

CMIP6 CMIP historical. *Earth System Grid Federation*. [Online]. Available from: https://doi.org/10.22033/ESGF/CMIP6.1423.

Wan, Z. 1999. *MODIS Land-Surface Temperature Algorithm Theoretical Basis Document (LST ATBD)* [Online]. Available from: https://lpdaac.usgs.gov/documents/119/MOD11_ATBD.pdf.

Wan, Z., Hook, S. and Hulley, G. 2021a. MODIS/Aqua Land Surface Temperature/Emissivity 8-Day L3 Global 1km SIN Grid V061 [Data set]. *NASA EOSDIS Land Processes DAAC*., https://doi.org/10.5067/MODIS/MYD11A2.061.

Wan, Z., Hook, S. and Hulley, G. 2021b. MODIS/Terra Land Surface Temperature/Emissivity 8-Day L3 Global 1km SIN Grid V061 [Data set]. *NASA EOSDIS Land Processes DAAC*., https://doi.org/10.5067/MODIS/MOD11A2.061.

Willmott, C.J., Rowe, C.M. and Philpot, W.D. 1985. Small-Scale Climate Maps: A Sensitivty Analysis of Some Common Assumptions Associated with Grid-Point Interpolation and Contouring. *The American Cartographer*. **12**(1), pp.5–16.

Winckler, J., Reick, C.H. and Pongratz, J. 2017. Robust identification of local biogeophysical effects of land-cover change in a global climate model. *Journal of Climate*. **30**(3), pp.1159–1176.

Xie, P., Joyce, R., Wu, S., Yoo, S.-H., Yarosh, Y., Sun, F. and Lin, R. 2019. NOAA Climate Data Record (CDR) of CPC Morphing Technique (CMORPH) High Resolution Global Precipitation Estimates, Version 1. *NOAA National Centers for Environmental Information*., https://doi.org/10.25921/w9va-q159.

Xie, P., Yatagai, A., Chen, M., Hayasaka, T., Fukushima, Y., Liu, C. and Yang, S. 2007. A gauge-based analysis of daily precipitation over East Asia. *Journal of Hydrometeorology*. **8**(3), pp.607–626.

Zhang, K., Kimball, J.S., Nemani, R.R. and Running, S.W. 2010. A continuous satellite-derived global record of land surface evapotranspiration from 1983 to 2006. *Water Resources Research*. **46**(9), pp.1–21.

Zhao, M., Heinsch, F.A., Nemani, R.R. and Running, S.W. 2005. Improvements of the MODIS terrestrial gross and net primary production global data set. *Remote Sensing of Environment*. **95**(2), pp.164–176.

Zhuang, J. 2022. xESMF. Available from: https://doi.org/10.5281/zenodo.1134365.

Ziehn, T., Chamberlain, M., Lenton, A., Law, R., Bodman, R., Dix, M., Wang, Y., Dobrohotoff, P., Srbinovsky, J., Stevens, L., Vohralik, P., Mackallah, C., Sullivan, A., O'Farrell, S. and Druken, K.

2019. CSIRO ACCESS-ESM1.5 model output prepared for CMIP6 CMIP historical historical. *Federation, Grid Earth System*. [Online]. Available from: https://doi.org/10.22033/ESGF/CMIP6.4272.

Chapter 3

3 Driver of forest loss impacts temperature changes due to tropical forest loss

Callum Smith[1], Jessica C. A. Baker[1], and Dominick V. Spracklen[1]

[1] School of Earth and Environment, University of Leeds, Leeds, UK

Manuscript *in preparation*

Abstract

Rapid tropical deforestation is resulting in substantial changes to local and regional climate. Tropical forest loss is caused by a range of factors including agriculture and forestry, but it is not known whether the climate impacts of forest loss differ for different drivers of forest loss. We used remotely sensed atmospheric and land-surface datasets to analyse whether the local climate impacts of tropical forest loss from 2001 to 2019 varied with the driver of deforestation. We show forest loss caused by commodity agriculture leads to double the warming of forest loss from shifting agriculture. If the transition from shifting agriculture to commodity driven deforestation continues across the tropics as projected, we suggest the warming due to forest loss could increase. Our study highlights the differing local climate impacts of forest loss across the tropics and the important role of deforestation drivers in modulating the climate response.

Plain language summary

Tropical forests provide a range of biophysical services to their ecosystems, from recycling moisture to moderating local temperatures. When forests are lost, these services are altered. We quantified, using remotely sensed data, the amount by which tropical forest loss impacts the climate local to the forest loss. Over the 2001-2019 period, we found warming across the tropics as a result of forest loss, with the greatest warming in the Amazon. This warming increased when greater amounts of the forest canopy were removed. Warming due to forest loss in the Congo was lower because of the less industrialised nature of the forest loss. We show that a shift to commodity agriculture has the potential to double the warming currently found in the Congo.

Key points:

1. Local climate impacts of forest loss vary across the tropics
2. Tropical forest loss induces local warming
3. Commodity agriculture drives double the warming of shifting agriculture

3.1 Introduction

Tropical forests cover around 7% of the world's land surface (Estoque et al., 2019) and account for around 45% of global forests (FAO and UNEP, 2020). Rapid deforestation is occurring across the tropics (Hansen et al., 2013, van Cutsem et al., 2023), causing loss of biodiversity and ecosystem services and changes to climate (IPBRES, 2019). Tropical deforestation impacts the climate at local (Alkama and Cescatti, 2016; Baker and Spracklen, 2019), regional (Spracklen et al., 2018; Marengo et al., 2018; Cohn et al., 2019) and global (Scott et al., 2018; Johannes Winckler et al., 2019) scales through altering the exchange of moisture, energy and trace gases between the land surface and the atmosphere (Silva Dias et al., 2002; Bonan, 2008).

Forest loss can occur and manifest in a variety of ways and can be driven by both natural and anthropogenic processes. Curtis et al. (2018) categorised these differences into five drivers of forest loss, commodity driven, shifting agriculture, forestry, wildfire, and urbanisation. Whilst there are widely accepted to be further categories of natural deforestation, such as drought, windthrow and pests, Curtis et al. (2018) assert that their "categories account for the majority of recent observed forest loss". Each is characterised by traits, and each will leave a different climate impacts signature.

Agriculture is the most common driver of forest loss in the tropics (Pendrill et al., 2022; Fritz et al., 2022), with the two most common drivers of forest loss being commodity agriculture (CA) and shifting agriculture (SA). Commodity agriculture is typified by large scale, industrial conversion of forest for plantation and pasture, but also includes forest loss associated with mining and industry. It is commonly found in the heavily deforested south-eastern arc of deforestation in the Amazon and Sumatra, where oil palm and rubber are the principal crops (Jamaludin et al., 2022). It is typified by large-scale intensive and long term or permanent conversion of forest. Shifting agriculture produces a heterogenous landscape of mixed small-scale rotational agriculture, common across much of the Congo basin (Curtis et al., 2018; Fritz et al., 2022). Of the deforested land, only 45-65% becomes agriculturally suitable, indicating that land abandonment is likely and with it, regrowth. Both Curtis et al. (2018) and Pendrill et al. (2022) highlight difficulties with defining land as cleared by SA, including outlining the period of time land is allowed to take to regenerate. The amount of both CA and SA has varied over time, but as parts of the tropics become more industrialised and access increases, SA may decline in favour of CA Heinimann et al., 2017; Tyukavina et al., 2017), with potential implications for climate. We currently have poor understanding of how the climate impacts of forest loss vary across the tropics. Indeed, observationally little is known about the impact that these different drivers of deforestation have on climate.

Satellite observations have provided high-resolution, spatially comprehensive insights into how land use and land use change impacts local climate (Li et al., 2015; Li et al., 2016; Alkama and Cescatti, 2016; Bright et al., 2017; Duveiller et al., 2018; Baker and Spracklen, 2019). Many studies have focussed on impacts on local surface temperature. Alkama and Cescatti (2016) showed that daytime surface temperature increases by ~1.5 K in regions of tropical forest loss. Li et al. (2016) examined the impact of deforestation on temperature trends and showed that forest loss generates a 0.28 K decade^{-1} warming trend across tropical forests. In the Amazon, Baker and Spracklen (2019) found that forest loss can increase mean annual mean daytime surface temperatures by 0.44 K, with increases up to 1.5 K in the dry season. Schultz et al. (2017) found daytime surface temperature of tropical forests were on average 4.4 K warmer than neighbouring non-forest.

Here we analyse satellite remote-sensed data to assess how the local climate impact of tropical deforestation depends on and is different for the different drivers of deforestation. We set out to explore the possible reasons that forest loss generates climate impacts and examine these across the tropics and also regionally.

3.2 Data and Methods

To assess the impact of tropical forest loss on local climate, we used satellite observed forest loss from the Global Forest Change (GFC) version 1.9 (Hansen et al., 2013), combined with remotely sensed climate and land-surface variables. GFC v1.9 provides forest canopy cover in 2000 and subsequent annual forest loss from 2001–2021 at 30-meter (m) resolution. We used Terra MODIS collection 6.1 daytime and night time land surface temperature (LST) (MOD11C3), black sky albedo (BSA) (MCD43A3), evapotranspiration (ET) (MOD16A2GF), leaf area index (LAI) (MOD15A2). We used precipitation (P) data from the Climate Hazards Centre (Climate Hazards Group InfraRed Precipitation with Station data, CHIRPS v2.0). Information on the drivers of forest loss is from Curtis et al. (2019) and is available at 0.1x0.1°. Drivers of forest loss were categorised as either commodity-driven deforestation (comm), shifting agriculture (SA), forestry (For), wildfire (WF), and urbanization (urb). All datasets were available over the period 2001 – 2019. Information about the datasets used in this study can be found in Table 3.1.

The MODIS datasets are supplied with accompanying quality-control (QC) data layers, with which we masked each dataset, removing pixels that had cloud-contamination and where the quality was not ranked at least 'good'. For ET we utilised the gap-filled product which takes a range of inputs including LAI (which has had QC applied), vegetation dynamics, albedo, land cover and meteorological reanalysis data, proving computed, homogenous ET using the Penman-Monteith equation (Monteith, 1965). We therefore didn't apply any further QC to this dataset. In this analysis we used BSA, which is the integration of the bi-directional hemispherical reflectance. It assumes the absence of a diffuse component (i.e., cloud), and it is a function of the solar zenith angle. We chose to use BSA over white sky albedo, which is the integration of directional bi-hemispherical reflection, as it assumes the presence of a diffuse component. When analysed both BSA and WSA produced similar results. We chose to use LST rather than air temperature or near surface temperature to allow for direct comparisons with other similar studies (Li et al., 2015; Alkama and Cescatti, 2016; Bright et al., 2017; Baker and Spracklen, 2019) and because there is evidence that LST and near-surface air temperature from weather stations are closely correlated (Good et al., 2017).

We analysed the impacts of forest loss at 0.05x0.05° resolution, approximately 5 km length at the equator. The datasets were regridded to consistent grids using the python package xESMF (Zhuang, 2022). In this analysis we used both datasets with continuous data, for example land surface temperature and categorical data such as land cover type. With these differences, we used the 'bilinear' scheme for the continuous datasets which creates an average through space, whilst we used 'nearest s2d' (nearest source to destination) for the categorical datasets enabling integer values were conserved. We also regridded using the python package Iris (Met Office, 2023) using the area weighted scheme and found consistent results. We calculated forest loss using the original 30 m data for GFC resolution data, then regridded it to 0.05x0.05° by taking the sum of all 30 m pixels within each larger pixel, thereby upscaling fine-scale data of complete forest loss. We linearly interpolated forest driver data using the python package SciPy (Virtanen et al., 2020). We constrained our analysis to the evergreen broadleaf tropical (30°S to 30°N) biome using MODIS land cover (MCD12Q1). To isolate impacts in the Amazon Basin, Congo Basin and maritime SEA we used shapefiles to delineate those specific regions, the extents of which can be seen in the map in Figure 3.1.

To analyse the local climate impacts of land cover change, we used a moving window nearest neighbour approach, as used previously in Baker and Spracklen (2019) and Smith et al. (2023). This approach isolates the changes occurring locally due to forest loss, mitigating the changes due to differences in geography and background climate. With a pixel size of ~5 km length at the equator, the 3x3 grid we used has a length of ~15 km (~225 km^2). To test the impact of different grid sizes on the results, we used a 5x5 grid (~25 km length) finding the results to be consistent (Supplementary Figure A.1). This approach allowed us to find the climate changes that have taken place over time and compare these changes in deforested regions with those from nearby forests. When calculating the changes over time, we compared 5 year means at the start (2001-2005) and end (2015-2019) to reduce the impact of interannual variability on the results. We carried out a sensitivity test using 3-year means (2001-2003 and 2017-2019) finding the results to be robust to this change (Supplementary Figure A.1).

To calculate the impact to local climate due to forest loss we used two slightly different methodologies. First, we used a threshold approach, where we defined forest and deforested categories using the GFC dataset. Forest was defined as an area where 'forest' cover remained greater than 90% for the entire analysis period, whilst 'deforested' started (in year 2001) as forest with greater than 90% forest cover and transitioned to forest covers of less than 70% at the end period (2019). We then found the difference between the two categories, presenting the change to climate in terms of each climate variables units. To test the impact of the defined forest transition thresholds, we analysed the changes over an alternative forest-deforestation transition definition. Here we chose to define deforested pixels by those that had greater than 70% forest cover in 2001 and subsequently transitioned to less than 70% forest cover by 2019, whilst forest pixels maintained greater than 70% forest cover throughout the analysis period. We found similar results, indicating that our methodology has little impact on the result presented (Supplementary Figure A.2). We further tested the effect of methodology on our results by varying the size of the moving window from 3x3 to a 5x5 grid and by changing the length of the mean start and end periods from 5 years to 3 years, the results of which are presented in Supplementary Figure A.1d. We found that methodology choice didn't produce statistically different results. Broadly, we found that using a 5x5 grid and 3-year mean produced a slightly greater increase in temperature due to forest loss than the 3x3 grid and 5-year mean.

The second method calculates the forest loss of deforested pixels relative to forest loss in neighbouring forest pixels, providing the difference between the forest and deforested in terms of percentage point coverage. We plot the forest losses for deforested and control data points as histograms in Supplementary Figure A.3, showing the majority of forest control pixels changed less than 10% over time and the deforested pixels experienced changes of up to and exceeding 50% forest loss. Here we specified that the deforested pixel must have experienced more than 0.1 percentage points of forest loss over time than their control pixels, which excludes pixels where forest loss is similar to the control. The reported value is the change as a function of forest loss, divided by the difference in forest loss between deforested and nearby forest pixels. In both methods, we tested using the Student's t-test whether the changes over forest and paired deforested grid cells were statistically significantly different from one another. We used both methods to test the robustness of the climate change due to forest loss. We again present a range of sensitivity tests, calculating the impacts that methodology can have on our results (Supplementary Figure A.4), finding that analytical changes can have small impacts to our results.

We examined the climate impacts in different climate seasons, detecting changes in the dry, wet and transition seasons. We calculated the driest and wettest three months for each pixel and each year using the CHIRPS precipitation data. From this we found the mean value for the land surface and climate variables in those 3 dry and wet months. The transition season was calculated as the mean of the remaining 6 months in the year for each pixel in each year.

We related the impact of forest loss on the change in LST to the reduction in canopy cover in each grid cell. ΔLST was binned by the reduction in canopy cover (bin width = 2.5%, disregarding bins with fewer than 20 data points). We calculated linear regressions for each variable as function of canopy cover with 95% confidence intervals using the SciPy Stats python package.

Table 3.1. *Datasets used in this study, listing the variable and product names, their native resolutions and their references. The MODIS datasets all utilise the latest collection 6, version 6.1 data. Spatial resolutions are approximated at the equator.*

Dataset	Native Resolution (spatial and temporal)	Reference
MOD15A2H, Leaf Area Index (LAI)	500 m x 500 m, 8-day	Myneni et al., 2021
MOD16A2, Evapotranspiration (ET)	500 m x 500 m, 8-day	Running et al., 2021
MOD11A2, Land Surface Temperature (LST)	1 km x 1 km, 8-day	Wan et al., 2021b
MYD11A2, Land Surface Temperature (LST)	1 km x 1 km, 8-day	Wan et al., 2021a
MCD43C3, Black Sky Albedo (BSA)	500 m x 500 m, 8-day	Schaaf and Wang, 2021
MCD12Q1, Land Cover Type	500 m x 500 m, annual	Friedl and Sulla-Menashe, 2022
CHIRPS v2.0, Precipitation (P)	5 km x 5 km, monthly	Funk et al., 2015
Forest Loss, Global Forest Change (GFC) v1.9	30 m x 30 m, annual	Hansen et al., 2013
Driver of deforestation	10 km x 10 km	Curtis et al., 2018

To examine the relationships between changes in LST due to forest loss and changes in other land surface and climate variables, we fitted linear regressions using Pearson's correlation coefficient, (calculated using SciPy (Virtanen et al., 2020)) to scatter plots, only showing the regression lines where the computed correlation coefficients were found to be statistically significant and different from zero at the 5% level ($p<0.05$). We report errors throughout as the standard error of the mean.

3.3 Results and Discussion

Figure 3.1 shows the extent of tropical deforestation in the period 2001 to 2019, constrained by the MODIS evergreen broadleaf biome. The three main tropical rainforests, the Amazon, the Congo Basin, and Southeast Asia (SEA), are outlined in purple. Forest loss is coloured by the dominant driver of deforestation as calculated by Curtis et al. (2018), with the majority of deforestation in the tropics being driven by commodity agriculture (CA, Comm) and shifting agriculture (SA). In the Amazon, CA, which is dominant in the southern and eastern Amazon and SA are the most common drivers. SA is the dominant driver of deforestation in the Congo. Forest loss in SEA is driven by a wide range of drivers, with CA is prevalent in Sumatra and the exterior of Borneo. Forestry is the predominant driver in the interior of Borneo as well as in Laos and northern Vietnam. In Papua and Papua New Guinea, shifting agriculture is the dominant driver.

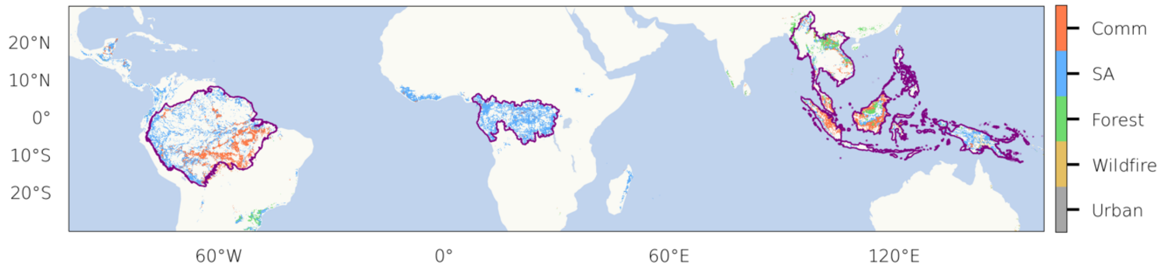

Figure 3.1. *Map showing the drivers of tropical forest loss. Drivers are categorised as Commodity Driven (Comm), Shifting Agriculture (SA), Forestry (Forest), Wildfire and Urbanisation (Urban). The area is constrained by tropical evergreen broadleaf biome using MODIS land cover type (Table 3.1). Purple outlines show the three main evergreen broadleaf tropical biomes, from left to right, the Amazon, the Congo basin and Southeast Asia.*

Land surface temperatures have changed over time, with changes to background climate. These changes are different in different tropical regions and within regions for different drivers of forest loss (Supplementary Figure A.5). Predominantly the main drivers of tropical forest loss are CA and SA, with fewer incidences of forestry, wildfire and urbanisation driving forest loss across the evergreen broadleaf tropics. As such we present and discuss results pertaining to changes due to CA and SA driven forest loss, with other drivers presented in the supplementary material.

To explore how forest loss has impacted land surface temperature, we compared changes in LST over deforested and nearby forest regions. Tropical forest loss resulted in annual mean LST increases of up to 0.7 K across all regions. Both CA and SA show statistically significant increases in temperature and the difference between the two groups of temperature changes are significant, showing that the two drivers are independent from one another. Across the tropical forest regions, CA results in larger increases in LST than shifting agriculture, most notably in the Amazon. Overall, across the tropics there are similar numbers of data points in each CA and SA categories, however split by region, there are bigger disparities. In the Congo there is almost no CA, as shown by the numbers displayed on each bar in Figure 3.2.

Commodity deforestation has a less variable response than SA to forest loss (Supplementary Figure A.6 and A.7d). This could be because CA is likely more industrial and uniform than SA which tends to be more heterogenous, and which may return permanently or on a rotational basis to forest. Tropical forests can be cooler (Li et al., 2015; Alkama and Cescatti, 2016; Bright et al., 2017; Duveiller et al., 2018; Lawrence et al., 2022 etc) and wetter (Lawrence and Vandecar, 2015; Spracklen et al., 2018; Smith et al., 2023 etc) than the croplands and pasture they are replaced with, however regrowth as secondary forest can decrease LST. This key difference could explain why in the Amazon, CA leads to double the warming of SA.

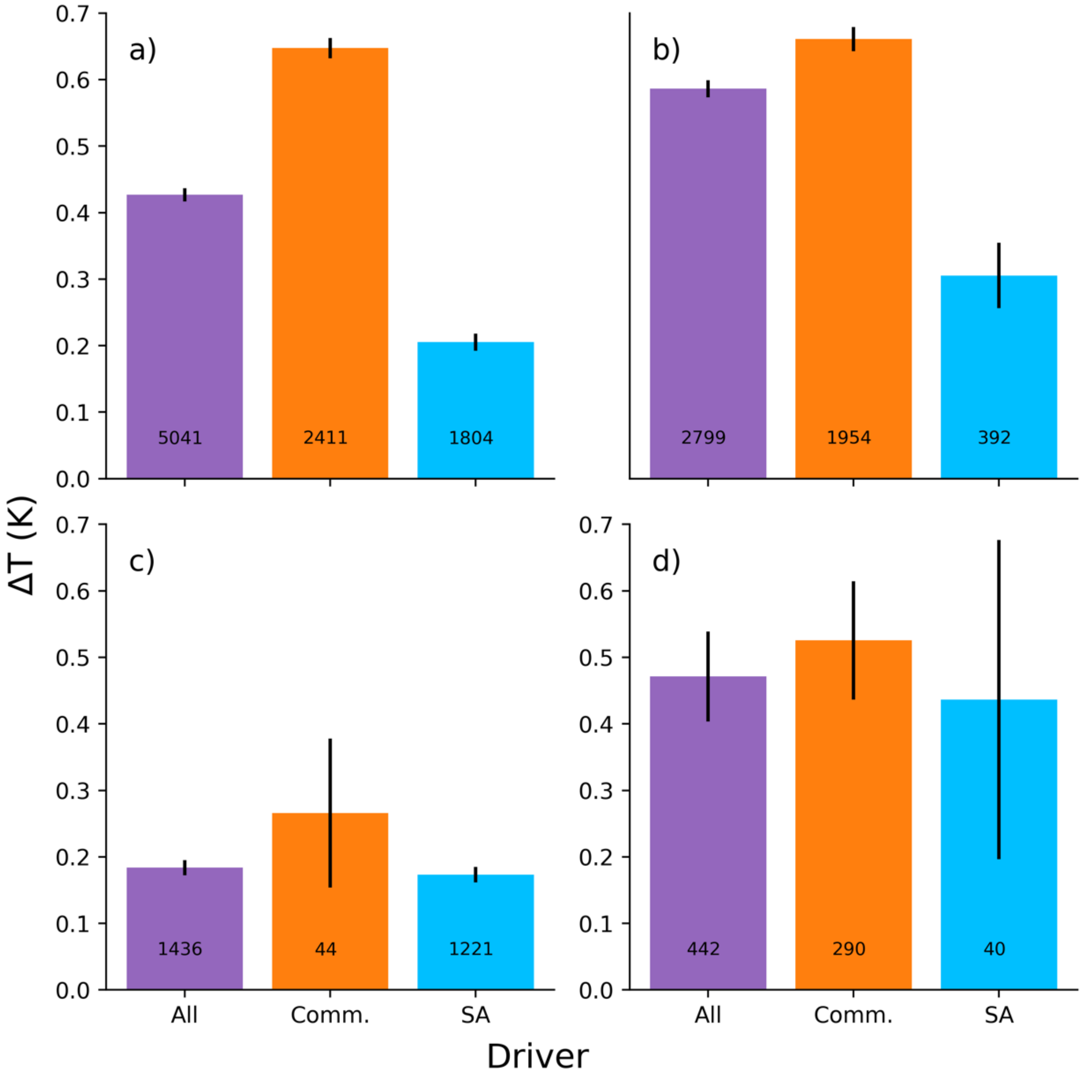

Figure 3.2. *Change in annual mean land surface temperature due to forest loss for (a) Tropics, b) Amazon, c) Congo, d) SEA. Results are categorised by driver of deforestation (All drivers, Commodity Driven deforestation (Comm.) and Shifting Agriculture (SA)) using data from* Curtis et al. (2018). *The change due to forest loss is calculated over the period 2001-2019 for deforested pixels compared to nearby forested pixels (K). Deforested pixels must have been >90% forest in 2001 and less than 70% by 2019, whilst forest pixels must maintain >90% forest cover. Error bars show the standard error of the mean and the black values on each bar report the number of data points in each category.*

The greater warming response of CA compared to the other drivers could result from greater amounts of forest loss in regions of CA. To understand how warming varied with the amount of forest loss for the different drivers, we plotted the LST change versus forest loss (Figure 3.3). Across the tropics, LST increases linearly with forest loss. Areas with CA experienced the greatest forest loss across the tropics. For each driver, the increase in LST was greater with increasing forest loss. Forest loss of 20 percentage points led to warming of 0.45 K for CA compared to 0.1 K for SA. The Congo overall sees less forest loss than the Amazon and SEA, with the maximum being around 75% (Figure 3.3c), however CA and SA drive equivalent maximum amounts of deforestation. Figure 3.3d shows that in SEA, after 60% forest loss there is a large increase in the variability the temperature response, with the shading overlapping zero. Due to few available pixels, the response of forestry, wildfire and urbanisation are presented only in Supplementary Figure A.8.

We found that tropical forest loss resulted in local daytime surface warming, as found in previous studies (Li et al., 2015; Silvério et al., 2015; Alkama and Cescatti, 2016; Duveiller et al., 2018; Baker and Spracklen, 2019). We found complete canopy loss in tropical forests led to annual mean warming of 1.52 K, similar to the warming of 1.53 K reported by Alkama and Cescatti (2016) based on analysis of similar data over the period 2003 to 2012. Prevedello et al. (2019) used a similar moving window analysis technique, to examine the effect of pantropical forest change over 2000 - 2010 on climate. They reported a stronger warming, with a 50% reduction in canopy cover causing a warming of 1.08 ± 0.25 K compared to 0.95 K in our analysis. Prevedello et al. (2019) use MODIS Collection 5 (C5) data and do not account for interannual variability when calculating climate changes, both of which, in addition to the different analysis period, could account for the difference in reported ΔT. Tropical forest loss is expected to cause a local daytime warming, due to the reduction of ET which decreases the latent heat flux, and reduced surface roughness which reduces turbulence and the transfer of heat from the surface, outweighing the cooling due to increased albedo (Li et al., 2016; Duveiller et al., 2018; J. Winckler et al., 2019). Schultz et al. (2017) analysed both daytime and night-time temperature and found that tropical forests were on average 4.4 K cooler than non-forest during the day but only 0.2 K cooler at night. The stronger daytime warming reported by Schultz et al. (2017) is likely due to the use of different datasets (MODIS C5 LST data), time periods (2003 - 2013), land cover classifications, (International Geosphere-Biosphere Programme) and analysis methods (8x8 grid cells in a 0.5^{o} x 0.5^{o} window).

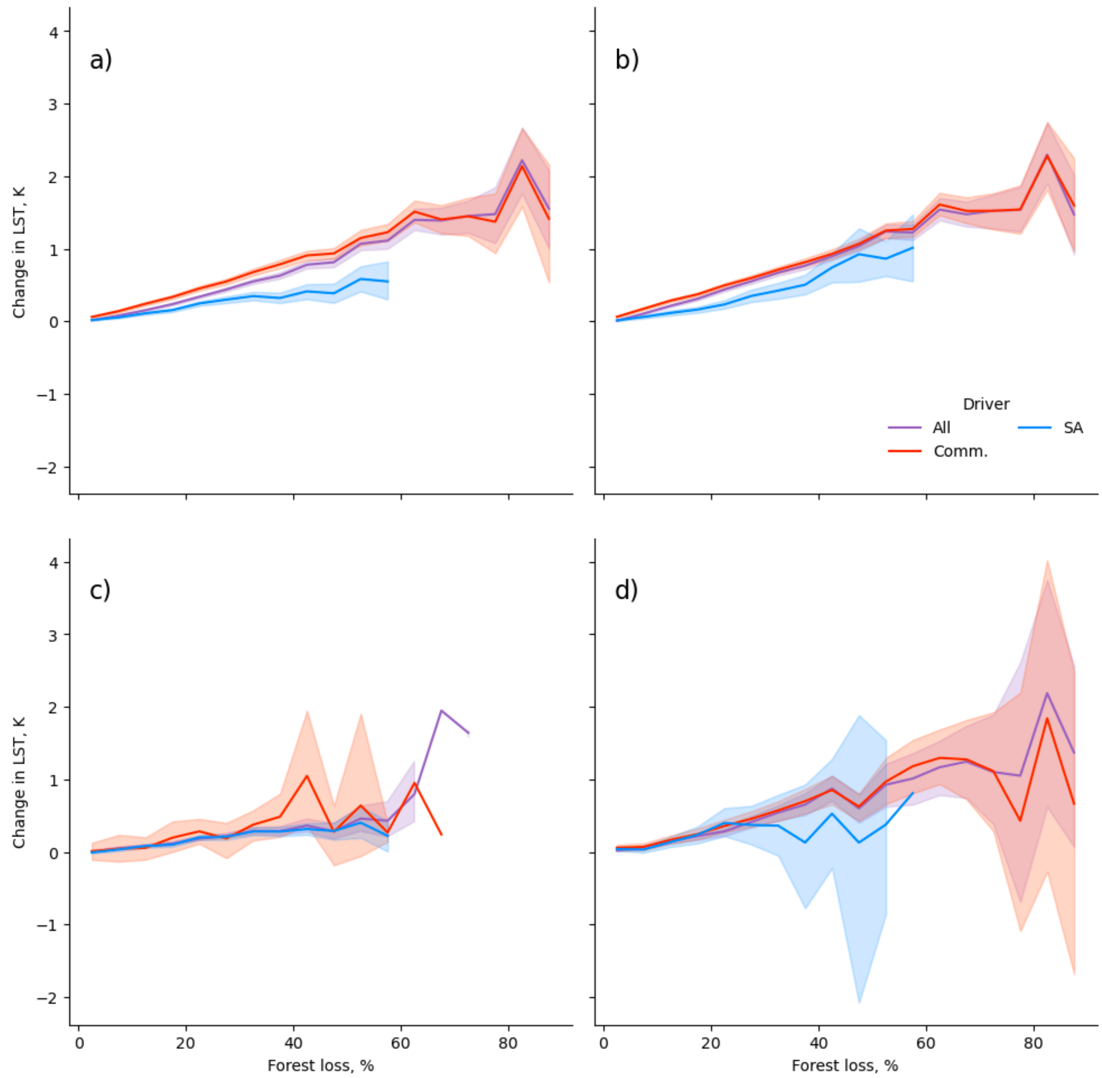

Figure 3.3. *Change in land surface temperature by forest loss for each region ((a) Tropics, b) Amazon, c) Congo and d) SEA) and each driver of deforestation (All drivers (All), commodity driven deforestation (Comm.) and shifting agriculture (SA)). Results are binned with widths of 2.5% forest loss, with each bin plotting the median value within the bin. To be plotted, each bin must have >20 data points. Additionally, no data points with >90% forest loss are included. The line shading shows the 95% confidence interval.*

Whilst calculating the LST response due to forest loss via a threshold approach allows us to directly compare with similar observational studies that utilise a similar threshold approach, the methodology limits the dataset to regions which have experienced the largest amounts of forest loss. This could provide a skewed view of climate impacts, by only selecting data points from certain tropical regions. The linear response of LST to forest loss (Figure 3.3) allows us to calculate the change in LST per percentage point of forest loss (Figure 3.4). Using this method allows us to consider a greater number and a more homogenous spatial spread of data points as we compare every pixel that has experienced loss and is adjacent to pixels that have experienced less (number of tropical data points is 182,924, compared to number in the threshold analysis, 5041). Whilst in Figure 3.2, changes in LST due to forest loss could be due either to different amounts of forest loss in each driver category or different response of LST to forest loss, Figure 3.4 shows that CA leads to greater warming per percentage point of forest loss. This shows that CA warming isn’t just due to greater forest loss. Across the tropics (Figure 3.4a), we find CA drives a warming of 0.02 K per percentage point of forest loss more than double the warming of forest loss arising from shifting agriculture (0.009 K per percentage point of forest loss). In the Amazon (Figure 3.4b), where both CA and SA are frequent drivers, commodity agriculture leads to a warming of 0.021 K/% compared to 0.0075 K/% for SA.

Likely we see lower increases in LST per percentage point of forest loss for areas of forest cleared by SA as these areas experience periodic land abandonment (Molinario et al., 2015; Curtis et al., 2018), leading to forest regrowth (Turubanova et al., 2018; McNicol et al., 2018). In contrast, forest cleared for commodity production is more likely to remain as agriculture.

Another possible explanation for the lower warming caused by SA is that areas of SA were previously partially degraded. This would mean that changes in LST for SA would be lower than for CA which fully transition from primary forest to deforested. To investigate this, we calculated the fraction of forest loss occurring within intact forest landscapes (Potapov et al. (2017) for each driver of deforestation (Supplementary Figure A.9). For CA and SA (whose classifications have the majority of data points), deforested pixels were equally more likely to been not intact (82 and 79% respectively), suggesting that pixels of SA were not previously deforested.

This analysis considers the impacts of forest loss on local climate, however recent work has shown that the non-local impacts can significantly change the observed impact. If forest loss also impacts the neighbouring forest areas as Cohn et al. (2019) have shown, which act as controls in this study, we may underestimate the local impacts of forest loss. Similarly, whilst the regional background climate has been controlled for via the nearest-neighbour analysis, there could still be small impacts on the results arising from differences in proximity to moisture sources, latitude and geography. These differences could in particular propagate when considering the different temperature responses due to forest loss from CA and SA, which have a tendency to occur in discrete locations (Figure 1), especially in the Amazon.

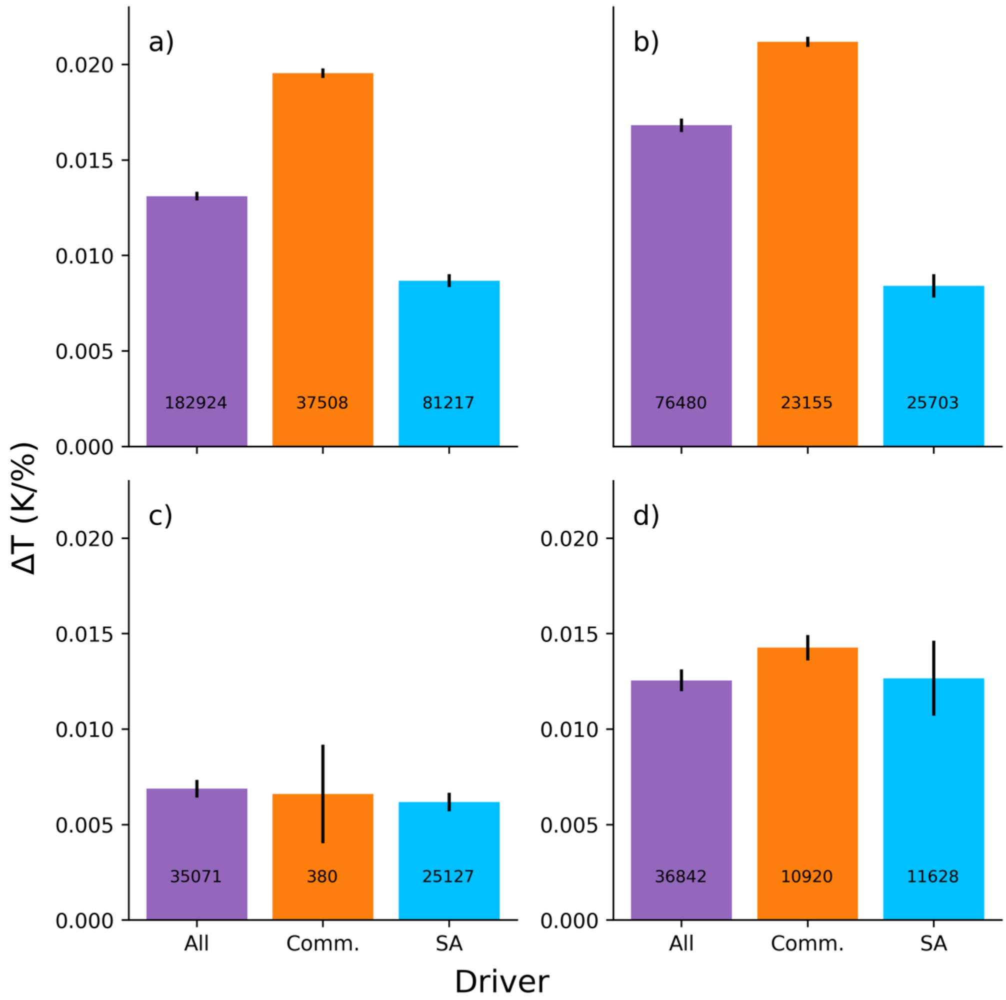

Figure 3.4. *Change in annual mean temperature due to forest loss per percentage point of forest loss categorised by driver of deforestation (All, Commodity Driven deforestation (Comm.) and Shifting Agriculture (SA)) using data from Curtis et al., (2018) for (a) Tropics, b) Amazon, c) Congo, d) SEA. The change in temperature is calculated change over time (2001-2019) for deforested pixels, compared to nearby forested pixels (K/ percentage point of forest loss (%)). Error bars show the standard error of the mean and the black values on each bar report the number of data points in each category.*

To understand how these changes may vary seasonally, we plotted the changes in LST in the driest and wettest three months of each year as well as for the transition season (Figure 3.5). Using the per percentage point of forest loss method, we found absolute increases in LST in all seasons, particularly in the dry season where there is an increase of 0.014 K/% in the tropics (Figure 3.5a). Tropics wide dry season temperatures increase more than wet season for both CA and SA and the transition season is approximately equal to the dry season response. The wet season also tends to have a larger associated error, produced by greater variability in the change in LST in that season. Regionally, for all drivers of deforestation, the largest increases in LST in the dry season are in the Amazon (0.0165 K/%), followed by SEA (0.0135 K/%) and the Congo (0.0085 K/%). In the wet season, there is increased cloud coverage, which results in fewer data points being retrieved and there being larger uncertainty in the results shown, than for the dry and transition seasons. We tested to see if the methodology impacted these results, finding similar pattern (Supplementary Figure A.10), however due to less data being available, particularly in the wet season, some categories were unable to be plotted.

To explore whether we can observationally explain these changes in LST due to forest loss, we calculated for each driver and region, the change in BSA, ET, LAI, night time LST and day night mean LST due to forest loss (Figure 3.6, additionally we relate these quantities graphically in Supplementary Figure A.11). We found forest loss consistently increased albedo across the tropics, with median increases of between 0.000075 $\%^{-1}$ to 0.000125$\%^{-1}$.

In-situ observations indicate conversion of tropical forests (albedo of 0.11 to 0.13) to pasture (albedo of 0.16 to 0.19) (Gash and Shuttleworth, 1991; Bastable et al., 1993; Fisch et al., 1994) would lead to albedo increase of around 0.05, substantially larger than in our analysis. We found surface albedo increased by only 0.01 even for grid cells with almost complete removal of canopy cover (Figure 3.6a). Loarie et al. (2011) also used MODIS data, finding small increases in albedo following deforestation in the southern Amazon with mean increases in albedo of 0.028. The small observed increase in albedo after forest loss in satellite data at this resolution (0.05°) is likely due to incomplete canopy cover loss at this scale or a rapid regrowth of vegetation after forest loss, further supported by the small reductions in LAI. Our analysis reports changes in LAI due to forest loss of -0.003 to 0.004.

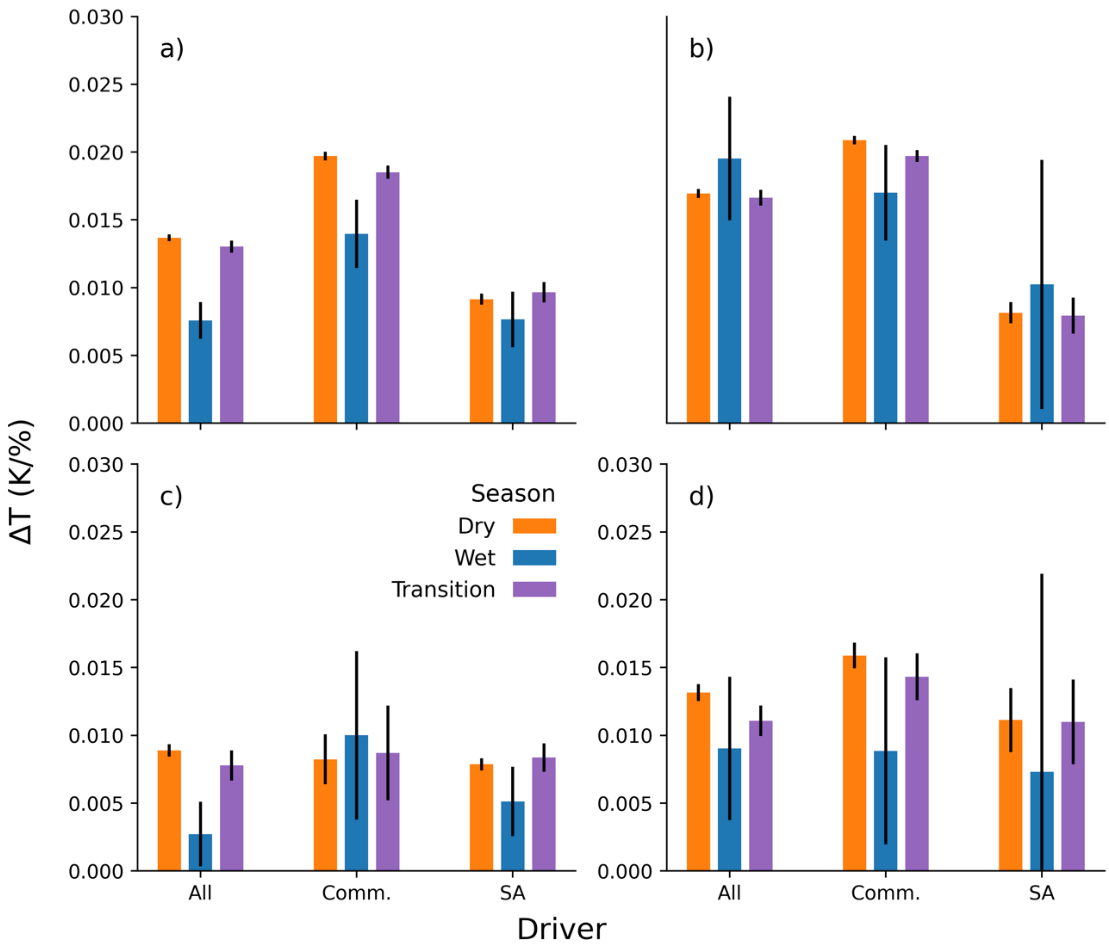

Figure 3.5. *Seasonal changes in mean land surface temperature per percentage point of forest loss in the dry (orange), wet (blue) and transition (purple) seasons for the (a) Tropics, b) Amazon, c) Congo and d) SEA. Results are categorised by driver of deforestation (All drivers, Commodity Driven deforestation (Comm.) and Shifting Agriculture (SA)) using data from Curtis et al. (2018).The change in temperature is calculated change over time (2001-2019) for deforested pixels, compared to nearby forested pixels. Error bars show the standard error of the mean.*

The majority of regions and drivers show decreases in LAI with forest loss, however in SEA, SA shows an increase. In SEA, the LST response to forest loss is lower than in the Amazon. In SEA, natural forests are usually cleared and replaced with palm oil, rubber or plantation forestry (Austin et al., 2019), which tend to have higher rates of ET and LAI than pasture and grasses, which leads to lower increase in LST through greater evaporative cooling. The conversion of forest to plantation could explain the increase in LAI in SEA. In Indonesia, plantations account for more than 50% of forest loss (Seymour and Harris, 2019), with oil palm plantations responsible for two fifths of this expansion (Austin et al., 2019). Palm oil tends to be hotter, drier and has 15-20% higher rates of ET than natural forests in SEA (Fan et al., 2019; Meijaard et al., 2020). This suggests that in SEA, the dominant driver of ΔT is the decrease in surface roughness associated with lower-stature, more homogenous vegetation.

In the Amazon, Figure 3.6 shows forest loss reduces LAI, increases albedo and increases in ET, similarly reported previously (Silvério et al., 2015). They found forest loss induced warming of ~0.3 K, compared to 0.44 K found by Baker and Spracklen (2019) and 0.7 K in this study. Chen et al., (2020) found inverse relationships between LAI and land surface T at the global scale which could primarily be attributed to changes in roughness and thus aerodynamic resistance. McAlpine et al. (2018) used MODIS satellite data to show 1.7 K of warming associated with lowland deforestation in central Kalimantan. Using ground-based measurements, Hardwick et al. (2015) found the expansion and fragmentation of forest by oil palm and other cash crops in Borneo has driven T increases of 2.8-6.5 K compared to neighbouring forest. Whilst this range is substantially greater than our mean value, we found forest loss causes ΔT in SEA of up to 0.6 K (Fig. 3.2). In the Congo, we found small changes in LAI, ET and albedo consistent with smaller reductions in canopy cover and substantial vegetation regrowth associated with shifting agriculture (Rudel, 2013; Molinario et al., 2015). Zeppetello et al. (2020) analysed MODIS land surface T and found warming of 0.5 K associated with small scale (0-10 km^2) forest loss in the Congo. This value exceeds our estimate; however, they used different degradation definitions and did not employ a paired approach in their analysis, which could explain the greater T increases they observed.

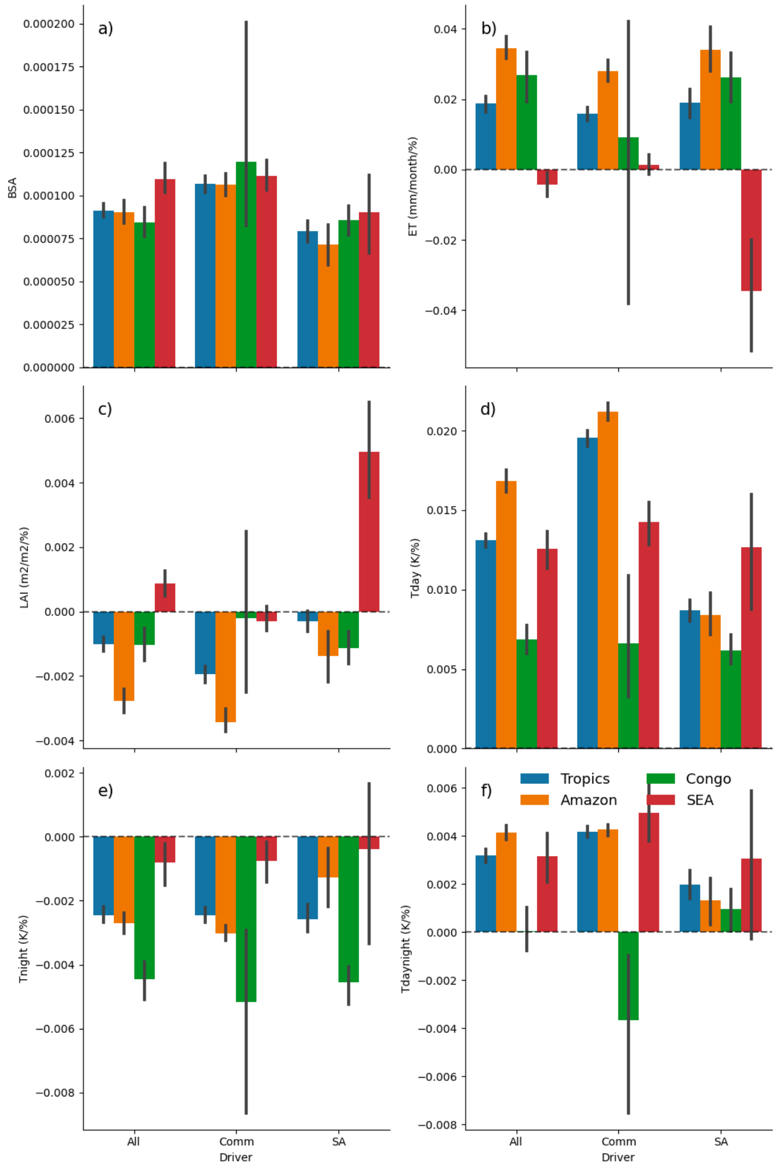

Figure 3.6. *Change in annual mean (a) BSA, b) ET c) LAI, d) LST $_{day}$, e) LST$_{night}$, f) LST$_{daynight}$ due to forest loss per percentage point of forest loss categorised by driver of deforestation (All, Commodity Driven deforestation (Comm.) and Shifting Agriculture (SA)) using data from Curtis et al., (2018) for (blue) Tropics, (orange) Amazon, (green) Congo, (red) SEA. The change in temperature is calculated change over time (2001-2019) for deforested pixels, compared to nearby forested pixels (K/ percentage point of forest loss (%)). Error bars show the standard error of the mean.*

Despite a range of policy and corporate commitments, the rate of forest loss driven by CA has not declined in recent years (Curtis et al., 2018). The increasing dominance of large-scale forest loss in many parts of the tropics (Austin et al., 2017), means that the local warming from forest loss has likely increased in recent years. In Brazil, policy initiatives targeting large-scale forest loss led to a shift of CA away from Brazil to elsewhere in the tropics (Curtis et al., 2018) and did not prevent an expansion of smaller-scale loss across the Amazon (Rosa et al., 2012; Kalamandeen et al., 2018; Escobar, 2019; Montibeller et al., 2020), which has expanded the spatial extent of deforestation-induced warming across the region. Until recently, CA driven deforestation has been relatively limited in the Congo. Our analysis indicates that if the scale and extent of CA driven deforestation in the Congo continues to increase (Tegegne et al., 2016), then the warming due to forest loss across the Congo could double.

Regional and global climate model simulations largely confirm a warming due to tropical forest loss (Boysen et al., 2020). Some models predict tropical deforestation leads to local cooling (Bell et al., 2015; Robertson, 2019; Boysen et al., 2020), in contrast to the observed response. In these model simulations, the cooling due to increased albedo dominates the warming due to reduced ET and surface roughness. We found daytime warming due to forest loss was positively related to albedo change (Fig. 3.6a). This confirms that the local cooling induced by increased albedo is outweighed by warming due to reduced ET and surface roughness associated with canopy cover loss. This remote-sensed analysis can be used to evaluate the climate models and ensure they correctly capture this important local climate response.

The local warming induced by tropical forest loss will have major impacts on human populations. Extensive social surveys in Indonesia found people appreciate the local cooling provided by tropical forests (Wolff et al., 2018). Masuda et al. (2020) found that warming due to forest loss reduced the cognitive performance of rural workers in Indonesia. In the future as populations expand, increased demand for food, fibre and fuel may accelerate forest loss into previously intact tropical forests (Potapov et al., 2017). Continuing rapid rates of tropical forest loss will result in additional warming that will pose major challenges to hundreds of millions of people, particularly as the threat of heat illness rises under global climate change. The carbon storage and resulting global climate benefits of tropical forests are now well recognised and are starting to be valued through international policy mechanisms such as REDD+. Our results highlight the important local cooling services provided by tropical forests, which are much less well recognised (McKinnon et al., 2016; Cheng et al., 2019). Tropical forests also cause cooling (Cohn et al., 2019) and rainfall enhancement (Spracklen et al., 2012) at regional scales. A wider appreciation of these local and regional climate impacts and the benefits for human well-being could provide a valuable argument for local policy makers to support reduced deforestation and conservation of remaining tropical forests.

3.4 Conclusions

This study examined the local climate impacts of tropical forest loss between 2001 and 2019 using remotely sensed data. We find tropical forest loss causes local land surface daytime warming across all three tropical forest regions. Forest loss caused mean daytime warming of 0.6 K in the Amazon, 0.47 K in South-East Asia and 0.18 K in the Congo. In all three regions, the local warming due to tropical forest loss exceeds the regional warming due to climate change over the 2001 to 2019 period. We show that the driver of deforestation has a large impact on the magnitude of the warming due to forest loss, with commodity driven deforestation producing double the warming of shifting agriculture. In the Congo, the smaller reduction in canopy cover, smaller deforestation extent and possible vegetation regrowth associated with shifting agriculture, explains the smaller warming induced by forest loss. Our analysis suggests that a transition to a commodity-driven forest loss regime in the Congo, similar to that of the Amazon, could double the local warming response. The projected expansion of commodity agriculture will have major impacts on livelihoods across the tropics. Climate and land use policies need to better recognise the local climate adaptation benefits of reducing tropical deforestation, particularly deforestation caused by commodity agriculture.

Acknowledgments

The research has been supported by funding from the European Research Council under the European Union's Horizon 2020 research and innovation programme (DECAF project, grant agreement no. 771492), and the Newton Fund, through the Met Office Climate Science for Service Partnership Brazil.

Data Availability Statement

*The observational datasets analysed in the study are freely available from the following online repositories: MODIS data (*MCD43A3, MOD16A2, MOD15A2, MOD11A2 and MCD12Q1*) from https://search.earthdata.nasa.gov/search, CHIRPS Precipitation from https://data.chc.ucsb.edu/products/CHIRPS-2.0/global_monthly/netcdf/, Global Forest Change data from https://storage.googleapis.com/earthenginepartners-hansen/GFC-2021-v1.9/download.html* and Deforestation Driver Classifications from *https://data.globalforestwatch.org/datasets/tree-cover-loss-by-dominant-driver-1.*

References

Alkama, R. and Cescatti, A. 2016. Biophysical climate impacts of recent changes in global forest cover. *Science*. **351**(6273), pp.600–604.

Austin, K.G., Schwantes, A., Gu, Y. and Kasibhatla, P.S. 2019. What causes deforestation in Indonesia? *Environmental Research Letters*. **14**(2).

Baker, J.C.A. and Spracklen, D. V 2019. Climate Benefits of Intact Amazon Forests and the Biophysical Consequences of Disturbance. *Frontiers in Forests and Global Change*. **2**, pp.1–13.

Bastable, H.G., Shuttleworth, W.J., Dallarosa, R.L.G., Fisch, G. and Nobre, C.A. 1993. Observations of Climate, Albedo, and Surface Radiation Over Cleared and Undisturbed Amazonian Forest. *International Journal of Climatology*. **13**(7), pp.783–796.

Bell, J.P., Tompkins, A.M., Bouka-Biona, C. and Sanda, I.S. 2015. A process-based investigation into the impact of the Congo basin deforestation on surface climate. *Journal of Geophysical Research*. **120**(12), pp.5721–5739.

Bonan, G.B. 2008. Forests and climate change: Forcings, feedbacks, and the climate benefits of forests. *Science*. **320**(5882), pp.1444–1449.

Boysen, L.R., Brovkin, V., Pongratz, J., Lawrence, D.M., Lawrence, P., Vuichard, N., Peylin, P., Liddicoat, S., Hajima, T., Zhang, Y., Rocher, M., Delire, C., Séférian, R., Arora, V.K., Nieradzik, L., Anthoni, P., Thiery, W., Laguë, M.M., Lawrence, D. and Lo, M.H. 2020. Global climate response to idealized deforestation in CMIP6 models. *Biogeosciences*. **17**(22), pp.5615–5638.

Bright, R.M., Davin, E., O'Halloran, T., Pongratz, J., Zhao, K. and Cescatti, A. 2017. Local temperature response to land cover and management change driven by non-radiative processes. *Nature Climate Change*. **7**(4), pp.296–302.

Chen, C., Li, D., Li, Y., Piao, S., Wang, X., Huang, M., Gentine, P., Nemani, R.R. and Myneni, R.B. 2020. Biophysical impacts of Earth greening largely controlled by aerodynamic resistance. *Science Advances*. **6**(47), pp.1–10.

Cheng, S.H., MacLeod, K., Ahlroth, S., Onder, S., Perge, E., Shyamsundar, P., Rana, P., Garside, R., Kristjanson, P., McKinnon, M.C. and Miller, D.C. 2019. A systematic map of evidence on the contribution of forests to poverty alleviation. *Environmental Evidence*. **8**(1), pp.1–22.

Cohn, A.S., Bhattarai, N., Campolo, J., Crompton, O., Dralle, D., Duncan, J. and Thompson, S. 2019. Forest loss in Brazil increases maximum temperatures within 50 km. *Environmental Research Letters*. **14**(8).

Curtis, P.G., Slay, C.M., Harris, N.L., Tyukavina, A. and Hansen, M.C. 2018. Classifying drivers of global forest loss. *Science*. **361**(6407), pp.1108–1111.

Duveiller, G., Hooker, J. and Cescatti, A. 2018. The mark of vegetation change on Earth's surface energy balance. *Nature Communications*. **9**(1), pp.1–12.

Escobar, H. 2019. Amazon fires clearly linked to deforestation, scientists say. *Science*. **365**(6456), pp.853–853.

Fan, Y., Meijide, A., Lawrence, D.M., Roupsard, O., Carlson, K.M., Chen, H.Y., Röll, A., Niu, F. and Knohl, A. 2019. Reconciling Canopy Interception Parameterization and Rainfall Forcing Frequency in the Community Land Model for Simulating Evapotranspiration of Rainforests and Oil Palm Plantations in Indonesia. *Journal of Advances in Modeling Earth Systems*. **11**(3), pp.732–751.

Fisch, G., Wright, I.R. and Bastable, H.G. 1994. Albedo of tropical grass: A case study of pre- and post-burning. *International Journal of Climatology*. **14**(1), pp.103–107.

Friedl, M. and Sulla-Menashe, D. 2022. MODIS/Terra+Aqua Land Cover Type Yearly L3 Global 500m SIN Grid V061 [Data set]. *NASA EOSDIS Land Processes DAAC*. [Online]. [Accessed 1 January 2022]. Available from: https://doi.org/10.5067/MODIS/MCD12Q1.061.

Fritz, S., Laso Bayas, J.C., See, L., Schepaschenko, D., Hofhansl, F., Jung, M., Dürauer, M., Georgieva, I., Danylo, O., Lesiv, M. and McCallum, I. 2022. A Continental Assessment of the Drivers of Tropical Deforestation With a Focus on Protected Areas. *Frontiers in Conservation Science*. **3**(February), pp.1–12.

Funk, C., Peterson, P., Landsfeld, M., Pedreros, D., Verdin, J., Shukla, S., Husak, G., Rowland, J., Harrison, L., Hoell, A. and Michaelsen, J. 2015. The climate hazards infrared precipitation with stations - A new environmental record for monitoring extremes. *Scientific Data*. **2**, pp.1–21.

Gash, J.H.C. and Shuttleworth, W.J. 1991. Tropical deforestation: Albedo and the surface-energy balance. *Climatic Change*. **19**(1–2), pp.123–133.

Good, E.J., Ghent, D.J., Bulgin, C.E. and Remedios, J.J. 2017. A spatiotemporal analysis of the relationship between near-surface air temperature and satellite land surface temperatures using 17 years of data from the ATSR series. *Journal of Geophysical Research: Atmospheres*. **122**(17), pp.9185–9210.

Hansen, M.C., Potapov, P. V., Moore, R., Hancher, M., Turubanova, S.A., Tyukavina, A., Thau, D., Stehman, S. V., Goetz, S.J., Loveland, T.R., Kommareddy, A., Egorov, A., Chini, L., Justice, C.O. and Townshend, J.R.G. 2013. High-Resolution Global Maps of 21st-Century Forest Cover Change. *Science*. **342**(6160), pp.850–853.

Hardwick, S.R., Toumi, R., Pfeifer, M., Turner, E.C., Nilus, R. and Ewers, R.M. 2015. The relationship between leaf area index and microclimate in tropical forest and oil palm plantation: Forest disturbance drives changes in microclimate. *Agricultural and Forest Meteorology*. **201**, pp.187–195.

IPBRES 2019. *IPBES - Global assessment - Full report* [Online]. Available from: https://www.ipbes.net/global-assessment.

Jamaludin, J., De Alban, J.D.T., Carrasco, L.R. and Webb, E.L. 2022. Spatiotemporal analysis of deforestation patterns and drivers reveals emergent threats to tropical forest landscapes. *Environmental Research Letters*. **17**(5), pp.1–15.

Kalamandeen, M., Gloor, E., Mitchard, E., Quincey, D., Ziv, G., Spracklen, D., Spracklen, B., Adami, M., Aragaõ, L.E.O.C., Galbraith, D., Spracklen, B., Mitchard, E., Galbraith, D., Kalamandeen, M., Gloor, E., Aragão, L.E.O.C., Spracklen, D. and Ziv, G. 2018. Pervasive Rise of Small-scale Deforestation in Amazonia. *Scientific Reports*. **8**(1), pp.1–10.

Lawrence, D., Coe, M., Walker, W., Verchot, L. and Vandecar, K. 2022. The Unseen Effects of Deforestation: Biophysical Effects on Climate. *Frontiers in Forests and Global Change*. **5**, pp.1–13.

Lawrence, D. and Vandecar, K. 2015. Effects of tropical deforestation on climate and agriculture. *Nature Climate Change*. **5**(1), pp.27–36.

Li, Y., Zhao, M., Mildrexler, D.J., Motesharrei, S., Mu, Q., Kalnay, E., Zhao, F., Li, S. and Wang, K. 2016. Potential and actual impacts of deforestation and afforestation on land surface temperature. *Journal of Geophysical Research*. **121**(24), pp.14372–14386.

Li, Y., Zhao, M., Motesharrei, S., Mu, Q., Kalnay, E. and Li, S. 2015. Local cooling and warming effects of forests based on satellite observations. *Nature Communications*. **6**, pp.1–8.

Loarie, S.R., Lobell, D.B., Asner, G.P. and Field, C.B. 2011. Land-Cover and surface water change drive large albedo increases in south america. *Earth Interactions*. **15**(7), pp.1–16.

Marengo, J.A., Souza, C.M., Thonicke, K., Burton, C., Halladay, K., Betts, R.A., Alves, L.M. and Soares, W.R. 2018. Changes in Climate and Land Use Over the Amazon Region: Current and Future Variability and Trends. *Frontiers in Earth Science*. **6**(228), pp.1–21.

Masuda, Y.J., Garg, T., Anggraeni, I., Wolff, N.H., Ebi, K., Game, E.T., Krenz, J. and Spector, J.T. 2020. Heat exposure from tropical deforestation decreases cognitive performance of rural workers: An experimental study. *Environmental Research Letters*. **15**, pp.1–12.

McAlpine, C.A., Salazar, A., Seabrook, L., Dargusch, P., Johnson, A., Wilson, K., Syktus, J., Meijaard, E., Nordin, H. and Sheil, D. 2018. Forest loss and Borneo's climate. *Environmental Research Letters*. **13**(4), pp.1–10.

McKinnon, M.C., Cheng, S.H., Dupre, S., Edmond, J., Garside, R., Glew, L., Holland, M.B., Levine, E., Masuda, Y.J., Miller, D.C., Oliveira, I., Revenaz, J., Roe, D., Shamer, S., Wilkie, D., Wongbusarakum, S. and Woodhouse, E. 2016. What are the effects of nature conservation on human well-being? A systematic map of empirical evidence from developing countries. *Environmental Evidence*. **5**(1), pp.1–25.

McNicol, I.M., Ryan, C.M. and Mitchard, E.T.A. 2018. Carbon losses from deforestation and widespread degradation offset by extensive growth in African woodlands. *Nature Communications*. **9**(1), pp.1–11.

Meijaard, E., Brooks, T.M., Carlson, K.M., Slade, E.M., Garcia-Ulloa, J., Gaveau, D.L.A., Lee, J.S.H., Santika, T., Juffe-Bignoli, D., Struebig, M.J., Wich, S.A., Ancrenaz, M., Koh, L.P., Zamira, N., Abrams, J.F., Prins, H.H.T., Sendashonga, C.N., Murdiyarso, D., Furumo, P.R., Macfarlane, N., Hoffmann, R., Persio, M., Descals, A., Szantoi, Z. and Sheil, D. 2020. The environmental impacts of palm oil in context. *Nature Plants*. **6**(12), pp.1418–1426.

Met Office 2023. Iris: A powerful, format-agnostic, and community-driven Python package for analysing and visualising Earth science data. Available from: http://scitools.org.uk/.

Molinario, G., Hansen, M.C. and Potapov, P. V. 2015. Forest cover dynamics of shifting cultivation in the Democratic Republic of Congo: A remote sensing-based assessment for 2000-2010. *Environmental Research Letters*. **10**(9).

Monteith, J.L. 1965. Evaporation and Environment. *Symposia of the Society for Experimental Biology*. **19**, pp.205–234.

Montibeller, B., Kmoch, A., Virro, H., Mander, Ü. and Uuemaa, E. 2020. Increasing fragmentation of forest cover in Brazil's Legal Amazon from 2001 to 2017. *Scientific Reports*. **10**(1), pp.1–13.

Myneni, R., Knyazikhin, Y. and Park, T. 2021. MODIS/Terra Leaf Area Index/FPAR 8-Day L4 Global 500m SIN Grid V061 [Data set]. *NASA EOSDIS Land Processes DAAC*., https://doi.org/10.5067/MODIS/MOD15A2H.061.

Pendrill, F., Gardner, T.A., Meyfroidt, P., Persson, U.M., Adams, J., Azevedo, T., Lima, M.G.B., Baumann, M., Curtis, P.G., Sy, V. De, Garrett, R., Godar, J., Goldman, E.D., Hansen, M.C., Heilmayr, R., Herold, M., Kuemmerle, T., Lathuillière, M.J., Ribeiro, V., Tyukavina, A., Weisse, M.J. and West, C. 2022. Disentangling the numbers behind agriculture-driven tropical deforestation. *Science*. **377**(1168), pp.1–11.

Potapov, P., Hansen, M.C., Laestadius, L., Turubanova, S., Yaroshenko, A., Thies, C., Smith, W., Zhuravleva, I., Komarova, A., Minnemeyer, S. and Esipova, E. 2017. The last frontiers of wilderness: Tracking loss of intact forest landscapes from 2000 to 2013. *Science Advances*. **3**(1), pp.1–14.

Prevedello, J.A., Winck, G.R., Weber, M.M., Nichols, E. and Sinervo, B. 2019. Impacts of forestation and deforestation on local temperature across the globe. *PLoS ONE*. **14**(3), pp.1–18.

Robertson, E. 2019. The local biophysical response to land-use change in HADGEM2-ES. *Journal of Climate*. **32**(22), pp.7611–7627.

Rosa, I.M.D., Souza, C. and Ewers, R.M. 2012. Changes in Size of Deforested Patches in the Brazilian Amazon. *Conservation Biology*. **26**(5), pp.932–937.

Rudel, T.K. 2013. The national determinants of deforestation in sub-Saharan Africa. *Philosophical Transactions of the Royal Society B: Biological Sciences*. **368**(1625), pp.1–7.

Running, S., Mu, Q., Zhao, M. and Moreno, A. 2021. MODIS/Terra Net Evapotranspiration Gap-Filled 8-Day L4 Global 500m SIN Grid V061 [Data set]. *NASA EOSDIS Land Processes DAAC*., https://doi.org/10.5067/MODIS/MOD16A2GF.061.

Schaaf, C. and Wang, Z. 2021. MODIS/Terra+Aqua BRDF/Albedo Daily L3 Global - 500m V061 [Data set]. *NASA EOSDIS Land Processes DAAC*., https://doi.org/10.5067/MODIS/MCD43A3.061.

Schultz, N.M., Lawrence, P.J. and Lee, X. 2017. Global satellite data highlights the diurnal asymmetry of the surface temperature response to deforestation. *Journal of Geophysical Research: Biogeosciences*. **122**(4), pp.903–917.

Scott, C.E., Arnold, S.R., Monks, S.A., Asmi, A., Paasonen, P. and Spracklen, D. V. 2018. Substantial large-scale feedbacks between natural aerosols and climate. *Nature Geoscience*. **11**(1), pp.44–48.

Seymour, F. and Harris, N.L. 2019. Reducing tropical deforestation. *Science*. **365**(6455), pp.756–757.

Silva Dias, M.A.F., Rutledge, S., Kabat, P., Silva Dias, P.L., Nobre, C., Fisch, G., Dolman, A.J., Zipser, E., Garstang, M., Manzi, A.O., Fuentes, J.D., Rocha, H.R., Marengo, J., Plana-Fattori, A., Sá, L.D.A., Alvalá, R.C.S., Andrcae, M.O., Artaxo, P., Gielow, R. and Gatti, L. 2002. Cloud and rain processes in a biosphere-atmosphere interaction context in the Amazon Region. *Journal of Geophysical Research D: Atmospheres*. **107**(20), pp.1–18.

Silvério, D. V., Brando, P.M., Macedo, M.N., Beck, P.S.A., Bustamante, M. and Coe, M.T. 2015. Agricultural expansion dominates climate changes in southeastern Amazonia: The overlooked non-GHG forcing. *Environmental Research Letters*. **10**(10).

Smith, C., Baker, J.C.A. and Spracklen, D. V 2023. Tropical deforestation causes large reductions in observed precipitation. *Nature*. **615**, pp.270–275.

Spracklen, D. V., Arnold, S.R. and Taylor, C.M. 2012. Observations of increased tropical rainfall preceded by air passage over forests. *Nature*. **489**, pp.282–285.

Spracklen, D.V., Baker, J.C.A., Garcia-Carreras, L. and Marsham, J.H. 2018. The Effects of Tropical Vegetation on Rainfall. *Annual Review of Environment and Resources*. **43**(1), pp.193–218.

Tegegne, Y.T., Lindner, M., Fobissie, K. and Kanninen, M. 2016. Evolution of drivers of deforestation and forest degradation in the Congo Basin forests: Exploring possible policy options to address forest loss. *Land Use Policy*. **51**, pp.312–324.

Turubanova, S., Potapov, P. V., Tyukavina, A. and Hansen, M.C. 2018. Ongoing primary forest loss in Brazil, Democratic Republic of the Congo, and Indonesia. *Environmental Research Letters*. **13**, pp.1–15.

Virtanen, P., Gommers, R., Oliphant, T.E., Haberland, M., Reddy, T., Cournapeau, D., Burovski, E., Peterson, P., Weckesser, W., Bright, J., van der Walt, S.J., Brett, M., Wilson, J., Millman, K.J., Mayorov, N., Nelson, A.R.J., Jones, E., Kern, R., Larson, E., Carey, C.J., Polat, \.Ilhan, Feng, Y., Moore, E.W., VanderPlas, J., Laxalde, D., Perktold, J., Cimrman, R., Henriksen, I., Quintero, E.A., Harris, C.R., Archibald, A.M., Ribeiro, A.H., Pedregosa, F., van Mulbregt, P. and SciPy 1.0 Contributors 2020. {SciPy} 1.0: Fundamental Algorithms for Scientific Computing in Python. *Nature Methods*. **17**, pp.261–272.

Wan, Z., Hook, S. and Hulley, G. 2021a. MODIS/Aqua Land Surface Temperature/Emissivity 8-Day L3 Global 1km SIN Grid V061 [Data set]. *NASA EOSDIS Land Processes DAAC*., https://doi.org/10.5067/MODIS/MYD11A2.061.

Wan, Z., Hook, S. and Hulley, G. 2021b. MODIS/Terra Land Surface Temperature/Emissivity 8-Day L3 Global 1km SIN Grid V061 [Data set]. *NASA EOSDIS Land Processes DAAC*., https://doi.org/10.5067/MODIS/MOD11A2.061.

Winckler, Johannes, Lejeune, Q., Reick, C.H. and Pongratz, J. 2019. Nonlocal Effects Dominate the Global Mean Surface Temperature Response to the Biogeophysical Effects of Deforestation. *Geophysical Research Letters*. **46**(2), pp.745–755.

Winckler, J., Reick, C.H., Bright, R.M. and Pongratz, J. 2019. Importance of Surface Roughness for the Local Biogeophysical Effects of Deforestation. *Journal of Geophysical Research: Atmospheres*. **124**(15), pp.8605–8618.

Wolff, N.H., Masuda, Y.J., Meijaard, E., Wells, J.A. and Game, E.T. 2018. Impacts of tropical deforestation on local temperature and human well-being perceptions. *Global Environmental Change*. **52**(December 2017), pp.181–189.

Zeppetello, L.R.V., Luke's, L.A., Spector, J.T., Naylor, R.L., Battisti, D.S., Masuda, Y.J. and Wolff, N.H. 2020. Large scale tropical deforestation drives extreme warming. *Environmental Research Letters*. **15**(8).

Zhuang, J. 2022. xESMF. Available from: https://doi.org/10.5281/zenodo.1134365.

Chapter 4

4 Tropical deforestation causes large reductions in observed precipitation

C. Smith[1], J.C.A. Baker[1], D.V. Spracklen[1]

[1] School of Earth and Environment, University of Leeds, UK

Published in *Nature* **615** 270-275 (2023), 1st March 2023. Available at
https://doi.org/10.1038/s41586-022-05690-1

Abstract

Tropical forests play a critical role in the hydrological cycle and can influence local and regional precipitation (Lawrence and Vandecar, 2015). Prior work has assessed the impacts of tropical deforestation on precipitation, but these efforts have been largely limited to case studies (Spracklen et al., 2018). A wider analysis of interactions between deforestation and precipitation – and especially how any such interactions might vary across spatial scale – is lacking. Here we show reduced precipitation over deforested regions across the tropics. Our results arise from a pan-tropical assessment of the impacts of 2003-2017 forest loss on precipitation using satellite, station-based and reanalysis datasets. The effect of deforestation on precipitation increased at larger scales, with satellite datasets showing that forest loss caused robust reductions in precipitation at scales greater than 50 km. The greatest declines in precipitation occurred at 200 km, the largest scale we explored, where 1 percentage point of forest loss reduced precipitation by 0.25±0.1 mm month^{-1}. Reanalysis and station-based products disagree on the direction of precipitation responses to forest loss, which we attribute to sparse in-situ tropical measurements. We estimate that future deforestation in the Congo will reduce local precipitation by 8-10% in 2100. Our findings

provide a compelling argument for tropical forest conservation to support regional climate resilience.

4.1 Main

Tropical forests play an important role in moderating local, regional and global climate through their impact on energy, water and carbon cycles (Bonan, 2008). Crucially, tropical forests control local to regional rainfall patterns (Lawrence and Vandecar, 2015; Spracklen et al., 2018). Evapotranspiration from tropical forests is a strong driver of regional precipitation (Spracklen et al., 2012; Staal et al., 2018) contributing up to 41% of basin-mean rainfall over the Amazon and up to 50% over the Congo (Baker and Spracklen, 2022). Evergreen tropical forests are dependent on high annual rainfall for their survival and productivity (Guan et al., 2015) and forest-rainfall feedbacks have been highlighted as an important determinant of tropical forest stability (Spracklen et al., 2012; Staal et al., 2018; Staal, Fetzer, et al., 2020), amid concerns that the exacerbating impacts of droughts and deforestation could threaten their viability (Zemp et al., 2017).

Rapid loss of forests is occurring across the tropics (Hansen et al., 2013). Tropical deforestation warms the climate at local through global scales by changing the surface energy balance and through emissions of carbon dioxide (Bonan, 2008). The impact of tropical deforestation on precipitation is less certain with a range of processes operating at different scales. Small-scale deforestation over the southern Amazon has been shown to increase precipitation frequency (Chagnon and Bras, 2005; Khanna et al., 2017) due to thermally (Garcia-Carreras and Parker, 2011) and dynamically (Khanna et al., 2017) induced circulations. At larger scales, deforestation reduces precipitation recycling leading to a reduction in precipitation (Lawrence and Vandecar, 2015; Leite-Filho et al., 2021). Over Indonesia, deforestation has been linked to declining precipitation (McAlpine et al., 2018), and exacerbation of El Niño impacts (Chapman et al., 2020). Global and regional climate models predict annual precipitation declines of 8.1 ± 1.4% for large-scale Amazonian deforestation by 2050 (Spracklen and Garcia-Carreras, 2015), but an observational study of the impacts of tropical deforestation on precipitation across spatial scales is lacking.

Here we present the first pan-tropical assessment of the impact of forest loss on precipitation based on measurements. We use a satellite dataset of forest cover change over the period 2003 – 2017 to identify areas of forest loss, with a focus on evergreen broadleaf forests of the Amazon, Congo and Southeast Asia (Fig. 4.1). To provide a robust assessment of the impacts of deforestation on precipitation, we analysed 18 different precipitation datasets, including satellite (n=10), station-based (n=4) and reanalysis (n=4) products (Extended Data Table B.1). We compared the precipitation change over pixels experiencing forest loss with neighbouring pixels that had experienced less forest loss (see Methods). Comparing against neighbouring pixels that will have experienced similar climate change focuses our analysis on the changes due to forest loss. To explore the impact of forest loss across scales, we analysed the impacts of forest loss on coincident precipitation at a series of spatial resolutions ranging from roughly 5 km to 200 km (0.05°, 0.1°, 0.25°, 0.5°, 1.0° and 2.0°).

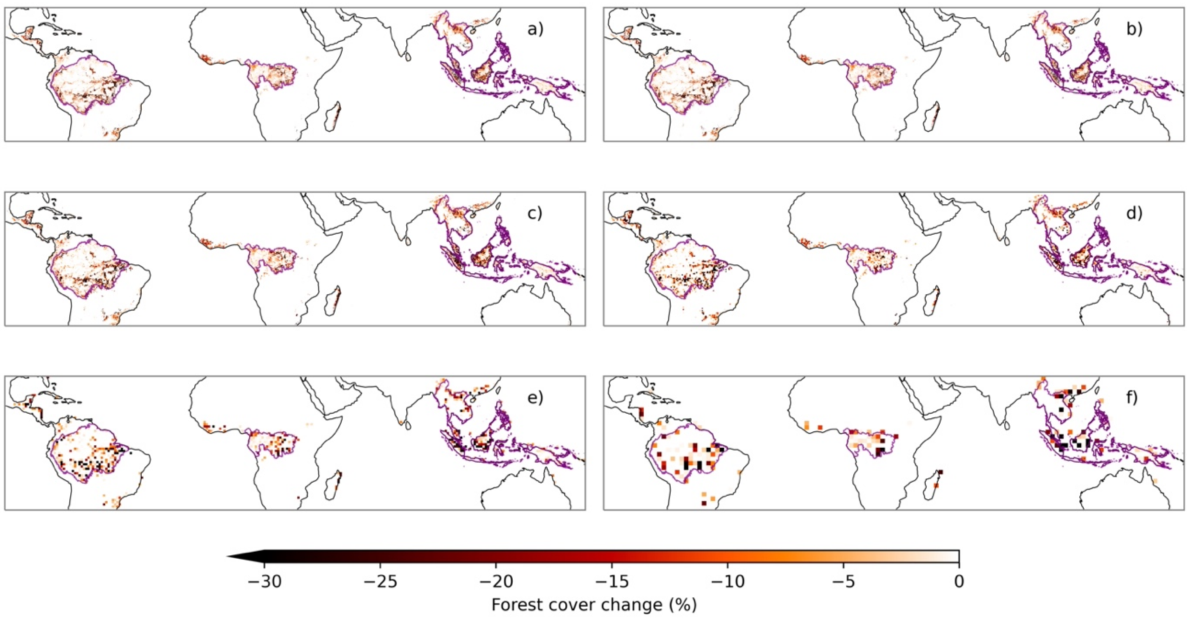

Figure 4.1. *Tropical evergreen broadleaf forest cover loss from 2003 to 2017. a) 0.05°, b) 0.1°, c) 0.25°, d) 0.5°, e) 1.0° and f) 2.0° resolution. The Amazon Basin, Congo Basin and Southeast Asia regions used in this study are outlined in purple. Map of the different regions made with Cartopy (Met Office, 2022) and Natural Earth. Forest loss data from (Hansen et al., 2013).*

4.1.1 Precipitation response to forest loss

Observed precipitation responses to tropical forest loss across multiple spatial scales and precipitation products are presented in Figure 4.2. Satellite-based precipitation datasets suggest that tropical forest loss causes statistically significant ($p<0.05$) declines in median annual-mean precipitation at all scales analysed. At larger scales (>0.5°), reductions exceed 0.03 mm month^{-1} for each percentage point loss of forest cover (Fig. 4.2d–f). The largest changes are observed at the 2.0° scale (approximately 220 km at the Equator) (Fig. 4.2f), where each percentage point reduction in forest cover causes 0.25 ± 0.1 mm month^{-1} reduction in annual precipitation.

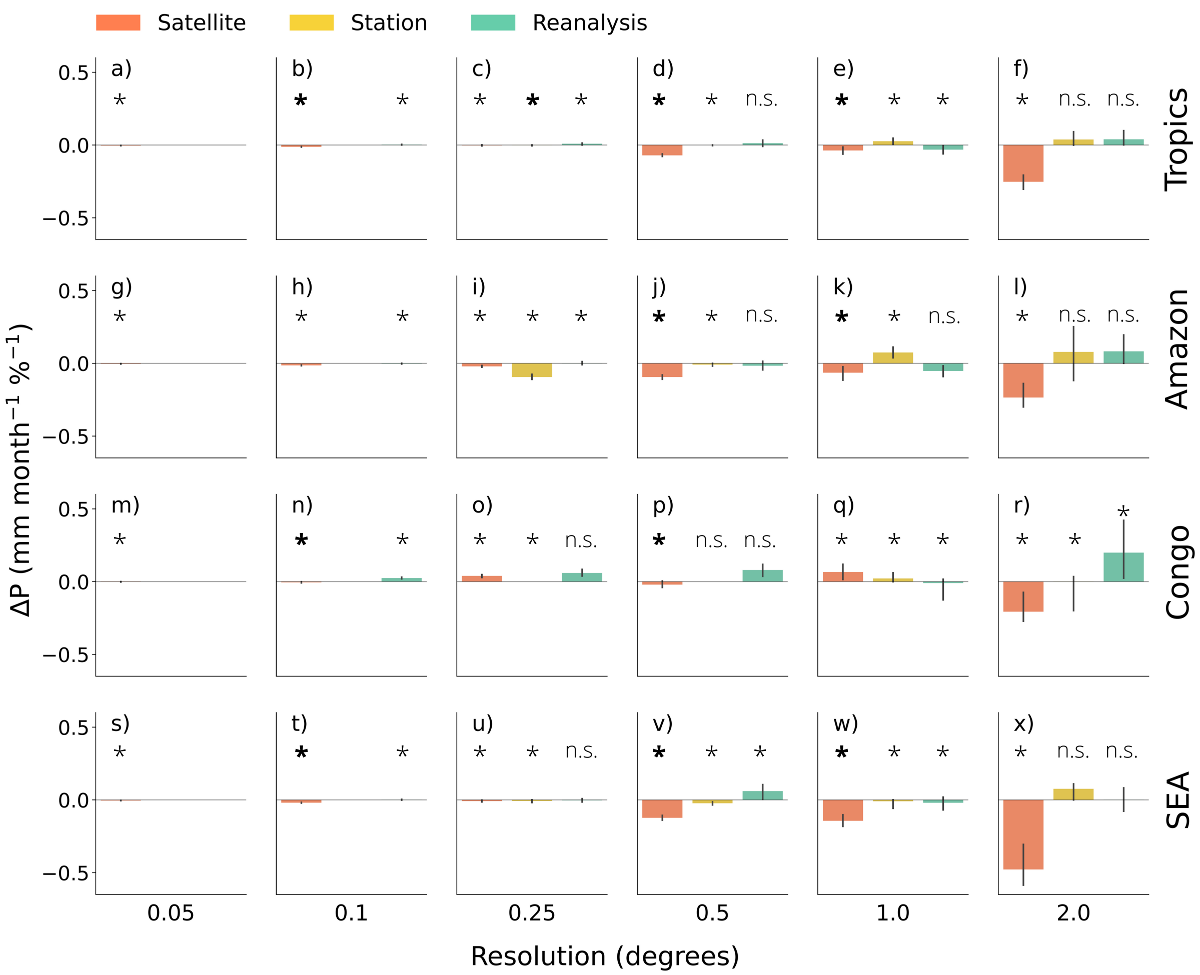

Figure 4.2. *Reductions in precipitation over regions of tropical forest loss. Bars indicate the median absolute change in annual precipitation (mm month^{-1}) per percentage point of forest loss over 2003 to 2017 in each region (Tropics (a-f), Amazon (g-l), Congo (m-r), Southeast Asia (SEA) (s-x)) for each precipitation dataset category (satellite, station, and reanalysis). Results are shown for forest loss scales of 0.05° (a, g, m, s), 0.1° (b, h, n ,t), 0.25° (c, i, o, u),*

0.5° (d, j, p ,v), 1.0° (e, k, q, w), 2.0° (f, l , r, x). Changes in mean precipitation (calculated as a multi-annual mean over 2003-2007 compared to 2013-2017) over deforested regions that are significantly (p<0.05) different from control regions are indicated by a '', bold '*' show changes that are significant at p<0.01, and non-significant results are denoted by 'n.s.'. Error bars show ± 1 standard error from the mean. Datasets used in this analysis detailed in Extended Data Table B.1.*

Analysis of precipitation change as a function of forest loss confirms larger reductions in precipitation for larger reductions in forest cover (Extended Data Fig. B.1), although with considerable variability, as seen in the modelled response (Jiang et al., 2021). At 2 degrees this analysis shows precipitation decreases with forest cover loss up to around 5%, thereafter there is an abatement in drying up to our maximum observed forest loss of around 35% (Extended Data Fig. B.1), highlighting the non-linearity of precipitation change due to forest loss. Linked to this, in Figure 4.2, the area represented by each percentage point change in forest loss is different at each resolution interval, with 1 percentage point equating to ~25 km^2 (approx. at equator) at 0.5 degrees or ~400 km^2 at 2 degrees. Scaling the precipitation change by area, we find that at 2 degrees, there is a 0.00063 mm $month^{-1}$ km^2 drying, whereas at 0.5 degrees, there is a drying of 0.0012 mm $month^{-1}$ km^2, or around twice the drying per unit area. Further to this, the area of a 2 degree cell (40,000 km^2) is 16 times greater than the area of a 0.5 degree cell (2500 km^2), meaning in absolute terms, there is 16 times more water being evaluated (40 Mm^3 vs 2.5 Mm^3). Hence, despite showing 2 degree cells have half the drying per unit area of 0.5 degree cells, in absolute terms, the reduction in precipitation is therefore 8 times greater in the 2 degree case.

Observed reductions in precipitation are consistent across satellite datasets, with all 10 satellite precipitation products agreeing on the sign of the rainfall response at 2° over the tropics (Extended Data Fig. B.2). At the 2° scale, significant (p<0.05) reductions in annual-mean precipitation with forest loss were observed across all tropical regions (Fig. 4.2). Reductions in precipitation at 2° based on satellite datasets ranged from 0.48 ± 0.36 mm $month^{-1}$ in SEA to 0.23 ± 0.12 mm $month^{-1}$ in the Amazon, and 0.21 ± 0.19 mm $month^{-1}$ in the Congo for each percentage point loss in forest cover, with at least 8 out of 10 satellite datasets agreeing on the sign of the response within each region (Extended Data Fig. B.2). In

SEA, it has been suggested that proximity to the ocean and the replacement of tropical forest with plantations as opposed to pasture or cropland may cause reduced sensitivity of precipitation to deforestation (Lawrence and Vandecar, 2015). Our analysis suggests that forest loss in SEA causes reductions in precipitation consistent with or greater than reductions in the Amazon and Congo.

Station-based datasets and reanalysis products exhibit contrasting annual-mean precipitation responses to deforestation at 2.0° (Fig. 4.2). Across the tropics, station-based and reanalysis datasets showed no statistically significant changes in annual-mean precipitation due to forest loss (Fig. 2f) and there was little agreement with satellite datasets at the regional scale (Fig. 4.2l,r,x), with some non-satellite precipitation products showing small increases in annual-mean precipitation due to forest loss. Sparse in-situ measurements across the tropics, particularly over regions of forest loss, mean that station-based datasets provide a weak constraint on precipitation changes. A comparison of station-based precipitation datasets revealed higher levels of uncertainty in the tropics, including the Amazon (Harris et al., 2020). In regions of sparse data such as tropical forests (Fassoni-Andrade et al., 2021), interpolation methods may mask precipitation changes driven by forest loss. Reanalysis products, which are numerical models constrained by empirical data, are also expected to be less reliable in regions where in-situ data are limited (Haiden et al., 2019). Our results suggest that precipitation data based on satellite remote-sensing measurements may have an advantage over tropical forest regions where in-situ measurements are sparse or unavailable. For these reasons, we focus our analysis on satellite-based datasets and identify where agreement between datasets exists.

Our results are robust (see Extended Data Fig. B.3) to a range of methodological assumptions including the length of analysis period, the choice of start and end period and the spatial extent of control pixels (See Methods). Our analysis period includes the 2015 - 2016 El Niño which resulted in negative precipitation anomalies over many tropical land regions (Supplementary Fig. B.1). We found the precipitation response to forest loss was robustly negative during both El Niño and non-El Niño years (Extended Data Fig. B.3). Over the Amazon and SEA, we see a stronger reduction in precipitation over regions of forest loss during El Niño years. The relative impact of El Niño on precipitation is smaller in the Congo (Esquivel-Muelbert et al., 2019) and correspondingly we do not see a stronger reduction here. A stronger precipitation response to forest loss in regions and periods impacted by El Niño is likely due to higher transpiration rates observed in tropical forests during El Niño years (Brum et al., 2018) and because rainfall is more sensitive to reductions in moisture recycling during drought years (Bagley et al., 2014; Staal et al., 2018). Climate change is expected to lead to increased droughts over many tropical regions (Wunderling et al., 2022), which may be further exacerbated by ongoing deforestation.

4.1.2 Seasonal precipitation reductions

Changes in precipitation due to forest loss during the dry, wet and transition seasons are nearly consistently negative (Fig. 4.3). For the tropics, absolute changes in precipitation with forest loss are greatest in the wet season (Fig. 4.3a, up to -0.6 mm $month^{-1}$ per percentage point forest loss) whereas relative changes of precipitation with forest loss are similar (-0.2 %/%) across dry, wet and transition seasons (Supplementary Fig. B.2).

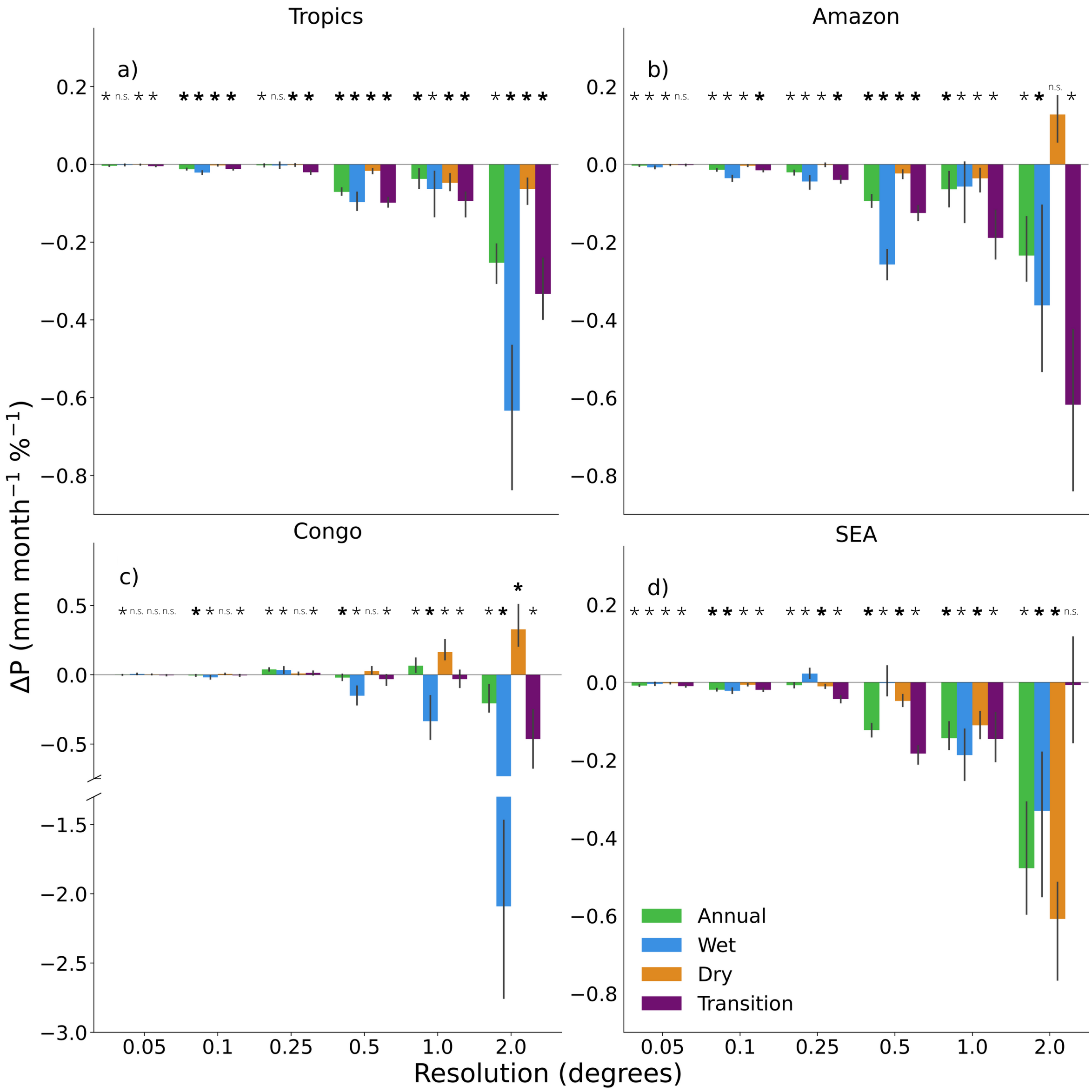

Figure 4.3. *Changes in seasonal precipitation due to forest loss. a) Tropics, b) Amazon, c) Congo, and d) Southeast Asia (SEA). Bars indicate the median change in precipitation per percentage point forest cover loss (mm month^{-1} %$^{-1}$) for satellite datasets during 2003 to 2017. Error bars indicate ± 1 standard error from the mean. Changes in mean precipitation over deforested regions significantly (p<0.05) different from controls are indicated by a '*', with '*****' showing changes significant at p<0.01, whereas non-significant results are denoted by 'n.s.'. Results are shown for the wettest 3 months (wet), the driest 3 months (dry) and the transition months (remaining 6 months). Datasets used in this analysis detailed in Extended Data Table B.1.*

In the Amazon, deforestation causes the largest reductions in precipitation during the transition season (Fig. 3b) as has been found previously (Fu and Li, 2004; Leite-Filho et al., 2019; Jiang et al., 2021).

Previous case studies have indicated that dry season precipitation can increase over deforestation in the Amazon (Negri et al., 2004; Chagnon et al., 2004; Chagnon and Bras, 2005). We observed a non-significant increase in dry season precipitation due to forest loss in the Amazon at 2° as well as increases in the Congo at 1° and 2° (Fig. 4.3). In SEA, forest loss causes reductions in dry season precipitation across all scales (Fig. 4.3d). The mechanism through which forest loss impacts precipitation is likely to change with both season and spatial scale. At the smallest scales (5 km) thermally driven impacts are likely to dominate, shifting to dynamically driven impacts through reductions to surface roughness, then to reductions in moisture fluxes and precipitation recycling at the largest scales (Khanna et al., 2017; Chambers and Artaxo, 2017). Our observations of greater reductions in precipitation due to deforestation at larger spatial scales is consistent with a reduction in moisture recycling emerging as the dominant mechanism (Lawrence and Vandecar, 2015).

4.1.3 Comparison with climate models

A meta-analysis of climate model studies (predominantly global models with > 2° resolution) found that forest loss in the Amazon resulted in a mean reduction in annual mean precipitation of 0.16±0.13%/% (Spracklen and Garcia-Carreras, 2015), overlapping with our value of 0.25%/% (Supplementary Fig. 4.2). Fewer simulations have been conducted for the Congo with models predicting a reduction in precipitation of 0.16±0.17%/% (Spracklen et al., 2018), similar to our reduction of 0.15%/% (Supplementary Fig. 4.2). The large range of model estimates highlights the substantial uncertainty in model predictions. Our observationally-derived analysis provides support for models that predict reductions in precipitation under regional deforestation at global climate model scales.

Our observational analysis documents for the first time the impacts of deforestation on precipitation across the tropics. Applying linear scaling to the reductions in precipitation observed in our analysis would suggest complete deforestation could result in reductions in annual precipitation of 10-20%. Previous estimates of the impact of complete deforestation on precipitation range from a 16% (Spracklen and Garcia-Carreras, 2015) to 55-70% (Baudena et al., 2021) reduction in the Amazon and an 18% (Spracklen et al., 2018) to 50% reduction (Duku and Hein, 2021) in the Congo.

4.1.4 Impacts of future deforestation

To further explore how future deforestation might modify precipitation we combined our observationally-derived estimates of precipitation responses to forest cover loss with future projections of land cover change from a high-deforestation scenario (see Methods). We estimate forest loss from 2015 to 2100 (Fig. 4.4a) could lead to reductions of annual mean precipitation of up to 16.5 ± 6.2 mm $month^{-1}$ in the Congo (Fig. 4.4b), equivalent to precipitation declines of 8-10%. Forest loss is projected to be greatest in the western and southern Congo (Fig. 4.4c), which will also experience the strongest reductions in precipitation (Fig. 4.4d).

The sensitivity of precipitation to the extent of forest loss is an uncertainty in our analysis, a result of the relatively short observational record, compounded by large spatial and temporal variability in precipitation. The response of precipitation to forest loss greater than 30%, a threshold beyond which large reductions in precipitation have been postulated (Lawrence and Vandecar, 2015), is one such uncertainty. Restricting our analysis to the 0-30% forest loss that are well sampled in our observational dataset (Supplementary Fig. B.3), through capping the impacts of greater forest loss at that of 30%, results in projected annual mean precipitation reductions of 6.5 ± 2.6 mm $month^{-1}$ in the Congo and 6.2 ± 2.5 mm $month^{-1}$ in SEA (Supplementary Fig. B.4). However, restricting our analysis in this way is likely to underestimate the precipitation impacts over regions projected to experience the most extensive deforestation, including the Congo where mean forest cover is projected to decline by 40 percentage points between 2015 and 2100 (Fig. 4.4a).

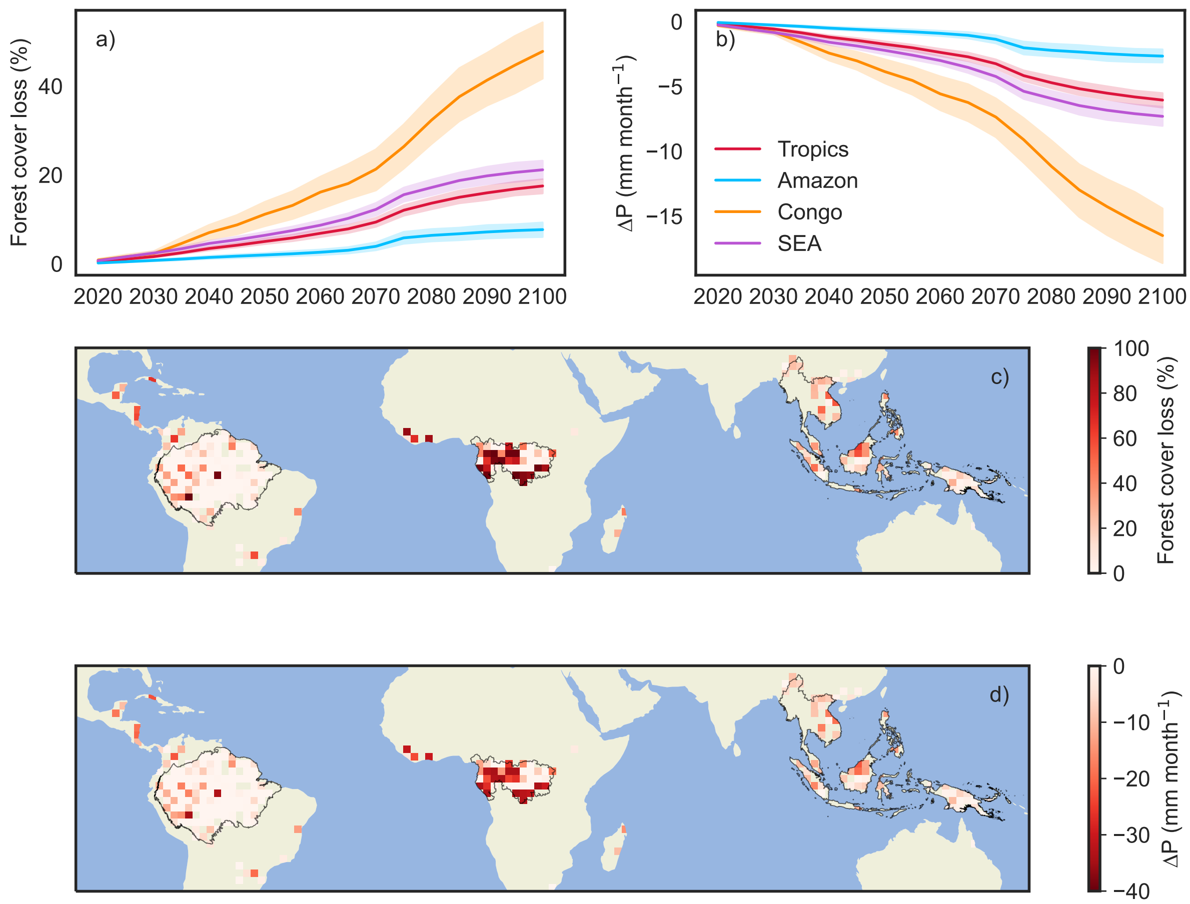

Figure 4.4. *Impact of projected future forest loss on annual mean precipitation. a) Mean forest cover loss over 2015 – 2100 under SSP3-4.5 for the tropics, Amazon, Congo and Southeast Asia (SEA); b) impact of projected forest cover loss on precipitation (P) (± 1 standard error from the mean); c) spatial pattern of forest cover loss and; d) predicted P change (ΔP) in 2100 due to forest cover loss. Results are shown for 2.0° resolution. Maps of the different regions generated using Cartopy (Met Office, 2022) and Natural Earth.*

Previous studies have identified both linear (Akkermans et al., 2014; Zemp et al., 2017) and non-linear (Lawrence and Vandecar, 2015; Baudena et al., 2021) responses of precipitation to forest loss. Such non-linear interactions and feedbacks have the potential to further amplify or moderate the responses predicted here (Staal, Flores, et al., 2020; Leite-Filho et al., 2021). Our analysis shows large reductions in precipitation for relatively small amounts of forest loss and evidence for reduced sensitivity of precipitation to additional amounts of forest loss (Extended Data Fig. B.1). Assuming a non-linear relationship between forest loss and precipitation (see Methods) reduces our projected reductions in precipitation by around factor 2 (Supp. Fig. B.5). Our observationally-based approach will miss tipping points in the climate system that might be reached as deforestation extent progresses further (Lawrence and Vandecar, 2015). Such tipping points have been postulated for the Amazon under future global change (Wunderling et al., 2022; Xu et al., 2022). Thus, the substantial declines in precipitation projected in our analysis should be viewed as a conservative estimate of the potential precipitation response to future deforestation. Nevertheless, our analysis suggests deforestation can drive local and regional precipitation changes that may match or exceed those predicted due to climate change over the same period (Kooperman et al., 2018; Z. Chen et al., 2020).

4.1.5 Implications of precipitation reductions

Reductions in precipitation induced by forest loss have important implications for society and the sustainability of remaining tropical forest. Deforestation-induced reductions in precipitation impact agriculture (Lawrence and Vandecar, 2015; Leite-Filho et al., 2021) and hydropower generation (Stickler et al., 2013). On average, crop yields decline by 0.5% for each percentage point reduction in precipitation (Challinor et al., 2014). Our results suggest that forest-loss induced changes to annual precipitation (Supp. Fig. B.2) could cause crop yields to decline by 1.25% for each 10-percentage point loss of forest cover, potentially exacerbating the impacts of climate change and future drought events. The maintenance of regional rainfall patterns due to forests in the Amazon has been valued at up to US$9 ha^{-1} yr^{-1} and US$1.84 ha^{-1} yr^{-1} though sustaining agricultural yields and hydropower generation, respectively (Strand et al., 2018). Global cropland area increased by 9% in the past two decades, with even higher increases in South America and tropical Africa (Potapov et al., 2022) largely at the expense of natural ecosystems. Further agricultural expansion in tropical forest regions may lead to overall reductions in production if declines in yield due to deforestation-induced reductions in rainfall outweigh increased production from expanded agricultural area (Leite-Filho et al., 2021).

Furthermore, reductions in rainfall over remaining areas of tropical forest are expected to lead to additional forest loss (Zemp et al., 2017) as well as impacting species composition (Esquivel-Muelbert et al., 2019), carbon sequestration (Li et al., 2022) and fire frequency (Aragão et al., 2008). Reductions in dry season precipitation pose a particular threat to forest viability by exacerbating seasonal droughts and potentially delaying the onset of the wet season and extending the length of the dry season. Increases in dry-season length over recent decades have previously been reported for the Amazon (Marengo et al., 2018), and the Congo (Jiang et al., 2019) possibly linked to land cover changes (Leite-Filho et al., 2019).

Deforestation may also shift precipitation patterns, increasing dry season rainfall immediately downwind of forest loss and decreasing rainfall in upwind areas (Khanna et al., 2017). Our approach is restricted to observing deforestation impacts up to scales of 200 km (see Methods). At larger scales, insufficient pixels experienced forest loss during the relatively short period of satellite observations for a robust analysis. Deforestation is also likely to alter precipitation at these larger scales through reducing moisture recycling leading to reductions in rainfall downwind of forest loss (Spracklen et al., 2012; Zemp et al., 2017; Staal et al., 2018; Xu et al., 2022). The length scale of moisture recycling has been estimated at 500 – 2,000 km in the tropics (Van Der Ent and Savenije, 2011) with a median value of 600 km in the Amazon (Staal et al., 2018). In regions downwind of extensive forests, such as the southwestern Amazon, up to 70% of precipitation could be sourced from upwind evapotranspiration (van der Ent et al., 2010; Sorí et al., 2017). Tropical forest loss could therefore have severe implications for precipitation in these regions that are 100s to 1,000s of km downwind of the forest loss (Staal et al., 2018). Through missing the impacts at these larger scales, our analysis is likely to underestimate the full impacts of deforestation on rainfall.

Our results highlight the importance of remaining tropical forests for sustaining regional precipitation. Despite efforts to reduce deforestation, rates of tropical forest loss have accelerated over the last two decades (Feng et al., 2022). Renewed efforts are needed to ensure recent commitments to reduce deforestation, including the New York Declaration on Forests and The Glasgow Leaders' Declaration on Forests and Land Use made at COP26, are successful. Global efforts to restore large areas of degraded and deforested land could enhance precipitation (Tuinenburg et al., 2022), reversing some of the reductions in precipitation due to forest loss observed here.

4.2 Methods

Datasets

We used 18 precipitation datasets, listed in Extended Data Table B.1. All datasets were downloaded at the highest available spatial resolution, which for some datasets was 0.04°, or approximately 4 km at the Equator. Data were obtained as monthly means or converted to monthly mean using the python package Xarray (Hoyer and Hamman, 2017). We categorised precipitation datasets as 'Satellite' (n=10), 'Station' (n=4) and 'Reanalysis' (n=4). Satellite datasets are those based primarily on data from satellite sensors and include datasets which have both satellite and station-based data (i.e., merged datasets). Station datasets only include ground-based information from weather stations and rain gauges. Reanalysis products are models constrained by surface and satellite data. Precipitation datasets have been compared previously over the Amazon (Fassoni-Andrade et al., 2021) highlighting the limited station data over tropical forest regions. Time series of precipitation (Supp. Fig. B.1) reveal variability across the different datasets highlighting the need to analyse impacts of deforestation across multiple datasets.

To analyse the changes in forest canopy cover, we used data from the Global Forest Change (GFC) version 1.9 (Hansen et al., 2013). GFC v1.9 provides forest canopy cover in the year 2000 and subsequent annual forest loss from 2001 – 2020 at 30 m resolution. We analysed forest cover and precipitation changes over the period 2003 to 2017, which was the period common to all datasets.

Analysis across multiple spatial scales

We analysed the impacts of forest loss across a range of scales (0.05°, 0.1°, 0.25°, 0.5°, 1.0°, and 2.0°). Each precipitation dataset was analysed at its native resolution and at all lower resolutions across this range of scales. Spatial regridding was performed using the Python package xESMF (Zhuang, 2022) with a bilinear re-gridding scheme. Two alternative regridding methods (xESMF: 'conservative-normalised' and iris: 'area weighted') were tested and had little impact on our results. For GFC data, we calculated forest loss using the original 30 m data and converted to each of the six spatial resolutions analysed by taking the sum of all 30 m pixels within each larger pixel. Change in canopy cover from 2003 to 2017 at each resolution is shown in Fig. 4.1.

Assessing impact of historical deforestation on precipitation

We used a moving-window nearest neighbour approach (Baker and Spracklen, 2019) to compare the forest loss and precipitation change of each pixel with that of its immediate neighbours. We tested the sensitivity of the analysis to the size of the moving window and found similar results for 3x3 and 5x5 (Extended Data Fig. B.2) moving windows. Results from the 3x3 moving window approach can been seen in the main paper. We calculated the forest loss of each deforested pixel relative to neighbouring control pixels as the forest loss of the deforested pixel minus forest loss of the control. We constrained our analysis to the tropical evergreen broadleaf biome using the MODIS land cover dataset (Schaaf and Wang, 2015). To be included in the analysis, deforested pixels must have experienced 0.1% more forest loss over time than their neighbouring control pixels. The number of deforested pixels analysed varied between analysis resolutions as follows: 0.05°, n=243,254; 0.1°, n=58,660; 0.25°, n=9,604; 0.5°, n=2,303; 1.0°, n=586; 2.0°, n=123. We observed similar distributions of canopy change for all spatial resolutions analysed (Supp. Fig. B.6).

We calculated the precipitation change of the deforested pixel relative to the precipitation change of the control pixel (ΔP) as the precipitation change of the deforested pixel over the analysis period (e.g., 2003 to 2017) minus the precipitation change over the control pixel. To reduce the impact of interannual variability in precipitation on our results, we calculated 5-year means for periods at the start (2003 – 2007) and end (2013 – 2017) (Extended Data Fig. B.5) of the analysis period. We then calculated the change in precipitation as the difference between the start and end of these multi-year means. We report precipitation changes (ΔP) as a function of forest loss by dividing by the difference in forest loss between deforestation and control pixels (units of mm month^{-1} %$^{-1}$). We also report precipitation change as the percentage change in precipitation (ΔP/P, units %) as a function of forest loss (units %/%).

To ensure that control pixels and deforested pixels experience a similar background climate we conducted a sensitivity test where we restricted our analysis to pixels where the pre-deforestation precipitation across the control and deforested pixels differed by less than 10%. Restricting our analysis in this way had little impact on our results (Supp. Fig. B.7) showing that our nearest neighbour approach is effective even at the largest scales analysed here.

To explore the role of the analysis period on our results we compared the results for 5-year means to shorter 3-year means (2003-2007 compared to 2015-2017) and found consistent results (Extended Data Fig. B.3). Our analysis period includes the strong 2015/2016 El Niño which resulted in reductions in precipitation over most tropical land regions, particularly in 2015 (Supp. Fig. B.1). To explore the potential impacts of the 2015/16 El Niño on our analysis we estimated the impact of forest loss on precipitation using 3-year (2003-2005 vs. 2018-2020) and 5-year (2003-2007 vs. 2016-2020) multi-annual means spanning an extended time period. The 3-year analysis completely excludes the 2015/2016 ENSO, whilst the 5-year analysis excludes 2015, which was the driest year (Extended Data Fig. B.3). Two datasets (TRMM and UDEL) were not available after 2017 so were removed from this sensitivity analysis.

Statistical Analysis

For each category of precipitation data (satellite, station and reanalysis), precipitation change values were grouped together for all deforestation pixels and all control pixels. We found that precipitation changes for deforested pixels and control pixels, and the difference in precipitation change between deforested and control pixels (Extended Data Fig. B.4) were normally distributed. Error bars (Fig. 4.2 and 4.3) show ± 1 standard error from the mean calculated and displayed using the python package Seaborn (Waskom, 2021). To test whether mean precipitation changes over regions of deforestation were statistically different from changes over the control areas we used a Student's t-test. We also used the Mann-Whitney test to test for significant differences between median precipitation change between control and deforested pixels and found similar results.

Seasonal Analysis

For the satellite datasets only, in addition to calculating precipitation changes at the annual timescale, we calculated changes for the dry season (driest 3 months of each year), wet season (wettest 3 months of each year) and transition season (remaining 6 months). The driest, wettest and transition months were identified for each pixel using each individual precipitation dataset. For each season and dataset, we calculated the median change in precipitation across all the pixels within the region of interest (see Supp. Fig. B.8-B.10).

Predicting future precipitation change due to forest loss

We used projections of forest cover change available at 0.05° from the Global Change Analysis Model (GCAM) for 2015 to 2100 based on the Shared Socioeconomic Pathway (SSP) - Representative Concentration Pathway (RCP) scenario SSP3 RCP4.5, which represents a high-deforestation future (M. Chen et al., 2020). GCAM includes the impacts of climate and land use on future forest cover. We summed forest cover from all forest categories and calculated forest cover loss in each year compared to a 2015 baseline. Forest cover loss data were regridded to 2°. We estimated the impact of forest loss on future precipitation at the 2° scale through multiplying the projected percentage point forest loss for each pixel (%) by the observed median change in precipitation per percentage point forest cover loss (mm month^{-1} %$^{-1}$) across the satellite datasets. To estimate the uncertainty in our predictions we applied an upper and lower limit on the sensitivity of precipitation to forest loss based on the median value ± 1 standard error from the mean (see error bars in Fig. 4.2) and rescale by forest loss. This provides a range of estimated precipitation impacts of future forest loss. We also tested the impact on our results of capping future forest loss in each pixel at 30%, which is the upper range of forest loss that is well sampled in the observations (Supp. Fig. B.3). For each region, we applied the tropical satellite precipitation response to forest loss (Fig. 4.2f), meaning our projected regional precipitation changes are a product of the regional canopy cover change and the median tropical precipitation response. Our approach assumes a linear precipitation response to forest loss, which recent work suggests could provide a conservative estimate of deforestation impacts (Baudena et al., 2021). We tested the sensitivity of assuming a linear response of precipitation to canopy cover loss. We fitted a non-linear function to the data presented in Extended Data Fig. B.1 through applying the median sensitivity of precipitation to forest cover loss (mm $month^{-1}$ $\%^{-1}$) within each forest cover loss bin. We then scaled by the projected forest cover loss. This approach reduces the projected reduction in precipitation to 2.4 mm $month^{-1}$ in SEA and 1.5 mm $month^{-1}$ in the Congo (Supp. Fig B.5).

Data Availability Statement

The data used to make the figures in the study are available via the source data links. Full results for all tested resolutions and the code used in this analysis are also available via https://doi.org/10.5281/zenodo.7373832. The original datasets are freely available to download from the following repositories: CHIRPS from

https://data.chc.ucsb.edu/products/?C=M;O=D, CMORPH from https://ftp.cpc.ncep.noaa.gov/precip/CMORPH_RT/GLOBE/data/, CPC from https://psl.noaa.gov/data/gridded/data.cpc.globalprecip.html, CRU from

https://crudata.uea.ac.uk/cru/data/hrg/, ERA5 from https://cds.climate.copernicus.eu/cdsapp#!/dataset/reanalysis-era5-single-levels?tab=overview, GPCC from https://opendata.dwd.de/climate_environment/GPCC/html/download_gate.html, GPCP from https://disc.gsfc.nasa.gov/datasets/GPCPMON_3.1/summary?keywords=GPCPMON, GPM from https://gpm1.gesdisc.eosdis.nasa.gov/data/GPM_L3/, JRA from https://climatedataguide.ucar.edu/climate-data/jra-55

https://jra.kishou.go.jp/JRA-55/index_en.html, MERRA-2 from https://disc.gsfc.nasa.gov/datasets?project=MERRA-2, NOAA (PREC/LAND) from

https://psl.noaa.gov/data/gridded/data.precl.html, PERSIANN (CCS, CDR, CCS-CDR, PDIR-NOW) from https://chrsdata.eng.uci.edu/, TRMM from https://disc.gsfc.nasa.gov/datasets/TRMM_3B43_7/summary, UDEL from https://psl.noaa.gov/data/gridded/data.UDel_AirT_Precip.html. Lastly, the GCAM model output used in this study is available from https://doi.org/10.25584/data.2020-07.1357/1644253

Acknowledgements

The research has been supported by funding from the European Research Council (ERC) under the European Union's Horizon 2020 research and innovation programme (DECAF project, Grant agreement no. 771492), and the Newton Fund, through the Met Office Climate Science for Service Partnership Brazil (CSSP Brazil). All observational datasets used in this study (listed in E.D. Table B.1) are publicly available and are cited in the Data Availability Statement.

References

Akkermans, T., Thiery, W. and Van Lipzig, N.P.M. 2014. The regional climate impact of a realistic future deforestation scenario in the congo basin. *Journal of Climate*. **27**(7), pp.2714–2734.

Aragão, L.E.O.C., Malhi, Y., Barbier, N., Lima, A., Shimabukuro, Y., Anderson, L. and Saatchi, S. 2008. Interactions between rainfall, deforestation and fires during recent years in the Brazilian Amazonia. *Philosophical Transactions of the Royal Society B: Biological Sciences*. **363**(1498), pp.1779–1785.

Bagley, J.E., Desai, A.R., Harding, K.J., Snyder, P.K. and Foley, J.A. 2014. Drought and deforestation: Has land cover change influenced recent precipitation extremes in the Amazon? *Journal of Climate*. **27**(1), pp.345–361.

Baker, J.C.A. and Spracklen, D. V 2019. Climate Benefits of Intact Amazon Forests and the Biophysical Consequences of Disturbance. *Frontiers in Forests and Global Change*. **2**, pp.1–13.

Baker, J.C.A. and Spracklen, D. V. 2022. Divergent Representation of Precipitation Recycling in the Amazon and the Congo in CMIP6 Models. *Geophysical Research Letters*. **49**(10), pp.1–11.

Baudena, M., Tuinenburg, O.A., Ferdinand, P.A. and Staal, A. 2021. Effects of land-use change in the Amazon on precipitation are likely underestimated. *Global Change Biology*. **27**(21), pp.5580–5587.

Bonan, G.B. 2008. Forests and climate change: Forcings, feedbacks, and the climate benefits of forests. *Science*. **320**(5882), pp.1444–1449.

Brum, M., López, J.G., Asbjornsen, H., Licata, J., Pypker, T., Sanchez, G. and Oiveira, R.S. 2018. ENSO effects on the transpiration of eastern Amazon trees. *Philosophical Transactions of the Royal Society B: Biological Sciences*. **373**(1760).

Chagnon, F.J.F. and Bras, R.L. 2005. Contemporary climate change in the Amazon. *Geophysical Research Letters*. **32**(13), pp.1–4.

Chagnon, F.J.F., Bras, R.L. and Wang, J. 2004. Climatic shift in patterns of shallow clouds over the Amazon. *Geophysical Research Letters*. **31**(24), pp.1–4.

Challinor, A.J., Watson, J., Lobell, D.B., Howden, S.M., Smith, D.R. and Chhetri, N. 2014. A meta-analysis of crop yield under climate change and adaptation. *Nature Climate Change*. **4**(4), pp.287–291.

Chambers, J.Q. and Artaxo, P. 2017. Biosphere-atmosphere interactions: Deforestation size influences rainfall. *Nature Climate Change*. **7**(3), pp.175–176.

Chapman, S., Syktus, J.I., Trancoso, R., Salazar, A., Thatcher, M.J., Watson, J.E., Meijaard, E., Sheil, D., Dargusch, P. and McAlpine, C.A. 2020. Compounding impact of deforestation on Borneo's climate during El Niño events. *Environmental Research Letters*. **15**(8).

Chen, M., Vernon, C.R., Graham, N.T., Hejazi, M., Huang, M., Cheng, Y. and Calvin, K. 2020. Global land use for 2015–2100 at 0.05° resolution under diverse socioeconomic and climate scenarios. *Scientific Data*. **7**(1), pp.1–11.

Chen, Z., Zhou, T., Zhang, L., Chen, X., Zhang, W. and Jiang, J. 2020. Global Land Monsoon Precipitation Changes in CMIP6 Projections. *Geophysical Research Letters*. **47**(14).

Duku, C. and Hein, L. 2021. The impact of deforestation on rainfall in Africa: A data-driven assessment. *Environmental Research Letters*. **16**(6).

Van Der Ent, R.J. and Savenije, H.H.G. 2011. Length and time scales of atmospheric moisture recycling. *Atmospheric Chemistry and Physics*. **11**(5), pp.1853–1863.

van der Ent, R.J., Savenije, H.H.G., Schaefli, B. and Steele-Dunne, S.C. 2010. Origin and fate of atmospheric moisture over continents. *Water Resources Research*. **46**(9), pp.1–12.

Esquivel-Muelbert, A., Baker, T.R., Dexter, K.G., Lewis, S.L., Brienen, R.J.W., Feldpausch, T.R., Lloyd, J., Monteagudo-Mendoza, A., Arroyo, L., Álvarez-Dávila, E., Higuchi, N., Marimon, B.S., Marimon-Junior, B.H., Silveira, M., Vilanova, E., Gloor, E., Malhi, Y., Chave, J., Barlow, J., Bonal, D., Davila Cardozo, N., Erwin, T., Fauset, S., Hérault, B., Laurance, S., Poorter, L., Qie, L., Stahl, C., Sullivan, M.J.P., ter Steege, H., Vos, V.A., Zuidema, P.A., Almeida, E., Almeida de Oliveira, E., Andrade, A., Vieira, S.A., Aragão, L., Araujo-Murakami, A., Arets, E., Aymard C, G.A., Baraloto, C., Camargo, P.B., Barroso, J.G., Bongers, F., Boot, R., Camargo, J.L., Castro, W., Chama Moscoso, V., Comiskey, J., Cornejo Valverde, F., Lola da Costa, A.C., del Aguila Pasquel, J., Di Fiore, A., Fernanda Duque, L., Elias, F., Engel, J., Flores Llampazo, G., Galbraith, D., Herrera Fernández, R., Honorio Coronado, E., Hubau, W., Jimenez-Rojas, E., Lima, A.J.N., Umetsu, R.K., Laurance, W., Lopez-Gonzalez, G., Lovejoy, T., Aurelio Melo Cruz, O., Morandi, P.S., Neill, D., Núñez Vargas, P., Pallqui Camacho, N.C., Parada Gutierrez, A., Pardo, G., Peacock, J., Peña-Claros, M., Peñuela-Mora, M.C., Petronelli, P., Pickavance, G.C., Pitman, N., Prieto, A., Quesada, C., Ramírez-Angulo, H., Réjou-Méchain, M., Restrepo Correa, Z., Roopsind, A., Rudas, A., Salomão, R., Silva, N., Silva Espejo, J., Singh, J., Stropp, J., Terborgh, J., Thomas, R., Toledo, M., Torres-Lezama, A., Valenzuela Gamarra, L., van de Meer, P.J., van der Heijden, G., van der Hout, P., Vasquez Martinez, R., Vela, C., Vieira, I.C.G. and Phillips, O.L. 2019. Compositional response of Amazon forests to climate change. *Global Change Biology*. **25**(1), pp.39–56.

Fassoni-Andrade, A.C., Fleischmann, A.S., Papa, F., Paiva, R.C.D. de, Wongchuig, S., Melack, J.M., Moreira, A.A., Paris, A., Ruhoff, A., Barbosa, C., Maciel, D.A., Novo, E., Durand, F., Frappart, F., Aires, F., Abrahão, G.M., Ferreira-Ferreira, J., Espinoza, J.C., Laipelt, L., Costa, M.H., Espinoza-Villar, R., Calmant, S. and Pellet, V. 2021. Amazon Hydrology From Space: Scientific Advances and Future Challenges. *Reviews of Geophysics*. **59**(4), pp.1–97.

Feng, Y., Zeng, Z., Searchinger, T.D., Ziegler, A.D., Wu, J., Wang, D., He, X., Elsen, P.R., Ciais, P., Xu, R., Guo, Z., Peng, L., Tao, Y., Spracklen, D. V., Holden, J., Liu, X., Zheng, Y., Xu, P., Chen, J., Jiang, X., Song, X.-P., Lakshmi, V., Wood, E.F. and Zheng, C. 2022. Doubling of annual forest carbon loss over the tropics during the early twenty-first century. *Nature Sustainability*. **4**(4), pp.441–451.

Fu, R. and Li, W. 2004. The influence of the land surface on the transition from dry to wet season in Amazonia. *Theoretical and Applied Climatology*. **78**(1–3), pp.97–110.

Garcia-Carreras, L. and Parker, D.J. 2011. How does local tropical deforestation affect rainfall? *Geophysical Research Letters*. **38**(19), pp.1–6.

Guan, K., Pan, M., Li, H., Wolf, A., Wu, J., Medvigy, D., Caylor, K.K., Sheffield, J., Wood, E.F., Malhi, Y., Liang, M., Kimball, J.S., Saleska, S.R., Berry, J., Joiner, J. and Lyapustin, A.I. 2015. Photosynthetic seasonality of global tropical forests constrained by hydroclimate. *Nature Geoscience*. **8**(4), pp.284–289.

Haiden, T., Janousek, M., Vitart, F., Ferranti, L. and Prates, F. 2019. Evaluation of ECMWF forecasts, including the 2019 upgrade. *ECMWF Technical Memoranda*. **853**(October), pp.1–54.

Hansen, M.C., Potapov, P. V., Moore, R., Hancher, M., Turubanova, S.A., Tyukavina, A., Thau, D., Stehman, S. V., Goetz, S.J., Loveland, T.R., Kommareddy, A., Egorov, A., Chini, L., Justice, C.O. and Townshend, J.R.G. 2013. High-Resolution Global Maps of 21st-Century Forest Cover Change. *Science*. **850**(November), pp.850–854.

Harris, I., Osborn, T.J., Jones, P. and Lister, D. 2020. Version 4 of the CRU TS monthly high-resolution gridded multivariate climate dataset. *Scientific Data*. **7**(1), pp.1–18.

Hoyer, S. and Hamman, J. 2017. xarray: N-D labeled Arrays and Datasets in Python. *Journal of Open Research Software*. **5**(1), p.10.

Jiang, Y., Wang, G., Liu, W., Erfanian, A., Peng, Q. and Fu, R. 2021. Modeled response of south american climate to three decades of deforestation. *Journal of Climate*. **34**(6), pp.2189–2203.

Jiang, Y., Zhou, L., Tucker, C.J., Raghavendra, A., Hua, W., Liu, Y.Y. and Joiner, J. 2019. Widespread increase of boreal summer dry season length over the Congo rainforest. *Nature Climate Change*., pp.1–8.

Khanna, J., Medvigy, D., Fueglistaler, S. and Walko, R. 2017. Regional dry-season climate changes due to three decades of Amazonian deforestation. *Nature Climate Change*. **7**(3), pp.200–204.

Kooperman, G.J., Chen, Y., Hoffman, F.M., Koven, C.D., Lindsay, K., Pritchard, M.S., Swann, A.L.S. and Randerson, J.T. 2018. Forest response to rising CO2 drives zonally asymmetric rainfall change over tropical land. *Nature Climate Change*. **8**(5), pp.434–440.

Lawrence, D. and Vandecar, K. 2015. Effects of tropical deforestation on climate and agriculture. *Nature Climate Change*. **5**(1), pp.27–36.

Leite-Filho, A.T., Soares-Filho, B.S., Davis, J.L., Abrahão, G.M. and Börner, J. 2021. Deforestation reduces rainfall and agricultural revenues in the Brazilian Amazon. *Nature Communications*. **12**(1), pp.1–7.

Leite-Filho, A.T., de Sousa Pontes, V.Y. and Costa, M.H. 2019. Effects of Deforestation on the Onset of the Rainy Season and the Duration of Dry Spells in Southern Amazonia. *Journal of Geophysical Research: Atmospheres*. **124**(10), pp.5268–5281.

Li, Y., Brando, P.M., Morton, D.C., Lawrence, D.M., Yang, H. and Randerson, J.T. 2022. Deforestation-induced climate change reduces carbon storage in remaining tropical forests. *Nature Communications*. **13**(1), pp.1–13.

Marengo, J.A., Souza, C.M., Thonicke, K., Burton, C., Halladay, K., Betts, R.A., Alves, L.M. and Soares, W.R. 2018. Changes in Climate and Land Use Over the Amazon Region: Current and Future Variability and Trends. *Frontiers in Earth Science*. **6**(December), p.288.

McAlpine, C.A., Salazar, A., Seabrook, L., Dargusch, P., Johnson, A., Wilson, K., Syktus, J., Meijaard, E., Nordin, H. and Sheil, D. 2018. Forest loss and Borneo’s climate. *Environmental Research Letters*. **13**(4).

Met Office 2022. Cartopy: A cartographic python library with a matplotlib interface. , http://scitools.org.uk/cartopy/.

Negri, A.J., Adler, R.F., Xu, L. and Surratt, J. 2004. The Impact of Amazonian Deforestation on Dry Season Rainfall. *Journal of Climate*. **17**, pp.1306–1319.

Potapov, P., Turubanova, S., Hansen, M.C., Tyukavina, A., Zalles, V., Khan, A., Song, X.P., Pickens, A., Shen, Q. and Cortez, J. 2022. Global maps of cropland extent and change show accelerated cropland expansion in the twenty-first century. *Nature Food*. **3**(1), pp.19–28.

Schaaf, C. and Wang, Z. 2015. MCD43A3 MODIS/Terra+Aqua BRDF/Albedo Daily L3 Global - 500m V006. *NASA EOSDIS Land Processes DAAC*., https://doi.org/10.5067/modis/mcd43a3.006.

Sorí, R., Nieto, R., Vicente-Serrano, S.M., Drumond, A. and Gimeno, L. 2017. A Lagrangian perspective of the hydrological cycle in the Congo River basin. *Earth System Dynamics*. **8**(3), pp.653–675.

Spracklen, D. V., Arnold, S.R. and Taylor, C.M. 2012. Observations of increased tropical rainfall preceded by air passage over forests. *Nature*. **489**(7415), pp.282–285.

Spracklen, D. V. and Garcia-Carreras, L. 2015. The impact of Amazonian deforestation on Amazon basin rainfall. *Geophysical Research Letters*. **42**(21), pp.9546–9552.

Spracklen, D.V., Baker, J.C.A., Garcia-Carreras, L. and Marsham, J.H. 2018. The Effects of Tropical Vegetation on Rainfall. *Annual Review of Environment and Resources*. **43**(1), pp.193–218.

Staal, A., Fetzer, I., Wang-Erlandsson, L., Bosmans, J., Dekker, S., van Nes, E., Rockström, J. and Tuinenburg, O. 2020. Hysteresis of tropical forests in the 21st century. *Nature Communications*. **11**(4978), pp.1–8.

Staal, A., Flores, B.M., Aguiar, A.P.D., Bosmans, J.H.C., Fetzer, I. and Tuinenburg, O.A. 2020. Feedback between drought and deforestation in the Amazon. *Environmental Research Letters*. **15**(4).

Staal, A., Tuinenburg, O.A., Bosmans, J.H.C., Holmgren, M., Van Nes, E.H., Scheffer, M., Zemp, D.C. and Dekker, S.C. 2018. Forest-rainfall cascades buffer against drought across the Amazon. *Nature Climate Change*. **8**(6), pp.539–543.

Stickler, C.M., Coe, M.T., Costa, M.H., Nepstad, D.C., McGrath, D.G., Dias, L.C.P., Rodrigues, H.O. and Soares-Filho, B.S. 2013. Dependence of hydropower energy generation on forests in the Amazon Basin at local and regional scales. *Proceedings of the National Academy of Sciences of the United States of America*. **110**(23), pp.9601–9606.

Strand, J., Soares-Filho, B., Costa, M.H., Oliveira, U., Ribeiro, S.C., Pires, G.F., Oliveira, A., Rajão, R., May, P., van der Hoff, R., Siikamäki, J., da Motta, R.S. and Toman, M. 2018. Spatially explicit valuation of the Brazilian Amazon Forest's Ecosystem Services. *Nature Sustainability*. **1**(11), pp.657–664.

Tuinenburg, O.A., Bosmans, J.H.C. and Staal, A. 2022. The global potential of forest restoration for drought mitigation. *Environmental Research Letters*. **17**(3).

Waskom, M. 2021. Seaborn: Statistical Data Visualization. *Journal of Open Source Software*. **6**(60), p.3021.

Wunderling, N., Staal, A., Sakschewski, B., Hirota, M., Tuinenburg, O.A., Donges, J.F., Barbosa, H.M.J. and Winkelmann, R. 2022. Recurrent droughts increase risk of cascading tipping events by outpacing adaptive capacities in the Amazon rainforest. *Proceedings of the National Academy of Sciences of the United States of America*. **119**(32), pp.1–11.

Xu, X., Zhang, X., Riley, W.J., Xue, Y., Nobre, C.A., Lovejoy, T.E. and Jia, G. 2022. Deforestation triggering irreversible transition in Amazon hydrological cycle. *Environmental Research Letters*. **17**(3).

Zemp, D.C., Schleussner, C.F., Barbosa, H.M.J., Hirota, M., Montade, V., Sampaio, G., Staal, A., Wang-Erlandsson, L. and Rammig, A. 2017. Self-amplified Amazon forest loss due to vegetation-atmosphere feedbacks. *Nature Communications*. **8**, pp.1–10.

Zhuang, J. 2022. xESMF. , https://doi.org/10.5281/zenodo.1134365.

Chapter 5

5 Observed and simulated local climate responses to tropical deforestation

Callum Smith[1], Jessica C.A. Baker[1], Eddy Robertson[2], Robin Chadwick[2], Douglas I. Kelley[3], Arthur P. K. Argles[2], Caio A.S. Coelho[4], Dayana C. de Souza[4], Paulo Y. Kubota[4], Isabela L. Talamoni[4] and Dominick V. Spracklen[1]

[1] School of Earth and Environment, University of Leeds, Leeds, LS2 9JT, UK

[2] Met Office Hadley Centre, FitzRoy Road, Exeter, EX1 3PB, UK

[3] UK Centre for Ecology and Hydrology, Wallingford. OX10 8BB UK

[4] Centro de Previsão de Tempo e Estudos Climáticos (CPTEC), Instituto Nacional de Pesquisas Espaciais (INPE), Rodovia Presidente Dutra, Km 40, SP-RJ, Cachoeira Paulista, SP, 12630-000, Brasil

Published in *Environmental Research Letters* **18**(10) (2023), 15th September 2023. Available at https://doi.org/10.1088/1748-9326/acf0da

Abstract

Tropical deforestation has local and regional effects on climate, but the sign and magnitude of these effects are still poorly constrained. Here we used satellite observations to evaluate the local land surface temperature and precipitation response to tropical deforestation in historical simulations from 24 CMIP6 models. We found tropical forest loss leads to an observed local dry season warming and reduced wet and dry season precipitation across the

range of scales (0.25° to 2°) analysed. At the largest scale analysed (2°), we observed a warming of 0.018±0.001 K per percentage point of forest loss (K $\%^{-1}$), broadly captured in the multi-model mean response of 0.017±0.005 K $\%^{-1}$. The multi-model mean correctly simulates reduced precipitation due to forest loss in the dry season but simulates increased precipitation due to forest loss in the wet season, opposite to the observed response. We found that the simulated dry season surface temperature and precipitation changes due to forest loss depend on the simulated surface albedo change, with less warming and less drying in models with greater increases in surface albedo due to forest loss. Increased recognition of the local and regional climate benefits of tropical forests is needed to support sustainable land use policy.

5.1 Introduction

Land cover change alters energy and water fluxes between the surface and atmosphere affecting the local and regional climate (Bonan, 2008; Pongratz et al., 2021). Tropical regions are experiencing rapid changes to land cover, particularly from deforestation (Hansen et al., 2013) and forest degradation (Vancutsem et al., 2021). Tropical deforestation has been shown to cause local surface warming of greater than 2 K (Alkama and Cescatti, 2016; Bright et al., 2017; Duveiller, Hooker, et al., 2018; Baker and Spracklen, 2019). The effect on precipitation is more complex and scale-dependent (Lawrence and Vandecar, 2015), with increases in precipitation over or near small-scale deforestation (Garcia-Carreras and Parker, 2011; Khanna et al., 2017; Taylor et al., 2022) and reductions over and downwind of large-scale deforestation (Spracklen and Garcia-Carreras, 2015). Analysis of satellite precipitation suggests tropical forest loss causes reductions in local precipitation, particularly at scales larger than 50 km (Smith et al., 2023).

Climate models have different representations of the land surface and the biophysical responses to land cover change, leading to different simulations of the climate response to land cover change (Boisier et al., 2015; Boysen et al., 2020; Baker, De Souza, et al., 2021; Luo et al., 2022; De Hertog et al., 2022). Most models agree that deforestation in the tropics causes local surface warming but disagree on the magnitude of the temperature response (Winckler et al., 2019; Boysen et al., 2020). In contrast, some models simulate local cooling over tropical deforestation due to strong increases in simulated surface albedo (Robertson, 2019). The simulated response of local precipitation to land cover change is even more varied. Luo et al. (2022) simulated the impacts of idealised deforestation scenarios and found a multi-model mean reduction in precipitation over regions of forest loss of -2.2%, with a range of -5.5% to +0.1% across 11 models. Spracklen and Garcia-Carreras (2015) synthesised simulated impacts of deforestation in the Amazon basin, finding an average of 12±11% reduction in annual precipitation due to basin-wide deforestation.

Previous assessments of climate model responses to land cover change have analysed both idealised (e.g., Davin and de Noblet-Ducoudre, 2010; Winckler et al., 2017; Boysen et al., 2020; Luo et al., 2022) and historical (De Noblet-Ducoudré et al., 2012; Kumar et al., 2013; Lejeune et al., 2017) land cover scenarios. Evaluation of simulated climate impacts against observations (Duveiller et al., 2018b) have largely focused on temperature from satellite (Li et al., 2015; Alkama and Cescatti, 2016; Duveiller, Hooker, et al., 2018) or in-situ measurements (Lee et al., 2011). Simulations of the impacts of land cover change on precipitation (Luo et al., 2022) have not yet fully been evaluated. We build on this previous work by evaluating the impacts of tropical deforestation in the historical CMIP6 simulations on both local land surface temperature (T) and precipitation (P) in a consistent manner, allowing for crucial model improvement insights to be gleaned. We focus on tropical deforestation because of the sustained need for clear evidence to support conservation of remaining tropical forests for climate change adaptation and mitigation (Windisch et al., 2021). We explore how the climate sensitivity to the extent of forest loss depends on simulated changes to surface albedo, evapotranspiration (ET), and leaf area index (LAI). We evaluate the simulated response using satellite observations, applying a before-after-control-impact (BACI) approach, where the change in local climate over regions of forest loss is compared against the change in climate over control areas with no forest loss. This allows us to analyse the simulated and observed responses to deforestation identically.

5.2 Data and Methods

We analysed data from 24 CMIP6 models (CMIP6 Tier 1: historical; dataset information listed in Table 5.1), with spatial resolution varying from 0.56 to 2.79 degrees latitudinally. We downloaded and processed monthly mean surface albedo, evapotranspiration, leaf area index, land surface temperature and precipitation for 1850-2014.

To evaluate the CMIP6 models, we used satellite data from the period 2003–2019. We calculated forest loss from the Global Forest Change (GFC) version 1.9 (Hansen et al., 2013), using forest canopy cover in 2000 and subsequent annual forest loss from 2003–2019 at 30 metre (m) resolution. We used MODIS albedo (MCD43A3), evapotranspiration (MOD16A2GF) and leaf area index (MOD15A2) available at 500 m resolution and land surface temperature day-night mean (MOD11C3) available at 1 km resolution. We used precipitation data from nine datasets, spanning a range of native resolutions from ~4–25 km (approx. at equator, Table 5.1 lists the details).

We analysed the observed impacts of forest loss across four spatial scales (0.25x0.25°, 0.5x0.5°, 1.0x1.0° and 2.0x2.0°), spanning the spatial resolution of the CMIP6 models. We performed Spatial regridding using the Python package Iris (Met Office, 2023) with the area-weighted regridding scheme. Two alternative regridding methods (xESMF (Zhuang, 2022): 'conservative-normalised' and 'bilinear') were tested and had little impact on our results. We calculated forest loss at each of spatial resolution by the sum of all 30 m pixels within each larger pixel.

We constrained our analysis to the tropics (30°S to 30°N). We additionally constrained satellite datasets by the tropical evergreen broadleaf biome, defined by the MODIS land cover dataset (MCD12Q1), and CMIP6 models by areas where their forest cover was greater than 70% at the start of the discrete analysis periods. This accounted for the fact that simulated forests may be in different geographical areas within each model. We tested both constraining CMIP6 models by MODIS evergreen broadleaf and by areas of forest cover greater than 70%, finding similar results with both methods.

Detecting a robust local climate response to deforestation requires long simulations (Winckler et al., 2017). For this reason, we analysed data over 16-year periods. For the satellite datasets, this period was 2003-2019, as this was the longest common period of precipitation data. For the CMIP6 models, we analysed ten 16-year periods starting in 1854 and ending in 2014. We selected 16-year periods to match the length of the satellite record and report model values as the median across the ten periods. To reduce the impact of interannual variability, we compared 5-year means at the start and end of each analysis period.

Land cover change causes both local and non-local climate impacts (Pongratz et al., 2021). The local climate impacts of land cover change can be assessed from a single simulation through comparing the climate change over regions of land cover change compared to neighbouring regions with little or no land cover change (Kumar et al., 2013; Lejeune et al., 2017). Comparing the change over a pixel with forest loss with its immediate neighbour with little or no forest loss removes the impacts of climate change and variability. We adopted this approach and analysed the local climate response to forest loss using a moving window nearest neighbour approach as used by previous studies (Baker and Spracklen, 2019; Smith et al., 2023), here employing a 3x3 grid size. We calculated the forest loss of each deforested pixel relative to neighbouring control pixels as the forest loss of the deforested pixel minus the forest loss of the control. Calculating the local climate response to land cover change in this way may underestimate the true climate response as we don't account for the non-local climate impacts. These non-local impacts are explored with respect to tropical land cover change in detail by Butt et al. (2023) and Cohn et al. (2019) who both find significant modifications to climate arising from the non-local effects. To be included in the analysis, deforested pixels must have experienced more than 0.1 percentage points of forest loss compared to their neighbouring control pixels. We calculated the change in each variable over the deforested pixel relative to the change of the control pixel. We report changes as a function of forest loss by dividing by the difference in forest loss between deforested and control pixels. To test whether these changes over regions of deforestation were statistically different from changes over the control areas, we used a Student's t-test and the Wilcoxon test, finding similar results from both paired tests.

We focused our temperature analysis on the dry season, where there was better availability of satellite data for albedo, ET, LAI, and T, as the wet season has more clouds which obstruct satellite retrievals. Dry season temperature is also more sensitive to tropical deforestation (Baker and Spracklen, 2019). For precipitation, we analysed dry, wet and transition seasons as the driest 3 months, wettest 3 months and remaining 6 months, respectively, of each year for each pixel. The satellite precipitation value is based on the median of the nine satellite precipitation datasets, whilst for the CMIP6 models, we derived each model's season from its own precipitation data.

To test the relationships between climate variables, we fitted linear regressions using Pearson's correlation coefficient, (calculated using SciPy (Virtanen et al., 2020)) to identify whether the computed correlation coefficients were found to be statistically significant and different from zero at the 5% level ($p<0.05$). We report errors throughout as the standard error of the mean.

5.3 Results and Discussion

Figure 5.1 shows the observed impacts of forest loss on local land surface temperature and precipitation. We observed dry season warming due to forest loss across all spatial scales analysed (Fig. 5.1a). This demonstrates that tropical forest loss caused local warming at spatial scales simulated in regional (0.25°x0.25°, ~25 km × 25 km) to global (2.0°x2.0°, ~200 km × 200 km) climate models. Warming varies from 0.009±0.002 K $\%^{-1}$ (median ± standard error of the mean) at 1.0°x1.0° to 0.018±0.001 K $\%^{-1}$ at 2.0°×2.0°. The local land surface warming we report here is similar to previous studies such as Alkama and Cescatti (2016) who reported that tropical forest deforestation caused a warming of 0.015±0.001 K $\%^{-1}$. Duveiller et al. (2020) used a space-for-time approach and reported a warming of 0.018±0.001 K $\%^{-1}$ for wet tropical forests using 1.0°x1.0° resolution data. In the Amazon, Baker & Spracklen (2019) reported deforestation caused dry season land surface warming of 0.014 K $\%^{-1}$ using 0.05° resolution data.

We observed reductions in precipitation over regions of forest loss at both an annual scale and in the dry, wet and transition seasons (Fig. 5.1b). Forest loss causes a decrease in precipitation across all analysed resolutions, with larger reductions as the scale of forest loss increases. At 2° resolution, the annual reduction was -0.18±0.07 mm month^{-1} %$^{-1}$. This sensitivity is slightly lower than reported by Smith et al. (2023) (-0.25±0.10 mm month^{-1} %$^{-1}$ at 2°) due to small methodological differences, including a longer analysis period (2003-2019 compared to 2003-2017). Reductions in precipitation were observed throughout the year, with the largest absolute reductions in precipitation over regions of forest loss in the wet season (-1.12±0.32 mm month^{-1} %$^{-1}$) compared to -0.06±0.05 mm month^{-1} %$^{-1}$ in the dry season and -0.33±0.24 mm month^{-1} %$^{-1}$ in the transition season.

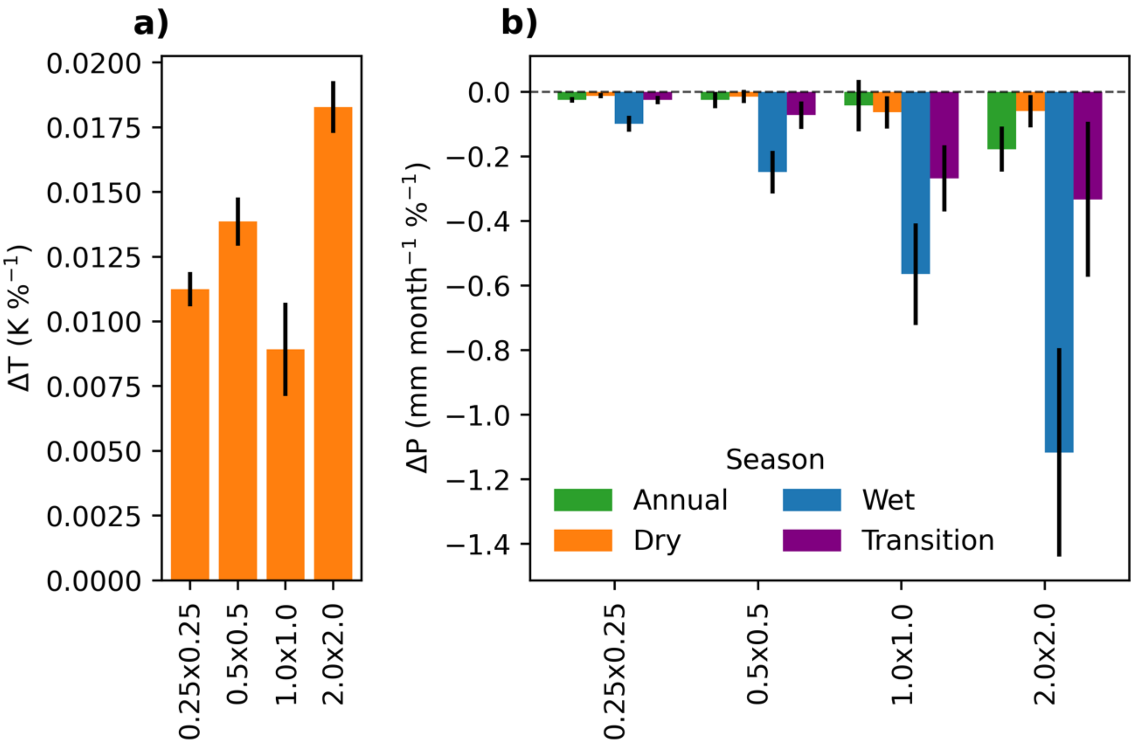

Figure 5.1. *Observed local response of temperature and precipitation to tropical forest loss from 2003 to 2019. a) Median dry-season land surface temperature change (ΔT) per percentage point of forest loss and b) median precipitation change (ΔP) per percentage point of forest loss for annual mean, dry, wet and transition seasons. Temperature data are from the MODIS MOD11C3 product and precipitation data from nine products (Supp. Table C.1). Results are shown at four spatial resolutions (0.25°, 0.5°, 1.0° and 2.0°). Error bars indicate the standard error of the mean. Values and significance presented in Supplementary Table C.1.*

Figure 5.2 compares the simulated and observed impact of forest loss on local dry season land surface temperature. Most models (22 out of 24) simulate a warming response consistent with the satellite observations. The simulated surface temperature response to forest loss varies from -0.038±0.008 K $\%^{-1}$ (GISS-E2-1-G) to +0.042±0.009 K $\%^{-1}$ (CESM2-WACCM-FV2). In idealised deforestation simulations, Boysen et al. (2020) found that the near-surface air temperature response simulated by CMIP6 models varied between -0.02 K $\%^{-1}$ to +0.08K $\%^{-1}$.

The local surface warming due to forest loss is relatively insensitive to spatial scale, both in the models and observations. The multi-model mean warming due to forest loss is +0.017±0.005 K $\%^{-1}$ (0.016±0.002 K $\%^{-1}$ for models <1° resolution and 0.017±0.006 K $\%^{-1}$ for models >1° resolution), which compares well to the observed warming of 0.018±0.001 K $\%^{-1}$ (at 2° resolution). Whilst the multi-model mean is close to the observed value, Figure 5.2 highlights the large variability across models.

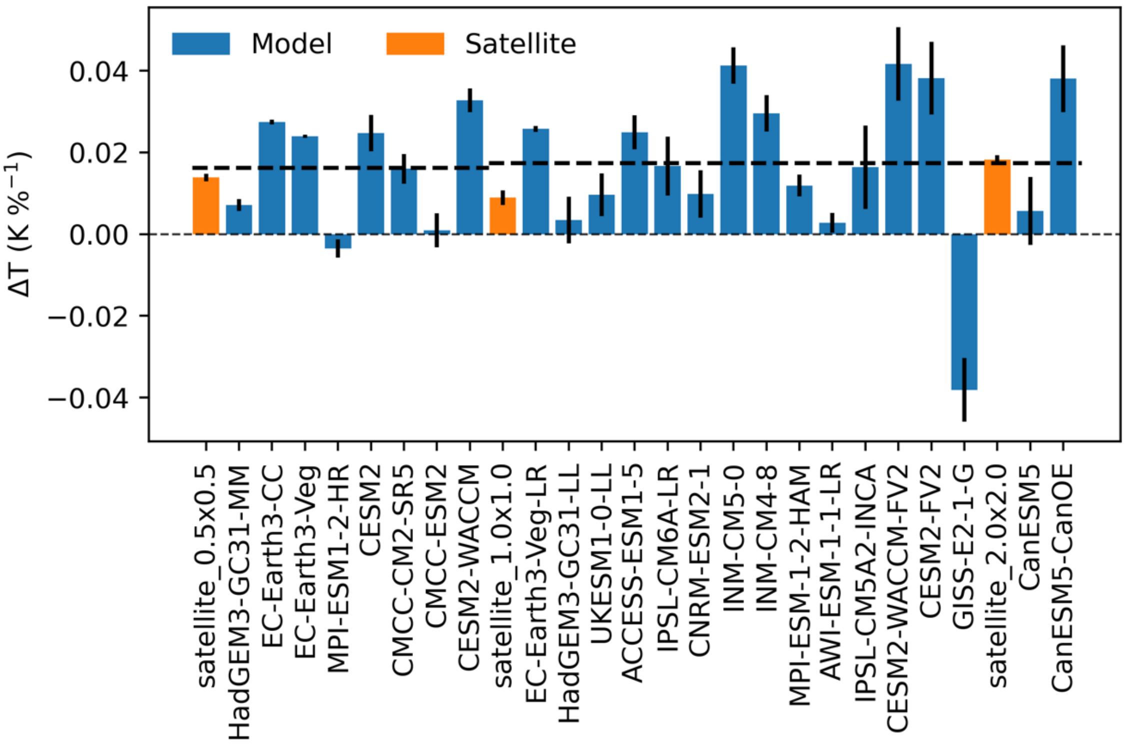

Figure 5.2. *Change in simulated and observed dry season local surface temperature per percentage point of forest loss (ΔT, K $\%^{-1}$), ordered by latitudinal resolution. Simulated changes from the CMIP6 models (blue bars; datasets listed in Table 5.1) are the median over ten 16-year periods from 1854 to 2014. Observed results from satellite (orange bars) (Table 5.1) are for 2003-2019, regridded to three resolutions (0.5° x 0.5°, 1.0° x 1.0°, 2.0° x 2.0°) to match the range of resolutions from the models. Satellite observed forest loss data were from GFC v1.9* (Hansen et al., 2013)*. Model results are for*

areas where initial forest cover exceeds 70%, whilst the satellite analysis is constrained by MODIS evergreen broadleaf land cover. Error bars show the standard error of the mean calculated across the 10 time periods for each model. The dashed line separately shows the multi-model mean value for <1 and >1° spatial resolution models. Values and significance presented in Supplementary Table C.2.

We also analysed the simulated temperature change due to forest loss for each model separately over the ten 16-year model periods (Supplementary Figure C.1). Only 7 models show consistent warming across all periods. Most models (17 out of 24) show warming and cooling in different periods, five of which (CanESM5, CMCC-ESM2, GISS-E2-1-G, MPI-ESM1-2-HR and UKESM1-0-LL) show a cooling response in four or more of the ten 16-year periods contrary to the observed temperature response. This further confirms the need for long simulations to robustly diagnose a climate response to land use change from climate models.

Figure 5.3 compares the simulated and observed changes in dry and wet season precipitation due to tropical forest loss. The simulated precipitation response to forest loss is less consistent than for temperature. In the dry season, 6 of the 24 models simulate increases in precipitation due to forest loss, whilst the remaining 18 models simulate reductions. In the wet season, 10 of the 24 models simulate an increase, whilst the remaining 14 simulate a decrease. Across all models, the multi-model mean response of dry season precipitation to forest loss is -0.06±0.08 mm month^{-1} %$^{-1}$, comparable to the observed change of -0.06±0.05 mm month^{-1} %$^{-1}$ (at 2°). The multi-model mean response in the wet season is 0.11±0.65 mm month^{-1} %$^{-1}$, opposite to the observed response of -1.12±0.32 mm month^{-1} %$^{-1}$. The individual CMIP6 models tend to be oversensitive to forest loss (either large increases or decreases) compared to observed changes.

At the annual scale, the multi-model mean precipitation sensitivity to forest loss is +0.06±0.23 % per percentage point of forest loss (% %$^{-1}$) (Supplementary Fig. C.2), opposite in sign to the observed sensitivity of -0.12±0.11 % %$^{-1}$ (at 2°). Previous studies have also reported a wide range in the simulated precipitation response to tropical deforestation. Luo et al. (2022) reported Amazon deforestation resulted in a regional annual mean precipitation response of –11% to +2% for a 50% reduction in forest cover, equivalent to –

0.18% to +0.04% per percentage forest loss, with eight out of the eleven models simulating decreased precipitation over regions forest loss in the western and southern Amazon basin. Spracklen and Garcia-Carreras (2015) reported multi-model mean annual mean sensitivity of -0.16±0.13% per percentage point forest loss in the Amazon.

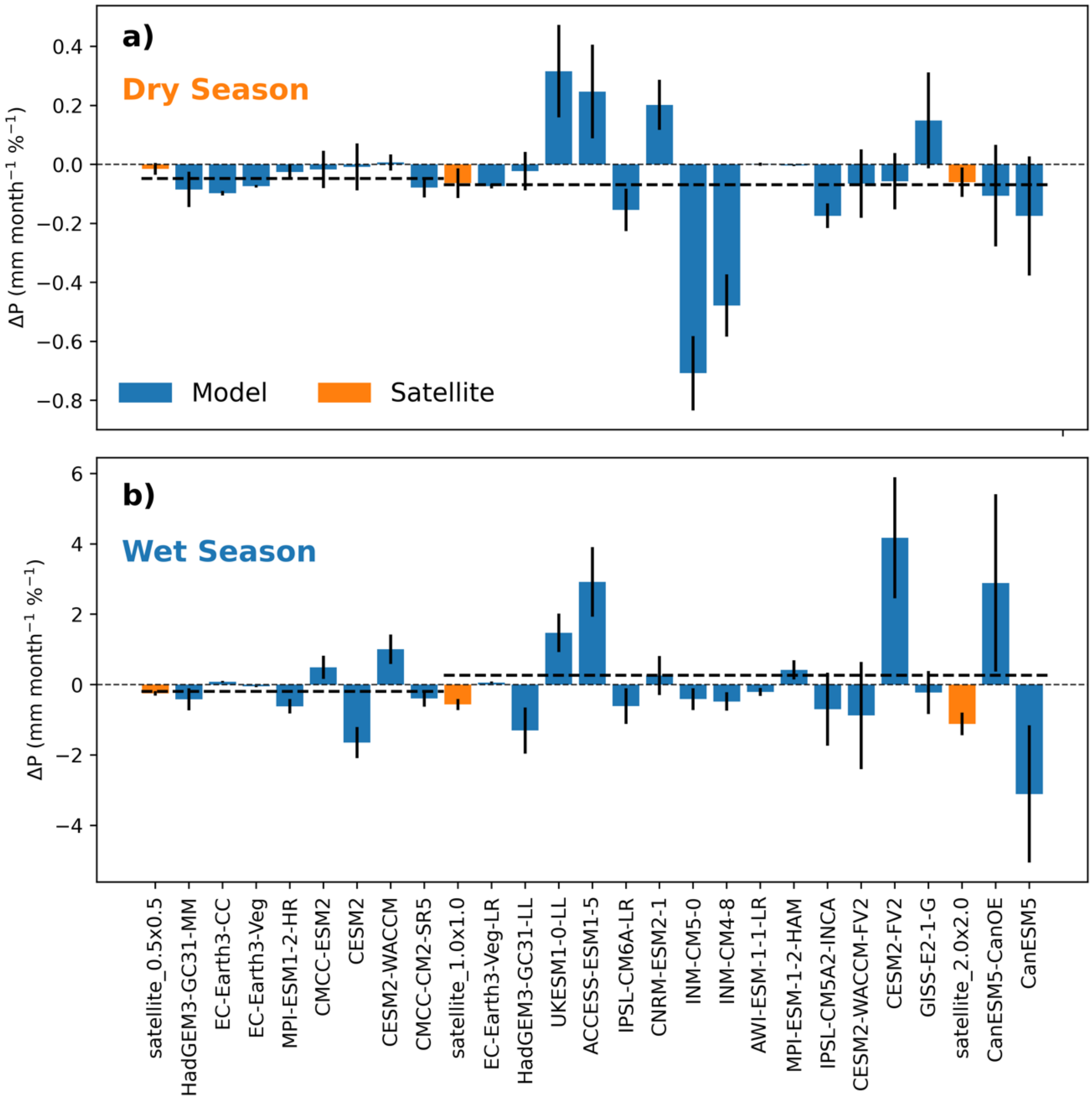

Figure 5.3. *Change in simulated and observed a) dry and b) wet season precipitation per percentage point of forest loss (ΔP, mm month^{-1} %$^{-1}$), ordered by latitudinal resolution. Simulated changes from the CMIP6 models (blue bars) (datasets listed in Table 5.1) are the median over ten 16-year periods from 1854 to 2014. Observed results from satellite (orange bars) (Table 5.1) are for 2003-2019, regridded to three resolutions (0.5x0.5°, 1.0x1.0°, 2.0x2.0°) to match the range of resolutions from*

the models. Model results are for areas where initial forest cover exceeds 70%, whilst the satellite results are constrained by MODIS evergreen broadleaf land cover. We calculate the standard error of the mean from the ten time periods for each model but from one time period for the satellite data. The dashed line separately shows the multi-model mean value for <1 and >1° spatial resolution models. Values and significance presented in Supplementary Table C.3.

Figure 5.4 compares the median dry season sensitivity of temperature and precipitation to forest cover loss against the equivalent sensitivity of different land surface variables (albedo, ET, LAI) to forest loss. There is substantial variability in the simulated sensitivity of albedo, ET and LAI to forest loss. We find large variability in the simulated sensitivity of surface albedo to forest loss varying from ~0 to 5.1×10^{-4} $\%^{-1}$, with 23 of the 24 models simulating an increase in surface albedo in regions of forest loss (INM-CM4-8 simulates a decrease). A previous assessment of the CMIP5 models also found large variability in the simulated albedo response to land use change (Lejeune et al., 2020). For ET, we find simulated sensitivity ranges from -1 to +0.5 mm $month^{-1}$ $\%^{-1}$. Luo et al. (2022) reported that forest loss caused annual mean changes of +50 to –150 mm $year^{-1}$. For LAI, we find a sensitivity of -0.006 to -0.002 m^2 m^{-2} $\%^{-1}$. For the Amazon, Luo et al. (2022) also reported a wide range in the sensitivity of LAI to forest loss ranging from –2 to +1 m^2 m^{-2}, equivalent to –0.02 to +0.01 m^2 m^{-2} $\%^{-1}$.

The local warming due to tropical forest loss can be caused by reducing both ET and surface roughness, which increase sensible heating and reduce turbulent heat fluxes (Bright et al., 2017; Duveiller et al., 2018b). For dry season temperature, we find statistically significant relationships ($P<0.05$) with albedo ($r^2 = 0.299$) and ET ($r^2 = 0.292$). As would be expected (Bright et al., 2017; Duveiller et al., 2018; J. Winckler et al., 2019), models with a stronger sensitivity of surface albedo (greater surface brightening) and ET (greater ET increases) to forest loss tend to show less warming from forest loss.

Figure 5.4 also shows satellite and in-situ observations. Albedo measurements from satellite also suggest increased albedo due to forest loss with a sensitivity of 8.0×10^{-5} to 1.31×10^{-4} $\%^{-1}$, equivalent to an increase in the albedo of 0.008 to 0.013 for complete forest loss. This albedo sensitivity to forest loss is relatively well captured by some models (3 simulating albedo within the satellite range), whereas 9 models underestimate (< 8.0×10^{-5} $\%^{-1}$) and 12 overestimate (> 1.31×10^{-4} $\%^{-1}$) the sensitivity. Models that overestimate the albedo sensitivity to forest loss underestimate the warming due to forest loss. Constraining the albedo sensitivity to deforestation is also important for accurate simulation of the radiative forcing due to historical land-use change (Lejeune et al., 2020).

Most models simulate a reduction in ET over forest loss (multi-model mean -0.19±0.06 mm month^{-1} %$^{-1}$), although there is large variability across models with a range of -1.17 to +0.62 mm month^{-1} %$^{-1}$. The sensitivity of ET to forest loss is related to the change in LAI, as has been shown previously (Luo et al., 2022), with models that simulate larger decreases in LAI tending to simulate larger decreases in ET following forest loss (Supplementary Fig. C.3). Forest loss causes a reduction in simulated ET due to the replacement of forests by grasses with lower ET rates, matching the response in idealised deforestation simulations (Boysen et al., 2020). Increased ET over regions of forest loss in some models (e.g., CESM) may be due to tropical forests being replaced by C4 grasses that are over productive in the moist tropics (Boysen et al., 2020), whilst in other models (e.g., GISS-E2-1-G) it may be due to increased simulated precipitation over regions of forest loss.

We found significant positive relationships for dry season precipitation with ET (r^2 = 0.564) and albedo (r^2 = 0.176). Luo et al. (2022) also reported positive relationships between changes in precipitation and ET due to deforestation. They also found that the inter-model spread in precipitation response to forest loss primarily results from divergent responses of evapotranspiration. Previous work has also suggested albedo as an important parameter controlling precipitation changes (Dirmeyer and Shukla, 1994; Berbet and Costa, 2003; Costa et al., 2007). Dirmeyer and Shukla (1994) found that the local precipitation response to forest loss showed a strong sensitivity to the assumed increase in albedo with forest loss over a range of 0 to 0.09 (9.0x10^{-4} %$^{-1}$). However, they found forest loss reduced precipitation when the albedo sensitivity was greater than 3.0x10^{-4} %$^{-1}$, opposite to our results of increased precipitation in models with greater brightening.

We note that the satellite-based sensitivity of albedo, ET and LAI to forest loss is less than would be expected based on in-situ measurements. In the Amazon, (Culf et al., 1995) observed annual mean albedo of 0.13 for tropical forest and 0.18 for pasture, suggesting deforestation causes increased albedo of 0.05 or 4.6x10^{-4} %$^{-1}$ (plotted as a red star in Figure

5.4a, d), about a factor 4 greater than in the satellite measurements. In-situ data represents a complete conversion from forest to pasture with correspondingly large changes in albedo. In comparison, satellite data observes forest loss at larger scales where remaining tree cover and vegetation regrowth may reduce the change in albedo caused by forest loss.

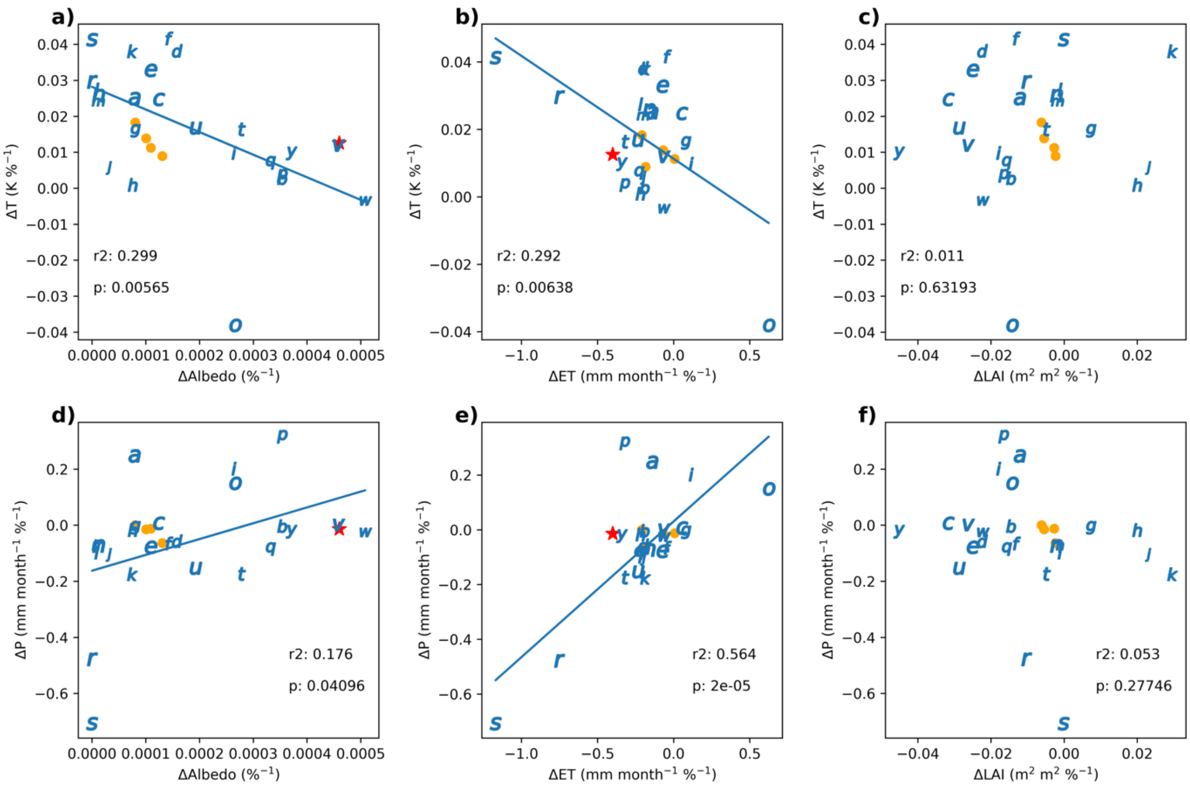

Figure 5.4. *Sensitivity of dry season (a-c) land surface temperature (T) and (d-f) precipitation (P) to surface albedo (Alb), evapotranspiration (ET), leaf area index (LAI), per percentage point of forest loss. Simulated (blue) values show the median change for each model's ten 16-year periods. We report the linear Pearson correlation coefficient squared (r^2) and the p-value (p) and plot the linear fit where $p < 0.05$. Results are for areas where initial forest cover exceeds 70%. Satellite values are plotted as orange circles, regridded to four resolutions (0.25x0.25°, 0.5x0.5°, 1.0x1.0°, 2.0x2.0°). These values are constrained by MODIS land cover evergreen broadleaf area. The red star indicates in-situ measurement from (Culf et al., 1995; Restrepo-Coupe et al., 2013). Model key; ACCESS-ESM1-5: 'a' , AWI-ESM-1-1-LR: 'b', CESM2: 'c', CESM2-FV2: 'd', CESM2-WACCM: 'e', CESM2-WACCM-FV2: 'f', CMCC-CM2-SR5: 'g', CMCC-ESM2: 'h', CNRM-ESM2-1: 'I', CanESM5: 'j', CanESM5-CanOE: 'k', EC-Earth3-CC: 'l', EC-Earth3-Veg: 'm', EC-Earth3-Veg-LR: 'n', GISS-E2-1-G: 'o', HadGEM3-GC31-LL: 'p', HadGEM3-GC31-MM: 'q', INM-CM4-8: 'r', INM-CM5-0: 's', IPSL-CM5A2-INCA: 't', IPSL-CM6A-LR: 'u', MPI-ESM-1-2-HAM: 'v', MPI-ESM1-2-HR: 'w', UKESM1-0-LL: 'y'.*

In situ observations of dry season ET in the Amazon are around 110 mm month^{-1} for tropical forests and 70 mm month^{-1} for pasture (Restrepo-Coupe et al., 2013), suggesting deforestation causes a reduction of 40 mm month^{-1} or 0.4 mm month^{-1} %$^{-1}$ (plotted as a red star in Figure 5.4b, e), around 3.5 times greater than seen in the satellite measurements. Challenges with remote-sensed ET data which combine remote sensed and model data (Baker, Garcia-Carreras, et al., 2021) may explain the discrepancy with in-situ data. The simulated temperature response to forest loss is strongly related to albedo and ET in the dry season but less so in the wet season (Baker, Garcia-Carreras, et al., 2021).

Our analysis focused on assessing the simulated local climate response to tropical deforestation and understanding how this depends on the modelled treatment of the land surface change. Additional climate responses also depend on simulated atmospheric feedback through altering mesoscale circulations (Khanna et al., 2017). Boysen et al. (2020) found that increased shortwave radiation due to reduced cloud cover over regions of tropical deforestation was more important than changes in surface albedo in some models. Luo et al. (2022) found mean reductions in ET over deforested areas (16.9 mm year^{-1}) were about 4 times greater than reductions in mean flow convergence (-4.3 mm year^{-1}), suggesting local reductions in ET dominate reduced rainfall rather than changes in circulation.

In addition to impacts on temperature and precipitation, deforestation can also impact other important climate variables such as causing reductions in low level cloud cover (Duveiller et al., 2021). We focused on the local land surface warming due to forest loss, though we note that air temperature's response to deforestation may differ (Winckler et al., 2019). Deforestation can also cause important changes in the timing and intensity of precipitation. In Amazonia, deforestation has extended dry season and delayed the onset of the rainy season (Leite-Filho et al., 2021; Commar et al., 2023). In West Africa, deforestation has enhanced storm frequency (Taylor et al., 2022). In addition to local impacts, deforestation may also change regional climate (Leite-Filho et al., 2020). Tropical deforestation can cause reductions in downwind precipitation through reductions in moisture recycling (Spracklen et al., 2012; Zemp et al., 2017; Staal et al., 2018) and can alter regional temperatures up to 50 km away from the location of land-use change (Cohn et al., 2019). Deforestation may even alter precipitation in regions far removed from the land use change through teleconnections (Werth and Avissar, 2005; Pitman et al., 2009; De Noblet-Ducoudré et al., 2012; Luo et al., 2022).

5.4 Conclusions and Implications

Our analysis provides further evidence of the local surface warming and drying (reduced precipitation) due to tropical deforestation. The multi-model mean captures the observed surface warming due to tropical forest loss, with 22 out of 24 CMIP6 models analysed simulating warming in response to tropical forest loss. The multi-model mean suggests increased annual mean precipitation over regions of tropical forest loss, opposite in sign to the observed response. There is large variability in the magnitude of the modelled temperature and precipitation responses to deforestation, some of which we attribute to different implementations of land use change within CMIP6 models and the subsequent changes to albedo and ET. We find the simulated local land surface warming due to forest loss is sensitive to the simulated surface albedo change.

The local warming and drying due to tropical deforestation will have negative impacts on human health (Wolff et al., 2018; Alves de Oliveira et al., 2021), agriculture (Lawrence and Vandecar, 2015; Leite-Filho et al., 2021), surrounding forests (Zemp et al., 2017; Staal et al., 2020; Li et al., 2022) and biodiversity (Pardini et al., 2017). A warmer and drier climate will also exacerbate the risk of forest fires causing additional forest loss and the potential for positive climate feedbacks (Cochrane et al., 1999). Some work has suggested the Amazon is close to a tipping point where additional deforestation would drive sufficient drying to induce forest dieback (Lovejoy and Nobre, 2019). Future work is needed to assess the resilience of remaining tropical forests to a warmer and drier climate. Overall, our analysis provides additional impetus for policymakers to account for the local climate impacts of tropical deforestation (Duveiller et al., 2020; Pongratz et al., 2021).

Table 5.1. *CMIP6 model and satellite datasets used in this analysis. Models are grouped by spatial resolution (<1°, and ≥1° resolution in latitude).*

Dataset	Institute	Resolution lon, lat (degrees)	Resolution grouping	Reference
Model				
ACCESS-ESM1-5	CSIRO	1.88 x 1.25	>1°	Ziehn et al. (2019)
AWI-ESM-1-1-LR	AWI	1.88 x 1.87	>1°	Danek et al. (2020)
CanESM5	CCCma	2.81 x 2.79	>1°	Swart et al. (2019a)
CanESM5-CanOE	CCCma	2.81 x 2.79	>1°	Swart et al. (2019b)
CESM2	NCAR	1.25 x 0.94	<1°	Danabasoglu (2019a)
CESM2-FV2	NCAR	2.50 x 1.89	>1°	Danabasoglu (2019b)
CESM2-WACCM	NCAR	1.25 x 0.94	<1°	Danabasoglu (2019c)
CESM2-WACCM-FV2	NCAR	2.50 x 1.89	>1°	Danabasoglu (2019d)
CMCC-CM2-SR5	CMCC	1.25 x 0.94	<1°	Lovato and Peano (2020)
CMCC-ESM2	CMCC	1.25 x 0.94	<1°	Lovato et al. (2021)
CNRM-ESM2-1	CNRM-CERFACS	1.41 x 1.40	>1°	Seferian (2018)
EC-Earth3-CC	EC-Earth-Consortium	0.70 x 0.70	<1°	EC-Earth-Consortium (2021)
EC-Earth3-Veg	EC-Earth-Consortium	0.70 x 0.70	<1°	EC-Earth-Consortium (2019)
EC-Earth3-Veg-LR	EC-Earth-Consortium	1.12 x 1.12	>1°	EC-Earth-Consortium (2020)
GISS-E2-1-G	NASA-GISS	2.50 x 2.00	>1°	NASA/GISS (2018)
HadGEM3-GC31-LL	MOHC	1.88 x 1.25	>1°	Ridley et al. (2019)
HadGEM3-GC31-MM	MOHC	0.83 x 0.56	<1°	Ridley et al. (2019)
INM-CM4-8	INM	2.00 x 1.50	>1°	Volodin et al. (2019a)
INM-CM5-0	INM	2.00 x 1.50	>1°	Volodin et al. (2019b)
IPSL-CM5A2-INCA	IPSL	3.75 x 1.89	>1°	Boucher et al. (2018)
IPSL-CM6A-LR	IPSL	2.50 x 1.27	>1°	Boucher et al. (2018)

MPI-ESM-1-2-HAM	HAMMOZ-Consortium	1.88 x 1.87	>1°	Neubauer et al. (2019)
MPI-ESM1-2-HR	MPI-M	0.94 x 0.94	<1°	Jungclaus et al. (2019)
UKESM1-0-LL	MOHC	1.88 x 1.25	>1°	Tang et al. (2019)
Satellite				
MODIS Albedo (MCD43A3)		0.05 x 0.05	n/a	Schaaf and Wang (2021)
MODIS Evapotranspiration (MOD16A2)		0.05 x 0.05	n/a	Running et al. (2021)
MODIS Leaf Area Index (MOD15A2)		0.05 x 0.05	n/a	Myneni et al. (2021)
MODIS Land Surface Temperature (MOD11A2)		0.05 x 0.05	n/a	Wan et al. (2021)
MODIS Land Cover Type (MCD12Q1)		0.05 x 0.05	n/a	Friedl and Sulla-Menashe (2022)
CHIRPS Precipitation (CHIRPS-2.0)		0.05 x 0.05	n/a	Funk et al. (2015)
CMORPH		0.25 x 0.25	n/a	Xie et al. (2019)
GPCP v3.2		0.5 x 0.5	n/a	Huffman et al. (2022)
GPM v0.6		0.1 x 0.1	n/a	Hou et al. (2014)
PERSIANN-CCS		0.04 x 0.04	n/a	Nguyen et al. (2019)
PERSIANN-CDR		0.25 x 0.25	n/a	Ashouri et al. (2015)
PERSIANN-CCSCDR		0.04 x 0.04	n/a	Sadeghi et al. (2021)
PERSIANN		0.25 x 0.25	n/a	Nguyen et al. (2019)
TRMM v3B43		0.25 x 0.25	n/a	Huffman et al. (2007)
Global Forest Change (GFC v1.9)		30 m x 30 m	n/a	Hansen et al. (2013)

Data Availability

The dataset used in this analysis are all freely available through the following repositories: CMIP6 historical data from https://esgf-index1.ceda.ac.uk/projects/cmip6-ceda/, CHIRPS from https://data.chc.ucsb.edu/products/?C=M;O=D, CMORPH from https://ftp.cpc.ncep.noaa.gov/precip/CMORPH_RT/GLOBE/data/, GPCP from https://disc.gsfc.nasa.gov/datasets/GPCPMON_3.1/summary?keywords=GPCPMON, GPM from https://gpm1.gesdisc.eosdis.nasa.gov/data/GPM_L3/, PERSIANN (CCS, CDR, CCS-CDR, PDIR-NOW) from https://chrsdata.eng.uci.edu/, TRMM from https://disc.gsfc.nasa.gov/datasets/TRMM_3B43_7/summary, MODIS (MCD43A3, MOD16A2, MOD15A2, MOD11A2 and MCD12Q1) from https://search.earthdata.nasa.gov/search and Global Forest Change data from https://storage.googleapis.com/earthenginepartners-hansen/GFC-2021-v1.9/download.html.

Acknowledgements

The research has been supported by funding from the European Research Council (ERC) under the European Union’s Horizon 2020 research and innovation programme (DECAF project, Grant agreement no. 771492), and the Newton Fund, through the Met Office Climate Science for Service Partnership Brazil (CSSP Brazil). We also acknowledge that DIK was supported by the NC-International programme [NE/X006247/1] delivering National Capability. No competing interests. We acknowledge the World Climate Research Programme, which, through its Working Group on Coupled Modelling, coordinated and promoted CMIP6. We thank the climate modelling groups for producing and making available their model output, the Earth System Grid Federation (ESGF) for archiving the data and providing access, and the multiple funding agencies that support CMIP6 and ESGF.

References

Alkama, R. and Cescatti, A. 2016. Biophysical climate impacts of recent changes in global forest cover. *Science*. **351**(6273), pp.600–604.

Alves de Oliveira, B.F., Bottino, M.J., Nobre, P. and Nobre, C.A. 2021. Deforestation and climate change are projected to increase heat stress risk in the Brazilian Amazon. *Communications Earth and Environment*. **2**(1), pp.1–8.

Ashouri, H., Hsu, K.L., Sorooshian, S., Braithwaite, D.K., Knapp, K.R., Cecil, L.D., Nelson, B.R. and Prat, O.P. 2015. PERSIANN-CDR: Daily precipitation climate data record from multisatellite observations for hydrological and climate studies. *Bulletin of the American Meteorological Society*. **96**(1), pp.69–83.

Baker, J.C.A., Garcia-Carreras, L., Gloor, M., Marsham, J.H., Buermann, W., Da Rocha, H.R., Nobre, A.D., De Carioca Araujo, A. and Spracklen, D. V. 2021. Evapotranspiration in the Amazon: Spatial patterns, seasonality, and recent trends in observations, reanalysis, and climate models. *Hydrology and Earth System Sciences*. **25**(4), pp.2279–2300.

Baker, J.C.A., De Souza, D.C., Kubota, P.Y., Buermann, W., Coelho, C.A.S., Andrews, M.B., Gloor, M., Garcia-Carreras, L., Figueroa, S.N. and Spracklen, D. V. 2021. An assessment of land–atmosphere interactions over south america using satellites, reanalysis, and two global climate models. *Journal of Hydrometeorology*. **22**(4), pp.905–922.

Baker, J.C.A. and Spracklen, D. V 2019. Climate Benefits of Intact Amazon Forests and the Biophysical Consequences of Disturbance. *Frontiers in Forests and Global Change*. **2**, pp.1–13.

Berbet, M.L.C. and Costa, M.H. 2003. Climate change after tropical deforestation: Seasonal variability of surface albedo and its effects on precipitation change. *Journal of Climate*. **16**(12), pp.2099–2104.

Boisier, J.P., Ciais, P., Ducharne, A. and Guimberteau, M. 2015. Projected strengthening of Amazonian dry season by constrained climate model simulations. *Nature Climate Change*. **5**(7), pp.656–660.

Bonan, G.B. 2008. Forests and climate change: Forcings, feedbacks, and the climate benefits of forests. *Science*. **320**(5882), pp.1444–1449.

Boucher, O., Denvil, S., Levavasseur, G., Cozic, A., Caubel, A., Foujols, M.-A., Meurdesoif, Y., Cadule, P., Devilliers, M., Ghattas, J., Lebas, N., Lurton, T., Mellul, L., Musat, I. and Migno, F. 2018. IPSL

IPSL-CM6A-LR model output prepared for CMIP6 CMIP historical. *Earth System Grid Federation*. [Online]. Available from: https://doi.org/10.22033/ESGF/CMIP6.5195.

Boysen, L.R., Brovkin, V., Pongratz, J., Lawrence, D.M., Lawrence, P., Vuichard, N., Peylin, P., Liddicoat, S., Hajima, T., Zhang, Y., Rocher, M., Delire, C., Séférian, R., Arora, V.K., Nieradzik, L., Anthoni, P., Thiery, W., Laguë, M.M., Lawrence, D. and Lo, M.H. 2020. Global climate response to idealized deforestation in CMIP6 models. *Biogeosciences*. **17**(22), pp.5615–5638.

Bright, R.M., Davin, E., O'Halloran, T., Pongratz, J., Zhao, K. and Cescatti, A. 2017. Local temperature response to land cover and management change driven by non-radiative processes. *Nature Climate Change*. **7**(4), pp.296–302.

Butt, E.W., Baker, J.C.A, Silva Bezerra, F.G., von Randow, C., Aguiar, A.P.D and Spracklen, D.V.S. 2023. Amazon deforestation causes strong regional warming. *PNAS*. **120**(45).

Cochrane, M.A., Alencar, A., Schulze, M.D., Souza, C.M., Nepstad, D.C., Lefebvre, P. and Davidson, E.A. 1999. Positive feedbacks in the fire dynamic of closed canopy tropical forests. *Science*. **284**(5421), pp.1832–1835.

Cohn, A.S., Bhattarai, N., Campolo, J., Crompton, O., Dralle, D., Duncan, J. and Thompson, S. 2019. Forest loss in Brazil increases maximum temperatures within 50 km. *Environmental Research Letters*. **14**(8).

Commar, L.F.S., Abrahão, G.M. and Costa, M.H. 2023. A possible deforestation-induced synoptic-scale circulation that delays the rainy season onset in Amazonia. *Environmental Research Letters*. **18**(4), p.044041.

Costa, M.H., Yanagi, S.N.M., Souza, P.J.O.P., Ribeiro, A. and Rocha, E.J.P. 2007. Climate change in Amazonia caused by soybean cropland expansion, as compared to caused by pastureland expansion. *Geophysical Research Letters*. **34**(7), pp.2–5.

Culf, A.D., Fisch, G. and Hodnett, M.G. 1995. The Albedo of Amazonian Forest and Ranch Land. *Journal of Climate*. **9**, pp.1544–1554.

Danabasoglu, G. 2019a. NCAR CESM2 model output prepared for CMIP6 CMIP historical. *Earth System Grid Federation*. [Online]. Available from: https://doi.org/10.22033/ESGF/CMIP6.10023.

Danabasoglu, G. 2019b. NCAR CESM2-FV2 model output prepared for CMIP6 CMIP historical. *Earth System Grid Federation*. [Online]. Available from: https://doi.org/10.22033/ESGF/CMIP6.11281.

Danabasoglu, G. 2019c. NCAR CESM2-WACCM model output prepared for CMIP6 CMIP historical. *Earth System Grid Federation*. [Online]. Available from: https://doi.org/10.22033/ESGF/CMIP6.10023.

Danabasoglu, G. 2019d. NCAR CESM2-WACCM-FV2 model output prepared for CMIP6 CMIP historical. *Earth System Grid Federation*. [Online]. Available from: https://doi.org/10.22033/ESGF/CMIP6.11282.

Danek, C., Shi, X., Stepanek, C., Yang, H., Barbi, D., Hegewald, J. and Lohmann, G. 2020. AWI AWI-ESM1.1LR model output prepared for CMIP6 CMIP historical. *Earth System Grid Federation*. [Online]. Available from: https://doi.org/10.22033/ESGF/CMIP6.9301.

Davin, E.L. and de Noblet-Ducoudre, N. 2010. Climatic impact of global-scale Deforestation: Radiative versus nonradiative processes. *Journal of Climate*. **23**(1), pp.97–112.

Dirmeyer, P.A. and Shukla, J. 1994. Albedo as a modulator of climate response to tropical deforestation. *Journal of Geophysical Research*. **99**(10), pp.20863–20877.

Duveiller, G., Caporaso, L., Abad-Viñas, R., Perugini, L., Grassi, G., Arneth, A. and Cescatti, A. 2020. Local biophysical effects of land use and land cover change: towards an assessment tool for policy makers. *Land Use Policy*. **91**, pp.1–11.

Duveiller, G., Filipponi, F., Ceglar, A., Bojanowski, J., Alkama, R. and Cescatti, A. 2021. Revealing the widespread potential of forests to increase low level cloud cover. *Nature Communications*. **12**(1), pp.1–15.

Duveiller, G., Forzieri, G., Robertson, E., Li, W., Georgievski, G., Lawrence, P., Wiltshire, A., Ciais, P., Pongratz, J., Sitch, S., Arneth, A. and Cescatti, A. 2018. Biophysics and vegetation cover change: A process-based evaluation framework for confronting land surface models with satellite observations. *Earth System Science Data*. **10**(3), pp.1265–1279.

Duveiller, G., Hooker, J. and Cescatti, A. 2018. The mark of vegetation change on Earth's surface energy balance. *Nature Communications*. **9**(1), pp.1–12.

EC-Earth-Consortium 2021. EC-Earth-Consortium EC-Earth-3-CC model output prepared for CMIP6 CMIP historical. *Earth System Grid Federation*. [Online]. Available from: https://doi.org/10.22033/ESGF/CMIP6.4702.

EC-Earth-Consortium 2019. EC-Earth-Consortium EC-Earth3-Veg model output prepared for CMIP6 CMIP historical. *Earth System Grid Federation*. [Online]. Available from: https://doi.org/10.22033/ESGF/CMIP6.692.

EC-Earth-Consortium 2020. EC-Earth-Consortium EC-Earth3-Veg-LR model output prepared for CMIP6 CMIP historical. *Earth System Grid Federation*. [Online]. Available from: https://doi.org/10.22033/ESGF/CMIP6.643.

Friedl, M. and Sulla-Menashe, D. 2022. MODIS/Terra+Aqua Land Cover Type Yearly L3 Global 500m SIN Grid V061 [Data set]. *NASA EOSDIS Land Processes DAAC*. [Online]. [Accessed 1 January 2022]. Available from: https://doi.org/10.5067/MODIS/MCD12Q1.061.

Funk, C., Peterson, P., Landsfeld, M., Pedreros, D., Verdin, J., Shukla, S., Husak, G., Rowland, J., Harrison, L., Hoell, A. and Michaelsen, J. 2015. The climate hazards infrared precipitation with stations - A new environmental record for monitoring extremes. *Scientific Data*. **2**, pp.1–21.

Garcia-Carreras, L. and Parker, D.J. 2011. How does local tropical deforestation affect rainfall? *Geophysical Research Letters*. **38**(19), pp.1–6.

Hansen, M.C., Potapov, P. V., Moore, R., Hancher, M., Turubanova, S.A., Tyukavina, A., Thau, D., Stehman, S. V., Goetz, S.J., Loveland, T.R., Kommareddy, A., Egorov, A., Chini, L., Justice, C.O. and Townshend, J.R.G. 2013. High-Resolution Global Maps of 21st-Century Forest Cover Change. *Science*. **342**(6160), pp.850–853.

De Hertog, S.J., Havermann, F., Vanderkelen, I., Guo, S., Luo, F., Manola, I., Coumou, D., Davin, E.L., Duveiller, G., Lejeune, Q., Pongratz, J., Schleussner, C.F., Seneviratne, S.I. and Thiery, W. 2022. The biogeophysical effects of idealized land cover and land management changes in Earth system models. *Earth System Dynamics*. **13**(3), pp.1305–1350.

Hou, A.Y., Kakar, R.K., Neeck, S., Azarbarzin, A.A., Kummerow, C.D., Kojima, M., Oki, R., Nakamura, K. and Iguchi, T. 2014. The global precipitation measurement mission. *Bulletin of the American Meteorological Society*. **95**(5), pp.701–722.

Huffman, G.J., Adler, R.F., Bolvin, D.T., Gu, G., Nelkin, E.J., Bowman, K.P., Hong, Y., Stocker, E.F. and Wolff, D.B. 2007. The TRMM Multisatellite Precipitation Analysis (TMPA): Quasi-global, multiyear, combined-sensor precipitation estimates at fine scales. *Journal of Hydrometeorology*. **8**(1), pp.38–55.

Huffman, G.J.A., Behrangi, R.F., Adler, D.T., Bolvin, E.J. and Nelkin, G.G. 2022. *Introduction to the New Version 3 GPCP Monthly Global Precipitation Analysis* [Online]. Available from: https://docserver.gesdisc.eosdis.nasa.gov/public/project/MEaSUREs/GPCP/Release_Notes.GPCPV3.2.pdf.

Jungclaus, J., Bittner, M., Wieners, K.-H., Wachsmann, F., Schupfner, M., Legutke, S., Giorgetta, M., Reick, C., Gayler, V., Haak, H., de Vrese, P., Raddatz, T., Esch, M. and Mauritsen, Thorst, E. 2019. MPI-M MPI-ESM1.2-HR model output prepared for CMIP6 CMIP historical. *Earth System Grid Federation*. [Online]. Available from: https://doi.org/10.22033/ESGF/CMIP6.762.

Khanna, J., Medvigy, D., Fueglistaler, S. and Walko, R. 2017. Regional dry-season climate changes due to three decades of Amazonian deforestation. *Nature Climate Change*. **7**(3), pp.200–204.

Kumar, S., Dirmeyer, P.A., Merwade, V., Delsole, T., Adams, J.M. and Niyogi, D. 2013. Land use/cover change impacts in CMIP5 climate simulations: A new methodology and 21st century challenges. *Journal of Geophysical Research Atmospheres*. **118**(12), pp.6337–6353.

Lawrence, D. and Vandecar, K. 2015. Effects of tropical deforestation on climate and agriculture. *Nature Climate Change*. **5**(1), pp.27–36.

Lee, X., Goulden, M.L., Hollinger, D.Y., Barr, A., Black, T.A., Bohrer, G., Bracho, R., Drake, B., Goldstein, A., Gu, L., Katul, G., Kolb, T., Law, B.E., Margolis, H., Meyers, T., Monson, R., Munger, W., Oren, R., Paw U, K.T., Richardson, A.D., Schmid, H.P., Staebler, R., Wofsy, S. and Zhao, L. 2011. Observed increase in local cooling effect of deforestation at higher latitudes. *Nature*. **479**, pp.384–387.

Leite-Filho, A.T., Costa, M.H. and Fu, R. 2020. The southern Amazon rainy season: The role of deforestation and its interactions with large-scale mechanisms. *International Journal of Climatology*. **40**(4), pp.2328–2341.

Leite-Filho, A.T., Soares-Filho, B.S., Davis, J.L., Abrahão, G.M. and Börner, J. 2021. Deforestation reduces rainfall and agricultural revenues in the Brazilian Amazon. *Nature Communications*. **12**(1), pp.1–7.

Lejeune, Q., Davin, E.L., Duveiller, G., Crezee, B., Meier, R., Cescatti, A. and Seneviratne, S.I. 2020. Biases in the albedo sensitivity to deforestation in CMIP5 models and their impacts on the associated historical radiative forcing. *Earth System Dynamics*. **11**(4), pp.1209–1232.

Lejeune, Q., Seneviratne, S.I. and Davin, E.L. 2017. Historical land-cover change impacts on climate: Comparative assessment of LUCID and CMIP5 multimodel experiments. *Journal of Climate*. **30**(4), pp.1439–1459.

Li, Y., Brando, P.M., Morton, D.C., Lawrence, D.M., Yang, H. and Randerson, J.T. 2022. Deforestation-induced climate change reduces carbon storage in remaining tropical forests. *Nature Communications*. **13**(1), pp.1–13.

Li, Y., Zhao, M., Motesharrei, S., Mu, Q., Kalnay, E. and Li, S. 2015. Local cooling and warming effects of forests based on satellite observations. *Nature Communications*. **6**, pp.1–8.

Lovato, T. and Peano, D. 2020. CMCC CMCC-CM2-SR5 model output prepared for CMIP6 CMIP historical. *Earth System Grid Federation*. [Online]. Available from: https://doi.org/10.22033/ESGF/CMIP6.3825.

Lovato, T., Peano, D. and Butenschön, M. 2021. CMCC CMCC-ESM2 model output prepared for CMIP6 CMIP historical. *Earth System Grid Federation*. [Online]. Available from: https://doi.org/10.22033/ESGF/CMIP6.13164.

Lovejoy, T.E. and Nobre, C. 2019. Amazon tipping point: Last chance for action. *Science Advances*. **5**(12), pp.4–6.

Luo, X., Ge, J., Guo, W., Fan, L., Chen, C., Liu, Y. and Yang, L. 2022. The biophysical impacts of deforestation on precipitation: results from the CMIP6 model intercomparison. *Journal of Climate*. **35**(11), pp.3293–3311.

Met Office 2023. Iris: A powerful, format-agnostic, and community-driven Python package for analysing and visualising Earth science data. Available from: http://scitools.org.uk/.

Myneni, R., Knyazikhin, Y. and Park, T. 2021. MODIS/Terra Leaf Area Index/FPAR 8-Day L4 Global 500m SIN Grid V061 [Data set]. *NASA EOSDIS Land Processes DAAC*., https://doi.org/10.5067/MODIS/MOD15A2H.061.

NASA/GISS 2018. NASA-GISS GISS-E2.1G model output prepared for CMIP6 CMIP historical. *Earth System Grid Federation*.

Neubauer, D., Ferrachat, S., Siegenthaler-Le Drian, C., Stoll, J., Folini, D.S., Tegen, I., Wieners, K.-H., Mauritsen, T., Stemmler, I., Barthel, S., Bey, I., Daskalakis, N., Heinold, B. and Kokkola, H, U. 2019. HAMMOZ-Consortium MPI-ESM1.2-HAM model output prepared for CMIP6 CMIP historical. *Earth System Grid Federation*. [Online]. Available from: https://doi.org/10.22033/ESGF/CMIP6.1622.

Nguyen, P., Shearer, E.J., Tran, H., Ombadi, M., Hayatbini, N., Palacios, T., Huynh, P., Braithwaite, D., Updegraff, G., Hsu, K., Kuligowski, B., Logan, W.S. and Sorooshian, S. 2019. The CHRS data portal, an easily accessible public repository for PERSIANN global satellite precipitation data. *Scientific Data*. **6**, pp.1–10.

De Noblet-Ducoudré, N., Boisier, J.P., Pitman, A., Bonan, G.B., Brovkin, V., Cruz, F., Delire, C., Gayler, V., Van Den Hurk, B.J.J.M., Lawrence, P.J., Van Der Molen, M.K., Müller, C., Reick, C.H., Strengers, B.J. and Voldoire, A. 2012. Determining robust impacts of land-use-induced land cover changes on surface climate over North America and Eurasia: Results from the first set of LUCID experiments. *Journal of Climate*. **25**(9), pp.3261–3281.

Pardini, R., Nichols, L. and Püttker, T. 2017. Biodiversity Response to Habitat Loss and Fragmentation. *Encyclopedia of the Anthropocene*. **3**, pp.229–239.

Pitman, A.J., De Noblet-Ducoudré, N., Cruz, F.T., Davin, E.L., Bonan, G.B., Brovkin, V., Claussen, M., Delire, C., Ganzeveld, L., Gayler, V., Van Den Hurk, B.J.J.M., Lawrence, P.J., Van Der Molen, M.K., Müller, C., Reick, C.H., Seneviratne, S.I., Strengen, B.J. and Voldoire, A. 2009. Uncertainties in climate responses to past land cover change: First results from the LUCID intercomparison study. *Geophysical Research Letters*. **36**(14), pp.1–6.

Pongratz, J., Schwingshackl, C., Bultan, S., Obermeier, W., Havermann, F. and Guo, S. 2021. Land Use Effects on Climate: Current State, Recent Progress, and Emerging Topics. *Current Climate Change Reports*. **7**(4), pp.99–120.

Restrepo-Coupe, N., da Rocha, H.R., Hutyra, L.R., da Araujo, A.C., Borma, L.S., Christoffersen, B., Cabral, O.M.R., de Camargo, P.B., Cardoso, F.L., da Costa, A.C.L., Fitzjarrald, D.R., Goulden, M.L., Kruijt, B., Maia, J.M.F., Malhi, Y.S., Manzi, A.O., Miller, S.D., Nobre, A.D., von Randow, C., Sá, L.D.A., Sakai, R.K., Tota, J., Wofsy, S.C., Zanchi, F.B. and Saleska, S.R. 2013. What drives the seasonality of photosynthesis across the Amazon basin? A cross-site analysis of eddy flux tower measurements from the Brasil flux network. *Agricultural and Forest Meteorology*. **182–183**, pp.128–144.

Ridley, J., Menary, M., Kuhlbrodt, T., Andrews, M. and Andrews, T. 2019. MOHC HadGEM3-GC31-MM model output prepared for CMIP6 CMIP historical. *Earth System Grid Federation*. [Online]. Available from: https://doi.org/10.22033/ESGF/CMIP6.420.

Robertson, E. 2019. The local biophysical response to land-use change in HADGEM2-ES. *Journal of Climate*. **32**(22), pp.7611–7627.

Running, S., Mu, Q., Zhao, M. and Moreno, A. 2021. MODIS/Terra Net Evapotranspiration Gap-Filled 8-Day L4 Global 500m SIN Grid V061 [Data set]. *NASA EOSDIS Land Processes DAAC*., https://doi.org/10.5067/MODIS/MOD16A2GF.061.

Sadeghi, M., Nguyen, P., Naeini, M.R., Hsu, K., Braithwaite, D. and Sorooshian, S. 2021. PERSIANN-CCS-CDR, a 3-hourly 0.04° global precipitation climate data record for heavy precipitation studies. *Scientific Data*. **8**(1), pp.1–11.

Schaaf, C. and Wang, Z. 2021. MODIS/Terra+Aqua BRDF/Albedo Daily L3 Global - 500m V061 [Data set]. *NASA EOSDIS Land Processes DAAC*., https://doi.org/10.5067/MODIS/MCD43A3.061.

Seferian, R. 2018. CNRM-CERFACS CNRM-ESM2-1 model output prepared for CMIP6 CMIP historical. *Earth System Grid Federation*. [Online]. Available from: https://doi.org/10.22033/ESGF/CMIP6.4068.

Smith, C., Baker, J.C.A. and Spracklen, D. V 2023. Tropical deforestation causes large reductions in observed precipitation. *Nature*. **615**, pp.270–275.

Spracklen, D. V., Arnold, S.R. and Taylor, C.M. 2012. Observations of increased tropical rainfall preceded by air passage over forests. *Nature*. **489**, pp.282–285.

Spracklen, D. V. and Garcia-Carreras, L. 2015. The impact of Amazonian deforestation on Amazon basin rainfall. *Geophysical Research Letters*. **42**(21), pp.9546–9552.

Staal, A., Flores, B.M., Aguiar, A.P.D., Bosmans, J.H.C., Fetzer, I. and Tuinenburg, O.A. 2020. Feedback between drought and deforestation in the Amazon. *Environmental Research Letters*. **15**(4).

Staal, A., Tuinenburg, O.A., Bosmans, J.H.C., Holmgren, M., Van Nes, E.H., Scheffer, M., Zemp, D.C. and Dekker, S.C. 2018. Forest-rainfall cascades buffer against drought across the Amazon. *Nature Climate Change*. **8**(6), pp.539–543.

Swart, N.C., Cole, J.N.S., Kharin, V. V., Lazare, M., Scinocca, J.F., Gillett, N.P., Anstey, J., Arora, V., Christian, J.R., Jiao, Y., Lee, W.G., Majaess, F., Saenko, O.A., Seiler, C. and Seinen, M. 2019a. CCCma CanESM5 model output prepared for CMIP6 CMIP historical. *Earth System Grid Federation*. [Online]. Available from: https://doi.org/10.22033/ESGF/CMIP6.1301.

Swart, N.C., Cole, J.N.S., Kharin, V. V., Lazare, M., Scinocca, J.F., Gillett, N.P., Anstey, J., Arora, V., Christian, J.R., Jiao, Y., Lee, W.G., Majaess, F., Saenko, O.A., Seiler, C. and Seinen, M. 2019b. CCCma CanESM5-CanOE model output prepared for CMIP6 CMIP historical. *Earth System Grid Federation*. [Online]. Available from: https://doi.org/10.22033/ESGF/CMIP6.10205.

Tang, Y., Rumbold, S., Ellis, R., Kelley, D., Mulcahy, J., Sellar, A., Walton, J. and Jones, C. 2019. MOHC UKESM1.0-LL model output prepared for CMIP6 CMIP historical. *Earth System Grid Federation*. [Online]. Available from: https://doi.org/10.22033/ESGF/CMIP6.6113.

Taylor, C.M., Klein, C., Parker, D.J., Gerard, F., Semeena, V.S., Barton, E.J. and Harris, B.L. 2022. “Late-stage” deforestation enhances storm trends in coastal West Africa. *Proceedings of the National Academy of Sciences*. **119**(2), pp.1–8.

Vancutsem, C., Achard, F., Pekel, J.F., Vieilledent, G., Carboni, S., Simonetti, D., Gallego, J., Aragão, L.E.O.C. and Nasi, R. 2021. Long-term (1990–2019) monitoring of forest cover changes in the humid tropics. *Science Advances*. **7**(10), pp.1–22.

Virtanen, P., Gommers, R., Oliphant, T.E., Haberland, M., Reddy, T., Cournapeau, D., Burovski, E., Peterson, P., Weckesser, W., Bright, J., van der Walt, S.J., Brett, M., Wilson, J., Millman, K.J., Mayorov, N., Nelson, A.R.J., Jones, E., Kern, R., Larson, E., Carey, C.J., Polat, \.Ilhan, Feng, Y., Moore, E.W., VanderPlas, J., Laxalde, D., Perktold, J., Cimrman, R., Henriksen, I., Quintero, E.A., Harris, C.R., Archibald, A.M., Ribeiro, A.H., Pedregosa, F., van Mulbregt, P. and SciPy 1.0 Contributors 2020. {SciPy} 1.0: Fundamental Algorithms for Scientific Computing in Python. *Nature Methods*. **17**, pp.261–272.

Volodin, E., Mortikov, E., Gritsun, A., Lykossov, V., Galin, V., Diansky, N., Gusev, A., Kostrykin, S., Iakovlev, N., Shestakova, A. and Emelina, S. 2019a. NM INM-CM4-8 model output prepared for CMIP6 CMIP historical. *Earth System Grid Federation*. [Online]. Available from: https://doi.org/10.22033/ESGF/CMIP6.1422.

Volodin, E., Mortikov, E., Gritsun, A., Lykossov, V., Galin, V., Diansky, N., Gusev, A., Kostrykin, S., Iakovlev, N., Shestakova, A. and Emelina, S. 2019b. NM INM-CM5-0 model output prepared for CMIP6 CMIP historical. *Earth System Grid Federation*. [Online]. Available from: https://doi.org/10.22033/ESGF/CMIP6.1423.

Wan, Z., Hook, S. and Hulley, G. 2021. MODIS/Terra Land Surface Temperature/Emissivity 8-Day L3 Global 1km SIN Grid V061 [Data set]. *NASA EOSDIS Land Processes DAAC*., https://doi.org/10.5067/MODIS/MOD11A2.061.

Werth, D. and Avissar, R. 2005. The local and global effects of African deforestration. *Geophysical Research Letters*. **32**(12), pp.1–4.

Winckler, J., Reick, C.H., Bright, R.M. and Pongratz, J. 2019. Importance of Surface Roughness for the Local Biogeophysical Effects of Deforestation. *Journal of Geophysical Research: Atmospheres*. **124**(15), pp.8605–8618.

Winckler, J, Reick, C.H., Luyssaert, S., Cescatti, A., Stoy, P.C., Lejeune, Q., Raddatz, T., Chlond, A., Heidkamp, M. and Pongratz, J. 2019. Different response of surface temperature and air temperature to deforestation in climate models. *Earth System Dynamics*. **10**(3), pp.473–484.

Winckler, J., Reick, C.H. and Pongratz, J. 2017. Robust identification of local biogeophysical effects of land-cover change in a global climate model. *Journal of Climate*. **30**(3), pp.1159–1176.

Windisch, M.G., Davin, E.L. and Seneviratne, S.I. 2021. Prioritizing forestation based on biogeochemical and local biogeophysical impacts. *Nature Climate Change*. **11**(10), pp.867–871.

Wolff, N.H., Masuda, Y.J., Meijaard, E., Wells, J.A. and Game, E.T. 2018. Impacts of tropical deforestation on local temperature and human well-being perceptions. *Global Environmental Change*. **52**(December 2017), pp.181–189.

Xie, P., Joyce, R., Wu, S., Yoo, S.-H., Yarosh, Y., Sun, F. and Lin, R. 2019. NOAA Climate Data Record (CDR) of CPC Morphing Technique (CMORPH) High Resolution Global Precipitation Estimates, Version 1. *NOAA National Centers for Environmental Information*., https://doi.org/10.25921/w9va-q159.

Zemp, D.C., Schleussner, C.F., Barbosa, H.M.J., Hirota, M., Montade, V., Sampaio, G., Staal, A., Wang-Erlandsson, L. and Rammig, A. 2017. Self-amplified Amazon forest loss due to vegetation-atmosphere feedbacks. *Nature Communications*. **8**, pp.1–10.

Zhuang, J. 2022. xESMF. Available from: https://doi.org/10.5281/zenodo.1134365.

Ziehn, T., Chamberlain, M., Lenton, A., Law, R., Bodman, R., Dix, M., Wang, Y., Dobrohotoff, P., Srbinovsky, J., Stevens, L., Vohralik, P., Mackallah, C., Sullivan, A., O'Farrell, S. and Druken, K. 2019. CSIRO ACCESS-ESM1.5 model output prepared for CMIP6 CMIP historical historical. *Federation, Grid Earth System*. [Online]. Available from: https://doi.org/10.22033/ESGF/CMIP6.4272.

Chapter 6

6 Conclusions

6.1 Synthesis of Findings

This thesis sought to explore and provide answers to the question of how tropical deforestation affects local climate. In Chapter 3 I investigated the local climate impacts on land surface temperature arising from tropical deforestation. I built upon existing knowledge that states tropical forest loss causes local warming, by investigating the role of the driver of forest loss on the warming. I showed that commodity driven forest loss drives up to triple the warming of forest loss due to shifting agriculture (Figure 6.1). This has strong implications for regions such as the Congo where forest loss is projected to transition away from shifting agriculture to commodity driven over the next century, resulting in intensified warming.

Following on, Chapter 4 presents published research showing evidence of large reductions in precipitation due to tropical forest loss. Here I analysed 18 satellite, station-based and reanalysis precipitation datasets across a range of spatial scales, demonstrating a clear link between increasing spatial scale of forest loss and larger reductions in rainfall (Figure 6.1). From this, I estimated that projected forest loss this century will decrease precipitation by 8-10% in the Congo, where LCC is predicted to be the most severe.

Lastly, I presented submitted research which evaluated using observations, the skill of CMIP6 climate models at simulating the climate response due to forest loss. I found that models can accurately simulate temperature changes due to forest loss, but they have less consistent skill at simulating the observed reduction in precipitation (Figure 6.1). The simulated temperature and precipitation responses depended on the change in surface albedo, with less warming and drying in models with greater increases in albedo due to forest loss.

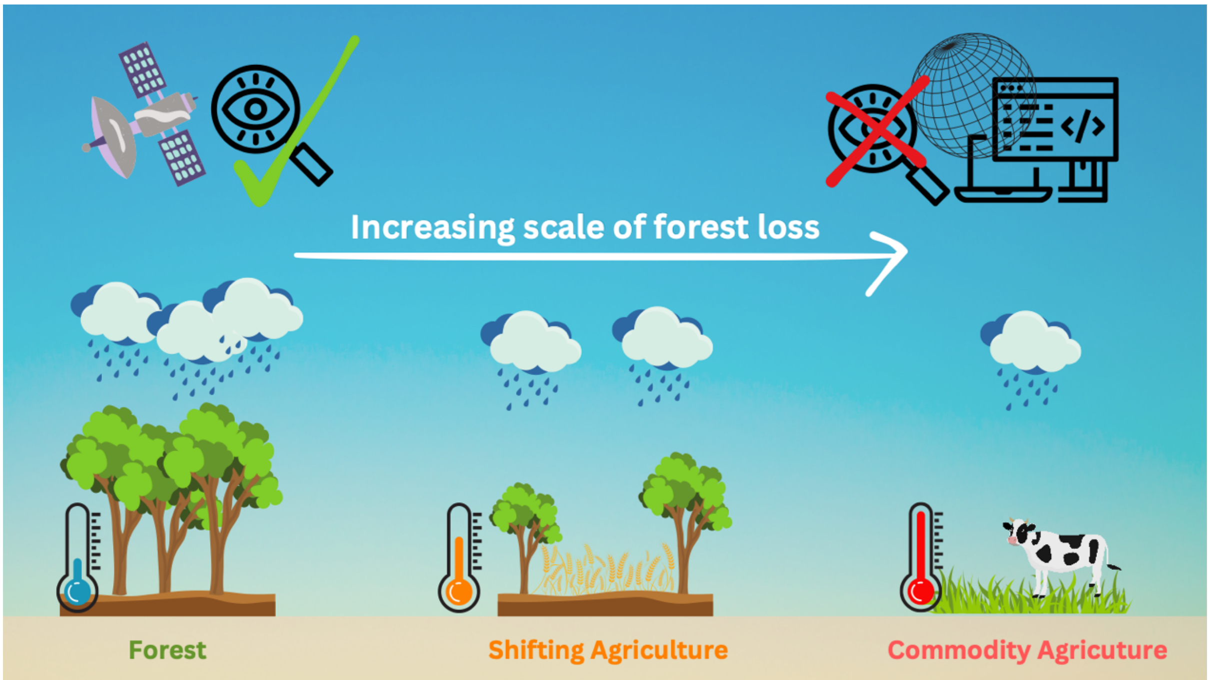

Figure 6.1. *Schematic highlighting the main findings of this thesis. Forest loss warms and dries the local climate. These impacts are more severe with a transition to more industrial and larger spatial scale deforestation. Satellite observations can unpick these trends in temperature and precipitation, whilst climate models can simulate changes in temperature accurately, but not precipitation.*

6.2 Key Results and Discussion

6.3 The Driver of Forest Loss Matters

In spite of concerted efforts from governments, NGOs and local communities, the rate of tropical deforestation has yet to robustly decline (Curtis et al., 2018; Feng et al., 2022). In Brazil, whilst policy initiatives have resulted in a shift from large-scale commodity driven deforestation to smaller scale pervasive deforestation (Rosa et al., 2012; Kalamandeen et al., 2018; Escobar, 2019; Montibeller et al., 2020), in other tropical regions, such as the Congo large-scale deforestation is becoming more common-place (Tegegne et al., 2016; Austin et al., 2017).

In Chapter 3 we quantified the impact that the type of deforestation had on the local climate, through examining the changes in tropical forest cover over the period 2001 - 2019.

We found that across the tropics daytime land surface temperatures warmed by 0.014 K/% due to forest loss and that this warming is strongest over regions that had been deforested by commodity agriculture (0.02 K/%). This type of deforestation is characterised by large-scale industrial clear felling for the purpose of cattle rearing or cash crops such as soya. Over regions deforested by shifting agriculture, where land is periodically cleared for small-scale agricultural purposes, the warming is 0.009 K/%, less than half the observed warming of areas deforested by commodity agriculture. This result has particularly strong implications for the Congo, where it is projected that forest loss will become more commodity based (Tegegne et al., 2016) in the future, which could result in increased warming.

When compared to shifting agriculture, areas experiencing commodity driven deforestation see greater total amounts of forest loss. Across the tropics, we showed that the temperature response to forest loss increased linearly. Correspondingly total deforestation would lead to ~1.5 K of warming in areas deforested by commodity agriculture (~0.9 K for shifting agriculture). These values are similar to those seen in other studies observing warming due to tropical forest loss. Alkama and Cescatti (2016) show around 1.53 K warming with total forest loss, whilst Prevedello et al. (2019) find 1.08 K for 50% forest loss (comparing well our value of 0.95 K). The greater total amount of forest loss therefore only goes someway to explaining the greater warming seen in areas of commodity driven forest loss. Other possibilities are that regions of shifting agriculture regrow as a result of land abandonment, leading to a reduced warming over time. Similar to the work of Poorter et al. (2021), further analysis would need to assess the impact of secondary regrowth on the warming response.

Communities that live in the tropical forests and surrounding regions are aware of and appreciate the cooling benefit that forests provide (Wolff et al., 2018). Continuing rates of tropical forest loss will contribute to the climate warming that in the coming decades will make the tropical regions more inhospitable for human life (Masuda et al., 2020; Masuda et al., 2021; and references therein). The warming will also impact the ability of forests to store carbon (Li et al., 2022), in effect compounding the warming due to climate change further. Combined, the local climate impacts of forest loss make for compelling evidence, which alongside improved understanding and prediction of weather and climate changes (Senior et al., 2021) can help inform and enact policy to move away from destructive environmental practices.

6.3.1 Observations of Reductions in Rainfall due to Forest Loss

In Chapter 4 we analysed 10 satellite precipitation datasets, finding robust reductions in rainfall as a result of forest loss, particularly strongly at the largest spatial scales. We found there was a strong scale dependence, whereby at small scales (5 - 50 km length scales), there was no substantial change to precipitation. At scales greater than 50 km, there was a robust decline in precipitation up to 0.25 mm month-1 per percentage point of forest loss.

The maintenance of consistent precipitation is aided by the forest's own existence, through the recycling of precipitated water (Eltahir and Bras, 1996). The availability of rainfall and stored rainwater is crucial for agriculture (Zemp et al., 2014), hydropower (Strand et al., 2018) and human populations. The process of precipitation recycling occurs at scales of around 600 km in the tropics (Van Der Ent and Savenije, 2011; Staal et al., 2018), so our analysis, which had a maximum scale of 200 km was unable to fully capture this process, likely underestimating the impact of forest loss on precipitation. Studies show that forest loss is likely to interrupt this crucial process, reducing the transport of moisture which is essential for downwind forests and communities (Zemp et al., 2017; Xu, Zhang, et al., 2022). Using a combination of observations and models (both moisture and atmosphere), Staal, Fetzer, et al. (2020) find this recycling, or forest-precipitation feedback enhances the geographic range that tropical forests can exist in, therefore reductions in rainfall could reduce their viable range. The southwestern Amazon is the furthest forested area from the oceanic moisture source, and as such relies on upwind forests for its moisture, with up to 70% coming from upwind ET (Van Der Ent et al., 2010; Sorí et al., 2017). This reliance on upwind conditions places regions such as the SW Amazon in a precarious position where their resilience is dependent on the forest as a whole.

The analysis in Chapter 4 considers the tropical impacts of forest loss, however there are likely different climate responses in regions with different mechanisms or climatologies (Taylor et al., 2013; Taylor et al., 2022). In West Africa, Taylor et al. (2022) find that deforestation enhances precipitation, due to increased afternoon storm frequency and that precipitation impacts scale with spatial scale of forest loss. In coastal regions, Taylor et al. (2022) find a doubling in frequency of storms, due to the enhancement of land-sea mesoscale convection. These findings highlight the importance of mesoscale dynamics and soil-moisture (Taylor et al., 2013) in driving changes to precipitation. They provide additional insight into why we might find differences in rainfall response between the continental Amazon and the coastal SEA.

The reductions that we observed in tropical precipitation have far reaching consequences that span society, yet the impacts are unequal. These changes to forest structure and functioning will have impacts on species composition (Esquivel-Muelbert et al., 2019), carbon sequestration (Li et al., 2022) and fire frequency (Aragão et al., 2008). Consumers in the global north are sheltered from the direct impacts of forest loss, whilst tropical communities, who are often poorer are strongly affected (Mills Busa, 2013). Consumers can use their influence and purchasing power to dissuade tropical governments from incentivising destructive practices. A successful policy example is Brazil's Soy Moratorium which produced significant decreases in deforestation (84% decrease between 2004 – 2012 (Heilmayr et al., 2020)) in response to pressure from NGOs. Deforestation from soy decreased to 1% of pre-moratorium expansion, with part of the success due to tracking farms which continued to deforest using satellite and airborne sensing (Gibbs et al., 2015).

As a result of reductions in rainfall due to forest loss, we estimate that crop yields will decline by 1.25% for each 10-percentage point loss of forest cover (Challinor et al., 2014). The decline of agricultural yields may incentivise further deforestation (Leite-Filho et al., 2021) and more intensive fertiliser use to keep up with production demand. With further deforestation, precipitation will decline again, compounding the issue (Zemp et al., 2017; Leite-Filho et al., 2021; Wunderling et al., 2022). Staal, Flores, et al. (2020) highlight this by estimating deforestation has caused 4% of the recent observed drying in the Amazon, with the reinforcing drought-deforestation feedback predicted to become stronger with greater cumulative deforestation.

These decreases are in addition to a backdrop of climate change, which will make rainfall more variable and exacerbate the extreme droughts and floods (Seneviratne et al., 2021).

Climate change has been linked to increasing dry-season length in the Amazon and Congo in recent years (Marengo et al., 2018; Jiang et al., 2019) and deforestation has the potential to further shift and modify these seasons (Leite-Filho et al., 2019). In addition to being impacted by land cover change, rainfall can be impacted by the shifting and modifying of the dry season (Khanna et al., 2017). These changes may move rainfall geographically with increases downwind of forest loss and decreases upwind. These changes could lead to increased drought and subsequent forest dieback, ultimately leading to a tipping point (Lovejoy and Nobre, 2018).

In Chapter 4 we showed that for sustained habitability of the tropics, we must drastically reduce forest loss in order to abate reductions in rainfall and the precipitous decline of the species who live there. Despite decades of calls from around the globe to halt deforestation, rates are still increasing (Feng et al., 2022). As we pass another year, with global communities increasingly aware of the impact we have on our planet, we must maintain pressure on governments to uphold current and future commitments to deforestation reductions.

6.3.2 Models Struggle to Simulate Drying due to Forest Loss

Bringing together our understanding of the impacts of forest loss on local climate, we evaluated the skill of the CMIP6 models at simulating observed warming and drying in the tropics. Our analysis jointly focussed on evaluating the skill of the models and understanding the reasons they exhibited that behaviour. 23 of the 24 CMIP6 models analysed, accurately simulated warming due to forest loss, however the response of precipitation due to forest loss was divergent.

Several studies have previously investigated the changes that forest loss can have on simulated climate, each with different results. Boysen et al. (2020) found reduced cloud cover from idealised deforestation in CMIP5 models led to increased shortwave radiation and LST, and a dominance over surface albedo changes. This is opposed by an observational study from Duveiller et al. (2021) in which they show that forest loss can increase low level cloud, which can act to increase LST. Considering the impact on ET from forest loss, Luo et al. (2022) showed how reductions in ET were four times greater than the reductions in mean flow convergence suggesting, as observed by others (Baker and Spracklen, 2019), that ET flux is the dominant reason warming occurs due to forest loss. Our analysis showed that the simulated response of LST and precipitation to forest loss depended on the change in simulated albedo. There was less drying and less warming in models with larger increases in surface albedo. This indicates that albedo is an important value to model accurately in order to correctly simulate land surface impacts on climate.

As we considered in Chapter 4 when examining the impacts of observed forest loss on precipitation, land cover changes can affect the frequency, intensity and location of precipitation (Leite-Filho et al., 2021; Taylor et al., 2022; Commar et al., 2023). Whilst our analysis evaluated average changes, we didn’t quantify spatial and temporal shifts in simulated precipitation changes due to forest loss. Further work should examine these processes and build upon existing knowledge of the important role of precipitation recycling (Spracklen et al., 2012; Zemp et al., 2017; Staal et al., 2018; Baker and Spracklen, 2022) and the detriment that forest loss can have on this process. Considering the global impacts of tropical forest loss, deforestation can impact precipitation across continents through teleconnections (Werth and Avissar, 2005; Pitman et al., 2009; De Noblet-Ducoudré et al., 2012; Luo et al., 2022). Evaluating the differing ability of models to simulate these changes and how observations could be used to verify this, is a clear next step.

Overall, the findings of this thesis highlight the importance of forest conservation by observing significant increases in temperature and reductions in precipitation due to forest loss (Figure 6.2). Climate models can also simulate these changes, validating their projections of future land cover impacts on climate. As shown in Figure 6.2, these changes will have a range of impacts, spanning beyond the well understood carbon implications (Seymour et al., 2022). Forest loss will negatively impact agriculture (Lawrence and Vandecar, 2015; Leite-Filho et al., 2021), surrounding forests (Foley et al., 2007; Zemp et al., 2017; Staal, Fetzer, et al., 2020; Li et al., 2022), carbon storage (Li et al., 2022), biodiversity (Pardini et al., 2017) and human health (Wolff et al., 2018; Alves de Oliveira et al., 2021).

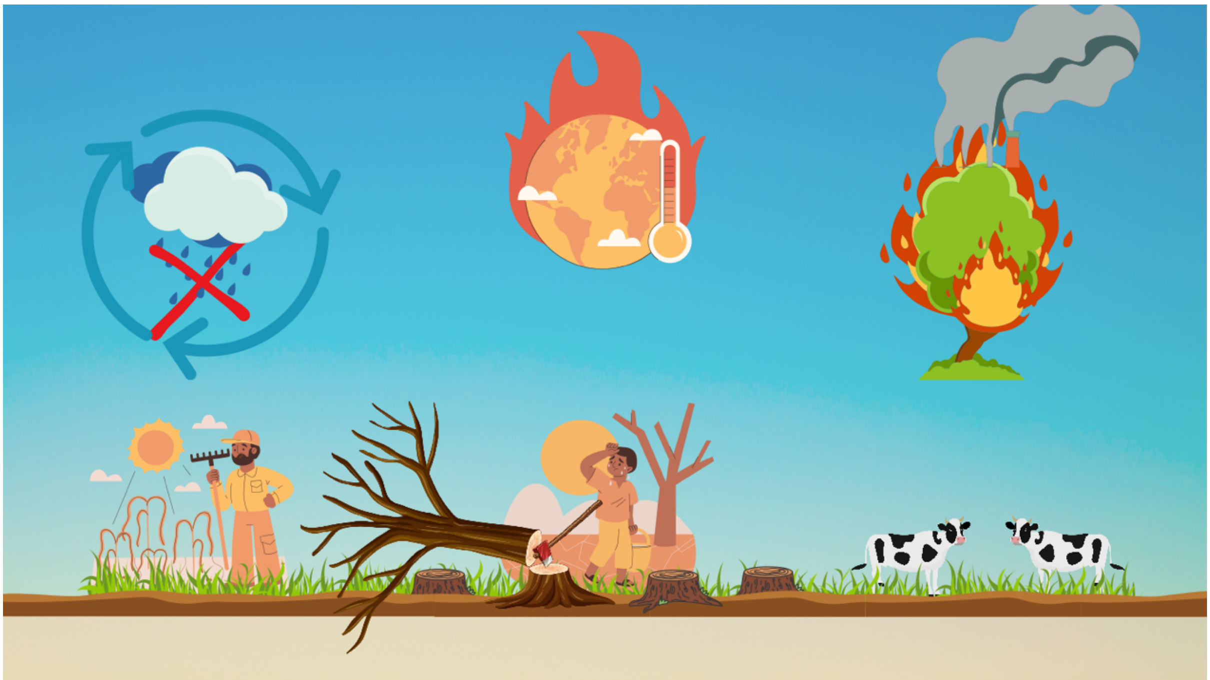

Figure 6.2. *Schematic outlining the main implications of tropical forest lost. Tropical forest leads to warming and drying, which can feedback, enhancing further forest loss. Agriculture, biodiversity, carbon storage and humans are negatively impacted as a result of forest loss. Forest loss can be driven, or drive fires which can worsen air quality.*

Life in the tropics will also be adversely impacted by increased forest fire risk (Escobar, 2019; Davies-Barnard et al., 2023) as remaining forests dry out, secondarily causing increases in particulate matter which will have local, regional and global health impacts (Butt et al., 2020). In addition to health impacts, smoke from fires will have potential positive climate feedbacks (Cochrane et al., 1999). Humans, animals and plants will be displaced in great numbers in coming decades as climate change creates increasingly inhospitable environments (Berchin et al., 2017). These changes will be compounded by forest loss (Flores and Staal, 2022), adding to the importance and urgency of conserving the remaining forests and afforesting where appropriate. The analysis throughout this thesis provides strong evidence and impetus for governments and communities around the world to adhere to net zero emission and deforestation pledges and policies.

6.4 Discussion of Uncertainties and Limitations

Uncertainty exists in a variety of settings throughout this thesis and can be broadly broken down into three main areas: observational, modelling and analytical uncertainty. Specific uncertainties are considered in the individual analysis chapters (3 - 5) whilst here I provide an overview of some of the larger sources of uncertainties and limitations.

6.4.1 Observational Uncertainty and Limitations

There is inherent uncertainty built into the observational datasets used in this thesis. Remotely sensed observations from instruments onboard satellites are subject to errors and have an associated uncertainty attached to them. Sources of uncertainty arise both from sensing the radiation and the mathematical derivation of quantities which can contain approximations or parametrisations (Zhao et al., 2020). Cloud is a persistent issue affecting the quality of remotely sensed datasets. For most of the datasets used in this thesis, a quality control layer was supplied, allowing the user to self-determine which level of quality control they wish to apply. Throughout, we have selected pixels that are subject to clear sky and where applicable, of 'good' data quality. This ensures that we selected the best possible quality data to use. This process is limited by the quality of the cloud assessment for each of the products, with each instrument providing a different determination of what constitutes a cloudy scene. This creates a limitation whereby each product's cloudy scene doesn't necessarily overlap, so each quality control routine isn't comparable.

In the tropics, forests have very dense canopy covers, which create issues for accurately assessing LAI from both the ground and remotely (Fang et al., 2019). In Chapters 3 and 5 we assess the changes in LAI due to forest loss, finding there to be a variable and inconsistent change. This could in part be explained by LAI and NDVI saturation, whereby dense, multi-layered canopies become indistinguishable as they approach the maximum values. This can potentially lead to under/overestimating the change in LAI due to forest loss as saturated values are retrieved using a look up table of values (Fang et al., 2019) determined by MODIS land cover. Fang et al. (2019) state that LAI saturation could be mitigated by using narrower band reflectance (Diner et al., 1999; Gemmell and McDonald, 2000) or non-parametric machine learning such as gaussian regression (Verrelst et al., 2015).

All land surface products face challenges in representing the land surface accurately, especially when pixels fall on transitions between different land cover types. In the case of MODIS LST, the assumption is that the pixel can be quantified using the different spectral emissions and the thermal infrared band, however this may not always be reliable, especially on land cover boundaries or where there are sub-grid fires (Wan, 1999). Common to all remotely sensed products is their uncertainty generated when surveying topographically complex or structurally heterogenous areas. Since high resolution digital elevation models aren't always integrated into the algorithms which generate these datasets (Wan, 1999), there is uncertainty inherent. This can arise when fires within the shadows of hills return lower values than they should due to the shadow producing a band reflectivity that is close to zero. Similarly, in rugged terrain, radiation can be scattered randomly by complex surfaces, meaning it is difficult to completely correct for radiation originating from adjacent pixels (Wan, 1999).

ET is highly derived from other proxy quantities and computed using the Penman-Monteith equations (Monteith, 1965), more information about this can be found in Chapter 2. There are several sources of uncertainty associated with this product and its derivation. Firstly, and most importantly, MOD16A2GF relies heavily on MODIS land cover type, which is a 17-class land cover classification map (Running et al. 1994, Belward et al. 1999, Friedl et al. 2010). The main limitation to using the approach is that there is an assumption that the biome specific parameters from which ET is derived, do not change with space within the biome nor time throughout the year. Borrowing the example given in the MOD16 user guide, "... a semi-desert grassland in Mongolia is treated the same as a tallgrass prairie in the Midwestern United States. Likewise, a sparsely vegetated boreal evergreen needleleaf forest in Canada is functionally equivalent to its coastal temperate evergreen needleleaf forest counterpart" (Running et al., 2021). In addition to this, a known limitation of the MODIS land cover dataset is that the relatively coarse spatial resolution of 500 m means small-scale croplands are often sub-grid and therefore underrepresented and reported as natural vegetation (Sulla-Menashe and Friedl, 2022). For ET this could result in an overestimated flux as natural vegetation will have higher ET rates than the cropland. A small uncertainty comes from the integration of FPAR/LAI into ET, which is an 8-day composite product and takes only the maximum value of FPAR/LAI across the 8-days. This produces the assumption that LAI doesn't vary within those 8-days, which is a limitation when the ET product is produced daily. This process of maximum selection is necessary in order to create a composite to account for cloud contamination, which is a particular issue in the tropics. Gap-filled ET utilises data from non-cloudy temporally adjacent scenes to fill in scenes where there is cloud present. This process artificially inserts data where other remotely sensed products, such as MODIS LAI and albedo don't retrieve, creating an inconsistency and a limitation when comparing the datasets.

MODIS ET is a daily product, taking meteorological inputs including air temperature, incident PAR and specific humidity, provided by NASA's Global Modelling and Assimilation Office (GMAO or MERRA GMAO). These data are derived from a global circulation model which has a resolution of around 0.5°, considerably coarser than the 500 m that ET is presented at. This is a limitation as the assumption is made that the coarse meteorological is representative of the heterogenous surface. To achieve assimilation, the coarse grid data is linearly interpolated, taking data from the four pixels surrounding the 500 m pixel. The quality of this process is assessed using ground-based station data from the World Meteorological Organisation of >5000 stations. This process is a limitation, as in spatially heterogenous areas, with rugged terrain and complex micro-biophysical processes, coarse grid meteorological data won't be sufficient to represent processes at 500 m.

Alongside remotely sensed climate variables, we widely used the Global Forest Change (GFC) dataset (Hansen et al., 2013) to estimate changes in tropical forest cover over time. There are three key limitations of our use this dataset, firstly, forest regrowth is provided only for the years 2001 - 2012 and as such we exclude this from our analysis. Therefore, throughout our analysis we likely mis-calculate the effects of tropical deforestation on climate as it is probable that some forests have regrown partially after being deforested, reducing the change in the surface properties and fluxes. The second key limitation pertains to differences in sensor technology, with the original 2001 - 2012 data using data from Landsat 7 which used a 'whiskbroom' sensor, whereas a 'pushbroom' sensor is used on Landsat 8 and 9. This newer sensor increases per observation dwell time, producing better detection of land cover change and creating an inconsistency through time. As well as sensor changes, the number of viable observations vary through time, generally increasing as the acquisition strategy improves from 150k in the early 2000s to exceeding 250k in 2021.

This notably decreased in 2012 where there <100k observations due to a gap between Landsat 5's decommission and Landsat 8 becoming operational. Both of these factors create issues when comparing changes through time (GLAD, 2023). The third limitation of the GFC data arises from algorithmic changes that were made after 2012. Originally the dataset, based on a machine learning algorithm was trained using one algorithm run, however subsequent years have been added iteratively. This could result in inter-annual inconsistencies (Hansen et al., 2013). Our analysis does not focus on the change in the rate of forest loss over time, so it is not heavily impacted by these uncertainties.

When observing the changes in precipitation due to forest loss, we used data from several station based or merged datasets, which combine satellite and station data. In the tropics, there are very limited numbers of weather stations, especially in the forest interiors. Data is interpolated between stations, providing accurate data within the well covered mid-latitudes, but less reliable data in the sparsely surveyed tropical forests (Schneider et al., 2022). This affects station-based datasets, but also merged datasets which integrate or validate using station data.

We take steps to mitigate these limitations, notably by not comparing the forest cover change as a time series, which is as discussed would pose problems due to substantial inter-annual inconsistency. Similarly, we tested our results by carrying out several methodological sensitivity tests to ensure robustness.

6.4.2 Model Uncertainty and Limitations

Climate models carry inherent uncertainty, which can come from a variety of sources, such as parameterisations, the quality of forecasts and projected scenarios. In this thesis, I used historical simulations from the CMIP6 climate models to assess the impact of historical land use change on climate. The most relevant aspect of uncertainty is how well the models can represent sub-grid processes in parametrisations.

A substantial element contributing to uncertainty is our ability to represent clouds (Seneviratne et al., 2021). Clouds are difficult to simulate, and they have great importance as they can both warm and cool the atmosphere and land surface. At local scales, the formation or not of clouds can be strongly altered by the land surface (Yue et al., 2017). On hot days or over warm surfaces, convection can drive rainfall, which can occur on short time scales and over small distances (Cutrim et al., 2002). The coarse grid of climate models can't capture these events (Birch et al., 2015), so models use parametrisations to represent the average of all the processes. This creates a limitation for observing direct changes from land use change which are often sub-grid in scale, particularly in areas experiencing patchy or shifting deforestation. In Chapter 5 I evaluated the ability of CMIP6 models to represent change in rainfall due to deforestation. There is a substantial spread of results, with some models finding increases in rainfall, whilst others find decreases. This uncertainty could in part be due to the different resolutions of the models and how they parametrise sub-grid processes. ET is another process that may provide a source of model uncertainty. We found some models show ET increases (Figure 5.4) with deforestation, which is the opposite to observed changes shown by (Chen and Dirmeyer, 2020). This is a known problem in several climate models (Cai et al., 2019) and could be responsible for some of the inter-model variability in precipitation response. Future atmospheric CO_2 increases will provide another source of uncertainty as they can modify the land surface properties and fluxes. These CO_2 increases may drive reductions in ET via the plant physiological effect (Chadwick et al., 2019), which will affect the water budget of some tropical regions. This is strongly region dependent and will likely feedback into further land cover change as a result of drought and warming.

6.4.3 Analytical Uncertainty and Limitations

As well as observational and simulated uncertainty, some analytical methods used in this thesis carry uncertainty. We attempted where possible to add robustness to the discussed results by completing sensitivity analysis. An example of which is in Chapter 4 where we tested the effect of different analysis period lengths, finding that our results are insensitive to this change. Despite this, there are still areas where our methods are limited or carry uncertainty.

In Chapter 4 we calculated future precipitation changes due to forest loss based on our understanding of the historical precipitation change. Here we estimated that forest loss in the future will linearly impact precipitation. There is evidence, that we (Extended Data Figure B.1) and others (Akkermans et al., 2014; Lawrence and Vandecar, 2015; Zemp et al., 2017; Baudena et al., 2021; Wunderling et al., 2022) present, that suggests that future changes in land cover could drive linear or non-linear changes to precipitation. In this way, we likely underestimate the impacts of deforestation on rainfall.

We calculated the difference in climate and land surface variables over relatively short time periods, less than 20 years. We took account of inter-annual variability by predominantly using 5 year averages at the start and end periods to calculate the change over time. Whilst we have shown there to be little difference between 3 and 5 year averages (Extended Data Figure B.3), 5 years is still short enough for large scale climate oscillations (such as ENSO) to potentially influence our results. We tested for the impact of El Niño on our results (shown in Extended Data Figure B.3) by shifting the analysis period outside of the strong 2015/16 El Niño period, finding consistent results.

A source of uncertainty, previously discussed, is the climate impact of forest regrowth. Throughout this analysis we used the GFC forest loss dataset, which excludes forest regrowth. In this way, we expect to underestimate the impacts of forest loss on climate, as vegetation replacing clear-cut will have climate and land surface properties more similar to the forests, they replaced (Poorter et al., 2021). In SEA, land is predominantly deforested for oil palm plantations. Sabajo et al. (2017) show that compared to clear cut land, young oil palm has a lower warming impact, which then decreases further when the plantation matures.

The choice of grid size is differently important for different climate and land surface variables. For mechanistic changes that occur on sub-grid scales, such as LST changes, the smallest analysis scales we use (5 km grid length) will average many sub-grid processes. Studies such as Sabajo et al. (2017) use very high-resolution land surface temperature (30 m) and land classification data to unpick specific case differences. As computing resources improve, researchers can utilise fully the very high resolution remotely sensed datasets that have recently become available, through which we can produce a more detailed picture of the impact of land use change on local climate. The impacts of land use change on precipitation are less dependent on very high-resolution data as the effects are often not local to the change and are spread over far larger areas. However, this presents a different source of uncertainty, namely attributing changes in precipitation to specific changes in land cover. The methods used in Chapter 4 assume that average land cover changes within a grid box correspond to precipitation changes in surrounding grid boxes. At small scales of deforestation, precipitation can increase, however we are unable to view this mechanism possibly because the scale of analysis is too coarse, but also because our analysis method cannot attribute specific forest loss to specific non-local precipitation changes.

When calculating the climate and land surface property changes in the wet and dry season, I calculated the wettest and driest three months of each year for each pixel. This allows for the possibility that the months selected won't be consecutive and may vary year to year. The impact of this is complicated to assess as the impact is likely to be small when averaged across all analysed data points. As we controlled for differences in background climate, the impact of inter-annual background temperature variability will be small, however it will carry a small uncertainty.

6.5 Future Research Directions

Much of the work in this thesis focusses on the local and semi-regional climate impacts of deforestation. Predominantly, previous studies such as Li et al. (2015); Alkama and Cescatti (2016); Li et al. (2016); Bright et al. (2017); Baker and Spracklen (2019) have taken similar approaches. There are several ways in which our understanding of the local and regional impacts of forest loss can be improved, which I detail below.

6.5.1 Non-local Climate Impacts of Deforestation

Recently the work of Cohn et al. (2019) has explored the regional climate impacts of deforestation, opening up a new range of remote-sensing research possibilities with their novel methodology. Cohn et al. (2019) show us that tropical land use change can have impacts on maximum air temperature up to 50 km from the site of disturbance. Zeppetello et al. (2020) similarly found warming due to forest loss increases with the size of disturbance. Considering precipitation, several studies show (Staal et al., 2018; O'Connor et al., 2021; and references therein) forest loss can negatively impact downwind precipitation. These studies often use lagrangian moisture tracking models (or atmospheric back trajectory models) to quantify the precipitation, or lack thereof transport, enabling a window into the regional impacts of land cover change. These studies outline the significance of considering remote impacts and how the local climate changes we observe, may in fact be influenced by surrounding disturbances. Using approaches that consider how climate impacts can overlap and interfere constructively or destructively is crucial to fully assess the effects that land use change can have.

Adjacent to this, building on our knowledge of the effectiveness of protected areas (Xu, Huang, et al., 2022), further work could be completed to analyse the potential for their relatively cool and wet climate to spill-over into surrounding forest or agriculture. A study which can quantify the economic benefit of this effect would be strong evidence to provide a case for their protection and expansion.

6.5.2 High Temporal and Spatial Resolution Analysis

Over the last decade, there have been huge leaps in the quality and availability of remote sensing data. Freely available satellite products now provide ultra-high resolution (<30 m) images of changes in land cover, surface properties and fluxes. These advances have been matched with increasing computing resources and the ability to process and analyse large amounts of data. Alongside this, the total observed record has been increasing, such that for commonly analysed quantities such as land surface temperature and precipitation, we have over 40 years' worth of data. With these long time series and high-resolution datasets, we can provide robust conclusions about the impacts of land use change on climate, and it provides the opportunity to observe mechanisms that previously weren't possible. For example, accurately and precisely remotely observing the effect of forest fragmentation on microclimate wasn't previously possible with 500 m resolution data, however with 2-30 m spatial resolution data we can start to isolate these impacts more confidently. It is also now possible to create satellite ensemble mean changes using the range of satellite products to create a more robust value, for example it is possible to use the freely available data from MODIS, Landsat and Palsar to create a land surface temperature ensemble.

Many of the studies described in this thesis focus on the climate impacts of tropical deforestation, however significant land use change occurs throughout the world (Hansen et al., 2013; Song et al., 2018; Potapov et al., 2022). In Europe, which has historically been heavily deforested, there is the opportunity for large scale reforestation. Models investigating the climate impacts of LCC find only small changes in precipitation (Strandberg and Kjellström, 2019), whilst Meier et al. (2021) show observationally, that reforestation can increase precipitation in the summer by 7.6%. In the mid-latitudes where there is expected to be large scale reforestation, climate change assessments can take advantage of the new generation of high temporal and spatial resolution observational datasets to unravel trends in often difficult to identify young forest growth.

In recent years, space borne lidar such as the Global Ecosystem Dynamics Investigation (GEDI) (Dubayah et al., 2021) have provided very high-resolution surface structure and height data, enabling the analysis of global canopy structure. This dataset could be utilised as a proxy for surface roughness and allow for the remote quantification of temperature and precipitation changes due to roughness changes.

With more data than ever being available at sub-daily time steps, we can accurately build a picture of how land use change can affect climate throughout the day. This allows us to calculate maximum and minimum temperatures as well as peak rainfalls, providing greater insight into the impacts of forest loss on climate extremes. Of particular interest to the people who live in tropical regions is the temperature and precipitation during extreme events of drought, flood and heatwave (Wolff et al., 2018; Zeppetello et al., 2020; Masuda et al., 2020). Temperature extremes are strong constraints on agricultural productivity (Challinor et al., 2014; Cohn et al., 2019) and as with all extremes, can have strongly non-linear impacts (Schlenker and Roberts, 2009; Lobell et al., 2013). These impacts can be explored using metrics such as wet bulb temperature, an often-cited metric for human habitability (Masuda et al., 2021). Alongside observations, climate models are critical to advancing our understand of climate extremes, however traditional cloud parametrising models inherently have difficulty accurately assessing impacts, especially in maritime regions such as SEA (Birch et al., 2015). Chapman et al. (2023) show that using convection permitting models, precipitation extremes can be simulated effectively, allowing us a window to view the future impacts of forest loss on climate. Further work that analyses the impacts of deforestation on extremes using these techniques, is crucial to abate forced climate change migration and maintain habitability.

6.5.3 Post-deforestation Climate Impacts

Largely the changes that occur after deforestation are overlooked by climate studies, therefore understanding how the land cover that replaces forest can evolve and how this can affect climate is important for future studies to consider. Adams and Garcia-Carreras (2023) consider how climate impacts vary with time after deforestation for a site in Africa, however this study could be expanded to span the tropics, allowing for an examination across different biomes and a wider range of deforestation trajectories. In the bigger picture, this analysis could provide evidence for how quickly replanting or secondary regrowth could reach climate equivalence of the previously situated primary forests and indeed whether it is a realistic ambition that these benefits could be restored. Datasets that track evolving land cover such as MapBiomass (MapBiomass, 2023), TerraClass (Almeida et al., 2008) and Vancutsem et al. (2021) would be able to provide insight into regrowth through time in the tropical forest regions.

The final main area for future research is to utilise machine learning techniques to project and simulate the impacts of future and present land use change on climate. Several studies and projects currently use machine learning to identify and classify tropical deforestation (Hansen et al., 2013; Curtis et al., 2018; and references therein). Using similar techniques and existing understanding of the climate impacts of historical deforestation, we could simulate the climate impacts of unseen, future deforestation. This could produce a powerful persuasive tool, providing evidence to the public and policy makers that persevering our remaining forests is an essential endeavour.

References

Adams, C.E. and Garcia-Carreras, L. 2023. Detection of Land-Use Change and Rapid Recovery of Vegetation after Deforestation in the Congo Basin. *Earth Interactions*. **27**(1), pp.1–12.

Akkermans, T., Thiery, W. and Van Lipzig, N.P.M. 2014. The regional climate impact of a realistic future deforestation scenario in the congo basin. *Journal of Climate*. **27**(7), pp.2714–2734.

Alkama, R. and Cescatti, A. 2016. Biophysical climate impacts of recent changes in global forest cover. *Science*. **351**(6273), pp.600–604.

Almeida, C.A. De, Coutinho, A.C., César, J., Mora, D., Adami, M., Venturieri, A., Diniz, C.G., Dessay, N., Durieux, L. and Gomes, A.R. 2008. High spatial resolution land use and land cover mapping of the Brazilian Legal Amazon in 2008 using Landsat-5 / TM and MODIS data. *Acta Amazonica*. **46**(3), pp.291–302.

Alves de Oliveira, B.F., Bottino, M.J., Nobre, P. and Nobre, C.A. 2021. Deforestation and climate change are projected to increase heat stress risk in the Brazilian Amazon. *Communications Earth and Environment*. **2**(1), pp.1–8.

Aragão, L.E.O.C., Malhi, Y., Barbier, N., Lima, A., Shimabukuro, Y., Anderson, L. and Saatchi, S. 2008. Interactions between rainfall, deforestation and fires during recent years in the Brazilian Amazonia. *Philosophical Transactions of the Royal Society B: Biological Sciences*. **363**(1498), pp.1779–1785.

Austin, K.G., González-Roglich, M., Schaffer-Smith, D., Schwantes, A.M. and Swenson, J.J. 2017. Trends in size of tropical deforestation events signal increasing dominance of industrial-scale drivers. *Environmental Research Letters*. **12**(5).

Baker, J.C.A. and Spracklen, D. V 2019. Climate Benefits of Intact Amazon Forests and the Biophysical Consequences of Disturbance. *Frontiers in Forests and Global Change*. **2**, pp.1–13.

Baker, J.C.A. and Spracklen, D. V. 2022. Divergent Representation of Precipitation Recycling in the Amazon and the Congo in CMIP6 Models. *Geophysical Research Letters*. **49**(10), pp.1–11.

Baudena, M., Tuinenburg, O.A., Ferdinand, P.A. and Staal, A. 2021. Effects of land-use change in the Amazon on precipitation are likely underestimated. *Global Change Biology*. **27**(21), pp.5580–5587.

Berchin, I.I., Valduga, I.B., Garcia, J. and de Andrade Guerra, J.B.S.O. 2017. Climate change and forced migrations: An effort towards recognizing climate refugees. *Geoforum*. **84**(June), pp.147–150.

Birch, C.E., Roberts, M.J., Garcia-Carreras, L., Ackerley, D., Reeder, M.J., Lock, A.P. and Schiemann, R. 2015. Sea-breeze dynamics and convection initiation: The influence of convective parameterization in weather and climate model biases. *Journal of Climate*. **28**(20), pp.8093–8108.

Boysen, L.R., Brovkin, V., Pongratz, J., Lawrence, D.M., Lawrence, P., Vuichard, N., Peylin, P., Liddicoat, S., Hajima, T., Zhang, Y., Rocher, M., Delire, C., Séférian, R., Arora, V.K., Nieradzik, L., Anthoni, P., Thiery, W., Laguë, M.M., Lawrence, D. and Lo, M.H. 2020. Global climate response to idealized deforestation in CMIP6 models. *Biogeosciences*. **17**(22), pp.5615–5638.

Bright, R.M., Davin, E., O'Halloran, T., Pongratz, J., Zhao, K. and Cescatti, A. 2017. Local temperature response to land cover and management change driven by non-radiative processes. *Nature Climate Change*. **7**(4), pp.296–302.

Butt, E.W., Conibear, L., Reddington, C.L., Darbyshire, E., Morgan, W.T., Coe, H., Artaxo, P., Brito, J., Knote, C. and Spracklen, D. V 2020. Large air quality and human health impacts due to Amazon forest and vegetation fires. *Environmental Research Communications*. **2**(9), p.095001.

Cai, X., Riley, W.J., Zhu, Q., Tang, J., Zeng, Z., Bisht, G. and Randerson, J.T. 2019. Improving Representation of Deforestation Effects on Evapotranspiration in the E3SM Land Model. *Journal of Advances in Modeling Earth Systems*. **11**(8), pp.2412–2427.

Chadwick, R., Ackerley, D., Ogura, T. and Dommenget, D. 2019. Separating the Influences of Land Warming, the Direct CO2 Effect, the Plant Physiological Effect, and SST Warming on Regional Precipitation Changes. *Journal of Geophysical Research: Atmospheres*. **124**(2), pp.624–640.

Challinor, A.J., Watson, J., Lobell, D.B., Howden, S.M., Smith, D.R. and Chhetri, N. 2014. A meta-analysis of crop yield under climate change and adaptation. *Nature Climate Change*. **4**(4), pp.287–291.

Chapman, S., Bacon, J., Birch, C.E., Pope, E., Marsham, J.H., Msemo, H., Nkonde, E., Sinachikupo, K. and Vanya, C. 2023. Climate Change Impacts on Extreme Rainfall in Eastern Africa in a Convection-Permitting Climate Model. *Journal of Climate*. **36**(1), pp.93–109.

Chen, L. and Dirmeyer, P.A. 2020. Reconciling the disagreement between observed and simulated temperature responses to deforestation. *Nature Communications*. **11**(1), pp.1–10.

Cochrane, M.A., Alencar, A., Schulze, M.D., Souza, C.M., Nepstad, D.C., Lefebvre, P. and Davidson, E.A. 1999. Positive feedbacks in the fire dynamic of closed canopy tropical forests. *Science*. **284**(5421), pp.1832–1835.

Cohn, A.S., Bhattarai, N., Campolo, J., Crompton, O., Dralle, D., Duncan, J. and Thompson, S. 2019. Forest loss in Brazil increases maximum temperatures within 50 km. *Environmental Research Letters*. **14**(8).

Commar, L.F.S., Abrahão, G.M. and Costa, M.H. 2023. A possible deforestation-induced synoptic-scale circulation that delays the rainy season onset in Amazonia. *Environmental Research Letters*. **18**(4).

Curtis, P.G., Slay, C.M., Harris, N.L., Tyukavina, A. and Hansen, M.C. 2018. Classifying drivers of global forest loss. *Science*. **361**(6407), pp.1108–1111.

Cutrim, E., Martin, D.W. and Rabin, R. 2002. Enhancement of Cumulus Clouds over Deforested Lands in Amazonia. *Bulletin of the American Meteorological Society*. **76**(10), pp.1801–1805.

Davies-Barnard, T., Catto, J.L., Harper, A.B., Imron, M.A. and Frank van Veen, F.J. 2023. Future fire risk under climate change and deforestation scenarios in tropical Borneo. *Environmental Research Letters*. **18**(2).

Diner, D.J., Asner, G.P., Davies, R., Knyazikhin, Y., Muller, J.P., Nolin, A.W., Pinty, B., Schaaf, C.B. and Stroeve, J. 1999. New Directions in Earth Observing: Scientific Applications of Multiangle Remote Sensing. *Bulletin of the American Meteorological Society*. **80**(11), pp.2209–2228.

Dubayah, R., Blair, J.B., Beck, J., Wirt, B., Armston, J., Hofton, M., Luthcke, S. and Tang, H. 2021. *GLOBAL Ecosystem Dynamics Investigation (GEDI) Level 2 User Guide For SDPS PGEVersion 3 (P003) of GEDI L2A Data and SDPS PGEVersion 3 (P003) of GEDI L2B Data* [Online]. Available from: https://lpdaac.usgs.gov/documents/986/GEDI02_UserGuide_V2.pdf.

Duveiller, G., Filipponi, F., Ceglar, A., Bojanowski, J., Alkama, R. and Cescatti, A. 2021. Revealing the widespread potential of forests to increase low level cloud cover. *Nature Communications*. **12**(1), pp.1–15.

Eltahir, E.A.B. and Bras, R.L. 1996. Precipitation and Recycling. *Reviews of Geophysics*. **34**(3), pp.367–378.

Van Der Ent, R.J. and Savenije, H.H.G. 2011. Length and time scales of atmospheric moisture recycling. *Atmospheric Chemistry and Physics*. **11**(5), pp.1853–1863.

Van Der Ent, R.J., Savenije, H.H.G., Schaefli, B. and Steele-Dunne, S.C. 2010. Origin and fate of atmospheric moisture over continents. *Water Resources Research*. **46**(9), pp.1–12.

Escobar, H. 2019. Amazon fires clearly linked to deforestation, scientists say. *Science*. **365**(6456), pp.853–853.

Esquivel-Muelbert, A., Baker, T.R., Dexter, K.G., Lewis, S.L., Brienen, R.J.W., Feldpausch, T.R., Lloyd, J., Monteagudo-Mendoza, A., Arroyo, L., Álvarez-Dávila, E., Higuchi, N., Marimon, B.S., Marimon-Junior, B.H., Silveira, M., Vilanova, E., Gloor, E., Malhi, Y., Chave, J., Barlow, J., Bonal, D., Davila Cardozo, N., Erwin, T., Fauset, S., Hérault, B., Laurance, S., Poorter, L., Qie, L., Stahl, C., Sullivan, M.J.P., ter Steege, H., Vos, V.A., Zuidema, P.A., Almeida, E., Almeida de Oliveira, E., Andrade, A., Vieira, S.A., Aragão, L., Araujo-Murakami, A., Arets, E., Aymard C, G.A., Baraloto, C., Camargo, P.B., Barroso, J.G., Bongers, F., Boot, R., Camargo, J.L., Castro, W., Chama Moscoso, V., Comiskey, J., Cornejo Valverde, F., Lola da Costa, A.C., del Aguila Pasquel, J., Di Fiore, A., Fernanda Duque, L., Elias, F., Engel, J., Flores Llampazo, G., Galbraith, D., Herrera Fernández, R., Honorio Coronado, E., Hubau, W., Jimenez-Rojas, E., Lima, A.J.N., Umetsu, R.K., Laurance, W., Lopez-Gonzalez, G., Lovejoy, T., Aurelio Melo Cruz, O., Morandi, P.S., Neill, D., Núñez Vargas, P., Pallqui Camacho, N.C., Parada Gutierrez, A., Pardo, G., Peacock, J., Peña-Claros, M., Peñuela-Mora, M.C., Petronelli, P., Pickavance, G.C., Pitman, N., Prieto, A., Quesada, C., Ramírez-Angulo, H., Réjou-Méchain, M., Restrepo Correa, Z., Roopsind, A., Rudas, A., Salomão, R., Silva, N., Silva Espejo, J., Singh, J., Stropp, J., Terborgh, J., Thomas, R., Toledo, M., Torres-Lezama, A., Valenzuela Gamarra, L., van de Meer, P.J., van der Heijden, G., van der Hout, P., Vasquez Martinez, R., Vela, C., Vieira, I.C.G. and Phillips, O.L. 2019. Compositional response of Amazon forests to climate change. *Global Change Biology*. **25**(1), pp.39–56.

Fang, H., Baret, F., Plummer, S. and Schaepman-Strub, G. 2019. An Overview of Global Leaf Area Index (LAI): Methods, Products, Validation, and Applications. *Reviews of Geophysics*. **57**(3), pp.739–799.

Feng, Y., Zeng, Z., Searchinger, T.D., Ziegler, A.D., Wu, J., Wang, D., He, X., Elsen, P.R., Ciais, P., Xu, R., Guo, Z., Peng, L., Tao, Y., Spracklen, D. V., Holden, J., Liu, X., Zheng, Y., Xu, P., Chen, J., Jiang, X., Song, X.-P., Lakshmi, V., Wood, E.F. and Zheng, C. 2022. Doubling of annual forest carbon loss over the tropics during the early twenty-first century. *Nature Sustainability*. **4**(4), pp.441–451.

Flores, B.M. and Staal, A. 2022. Feedback in tropical forests of the Anthropocene. . (May), pp.1–21.

Foley, J.A., Asner, G.P., Costa, M.H., Coe, M.T., DeFries, R., Gibbs, H.K., Howard, E.A., Olson, S., Patz, J., Ramankutty, N. and Snyder, P. 2007. Amazonia revealed: Forest degradation and loss of ecosystem goods and services in the Amazon Basin. *Frontiers in Ecology and the Environment*. **5**(1), pp.25–32.

Gemmell, F. and McDonald, A.J. 2000. View zenith angle effects on the forest information content of three spectral indices. *Remote Sensing of Environment*. **72**(2), pp.139–158.

Gibbs, H.K., Rausch, L., Munger, J., Schelly, I., Morton, D.C., Noojipady, P., Soares-Filho, B., Barreto, P., Micol, L. and Walker, N.F. 2015. Brazil's Soy Moratorium. *Science*. **347**(6220), pp.377–378.

GLAD 2023. Global Forest Change 2000-2020. *Global Land Analysis and Discovery, University of Maryland*. [Online]. Available from: https://storage.googleapis.com/earthenginepartners-hansen/GFC-2022-v1.10/download.html.

Hansen, M.C., Potapov, P. V., Moore, R., Hancher, M., Turubanova, S.A., Tyukavina, A., Thau, D., Stehman, S. V., Goetz, S.J., Loveland, T.R., Kommareddy, A., Egorov, A., Chini, L., Justice, C.O. and Townshend, J.R.G. 2013. High-Resolution Global Maps of 21st-Century Forest Cover Change. *Science*. **342**(6160), pp.850–853.

Heilmayr, R., Rausch, L.L., Munger, J. and Gibbs, H.K. 2020. Brazil's Amazon Soy Moratorium reduced deforestation. *Nature Food*. **1**(12), pp.801–810.

Jiang, Y., Zhou, L., Tucker, C.J., Raghavendra, A., Hua, W., Liu, Y.Y. and Joiner, J. 2019. Widespread increase of boreal summer dry season length over the Congo rainforest. *Nature Climate Change*., pp.1–8.

Kalamandeen, M., Gloor, E., Mitchard, E., Quincey, D., Ziv, G., Spracklen, D., Spracklen, B., Adami, M., Aragaõ, L.E.O.C., Galbraith, D., Spracklen, B., Mitchard, E., Galbraith, D., Kalamandeen, M., Gloor, E., Aragão, L.E.O.C., Spracklen, D. and Ziv, G. 2018. Pervasive Rise of Small-scale Deforestation in Amazonia. *Scientific Reports*. **8**(1), pp.1–10.

Khanna, J., Medvigy, D., Fueglistaler, S. and Walko, R. 2017. Regional dry-season climate changes due to three decades of Amazonian deforestation. *Nature Climate Change*. **7**(3), pp.200–204.

Lawrence, D. and Vandecar, K. 2015. Effects of tropical deforestation on climate and agriculture. *Nature Climate Change*. **5**(1), pp.27–36.

Leite-Filho, A.T., Soares-Filho, B.S., Davis, J.L., Abrahão, G.M. and Börner, J. 2021. Deforestation reduces rainfall and agricultural revenues in the Brazilian Amazon. *Nature Communications*. **12**(1), pp.1–7.

Leite-Filho, A.T., de Sousa Pontes, V.Y. and Costa, M.H. 2019. Effects of Deforestation on the Onset of the Rainy Season and the Duration of Dry Spells in Southern Amazonia. *Journal of Geophysical Research: Atmospheres*. **124**(10), pp.5268–5281.

Li, Y., Brando, P.M., Morton, D.C., Lawrence, D.M., Yang, H. and Randerson, J.T. 2022. Deforestation-induced climate change reduces carbon storage in remaining tropical forests. *Nature Communications*. **13**(1), pp.1–13.

Li, Y., Zhao, M., Mildrexler, D.J., Motesharrei, S., Mu, Q., Kalnay, E., Zhao, F., Li, S. and Wang, K. 2016. Potential and actual impacts of deforestation and afforestation on land surface temperature. *Journal of Geophysical Research*. **121**(24), pp.14372–14386.

Li, Y., Zhao, M., Motesharrei, S., Mu, Q., Kalnay, E. and Li, S. 2015. Local cooling and warming effects of forests based on satellite observations. *Nature Communications*. **6**, pp.1–8.

Lobell, D.B., Hammer, G.L., McLean, G., Messina, C., Roberts, M.J. and Schlenker, W. 2013. The critical role of extreme heat for maize production in the United States. *Nature Climate Change*. **3**(5), pp.497–501.

Lovejoy, T.E. and Nobre, C. 2018. Amazon Tipping Point. *Science Advances*. **4**(2), p.eaat2340.

Luo, X., Ge, J., Guo, W., Fan, L., Chen, C., Liu, Y. and Yang, L. 2022. The biophysical impacts of deforestation on precipitation: results from the CMIP6 model intercomparison. *Journal of Climate*. **35**(11), pp.3293–3311.

MapBiomass 2023. MapBiomas Amazonía Project - Collection 4 of annual land cover and land use maps. Available from: http://amazonia.mapbiomas.org.

Marengo, J.A., Souza, C.M., Thonicke, K., Burton, C., Halladay, K., Betts, R.A., Alves, L.M. and Soares, W.R. 2018. Changes in Climate and Land Use Over the Amazon Region: Current and Future Variability and Trends. *Frontiers in Earth Science*. **6**(228), pp.1–21.

Masuda, Y.J., Garg, T., Anggraeni, I., Ebi, K., Krenz, J., Game, E.T., Wolff, N.H. and Spector, J.T. 2021. Warming from tropical deforestation reduces worker productivity in rural communities. *Nature Communications*. **12**(1), pp.1–8.

Masuda, Y.J., Garg, T., Anggraeni, I., Wolff, N.H., Ebi, K., Game, E.T., Krenz, J. and Spector, J.T. 2020. Heat exposure from tropical deforestation decreases cognitive performance of rural workers: An experimental study. *Environmental Research Letters*. **15**(12), pp.1–12.

Meier, R., Schwaab, J., Seneviratne, S.I., Sprenger, M., Lewis, E. and Davin, E.L. 2021. Empirical estimate of forestation-induced precipitation changes in Europe. *Nature Geoscience*. **14**(7), pp.473–478.

Mills Busa, J.H. 2013. Deforestation beyond borders: Addressing the disparity between production and consumption of global resources. *Conservation Letters*. **6**(3), pp.192–199.

Monteith, J.L. 1965. Evaporation and Environment. *Symposia of the Society for Experimental Biology*. **19**, pp.205–234.

Montibeller, B., Kmoch, A., Virro, H., Mander, Ü. and Uuemaa, E. 2020. Increasing fragmentation of forest cover in Brazil's Legal Amazon from 2001 to 2017. *Scientific Reports*. **10**(1), pp.1–13.

De Noblet-Ducoudré, N., Boisier, J.P., Pitman, A., Bonan, G.B., Brovkin, V., Cruz, F., Delire, C., Gayler, V., Van Den Hurk, B.J.J.M., Lawrence, P.J., Van Der Molen, M.K., Müller, C., Reick, C.H., Strengers, B.J. and Voldoire, A. 2012. Determining robust impacts of land-use-induced land cover changes on surface climate over North America and Eurasia: Results from the first set of LUCID experiments. *Journal of Climate*. **25**(9), pp.3261–3281.

O'Connor, J.C., Dekker, S.C., Staal, A., Tuinenburg, O.A., Rebel, K.T. and Santos, M.J. 2021. Forests buffer against variations in precipitation. *Global Change Biology*. **27**(19), pp.4686–4696.

Pardini, R., Nichols, L. and Püttker, T. 2017. Biodiversity Response to Habitat Loss and Fragmentation. *Encyclopedia of the Anthropocene*. **3**, pp.229–239.

Pitman, A.J., De Noblet-Ducoudré, N., Cruz, F.T., Davin, E.L., Bonan, G.B., Brovkin, V., Claussen, M., Delire, C., Ganzeveld, L., Gayler, V., Van Den Hurk, B.J.J.M., Lawrence, P.J., Van Der Molen, M.K., Müller, C., Reick, C.H., Seneviratne, S.I., Strengen, B.J. and Voldoire, A. 2009. Uncertainties in climate responses to past land cover change: First results from the LUCID intercomparison study. *Geophysical Research Letters*. **36**(14), pp.1–6.

Poorter, L., Craven, D., Jakovac, C.C., Sande, M.T. Van Der, Amissah, L., Bongers, F., Chazdon, R.L., Farrior, C.E., Kambach, S. and Meave, J.A. 2021. Multidimensional tropical forest recovery. *Science*. **374**(December), pp.1370–1376.

Potapov, P., Turubanova, S., Hansen, M.C., Tyukavina, A., Zalles, V., Khan, A., Song, X.P., Pickens, A., Shen, Q. and Cortez, J. 2022. Global maps of cropland extent and change show accelerated cropland expansion in the twenty-first century. *Nature Food*. **3**(1), pp.19–28.

Prevedello, J.A., Winck, G.R., Weber, M.M., Nichols, E. and Sinervo, B. 2019. Impacts of forestation and deforestation on local temperature across the globe. *PLoS ONE*. **14**(3), pp.1–18.

Rosa, I.M.D., Souza, C. and Ewers, R.M. 2012. Changes in Size of Deforested Patches in the Brazilian Amazon. *Conservation Biology*. **26**(5), pp.932–937.

Running, S., Mu, Q., Zhao, M. and Moreno, A. 2021. *User's Guide: MODIS Global Terrestrial Evapotranspiration (ET) Product* [Online]. Available from: https://lpdaac.usgs.gov/documents/931/MOD16_User_Guide_V61.pdf.

Sabajo, C.R., Knohl, A., le Maire, G., Roupsard, O., June, T. and Meijide, A. 2017. Expansion of oil palm and other cash crops causes an increase of the land surface temperature in the Jambi province in Indonesia. *Biogeosciences*. **14**(20), pp.4619–4635.

Schlenker, W. and Roberts, M.J. 2009. Nonlinear temperature effects indicate severe damages to U.S. crop yields under climate change. *Proceedings of the National Academy of Sciences*. **106**(37), pp.15594–15598.

Schneider, U., Elke, R., Hänsel, S., Finger, P. and Ziese, M. 2022. Monthly Land-Surface Precipitation Climatology for Every Month and the Total Year from Rain-Gauges built on GTS-based and Historical Data. *GPCC Climatology Version 2022 at 0.25°*., 10.5676/DWD_GPCC/CLIM_M_V2022_025.

Seneviratne, S.I., Xuebin Zhang, Muhammad Adnan, Mafae Badi, Claudine Dereczynski, Alejandro Di Luca, Subimal Ghosh, Iskhaq Iskandar, James Kossin, Sophie Lewis, Friederike Otto, Izidine Pinto, Masaki Satoh, Sergio M. Vicente-Serrano, Michael Wehner and Botao Zhou 2021. *Weather and Climate Extreme Events in a Changing Climate*. Cambridge, United Kingdom and New York, NY, USA: Cambridge University Press.

Senior, C.A., Marsham, J.H., Berthou, S., Burgin, L.E., Folwell, S.S., Kendon, E.J., Klein, C.M., Jones, R.G., Mittal, N., Rowell, D.P., Tomassini, L., Vischel, T., Becker, B., Birch, C.E., Crook, J., Dougill, A.J., Finney, D.L., Graham, R.J., Hart, N.C.G., Jack, C.D., Jackson, L.S., James, R., Koelle, B., Misiani, H., Mwalukanga, B., Parker, D.J., Stratton, R.A., Taylor, C.M., Tucker, S.O., Wainwright, C.M., Washington, R. and Willet, M.R. 2021. Convection-permitting regional climate change simulations for understanding future climate and informing decision-making in Africa. *Bulletin of the American Meteorological Society*. **102**(6), pp.E1206–E1223.

Seymour, F., Wolosin, M. and Gray, E. 2022. *Not Just Carbon: Capturing All the Benefits of Forests for Stabilizing the Climate from Local to Global Scales* [Online]. Available from: 10.46830/wrirpt.19.00004.

Song, X.P., Hansen, M.C., Stehman, S. V., Potapov, P. V., Tyukavina, A., Vermote, E.F. and Townshend, J.R. 2018. Global land change from 1982 to 2016. *Nature*. **560**(7720), pp.639–643.

Sorí, R., Nieto, R., Vicente-Serrano, S.M., Drumond, A. and Gimeno, L. 2017. A Lagrangian perspective of the hydrological cycle in the Congo River basin. *Earth System Dynamics*. **8**(3), pp.653–675.

Spracklen, D. V., Arnold, S.R. and Taylor, C.M. 2012. Observations of increased tropical rainfall preceded by air passage over forests. *Nature*. **489**, pp.282–285.

Staal, A., Fetzer, I., Wang-Erlandsson, L., Bosmans, J., Dekker, S., van Nes, E., Rockström, J. and Tuinenburg, O. 2020. Hysteresis of tropical forests in the 21st century. *Nature Communications*. **11**(4978), pp.1–8.

Staal, A., Flores, B.M., Aguiar, A.P.D., Bosmans, J.H.C., Fetzer, I. and Tuinenburg, O.A. 2020. Feedback between drought and deforestation in the Amazon. *Environmental Research Letters*. **15**(4).

Staal, A., Tuinenburg, O.A., Bosmans, J.H.C., Holmgren, M., Van Nes, E.H., Scheffer, M., Zemp, D.C. and Dekker, S.C. 2018. Forest-rainfall cascades buffer against drought across the Amazon. *Nature Climate Change*. **8**(6), pp.539–543.

Strand, J., Soares-Filho, B., Costa, M.H., Oliveira, U., Ribeiro, S.C., Pires, G.F., Oliveira, A., Rajão, R., May, P., van der Hoff, R., Siikamäki, J., da Motta, R.S. and Toman, M. 2018. Spatially explicit valuation of the Brazilian Amazon Forest's Ecosystem Services. *Nature Sustainability*. **1**(11), pp.657–664.

Strandberg, G. and Kjellström, E. 2019. Climate impacts from afforestation and deforestation in Europe. *Earth Interactions*. **23**(1), pp.1–27.

Sulla-Menashe, D. and Friedl, M.A. 2022. *User guide to collection 6 MODIS land cover (MCD12Q1 and MCD12C1) product* [Online]. Available from: https://lpdaac.usgs.gov/documents/1409/MCD12_User_Guide_V61.pdf.

Taylor, C.M., Birch, C.E., Parker, D.J., Dixon, N., Guichard, F., Nikulin, G. and Lister, G.M.S. 2013. Modeling soil moisture-precipitation feedback in the Sahel: Importance of spatial scale versus convective parameterization. *Geophysical Research Letters*. **40**(23), pp.6213–6218.

Taylor, C.M., Klein, C., Parker, D.J., Gerard, F., Semeena, V.S., Barton, E.J. and Harris, B.L. 2022. "Late-stage" deforestation enhances storm trends in coastal West Africa. *Proceedings of the National Academy of Sciences*. **119**(2), pp.1–8.

Tegegne, Y.T., Lindner, M., Fobissie, K. and Kanninen, M. 2016. Evolution of drivers of deforestation and forest degradation in the Congo Basin forests: Exploring possible policy options to address forest loss. *Land Use Policy*. **51**, pp.312–324.

Vancutsem, C., Achard, F., Pekel, J.F., Vieilledent, G., Carboni, S., Simonetti, D., Gallego, J., Aragão, L.E.O.C. and Nasi, R. 2021. Long-term (1990–2019) monitoring of forest cover changes in the humid tropics. *Science Advances*. **7**(10), pp.1–22.

Verrelst, J., Rivera, J.P., Veroustraete, F., Muñoz-Marí, J., Clevers, J.G.P.W., Camps-Valls, G. and Moreno, J. 2015. Experimental Sentinel-2 LAI estimation using parametric, non-parametric and physical retrieval methods - A comparison. *ISPRS Journal of Photogrammetry and Remote Sensing*. **108**, pp.260–272.

Wan, Z. 1999. *MODIS Land-Surface Temperature Algorithm Theoretical Basis Document (LST ATBD)* [Online]. Available from: https://lpdaac.usgs.gov/documents/119/MOD11_ATBD.pdf.

Werth, D. and Avissar, R. 2005. The local and global effects of African deforestation. *Geophysical Research Letters*. **32**(12), pp.1–4.

Wolff, N.H., Masuda, Y.J., Meijaard, E., Wells, J.A. and Game, E.T. 2018. Impacts of tropical deforestation on local temperature and human well-being perceptions. *Global Environmental Change*. **52**, pp.181–189.

Wunderling, N., Staal, A., Sakschewski, B., Hirota, M., Tuinenburg, O.A., Donges, J.F., Barbosa, H.M.J. and Winkelmann, R. 2022. Recurrent droughts increase risk of cascading tipping events by outpacing adaptive capacities in the Amazon rainforest. *Proceedings of the National Academy of Sciences of the United States of America*. **119**(32), pp.1–11.

Xu, X., Huang, A., Belle, E., De Frenne, P. and Jia, G. 2022. Protected areas provide thermal buffer against climate change. *Science Advances*. **8**(44), pp.1–12.

Xu, X., Zhang, X., Riley, W.J., Xue, Y., Nobre, C.A., Lovejoy, T.E. and Jia, G. 2022. Deforestation triggering irreversible transition in Amazon hydrological cycle. *Environmental Research Letters*. **17**(3).

Yue, Q., Kahn, B.H., Fetzer, E.J., Wong, S., Frey, R. and Meyer, K.G. 2017. On the response of MODIS cloud coverage to global mean surface air temperature. *Journal of Geophysical Research*. **122**(2), pp.966–979.

Zemp, D.C., Schleussner, C.F., Barbosa, H.M.J., Van Der Ent, R.J., Donges, J.F., Heinke, J., Sampaio, G. and Rammig, A. 2014. On the importance of cascading moisture recycling in South America. *Atmospheric Chemistry and Physics*. **14**(23), pp.13337–13359.

Zemp, D.C., Schleussner, C.F., Barbosa, H.M.J., Hirota, M., Montade, V., Sampaio, G., Staal, A., Wang-Erlandsson, L. and Rammig, A. 2017. Self-amplified Amazon forest loss due to vegetation-atmosphere feedbacks. *Nature Communications*. **8**, pp.1–10.

Zeppetello, L.R.V., Luke's, L.A., Spector, J.T., Naylor, R.L., Battisti, D.S., Masuda, Y.J. and Wolff, N.H. 2020. Large scale tropical deforestation drives extreme warming. *Environmental Research Letters*. **15**(8).

Zhao, Y., Chen, X., Smallman, T.L., Flack-Prain, S., Milodowski, D.T. and Williams, M. 2020. Characterizing the error and bias of remotely sensed LAI products: An example for tropical and subtropical evergreen forests in South China. *Remote Sensing*. **12**(19), pp.1–20.

Appendix A

Supplementary Materials for Chapter 3

Figures

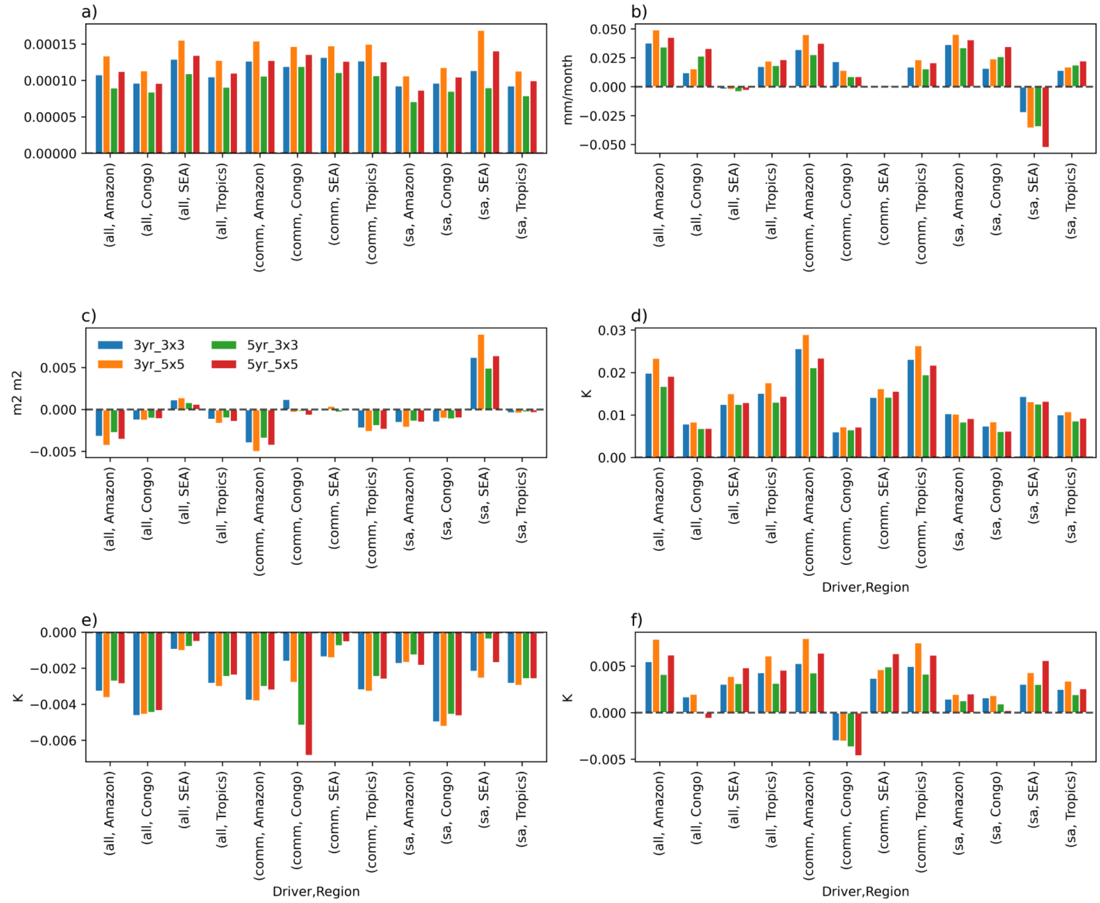

Supplementary Figure A.1. *The change in (a) Black Sky Albedo, b) ET c) LAI, d) LST_{day}, e) LST_{night}, f) $LST_{daynight}$) due to forest loss over time (2001-2019), grouped by region and driver of deforestation (all, commodity driven (comm) and shifting agriculture (SA)). The change in each variable is the change over time (2001-2019) for deforested pixels compared to nearby forested pixels (K). Deforested pixels must have been >90% forest in 2001 and less than 70% by 2019, whilst forest pixels must maintain >90% forest cover. Colours show the sensitivity tests carried out to assess the robustness of the methods used. Here we test using 3 year means at start and end period vs 5 year means (as presented in main text), and 5x5 nearest neighbour grid vs 3x3 grid (as presented in main text).*

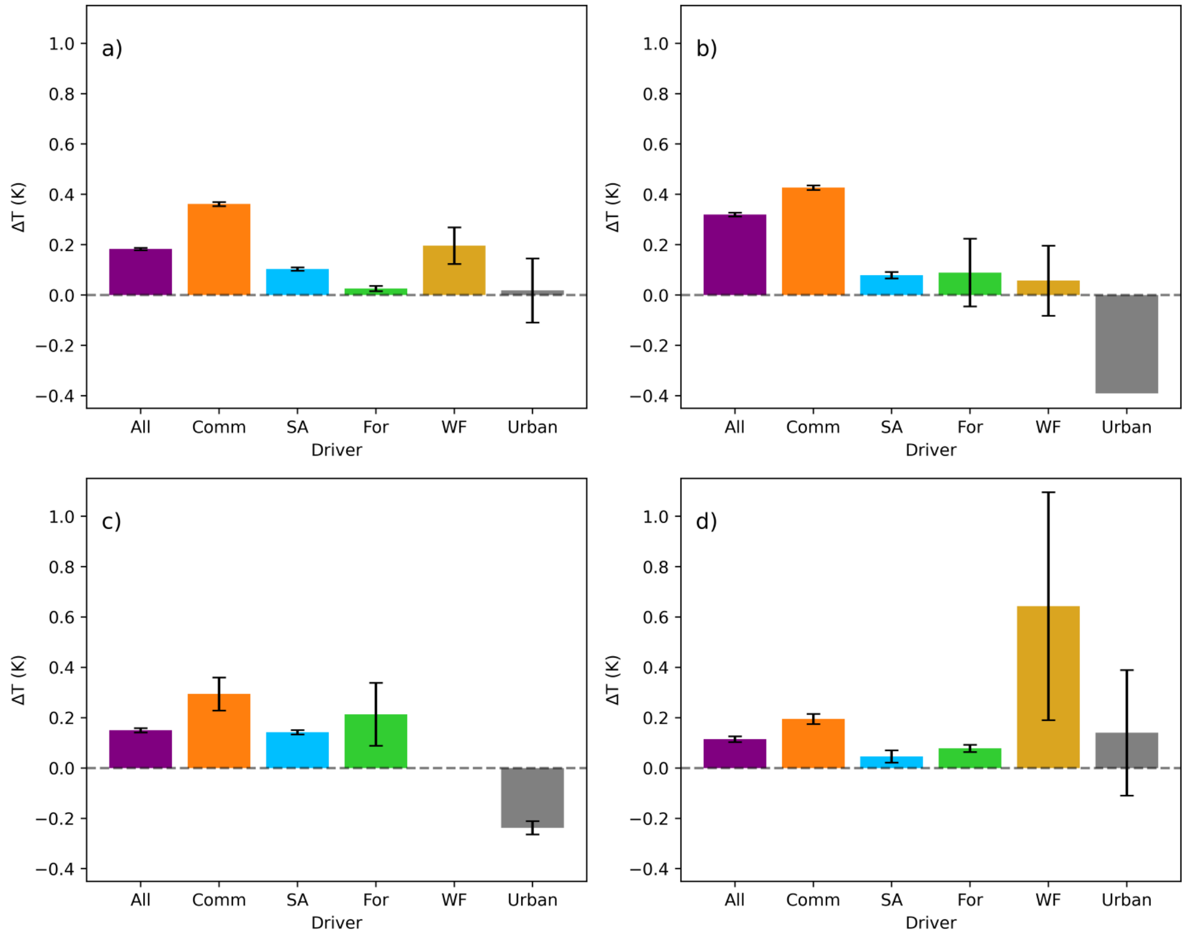

Supplementary Figure A.2. *Change in annual mean land surface temperature due to forest loss for the (a) Tropics, b) Amazon, c) Congo, d) SEA, using an alternative forest-deforestation threshold method. Results are categorised by driver of deforestation (All drivers, Commodity Driven deforestation (Comm.), Shifting Agriculture (SA), Forestry (for), Wildfire (WF) and Urbanisation (Urb)) using data from Curtis et al. (2018). The change in temperature is the change over time (2001-2019) for deforested pixels compared to nearby forested pixels (K). Deforested pixels must have been >70% forest in 2001 and less than 70% by 2019, whilst forest pixels must maintain >70% forest cover. Error bars show the standard error of the mean.*

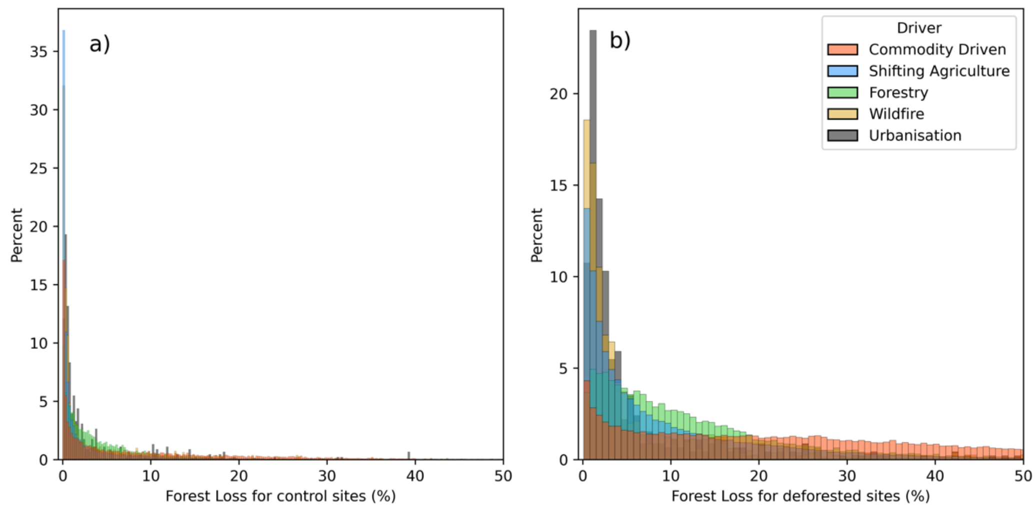

Supplementary Figure A.3. *The distribution of forest loss for control (forest, a) and deforested pixels (b) for each of the deforestation drivers across the tropics.*

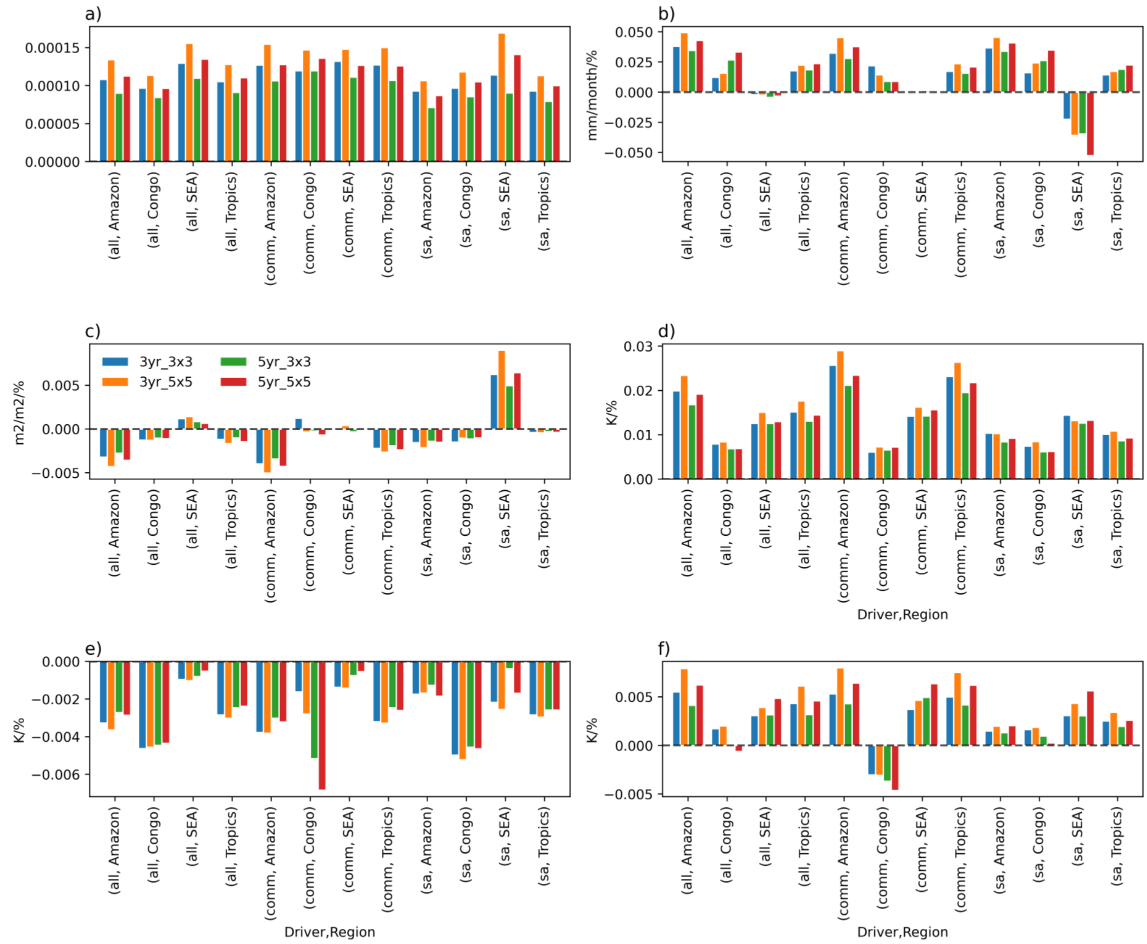

Supplementary Figure A.4. *The change in (a) Black Sky Albedo, b) ET c) LAI, d) LST_{day}, e) LST_{night}, f) $LST_{daynight}$) per percent forest loss over time (2001-2019), grouped by region and driver of deforestation (all, commodity driven (comm) and shifting agriculture (SA)). Colours show the sensitivity tests carried out to assess the robustness of the methods used. Here we test using 3 year means at start and end period vs 5 year means (as presented in main text), and 5x5 nearest neighbour grid vs 3x3 grid (as presented in main text).*

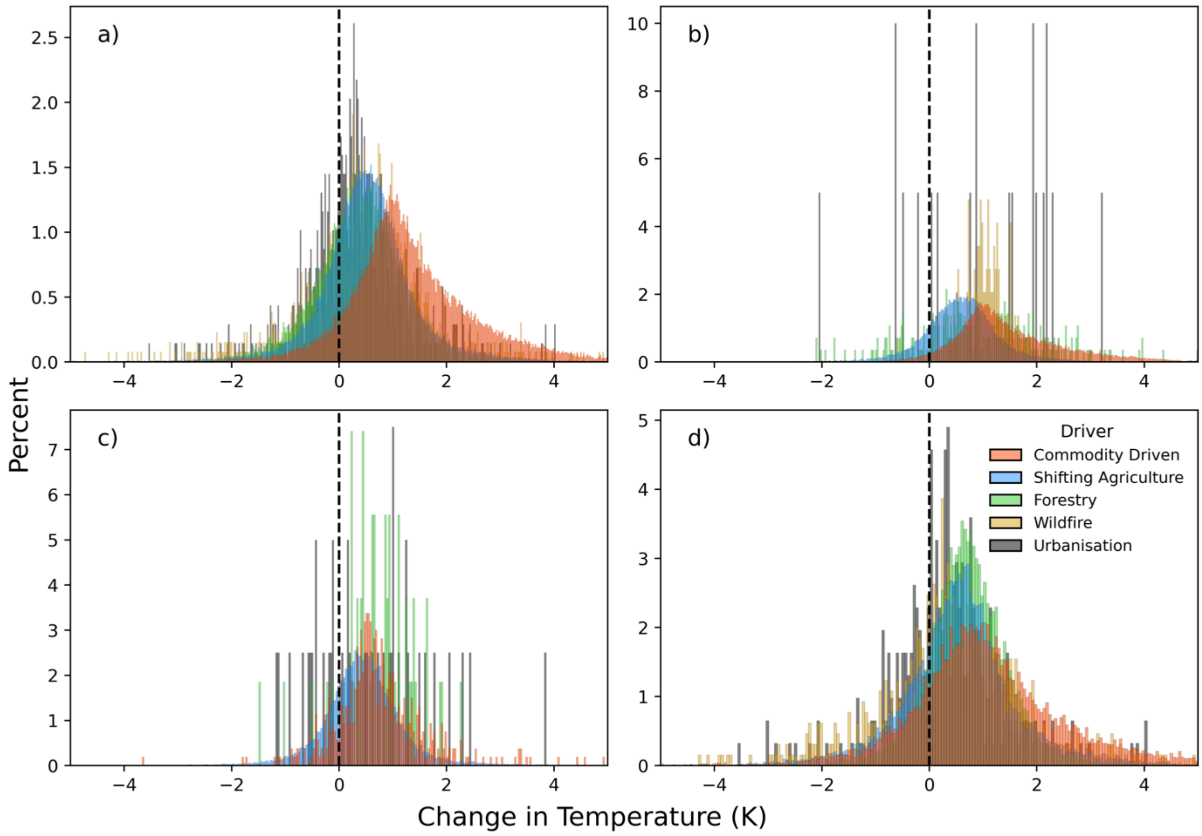

Supplementary Figure A.5. *Histograms showing the change over time in annual mean daytime land surface temperature for the Tropics (a), Amazon (b), Congo (c) and SEA (d). Categories are normalised such that bar heights sum to 100. Forest loss are categorised by driver of deforestation using data from* Curtis et al. (2018). *Results shown for the period 2001-2019, for areas of forest in 2001 as defined by GFC forest cover (Hansen et al., (2013) and the MODIS evergreen broadleaf biome.*

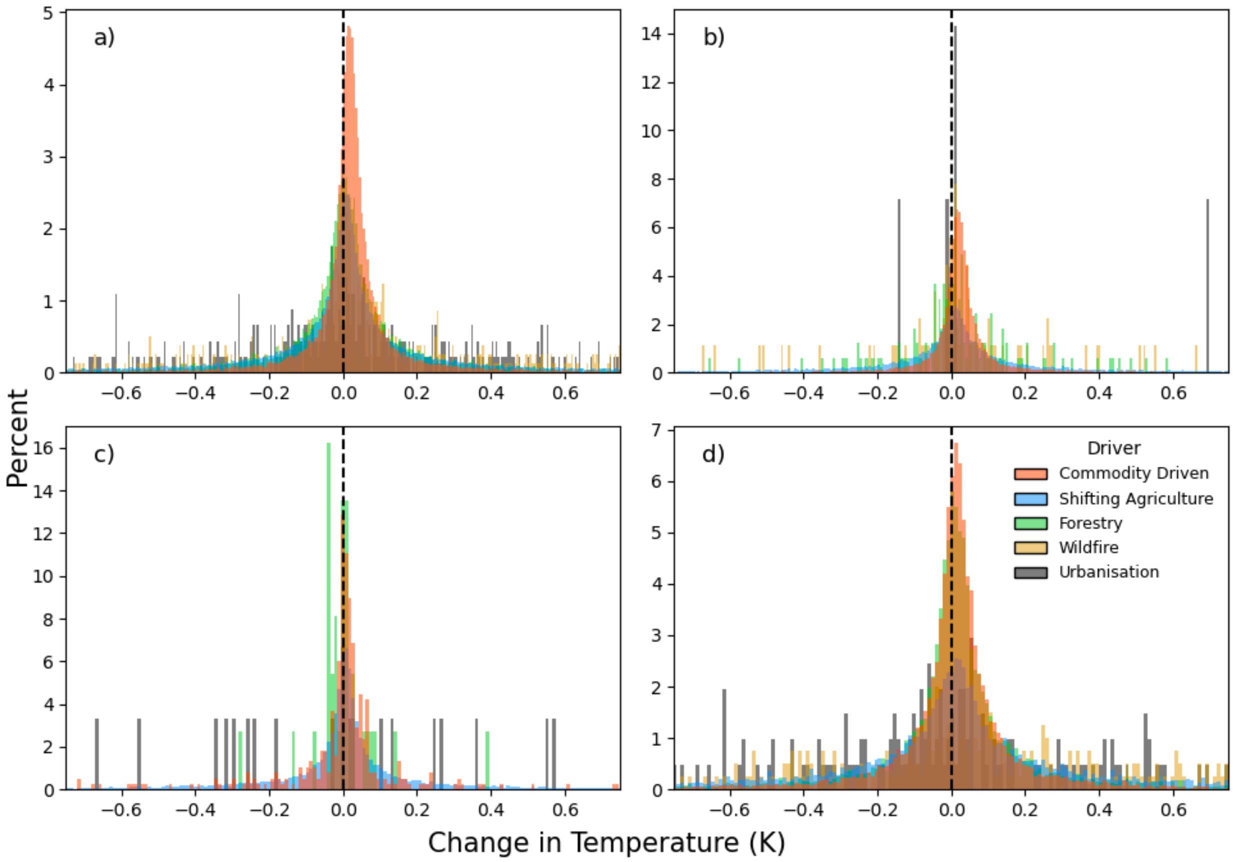

Supplementary Figure A.6. *Histograms showing the change in annual mean daytime land surface temperature due to forest loss for the Tropics (a), Amazon (b), Congo (c) and SEA (d). Categories are normalised such that bar heights sum to 100. Forest loss are categorised by driver of deforestation using data from* Curtis et al. (2018). *Results shown for the period 2001-2019, for areas of forest in 2001 as defined by GFC forest cover (Hansen et al., (2013) and the MODIS evergreen broadleaf biome.*

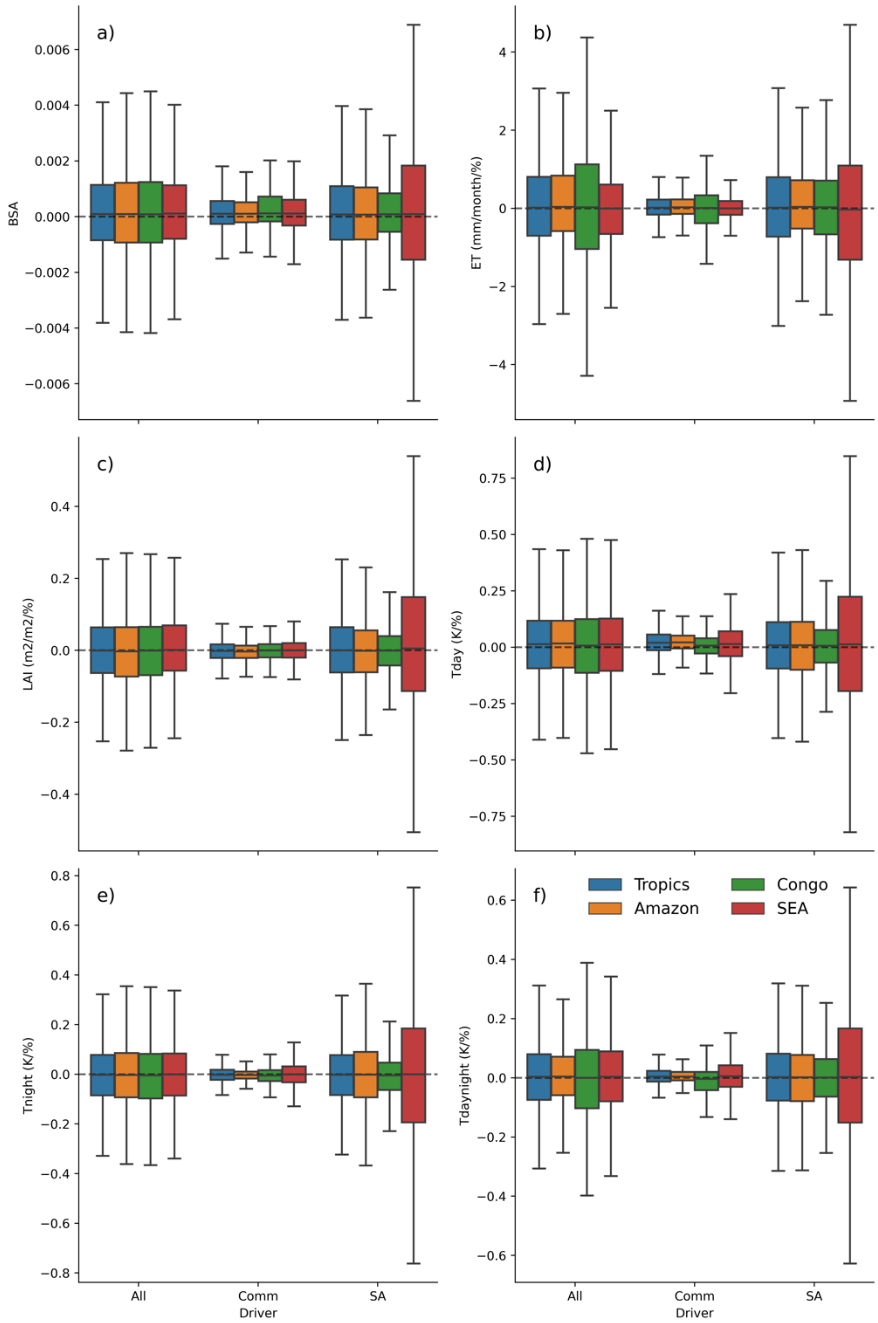

Supplementary Figure A.7. *The distribution of changes in each variable (a) BSA, b) ET c) LAI, d) LST $_{day}$, e) LST$_{night}$, f) LST$_{daynight}$) due to forest loss using the threshold analysis method. Deforested pixels transition from >90% forest cover to <70% forest cover over the period 2001-2019, whereas forest maintains >90% forest cover. Results are grouped by region (Tropics, Amazon, Congo and SEA) and driver of deforestation (All, commodity driven (Comm) and shifting agriculture (SA)).*

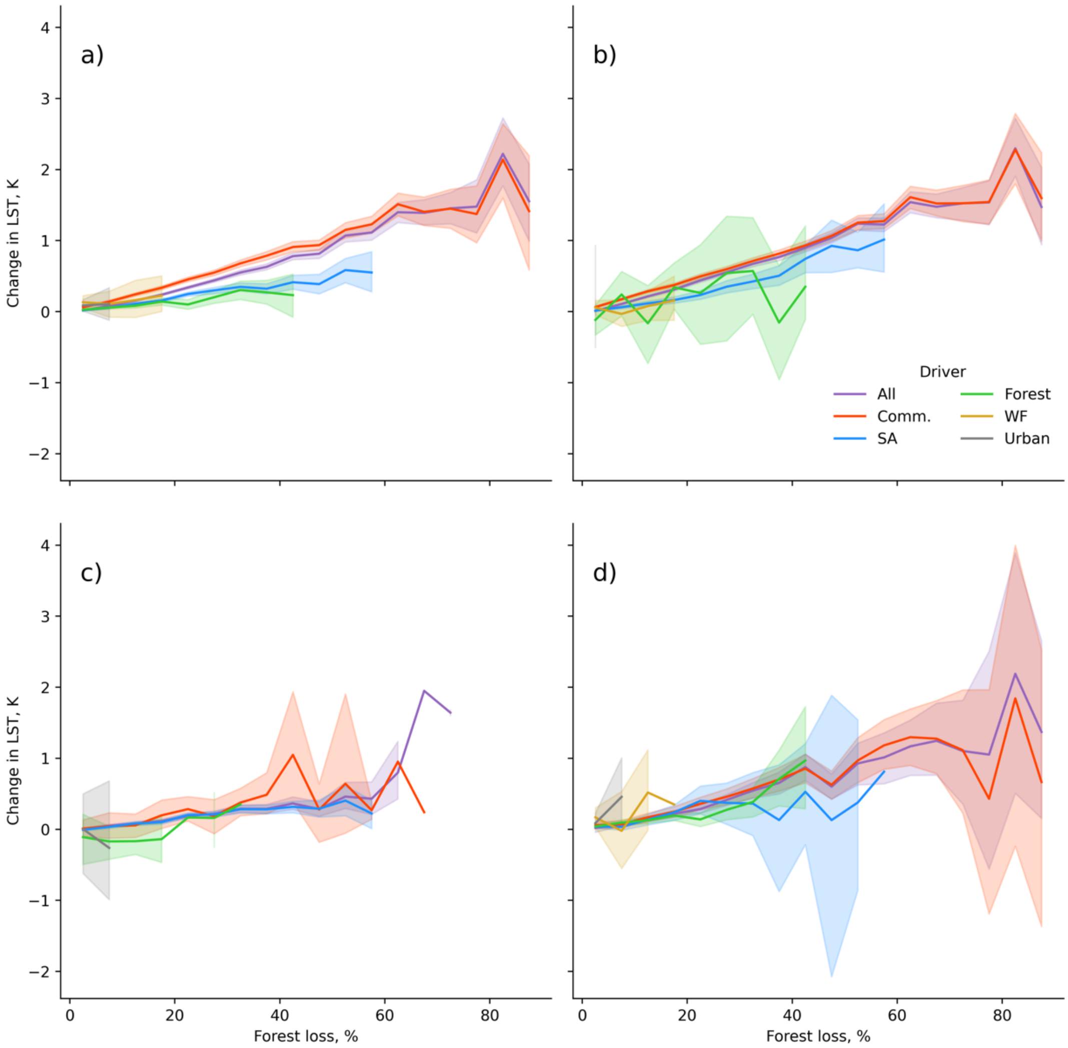

Supplementary Figure A.8. *Change in land surface temperature by forest loss for each region ((a) Tropics, b) Amazon, c) Congo and d) SEA) and each driver of deforestation (All drivers (All), commodity driven deforestation (Comm.), shifting agriculture (SA), forestry (Forest), wildfire (WF) and urbanisation (Urban)). Results are binned with widths of 2.5% forest loss, with each bin plotting the median value within the bin. To be plotted, each bin must have >20 data points. Additionally, no data points with >90% forest loss are included. The line shading shows the 95% confidence interval.*

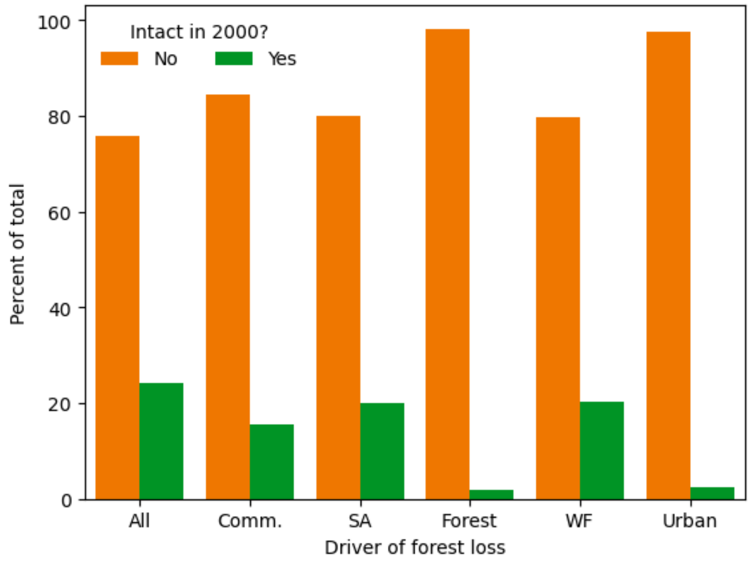

Supplementary Figure A.9. *The percentage of deforested pixels in the per percentage point of forest loss analysis, grouped by driver of deforestation (All drivers (All), commodity driven deforestation (Comm.), shifting agriculture (SA), forestry (Forest), wildfire (WF) and urbanisation (Urban)) and by their intact status in the year 2000, as defined by the Intact Forest Landscapes dataset (Potapov et al., 2017).*

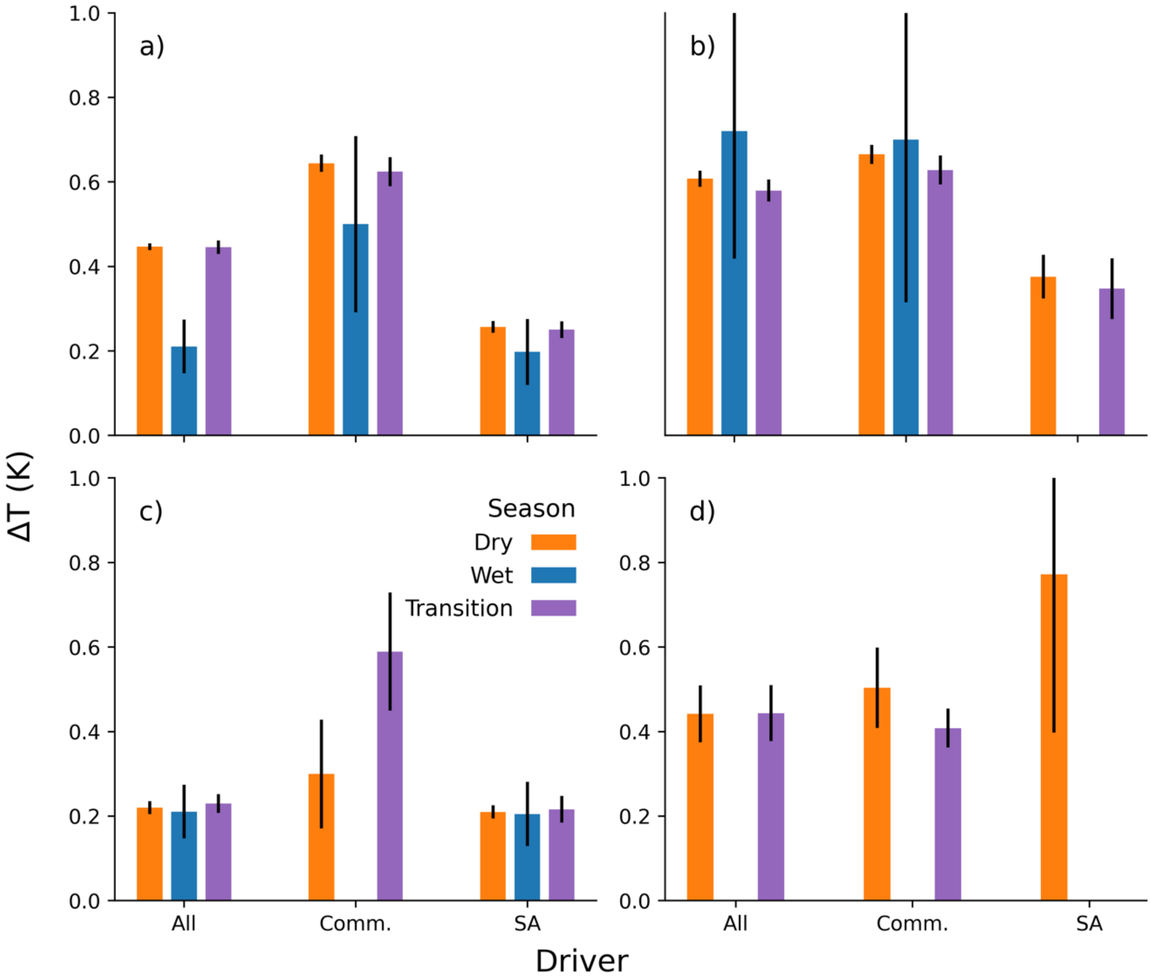

Supplementary Figure A.10. Seasonal *changes in mean land surface temperature per percentage point of forest loss in the dry (orange), wet (blue) and transition (purple) seasons for the (a) Tropics, b) Amazon, c) Congo and d) SEA. Results are categorised by driver of deforestation (All drivers, Commodity Driven deforestation (Comm.) and Shifting Agriculture (SA)) using data from* Curtis et al. (2018). The *change in temperature is calculated change over time (2001-2019) for deforested pixels, compared to nearby forested pixels. Deforested pixels must have been >90% forest in 2001 and less than 70% by 2019, whilst forest pixels must maintain >90% forest cover. Error bars show the standard error of the mean.*

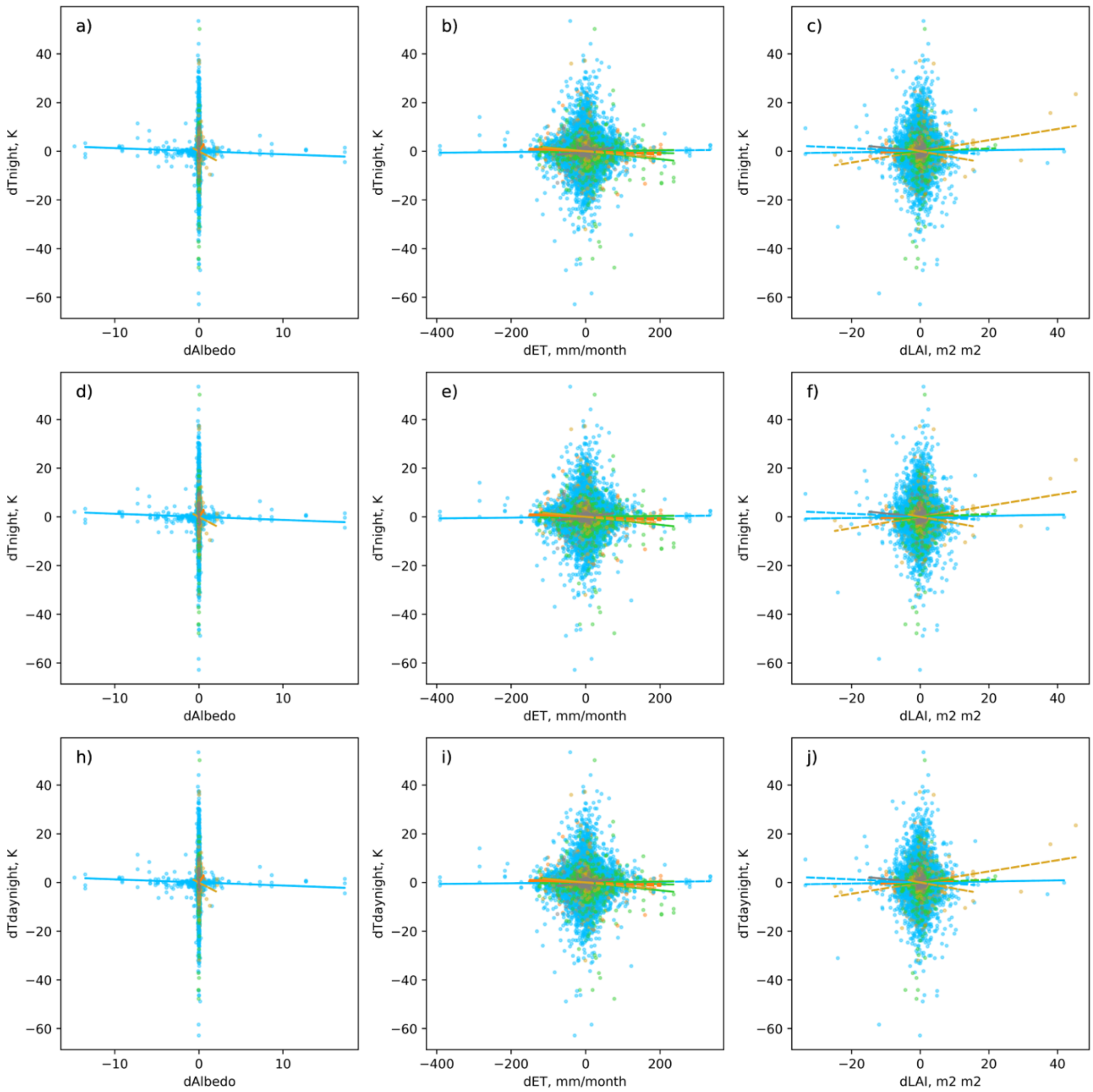

Supplementary Figure A.11. *Scatter plot showing the change in daytime (a-c), night (d-f) and day-night mean (h-j) tropical land surface temperature per percentage point of forest loss versus the change in tropical Albedo (a,d,h), ET (b,e,i) and LAI (c,f,j) per percentage point of forest loss, for each driver of deforestation. Linear fits are plotted where the relationships between the variables are statistically significant (p<0.05).*

References

Curtis, P.G., Slay, C.M., Harris, N.L., Tyukavina, A. and Hansen, M.C. 2018. Classifying drivers of global forest loss. *Science*. **361**(6407), pp.1108–1111.

Potapov, P., Hansen, M.C., Laestadius, L., Turubanova, S., Yaroshenko, A., Thies, C., Smith, W., Zhuravleva, I., Komarova, A., Minnemeyer, S. and Esipova, E. 2017. The last frontiers of wilderness: Tracking loss of intact forest landscapes from 2000 to 2013. *Science Advances*. **3**(1), pp.1–14.

Appendix B

Extended Data for Chapter 4

Extended Data Table B.1. *Precipitation datasets used in Chapter 4.*

Dataset	Date Range	Highest Res	Inputs	Category	Reference
CHIRPS v2.0	1981 - 2021	0.05	Satellite + station	Satellite	Funk et al. (2015)
CMORPH	1998 - 2020	0.25	Satellite + GPCP	Satellite	Xie et al. (2019)
CPC	1979 - 2021	0.5	GTS + COOP	Station	Xie et al. (2007)
CRU TS v4.06	1901 - 2021	0.5	Station	Station	Harris et al. (2020)
ERA5	1979 - 2021	0.1	Numerous	Reanalysis	Hersbach et al. (2020)
GPCC v2022	1891 - 2020	0.25	Stations	Station	Schneider et al. (2022)
GPCP v3.2	1996 -2020	0.5	PERSIANN, GPROF TORVS/AIRS, GPCC GAUGE	Satellite	Huffman et al. (2022)
GPM v0.6	2000 - 2020	0.1	9 satellites	Satellite	Hou et al. (2014)
JRA v7.0	1979 - 2020	0.5625	Numerous	Reanalysis	Kobayashi et al. (2015)
MERRA-2	1980 - 2020	0.625	Numerous	Reanalysis	Gelaro et al. (2017)
PERSIANN-CCS	2003 - 2020	0.04	Cloud class system	Satellite	Nguyen et al. (2019)

PERSIANN-CDR	1983 - 2020	0.25	GridSat B1, GPCP	Satellite	Ashouri et al. (2015)
PERSIANN-CCS-CDR	2003 - 2020	0.04	GridSat B1, GPCP	Satellite	Sadeghi et al. (2021)
PDIR-Now	2000 - 2020	0.04	IR data, IMERG, WorldClim 2, PERSIANN-CDR, NCEP, GPCP, GSMAP-NOW	Satellite	Nguyen et al. (2020)
PERSIANN	2000 - 2020	0.25	AI on IR and VIS from geostat	Satellite	Nguyen et al. (2019)
TRMM v3B43	1998 - 2019	0.25	PR, TMI, VIRES CERES, LSI	Satellite	Huffman et al. (2007)
UDEL v5.01	1990 - 2017	0.5	GHCN, GSOD	Station	Matsuura and Willmott (2018)

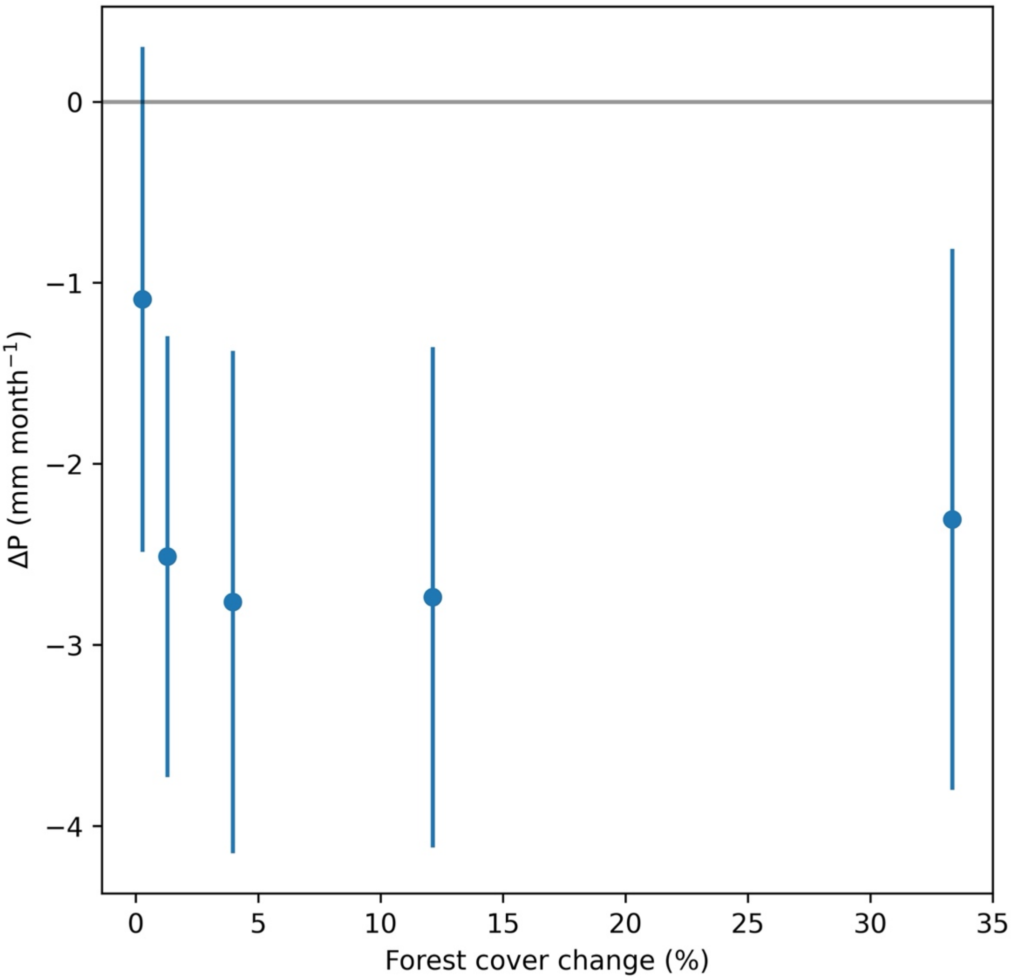

Extended Data Figure B.1. Annual precipitation change as a function of forest loss. *Results are shown at 2° spatial resolution for all satellite precipitation (P) datasets calculated as the change in P over time for deforested data pixels minus change over time for control data pixels. Data is binned according to forest cover change (%) with an equal number of pixels in each bin. Points show the median and error bars shows ± 1 standard error from the mean. Details of each data product are provided in Extended Data Table B.1.*

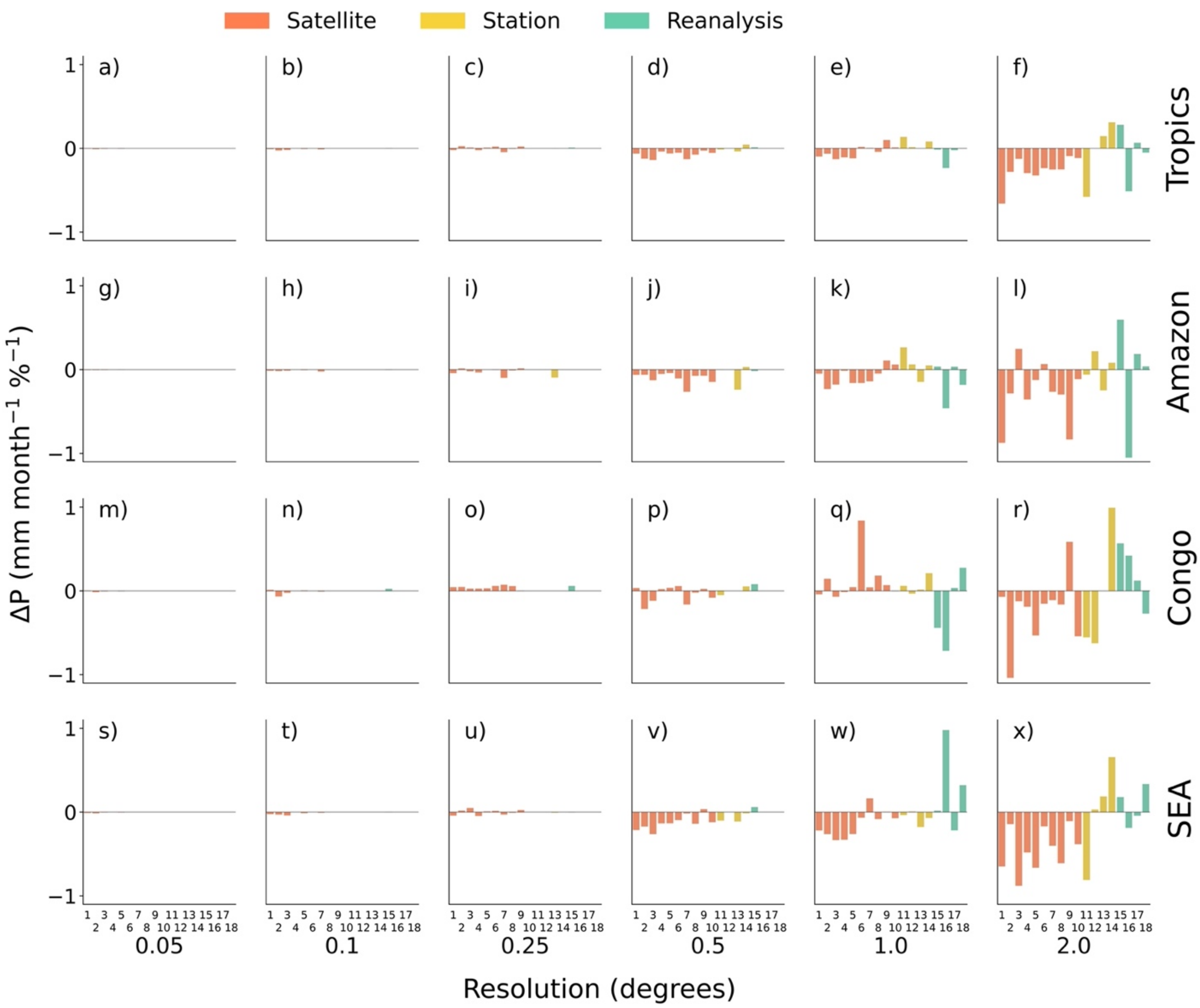

Extended Data Figure B.2. Annual precipitation change due to forest loss for individual datasets. *Results are shown for 2003 – 2017 for 5 year averages and 3x3 moving window. Bars show the median absolute change in annual P (mm month^{-1}) per percentage point tree cover loss in each region (Tropics, Amazon, Congo, SEA). Each P dataset is shown separately and ordered and coloured by category: satellite (orange), station (yellow) and reanalysis (turquoise). The datasets are numbered; 1) CHIRPS, 2) CMORPH, 3) CPC, 4) CRU, 5) ERA5, 6) GPCC, 7) GPCP, 8) GPM, 9) JRA, 10) MERRA-2, 11) NOAA 12) PERSIANN-CCS, 13) PERSIANN-CCSCDR, 14) PERSIANN-CDR, 15) PERSIANN-NOW, 16) PERSIANN, 17) TRMM, 18) UDEL. Results are shown for forest loss scales of 0.05°, 0.1°, 0.25°, 0.5°, 1.0°, 2.0°. Details of each data product are provided in Extended Data Table B.1.*

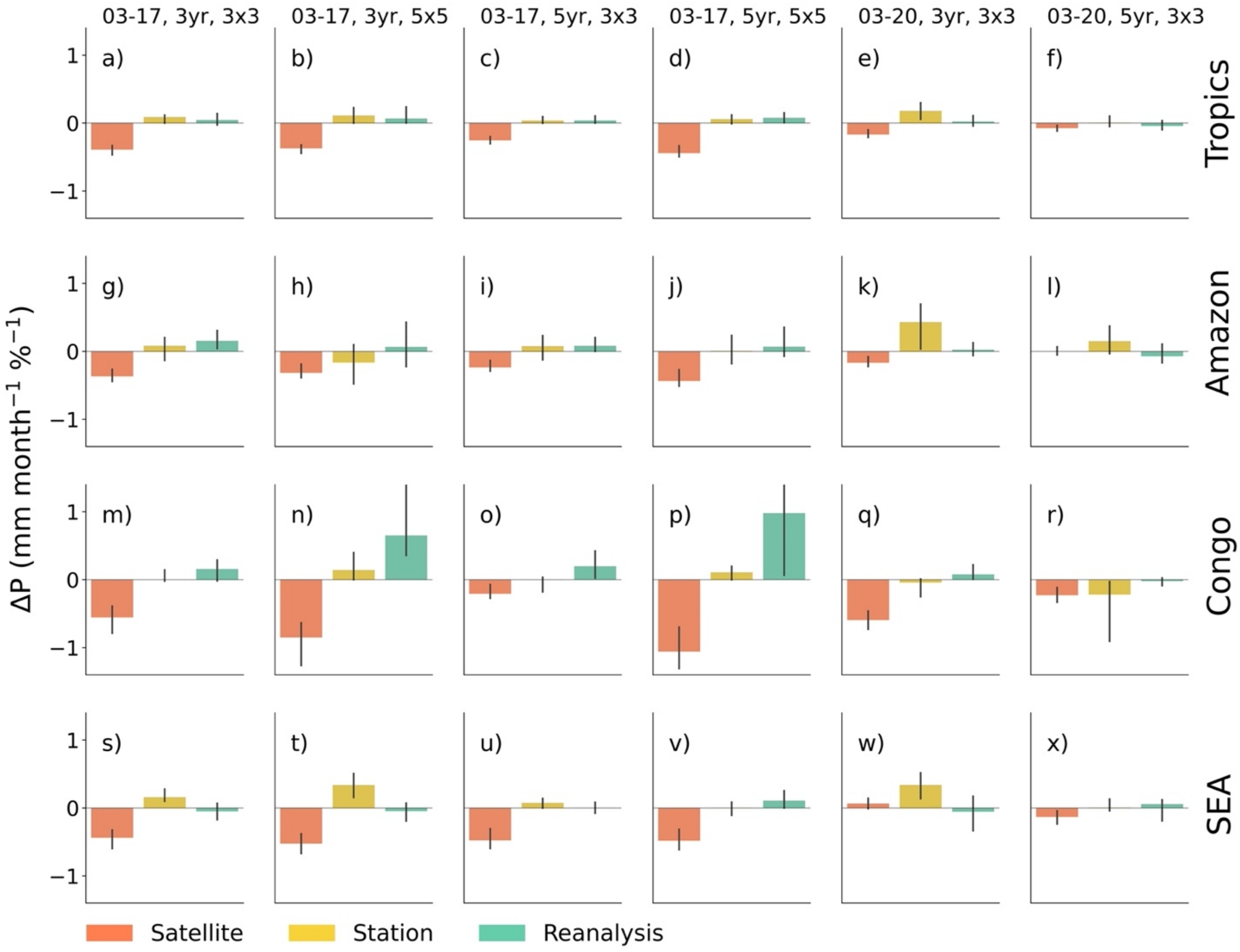

Extended Data Figure B.3: Changes in precipitation due to forest loss for different time periods and nearest neighbour comparisons. *Changes in annual mean precipitation at 2.0° resolution are shown for satellite (red), station (yellow) and reanalysis (green) datasets for the tropics (a-f), Amazon (g-l), Congo (m-r) and Southeast Asia (SEA, s-x). Columns show the sensitivity of our results to changes in the analysis period, number of years used to compute multi-annual means at start and end of the analysis period, and size of the moving window used for nearest neighbour comparisons: 2003-2017, 3-year averages and 3x3 nearest neighbour (Column 1, a,g,m,s); 2003-2017, 3-year, 5x5 (Column 2; b,g,n,t); 2003-2017, 5-year, 3x3 (Column 3; c,i,o,u); 2003-2017, 5-year, 5x5 (Column 4; d,j,p,v); 2003-2020, 3-year, 3x3 (Column 5; e,k,q,w); 2003-2020, 5-year, 3x3 (Column 6; f,l,r,x). Error bars show ± 1 standard error from the mean. Details of each data product are provided in Extended Data Table B.1. Full results for all tested resolutions are available in an online repository [https://doi.org/10.5281/zenodo.7373832].*

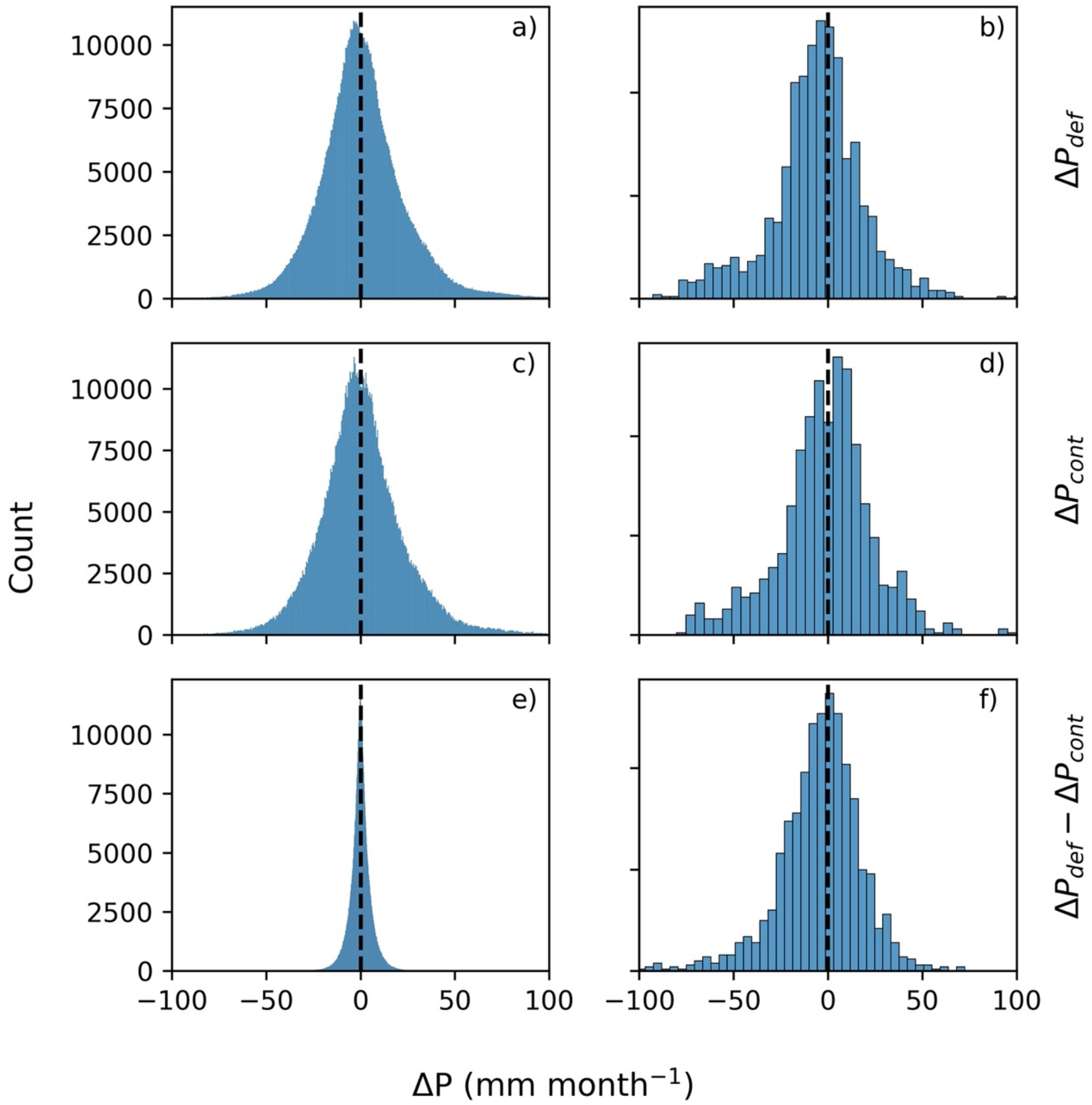

Extended Data Figure B.4: Change in precipitation over deforested, control and difference between deforested and control pixels. *Change in precipitation over 2003 to 2017 is shown for deforested (a, b), control (c, d) and difference between deforested and control pixels (e, f) for 0.05° (a, c, e) and 2.0° (b, d, f) resolution. Details of each data product are provided in Extended Data Table B.1.*

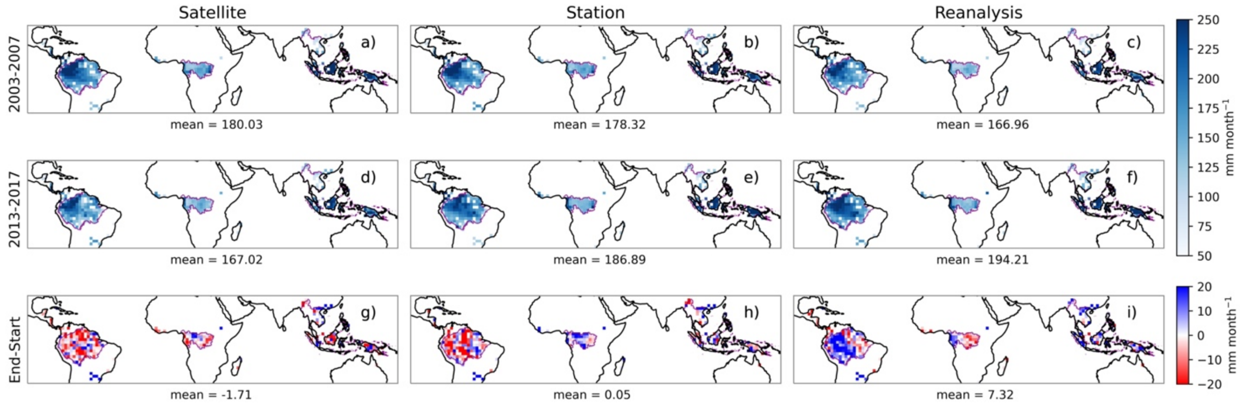

Extended Data Figure B.5: Mean precipitation from satellite, station and reanalysis datasets. *For each class of dataset, satellite (a, d, g), station (b, e, h) and reanalysis (c, f, i), the median value for the 5-year multi-annual mean at the start (2003-2007; a, b, c) and end (2013-2017; d, e, f) of the analysis period as well as the change over the analysis period (end – start; g, h, i) is shown. Mean values across tropical evergreen broadleaf forests are shown in units of mm/month at the top of each panel. Maps of the different regions generated using Cartopy and Natural Earth. Details of each data product are provided in Extended Data Table B.1.*

Supplementary Materials for Chapter 4

Figures

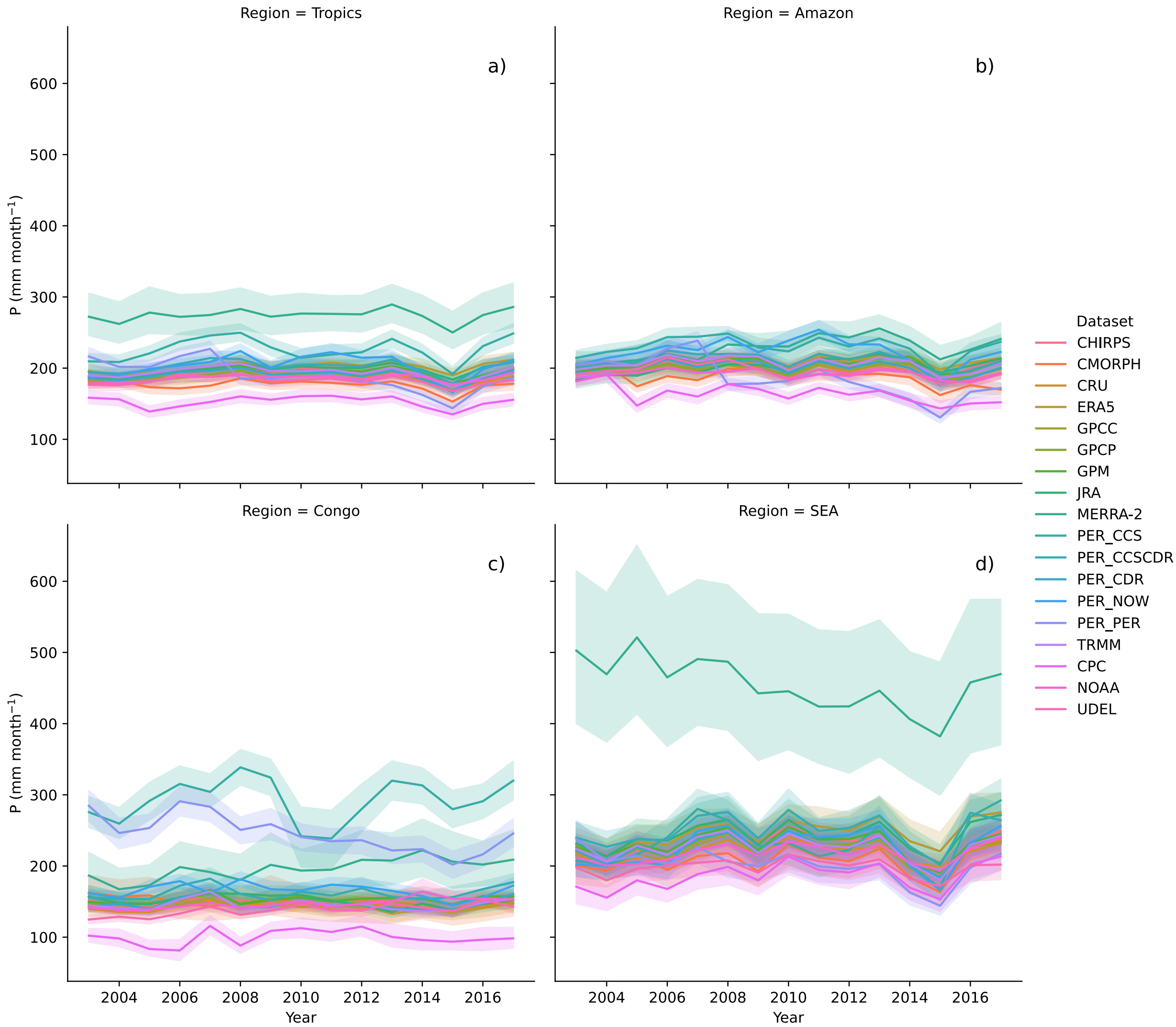

Supplementary Figure B.1. Mean annual precipitation (P, mm month^{-1}). *a) Tropics, b) Amazon, c) Congo and d) SEA. Details of each data product are provided in Extended Data Table B.1. Shading indicates 95% confidence intervals.*

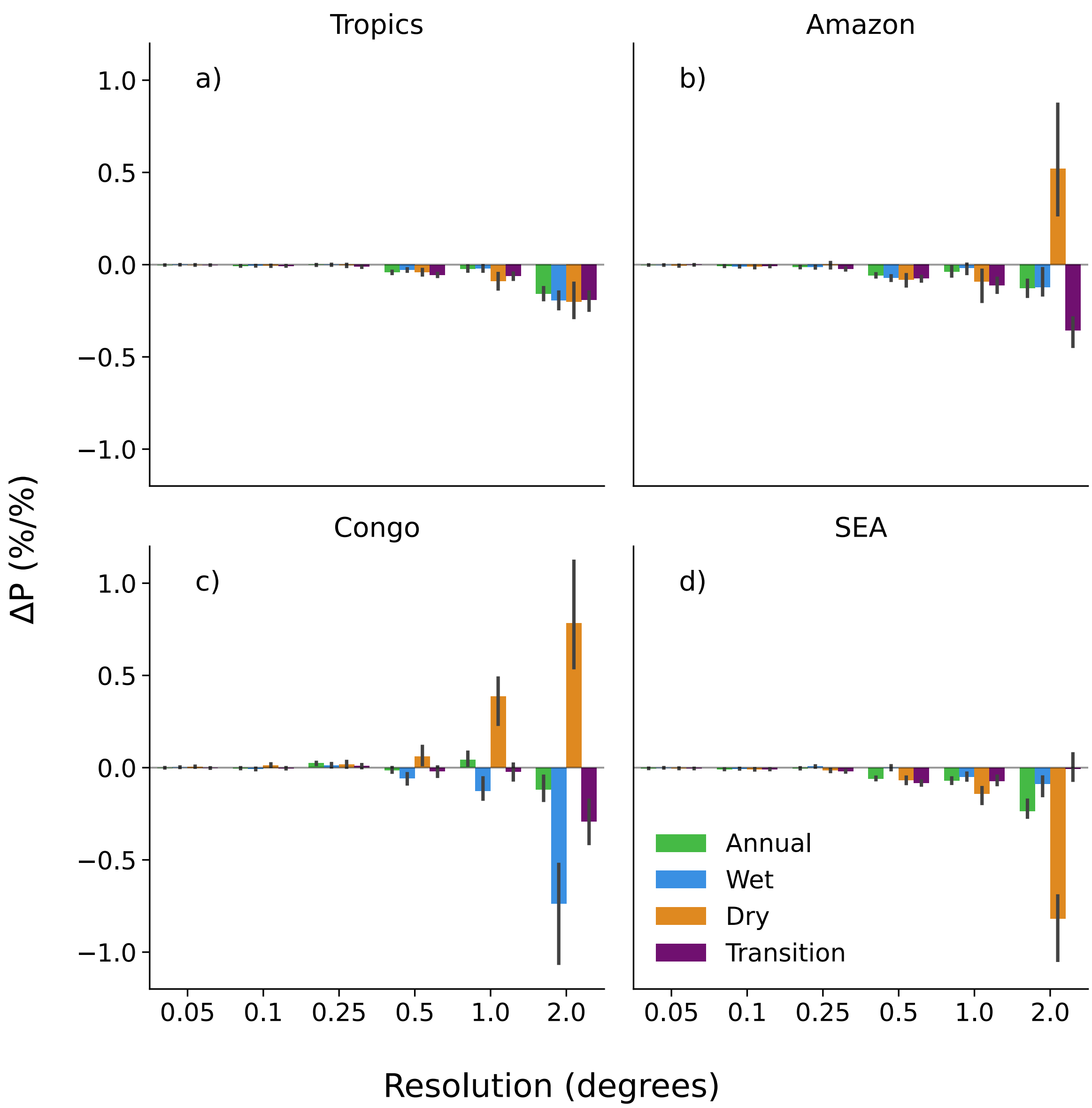

Supplementary Figure B.2. Relative annual and seasonal changes in precipitation (P) due to forest cover loss. *Bars show the median relative change in P per percentage point forest cover loss (%/%) for (a) Tropics, b) Amazon, c) Congo, d) SEA between 2003 - 2017. Results shown for forest loss scales of 0.05°, 0.1 0.25, 0.5°, 1.0°, 2.0° for satellite datasets. Error bar shows ± 1 standard error from the mean. Details of each data product are provided in Extended Data Table B.1.*

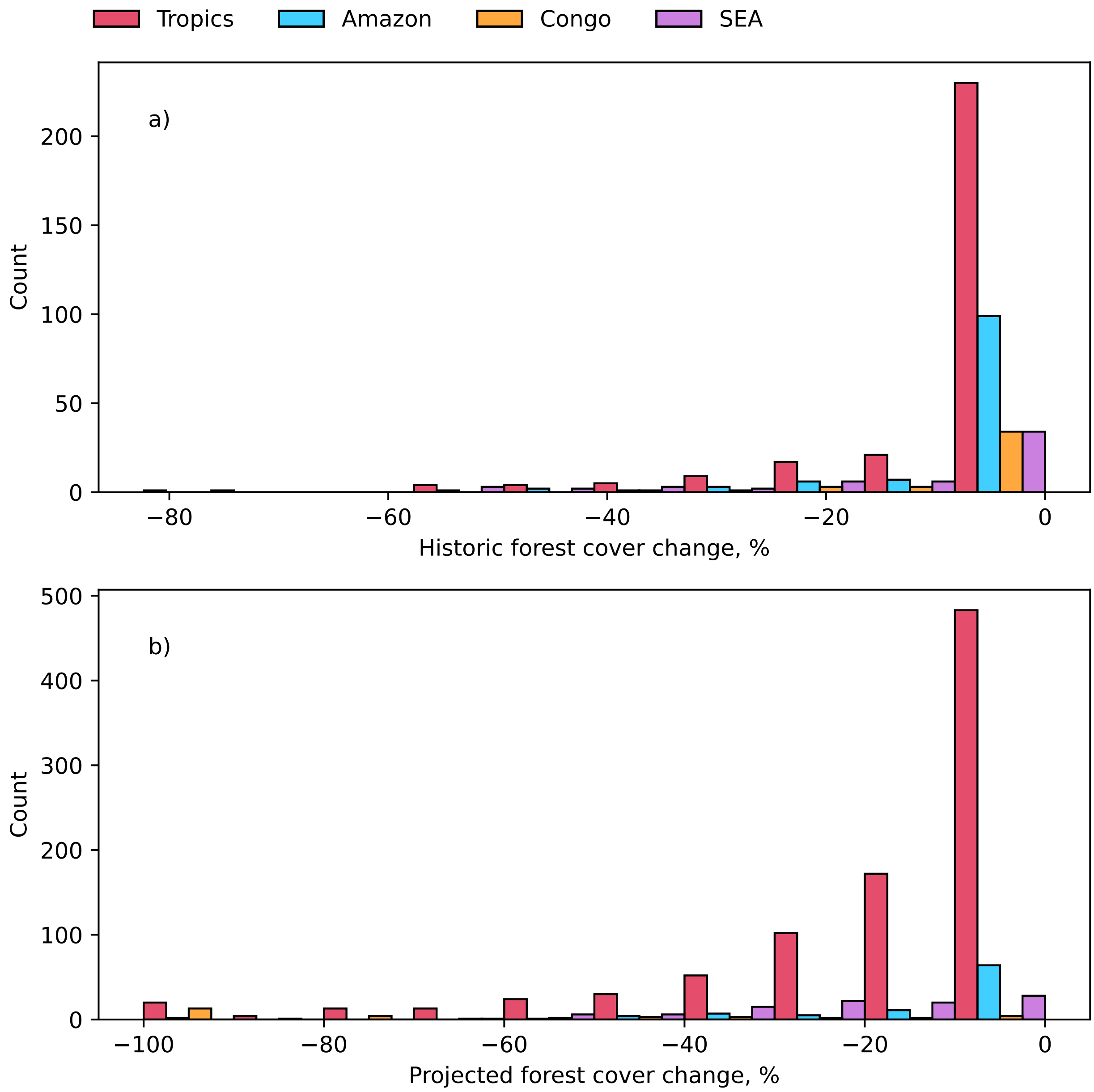

Supplementary Figure B.3. Distribution of historic and projected change in forest cover (%). *a) observed (2003-2017) from satellite and b) projected (2015-2100) from the GCAM model. Data analysed at 2° and coloured by region. Details of each data product are provided in Extended Data Table B.1. Full results are available in an online repository [https://doi.org/10.5281/zenodo.7373832].*

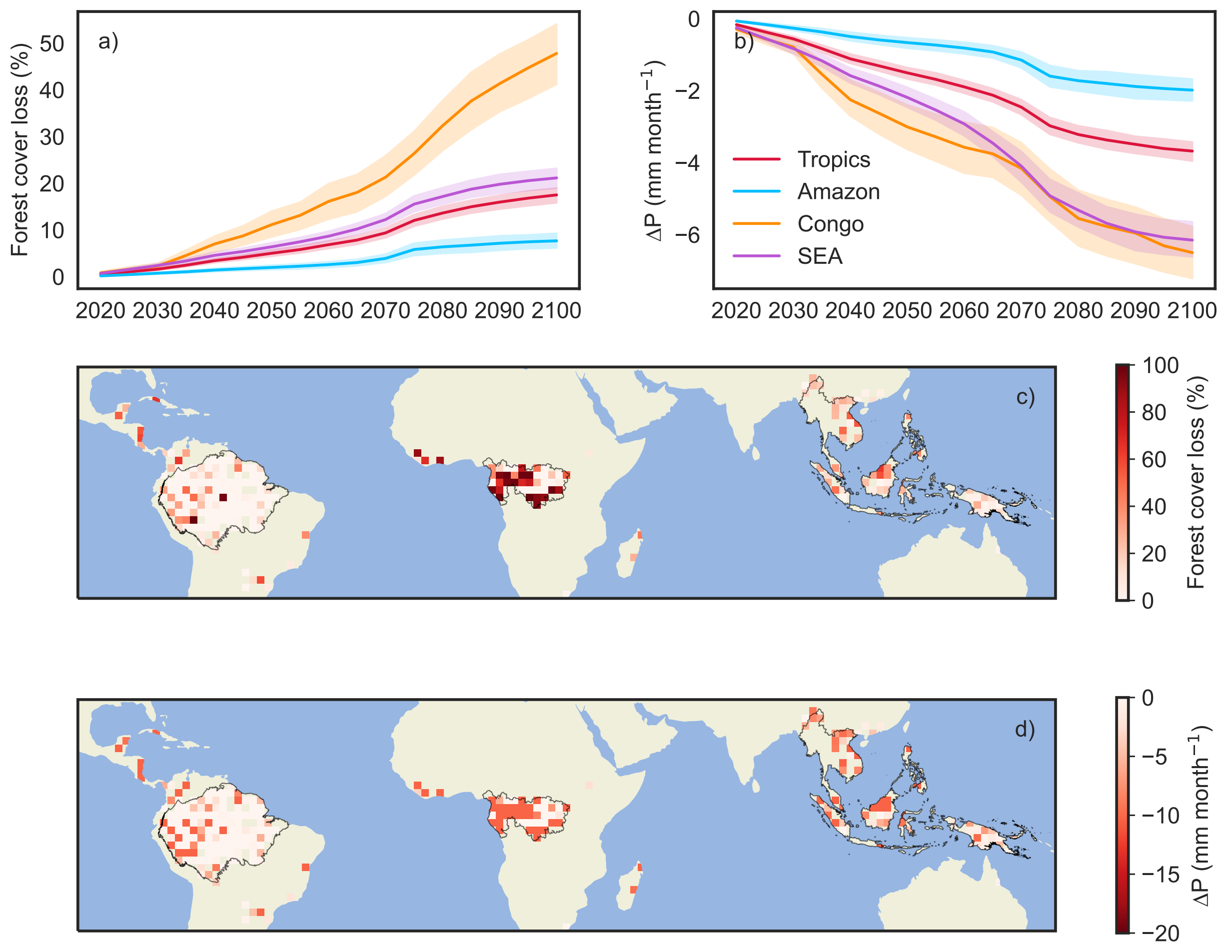

Supplementary Figure B.4. Impact of projected future forest loss capped to 30%, on annual-mean precipitation. *a) Mean forest cover loss over 2015 – 2100 under SSP3-4.5 for the tropics, Amazon, Congo and Southeast Asia (SEA); b) impact of projected forest cover loss on precipitation (P) (± 1 standard error from the mean); Spatial pattern of c) forest cover loss and; d) predicted P change (ΔP) in 2100 due to forest cover loss. Results are shown for 2.0° resolution. As Fig. 4 (main text) but impacts of forest loss on precipitation are capped at 30% forest loss (see methods). Maps of the different regions generated using Cartopy and Natural Earth. Details of each data product are provided in Extended Data Table B.1. Full results are available in an online repository [https://doi.org/10.5281/zenodo.7373832].*

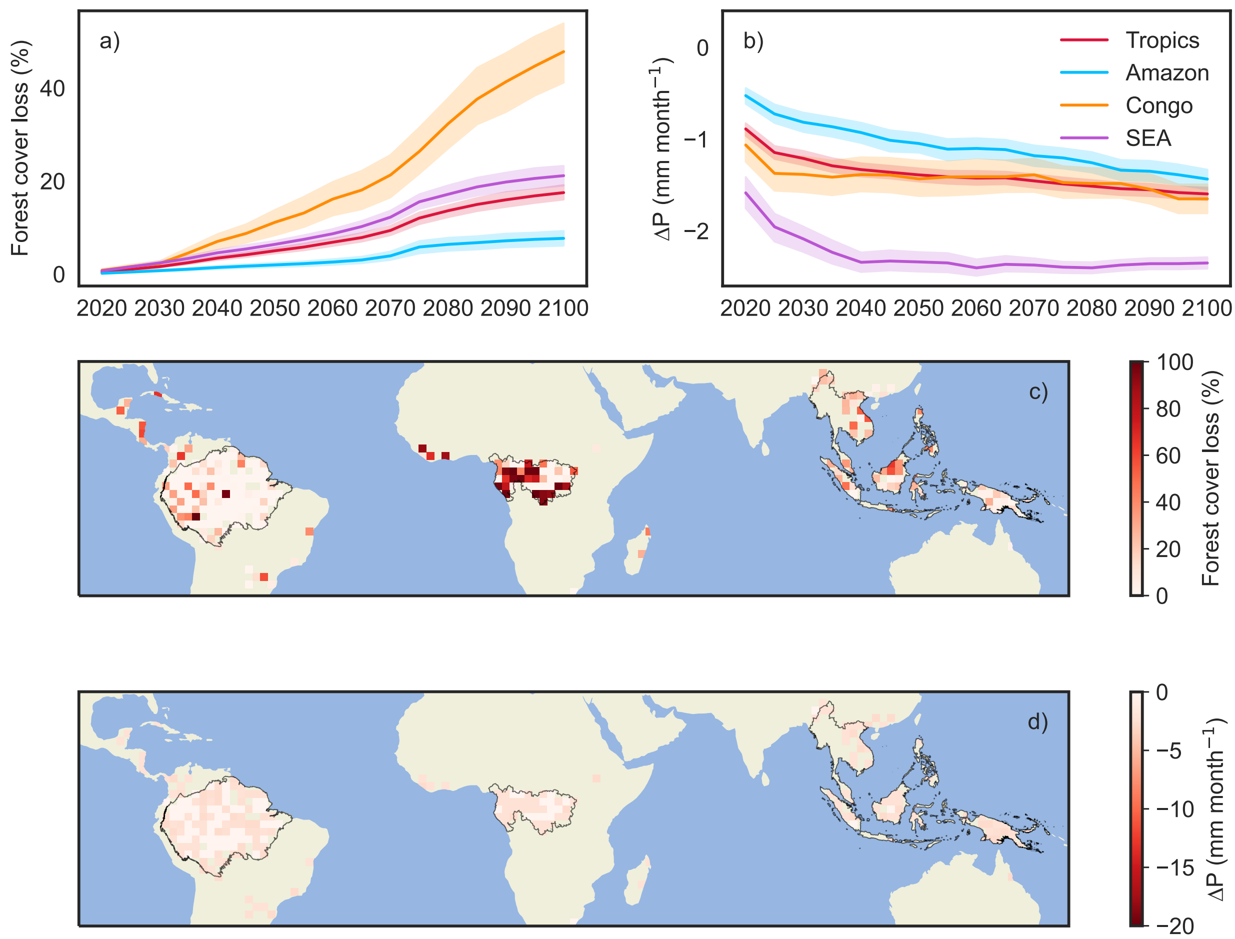

Supplementary Figure B.5. Impact of projected future forest loss from 2015 to 2100 on annual-mean precipitation using a non-linear function. *a) Mean forest cover loss under SSP3-4.5 for the tropics, Amazon, Congo and Southeast Asia (SEA); b) impact of projected forest cover loss on P (± 1 standard error from the mean); Spatial pattern of c) forest cover loss and d) predicted P change (ΔP) in 2100 due to forest cover loss. As Fig. 4 (main text) but impacts of forest loss on precipitation are capped at 30% forest loss and a non-linear function based on Extended Data Fig. 1 is used to relate precipitation change to forest loss (see methods). Maps of the different regions generated using Cartopy and Natural Earth. Details of each data product are provided in Extended Data Table B.1. Full results are available in an online repository [https://doi.org/10.5281/zenodo.7373832].*

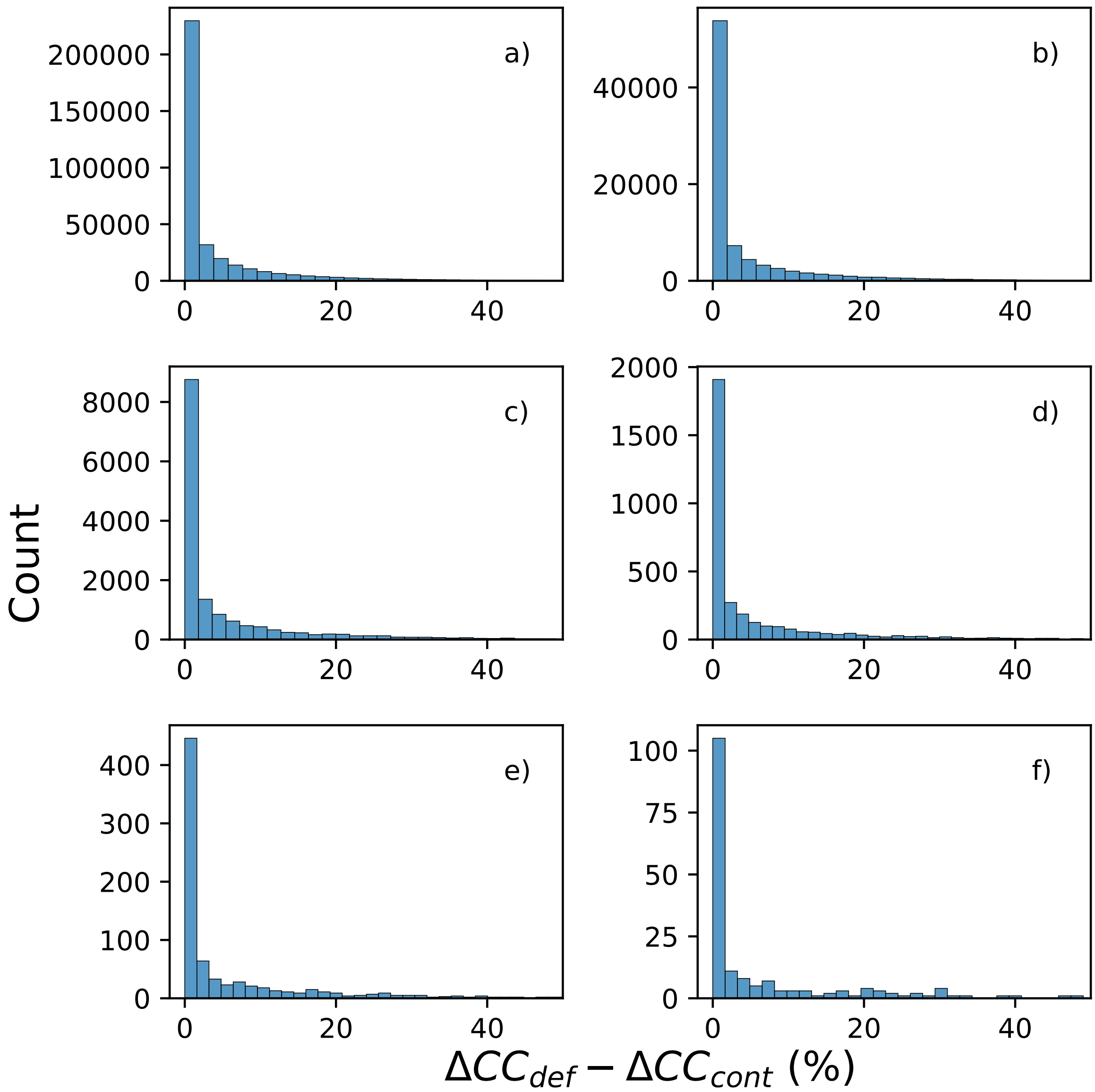

Supplementary Figure B.6. Distribution of change in canopy cover (CC) for deforested pixels minus the change in canopy cover for control pixels, over the period 2003-2017. *Results are shown at a) 0.05°, b), 0.1°, c) 0.25°, d) 0.5°, e) 1.0°, f) 2.0°. Details of each data product are provided in Extended Data Table B.1. Full results are available in an online repository [https://doi.org/10.5281/zenodo.7373832].*

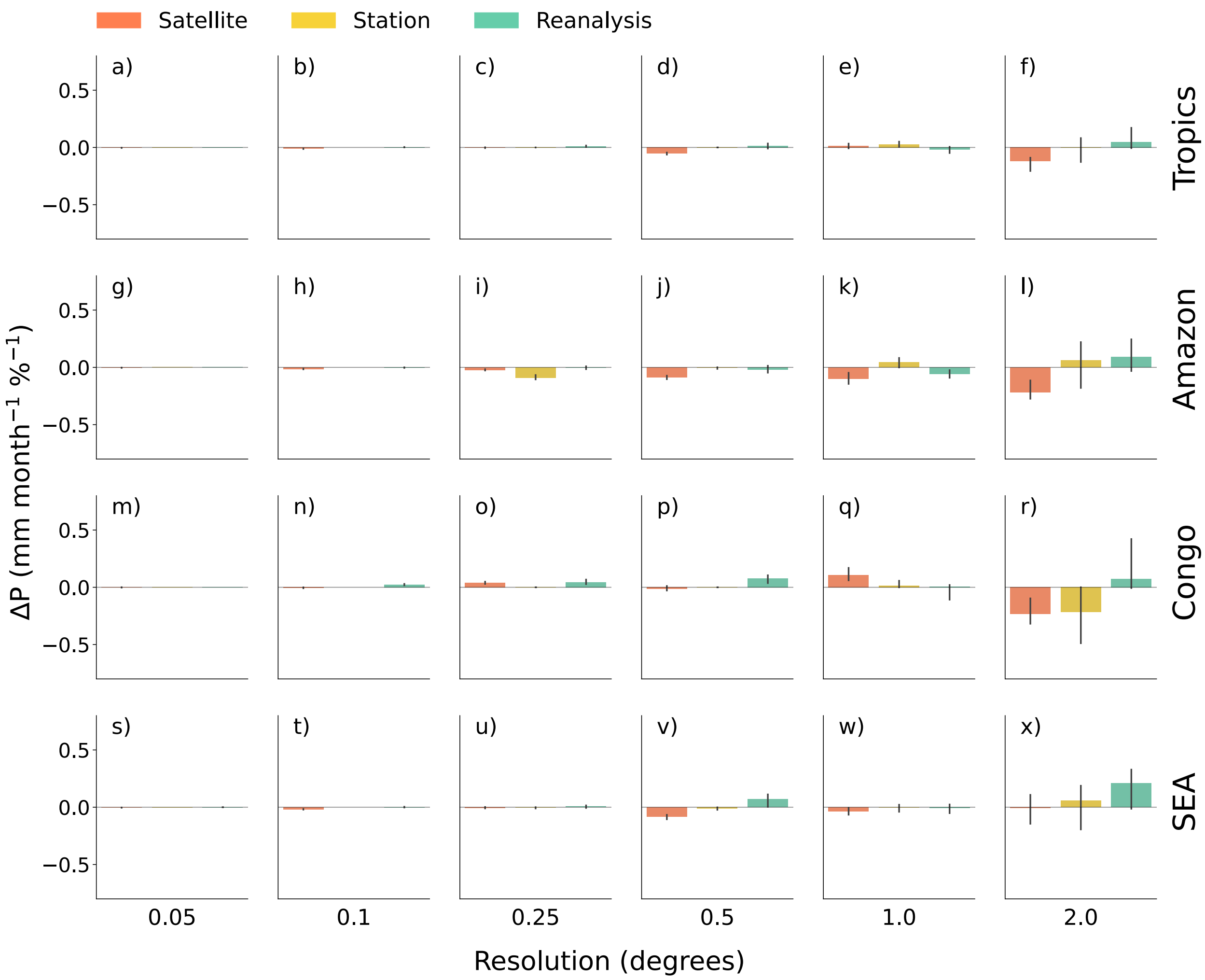

Supplementary Figure B.7. Annual precipitation (P) change due to forest loss calculated with restrictions on background P. *Results are shown for 5-year averages (2003-2007 & 2016-2020) with a 3x3 moving window and restricted to control and deforested pixels where the annual mean P differs by less than 10%. Bars show the median absolute change in annual P (mm month^{-1}) per percentage point tree cover loss in each region (Tropics (a-f), Amazon (g-l), Congo (m-r), Southeast Asia (SEA) (s-x)) and for each precipitation dataset category (satellite, station and reanalysis). Shown for forest loss scales of 0.05° (a, g, m, s), 0.1° (b, h, n ,t), 0.25° (c, i, o, u), 0.5° (d, j, p ,v), 1.0° (e, k, q, w), 2.0° (f, l , r, x). Error bars show ± 1 standard error from the mean. Details of each data product are provided in Extended Data Table B.1. Full results are available in an online repository [https://doi.org/10.5281/zenodo.7373832].*

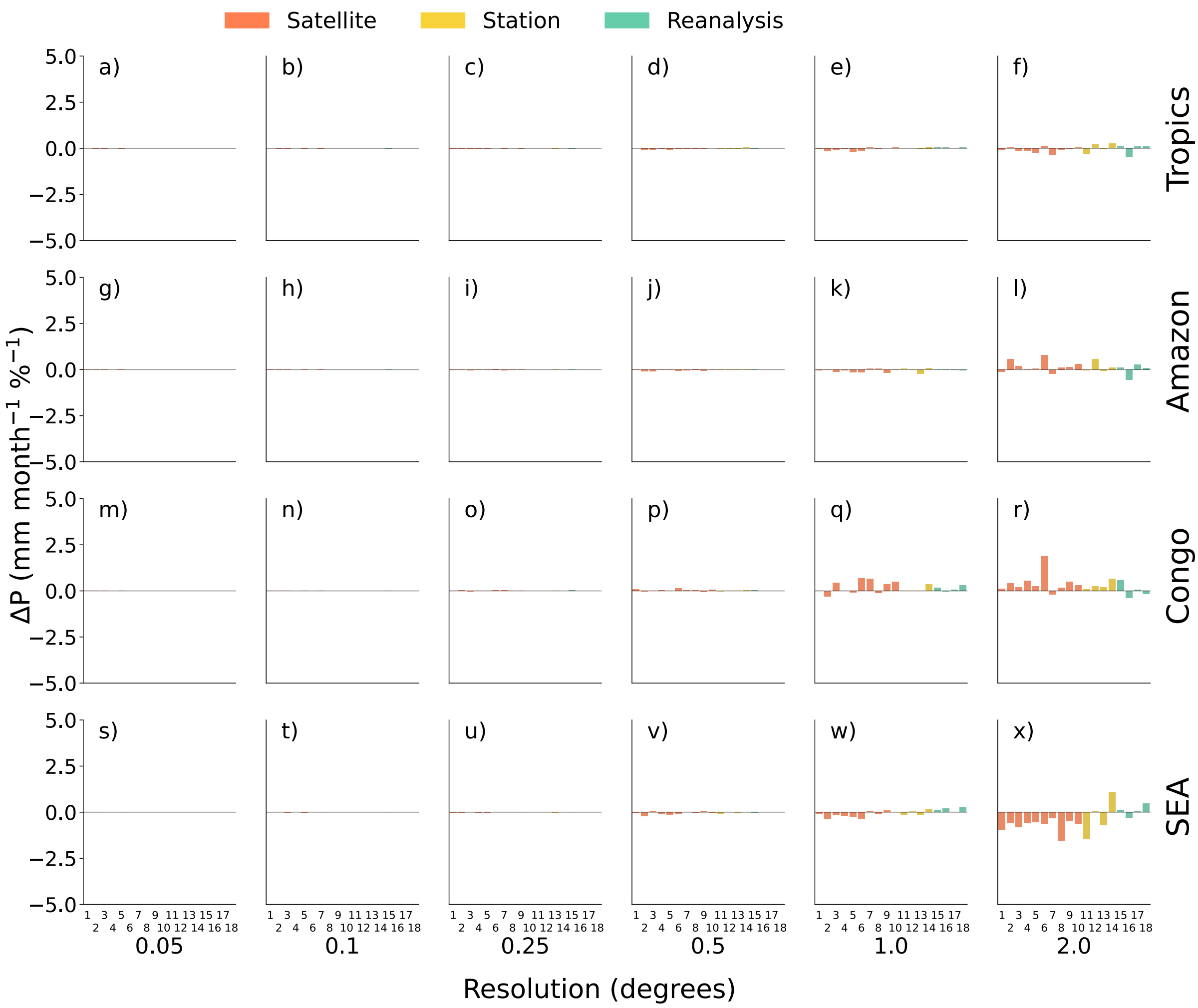

Supplementary Figure B.8. Dry season precipitation (P) change due to forest loss during 2003 – 2017 for individual P datasets. *Results are shown for 5 year averages and 3x3 moving window. Bars show the median absolute change in dry season P (mm month^{-1}) per percentage point forest cover loss in each region (Tropics, Amazon, Congo, SEA). Each P dataset is shown separately and ordered and coloured by category: satellite (orange), station (yellow) and reanalysis (turquoise). The datasets are numbered; 1) CHIRPS, 2) CMORPH, 3) CPC, 4) CRU, 5) ERA5, 6) GPCC, 7) GPCP, 8) GPM, 9) JRA, 10) MERRA-2, 11) NOAA 12) PERSIANN-CCS, 13) PERSIANN-CCSCDR, 14) PERSIANN-CDR, 15) PERSIANN-NOW, 16) PERSIANN, 17) TRMM, 18) UDEL. Results are shown for forest loss scales of 0.05°, 0.1°, 0.25°, 0.5°, 1.0°, 2.0°. Details of each data product are provided in Extended Data Table B.1. Full results are available in an online repository [https://doi.org/10.5281/zenodo.7373832].*

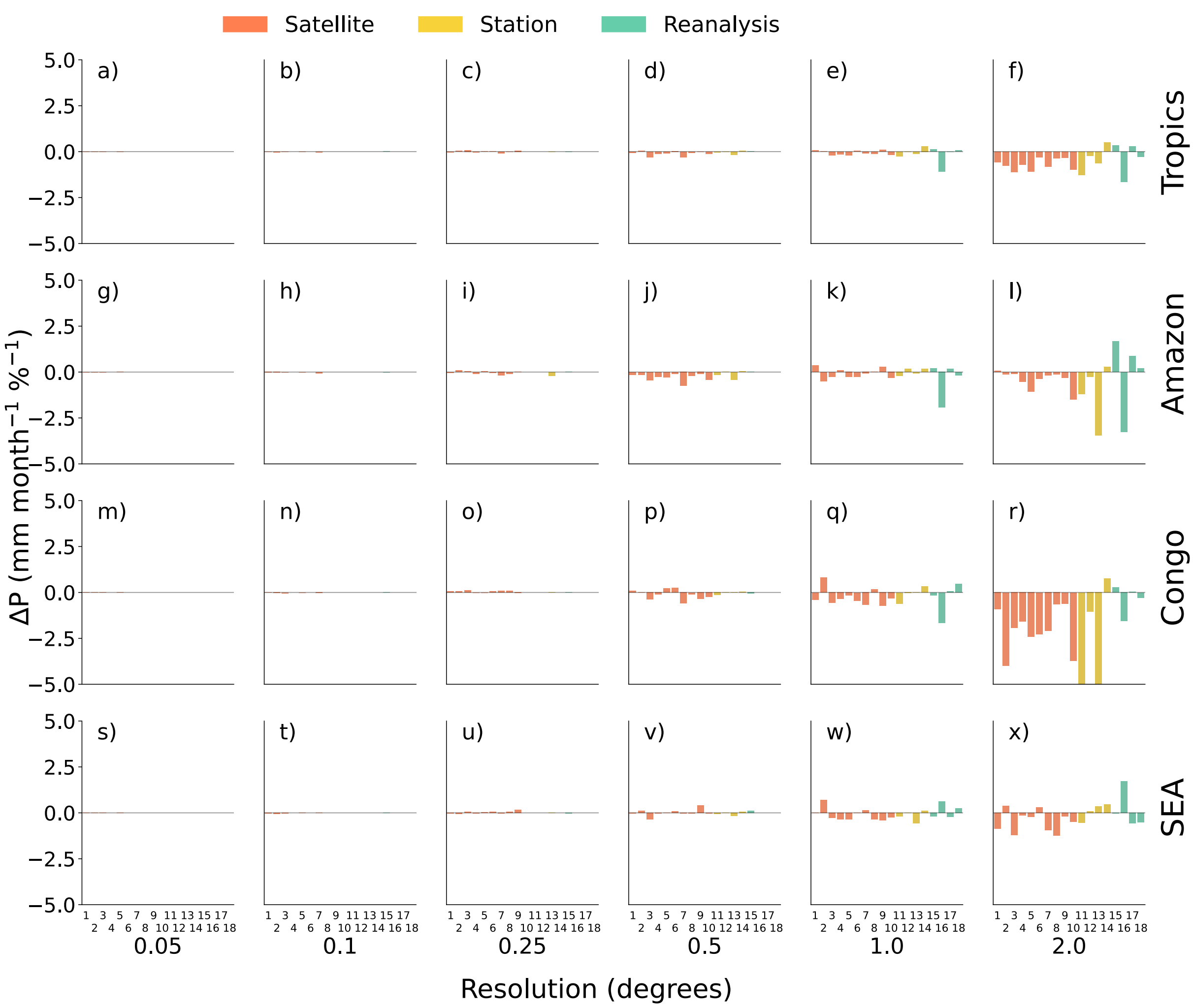

Supplementary Figure B.9. Wet season precipitation (P) change due to forest loss during 2003 – 2017 for individual P datasets. *Results are shown for 5-year averages and 3x3 moving window. Bars show the median absolute change in wet season P (mm month^{-1}) per percentage point forest cover loss in each region (Tropics, Amazon, Congo, SEA). Each P dataset is shown separately and ordered and coloured by category: satellite (orange), station (yellow) and reanalysis (turquoise). The datasets are numbered; 1) CHIRPS, 2) CMORPH, 3) CPC, 4) CRU, 5) ERA5, 6) GPCC, 7) GPCP, 8) GPM, 9) JRA, 10) MERRA-2, 11) NOAA 12) PERSIANN-CCS, 13) PERSIANN-CCSCDR, 14) PERSIANN-CDR, 15) PERSIANN-NOW, 16) PERSIANN, 17) TRMM, 18) UDEL. Results are shown for forest loss scales of 0.05°, 0.1°, 0.25°, 0.5°, 1.0°, 2.0°. Details of each data product are provided in Extended Data Table B.1. Full results are available in an online repository [https://doi.org/10.5281/zenodo.7373832].*

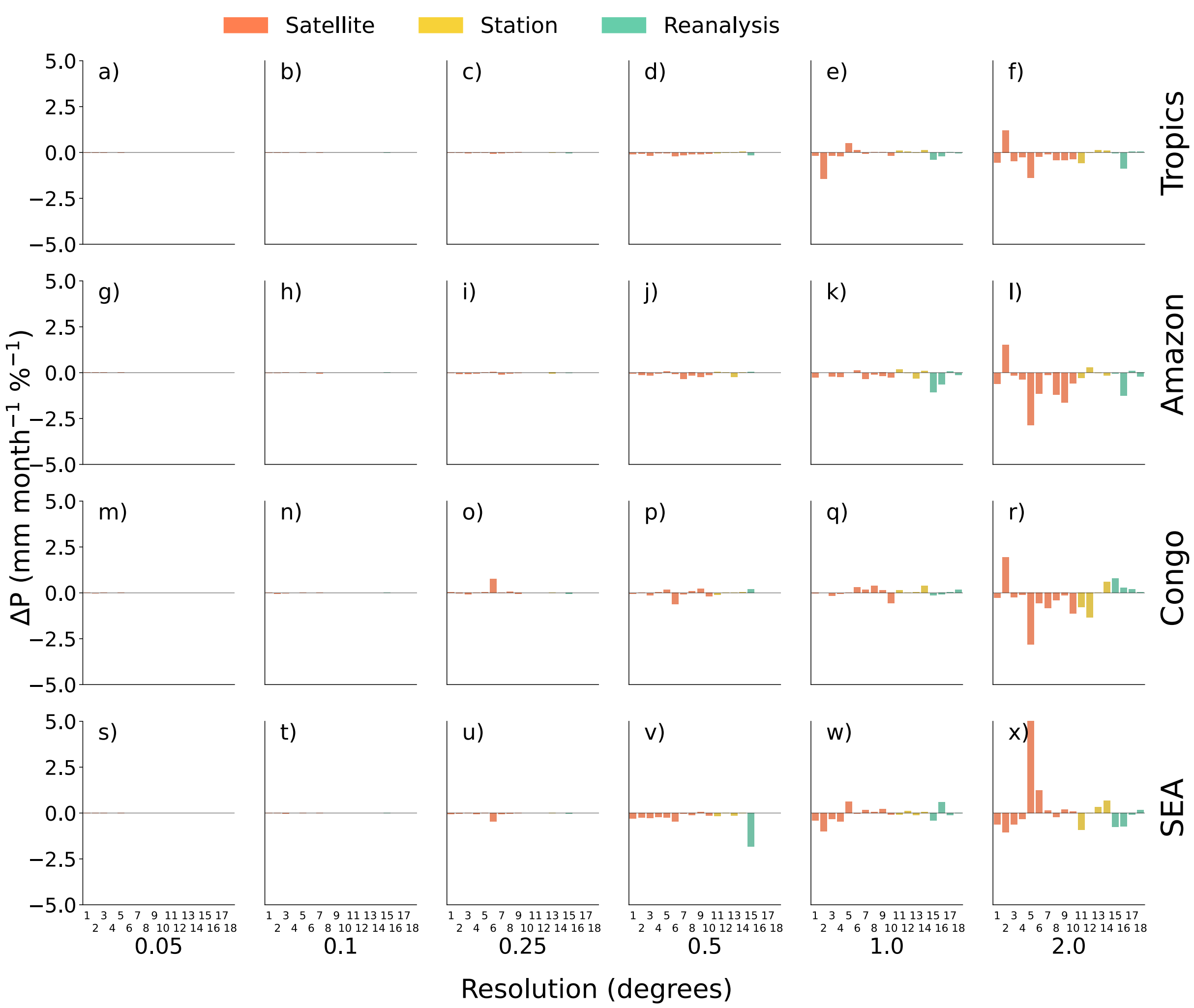

Supplementary Figure B.10. Transition season precipitation (P) change due to forest loss during 2003 – 2017 for individual P datasets. *Results are shown for 5-year averages and 3x3 moving window. Bars show the median absolute change in transition season P (mm month^{-1}) per percentage point forest cover loss in each region (Tropics, Amazon, Congo, SEA). Each P dataset is shown separately and ordered and coloured by category: satellite (orange), station (yellow) and reanalysis (turquoise). The datasets are numbered; 1) CHIRPS, 2) CMORPH, 3) CPC, 4) CRU, 5) ERA5, 6) GPCC, 7) GPCP, 8) GPM, 9) JRA, 10) MERRA-2, 11) NOAA 12) PERSIANN-CCS, 13) PERSIANN-CCSCDR, 14) PERSIANN-CDR, 15) PERSIANN-NOW, 16) PERSIANN, 17) TRMM, 18) UDEL. Results are shown for forest loss scales of 0.05°, 0.1°, 0.25°, 0.5°, 1.0°, 2.0°. Details of each data product are provided in Extended Data Table B.1. Full results are available in an online repository [https://doi.org/10.5281/zenodo.7373832].*

References

Ashouri, H., Hsu, K.L., Sorooshian, S., Braithwaite, D.K., Knapp, K.R., Cecil, L.D., Nelson, B.R. and Prat, O.P. 2015. PERSIANN-CDR: Daily precipitation climate data record from multisatellite observations for hydrological and climate studies. *Bulletin of the American Meteorological Society*. **96**(1), pp.69–83.

Funk, C., Peterson, P., Landsfeld, M., Pedreros, D., Verdin, J., Shukla, S., Husak, G., Rowland, J., Harrison, L., Hoell, A. and Michaelsen, J. 2015. The climate hazards infrared precipitation with stations - A new environmental record for monitoring extremes. *Scientific Data*. **2**, pp.1–21.

Gelaro, R., McCarty, W., Suárez, M.J., Todling, R., Molod, A., Takacs, L., Randles, C.A., Darmenov, A., Bosilovich, M.G., Reichle, R., Wargan, K., Coy, L., Cullather, R., Draper, C., Akella, S., Buchard, V., Conaty, A., da Silva, A.M., Gu, W., Kim, G.K., Koster, R., Lucchesi, R., Merkova, D., Nielsen, J.E., Partyka, G., Pawson, S., Putman, W., Rienecker, M., Schubert, S.D., Sienkiewicz, M. and Zhao, B. 2017. The modern-era retrospective analysis for research and applications, version 2 (MERRA-2). *Journal of Climate*. **30**(14), pp.5419–5454.

Harris, I., Osborn, T.J., Jones, P. and Lister, D. 2020. Version 4 of the CRU TS monthly high-resolution gridded multivariate climate dataset. *Scientific Data*. **7**(1), pp.1–18.

Hersbach, H., Bell, B., Berrisford, P., Hirahara, S., Horányi, A., Muñoz-Sabater, J., Nicolas, J., Peubey, C., Radu, R., Schepers, D., Simmons, A., Soci, C., Abdalla, S., Abellan, X., Balsamo, G., Bechtold, P., Biavati, G., Bidlot, J., Bonavita, M., De Chiara, G., Dahlgren, P., Dee, D., Diamantakis, M., Dragani, R., Flemming, J., Forbes, R., Fuentes, M., Geer, A., Haimberger, L., Healy, S., Hogan, R.J., Hólm, E., Janisková, M., Keeley, S., Laloyaux, P., Lopez, P., Lupu, C., Radnoti, G., de Rosnay, P., Rozum, I., Vamborg, F., Villaume, S. and Thépaut, J.N. 2020. The ERA5 global reanalysis. *Quarterly Journal of the Royal Meteorological Society*. **146**(730), pp.1999–2049.

Hou, A.Y., Kakar, R.K., Neeck, S., Azarbarzin, A.A., Kummerow, C.D., Kojima, M., Oki, R., Nakamura, K. and Iguchi, T. 2014. The global precipitation measurement mission. *Bulletin of the American Meteorological Society*. **95**(5), pp.701–722.

Huffman, G.J., Adler, R.F., Bolvin, D.T., Gu, G., Nelkin, E.J., Bowman, K.P., Hong, Y., Stocker, E.F. and Wolff, D.B. 2007. The TRMM Multisatellite Precipitation Analysis (TMPA): Quasi-global, multiyear, combined-sensor precipitation estimates at fine scales. *Journal of Hydrometeorology*. **8**(1), pp.38–55.

Huffman, G.J.A., Behrangi, R.F., Adler, D.T., Bolvin, E.J. and Nelkin, G.G. 2022. *Introduction to the New Version 3 GPCP Monthly Global Precipitation Analysis*.

Kobayashi, S., Ota, Y., Harada, Y., Ebita, A., Moriya, M., Onoda, H., Onogi, K., Kamahori, H., Kobayashi, C., Endo, H., Miyaoka, K. and Kiyotoshi, T. 2015. The JRA-55 reanalysis: General specifications and basic characteristics. *Journal of the Meteorological Society of Japan*. **93**(1), pp.5–48.

Matsuura, K. and Willmott, C.J. 2018. Terrestrial Precipitation: 1900-2017 Gridded Monthly Time Series. *University of Delaware*., http://climate.geog.udel.edu/~climate/html_pages/G.

Met Office 2022. Cartopy: A cartographic python library with a matplotlib interface. , http://scitools.org.uk/cartopy/

Nguyen, P., Ombadi, M., Gorooh, V.A., Shearer, E.J., Sadeghi, M., Sorooshian, S., Hsu, K., Bolvin, D. and Ralph, M.F. 2020. Persiann dynamic infrared–rain rate (PDIR-now): A near-real-time, quasi-global satellite precipitation dataset. *Journal of Hydrometeorology*. **21**(12), pp.2893–2906.

Nguyen, P., Shearer, E.J., Tran, H., Ombadi, M., Hayatbini, N., Palacios, T., Huynh, P., Braithwaite, D., Updegraff, G., Hsu, K., Kuligowski, B., Logan, W.S. and Sorooshian, S. 2019. The CHRS data portal, an easily accessible public repository for PERSIANN global satellite precipitation data. *Scientific Data*. **6**, pp.1–10.

Sadeghi, M., Nguyen, P., Naeini, M.R., Hsu, K., Braithwaite, D. and Sorooshian, S. 2021. PERSIANN-CCS-CDR, a 3-hourly 0.04° global precipitation climate data record for heavy precipitation studies. *Scientific Data*. **8**(1), pp.1–11.

Schneider, U., Elke, R., Hänsel, S., Finger, P. and Ziese, M. 2022. Monthly Land-Surface Precipitation Climatology for Every Month and the Total Year from Rain-Gauges built on GTS-based and Historical Data. *GPCC Climatology Version 2022 at 0.25°*., 10.5676/DWD_GPCC/CLIM_M_V2022_025.

Xie, P., Joyce, R., Wu, S., Yoo, S.-H., Yarosh, Y., Sun, F. and Lin, R. 2019. NOAA Climate Data Record (CDR) of CPC Morphing Technique (CMORPH) High Resolution Global Precipitation Estimates, Version 1. *NOAA National Centers for Environmental Information*., https://doi.org/10.25921/w9va-q159.

Xie, P., Yatagai, A., Chen, M., Hayasaka, T., Fukushima, Y., Liu, C. and Yang, S. 2007. A gauge-based analysis of daily precipitation over East Asia. *Journal of Hydrometeorology*. **8**(3), pp.607–626.

Appendix C

Supplementary Materials for Chapter 5

Tables

Supplementary Table C.1. *Changes (value) in satellite observed land surface temperature (LST) and precipitation (P), reported alongside number of data points in each category and statistical significance (p values from both Student's t-test and Wilcoxon test). Values shown for each season and resolution (latitudinal degrees) of satellite dataset.*

Season	Model	Resolution	Variable	Value	# data points	p-value (t-test)	p-value (Wilcoxon)
Dry	Satellite	0.25	LST	0.01	32540	2.95E-44	1.43E-194
Dry	Satellite	0.50	LST	0.01	8660	3.99E-13	6.77E-51
Dry	Satellite	1.00	LST	0.01	2271	1.79E-05	2.02E-15
Dry	Satellite	2.00	LST	0.02	564	8.42E-02	3.50E-03
Annual	Satellite	0.25	P	-0.03	36354	1.87E-02	4.17E-18
Dry	Satellite	0.25	P	-0.01	36354	7.86E-01	4.45E-01
Wet	Satellite	0.25	P	-0.10	36354	1.24E-08	2.09E-33
Transition	Satellite	0.25	P	-0.03	36354	5.65E-06	1.93E-18
Annual	Satellite	0.50	P	-0.03	10256	3.33E-02	4.61E-11
Dry	Satellite	0.50	P	-0.01	10256	2.87E-02	1.76E-01
Wet	Satellite	0.50	P	-0.25	10256	4.06E-08	1.39E-25
Transition	Satellite	0.50	P	-0.07	10256	1.11E-05	2.04E-12
Annual	Satellite	1.00	P	-0.04	2918	1.76E-02	7.76E-07

Dry	Satellite	1.00	P	-0.06	2918	1.09E-02	2.19E-02
Wet	Satellite	1.00	P	-0.56	2918	4.21E-07	4.02E-15
Transition	Satellite	1.00	P	-0.27	2918	6.23E-05	1.05E-08
Annual	Satellite	2.00	P	-0.18	861	1.95E-02	8.05E-03
Dry	Satellite	2.00	P	-0.06	861	8.67E-02	2.33E-01
Wet	Satellite	2.00	P	-1.12	861	2.10E-06	2.84E-10
Transition	Satellite	2.00	P	-0.33	861	2.70E-03	1.61E-04

Supplementary Table C.2. *Changes (value) in model simulated land surface temperature (LST), reported alongside number of data points in each category and statistical significance (p values from both Student's t-test and Wilcoxon test). Values shown for each season, resolution (latitudinal degrees) and model.*

Season	Model	Resolution	Variable	Value	# data points	p-value (t-test)	p-value (Wilcoxon)
Annual	ACCESS-ESM1-5	1.25	LST	0.01	133	2.37E-02	3.02E-03
Annual	AWI-ESM-1-1-LR	1.87	LST	0.00	224	5.56E-01	6.39E-01
Annual	CanESM5	2.79	LST	0.02	101	1.37E-01	3.79E-03
Annual	CanESM5-CanOE	2.79	LST	0.04	101	4.53E-01	1.46E-01
Annual	CESM2	0.94	LST	0.02	335	6.58E-01	2.33E-04
Annual	CESM2-FV2	1.89	LST	0.02	101	7.07E-02	1.13E-02
Annual	CESM2-WACCM	0.94	LST	0.00	335	3.81E-01	4.31E-02
Annual	CESM2-WACCM-FV2	1.89	LST	-0.01	101	2.90E-01	8.27E-03
Annual	CMCC-CM2-SR5	0.94	LST	0.01	351	1.49E-01	1.28E-02
Annual	CMCC-ESM2	0.94	LST	0.02	351	1.55E-01	3.75E-03
Annual	CNRM-ESM2-1	1.40	LST	0.01	46	4.62E-01	2.87E-01
Annual	EC-Earth3-CC	0.70	LST	0.00	733	2.02E-01	6.16E-02
Annual	EC-Earth3-Veg	0.70	LST	0.00	714	6.66E-03	3.57E-02
Annual	EC-Earth3-Veg-LR	1.12	LST	0.00	365	4.86E-01	2.92E-01
Annual	GISS-E2-1-G	2.00	LST	0.01	86	8.68E-01	3.53E-01
Annual	HadGEM3-GC31-LL	1.25	LST	0.00	72	7.15E-01	7.58E-01
Annual	HadGEM3-GC31-MM	0.56	LST	0.00	464	5.22E-01	3.76E-01

Annual	INM-CM4-8	1.50	LST	0.00	20	4.68E-01	1.54E-01
Annual	INM-CM5-0	1.50	LST	0.00	105	4.35E-01	1.58E-01
Annual	IPSL-CM5A2-INCA	1.89	LST	0.03	66	2.29E-03	5.29E-04
Annual	IPSL-CM6A-LR	1.27	LST	0.01	145	1.06E-02	1.61E-05
Annual	MPI-ESM-1-2-HAM	1.87	LST	0.00	316	6.14E-01	9.99E-01
Annual	MPI-ESM1-2-HR	0.94	LST	0.00	449	3.66E-01	9.12E-02
Annual	UKESM1-0-LL	1.25	LST	0.00	215	5.87E-01	3.59E-01
Dry	ACCESS-ESM1-5	1.25	LST	0.02	133	7.56E-01	6.08E-01
Dry	AWI-ESM-1-1-LR	1.87	LST	0.00	224	3.80E-01	4.95E-01
Dry	CanESM5	2.79	LST	0.02	101	2.51E-01	3.99E-02
Dry	CanESM5-CanOE	2.79	LST	0.04	101	1.11E-01	1.46E-03
Dry	CESM2	0.94	LST	0.03	335	2.22E-03	1.28E-05
Dry	CESM2-FV2	1.89	LST	0.04	101	1.60E-02	8.61E-03
Dry	CESM2-WACCM	0.94	LST	0.02	335	1.42E-01	9.72E-03
Dry	CESM2-WACCM-FV2	1.89	LST	0.00	101	4.72E-02	2.25E-02
Dry	CMCC-CM2-SR5	0.94	LST	0.01	351	8.70E-01	2.18E-01
Dry	CMCC-ESM2	0.94	LST	0.01	351	5.33E-01	1.89E-01
Dry	CNRM-ESM2-1	1.40	LST	0.04	46	3.56E-01	1.95E-01
Dry	EC-Earth3-CC	0.70	LST	0.03	733	5.89E-106	1.44E-109
Dry	EC-Earth3-Veg	0.70	LST	0.02	714	8.06E-103	5.47E-108
Dry	EC-Earth3-Veg-LR	1.12	LST	0.03	365	4.60E-71	6.45E-59
Dry	GISS-E2-1-G	2.00	LST	-0.04	86	4.85E-01	1.96E-01
Dry	HadGEM3-GC31-LL	1.25	LST	0.00	72	5.78E-01	1.33E-01

Dry	HadGEM3-GC31-MM	0.56	LST	0.01	464	2.13E-01	6.10E-03
Dry	INM-CM4-8	1.50	LST	0.03	20	1.37E-01	3.28E-02
Dry	INM-CM5-0	1.50	LST	0.04	105	4.10E-03	2.88E-05
Dry	IPSL-CM5A2-INCA	1.89	LST	0.02	66	9.85E-01	8.41E-01
Dry	IPSL-CM6A-LR	1.27	LST	0.02	145	2.31E-01	2.71E-02
Dry	MPI-ESM-1-2-HAM	1.87	LST	0.01	316	4.67E-01	1.35E-01
Dry	MPI-ESM1-2-HR	0.94	LST	0.00	449	9.54E-01	8.24E-01
Dry	UKESM1-0-LL	1.25	LST	0.01	215	7.40E-01	3.85E-01
Wet	ACCESS-ESM1-5	1.25	LST	0.02	133	1.56E-01	7.26E-02
Wet	AWI-ESM-1-1-LR	1.87	LST	0.00	224	1.37E-01	3.52E-03
Wet	CanESM5	2.79	LST	0.02	101	4.81E-01	4.55E-01
Wet	CanESM5-CanOE	2.79	LST	0.05	101	2.68E-01	9.52E-02
Wet	CESM2	0.94	LST	0.02	335	4.14E-01	2.80E-01
Wet	CESM2-FV2	1.89	LST	0.03	101	1.79E-01	2.96E-01
Wet	CESM2-WACCM	0.94	LST	0.00	335	8.07E-01	5.14E-02
Wet	CESM2-WACCM-FV2	1.89	LST	-0.01	101	6.18E-01	8.22E-01
Wet	CMCC-CM2-SR5	0.94	LST	0.00	351	1.97E-02	2.29E-06
Wet	CMCC-ESM2	0.94	LST	0.00	351	6.45E-03	5.54E-04
Wet	CNRM-ESM2-1	1.40	LST	0.02	46	7.33E-01	3.98E-01
Wet	EC-Earth3-CC	0.70	LST	0.00	733	6.02E-02	8.86E-04
Wet	EC-Earth3-Veg	0.70	LST	0.00	714	1.91E-01	6.86E-03
Wet	EC-Earth3-Veg-LR	1.12	LST	0.00	365	2.26E-01	8.72E-03

Wet	GISS-E2-1-G	2.00	LST	0.00	86	1.36E-01	3.38E-02
Wet	HadGEM3-GC31-LL	1.25	LST	0.01	72	3.21E-01	4.70E-02
Wet	HadGEM3-GC31-MM	0.56	LST	0.01	464	4.79E-01	3.13E-02
Wet	INM-CM4-8	1.50	LST	0.00	20	7.31E-01	7.29E-01
Wet	INM-CM5-0	1.50	LST	0.00	105	1.38E-01	2.18E-03
Wet	IPSL-CM5A2-INCA	1.89	LST	0.01	66	7.48E-02	5.17E-01
Wet	IPSL-CM6A-LR	1.27	LST	0.00	145	2.83E-01	7.29E-02
Wet	MPI-ESM-1-2-HAM	1.87	LST	0.00	316	1.05E-01	2.35E-02
Wet	MPI-ESM1-2-HR	0.94	LST	0.00	449	4.14E-01	6.22E-02
Wet	UKESM1-0-LL	1.25	LST	0.00	215	7.34E-01	2.05E-01
Transition	ACCESS-ESM1-5	1.25	LST	0.00	133	1.74E-01	1.14E-01
Transition	AWI-ESM-1-1-LR	1.87	LST	0.01	224	9.10E-01	3.51E-01
Transition	CanESM5	2.79	LST	0.02	101	5.52E-02	2.76E-03
Transition	CanESM5-CanOE	2.79	LST	0.03	101	3.12E-01	2.00E-01
Transition	CESM2	0.94	LST	0.03	335	8.10E-01	5.47E-04
Transition	CESM2-FV2	1.89	LST	-0.01	101	1.82E-01	2.10E-02
Transition	CESM2-WACCM	0.94	LST	0.00	335	7.19E-01	2.69E-01
Transition	CESM2-WACCM-FV2	1.89	LST	-0.01	101	4.55E-01	6.46E-02
Transition	CMCC-CM2-SR5	0.94	LST	0.02	351	9.00E-02	3.14E-03
Transition	CMCC-ESM2	0.94	LST	0.02	351	8.59E-02	2.79E-02
Transition	CNRM-ESM2-1	1.40	LST	0.02	46	5.71E-01	6.73E-01
Transition	EC-Earth3-CC	0.70	LST	0.00	733	2.96E-01	1.64E-01

Transition	EC-Earth3-Veg	0.70	LST	0.00	714	2.74E-02	1.13E-01
Transition	EC-Earth3-Veg-LR	1.12	LST	0.00	365	2.10E-01	4.33E-02
Transition	GISS-E2-1-G	2.00	LST	0.00	86	4.64E-01	5.89E-01
Transition	HadGEM3-GC31-LL	1.25	LST	0.00	72	8.77E-01	8.49E-01
Transition	HadGEM3-GC31-MM	0.56	LST	0.01	464	3.97E-01	2.16E-01
Transition	INM-CM4-8	1.50	LST	0.00	20	2.03E-01	2.40E-02
Transition	INM-CM5-0	1.50	LST	0.01	105	8.26E-01	6.77E-01
Transition	IPSL-CM5A2-INCA	1.89	LST	0.03	66	1.24E-02	9.26E-04
Transition	IPSL-CM6A-LR	1.27	LST	0.02	145	1.91E-03	2.31E-06
Transition	MPI-ESM-1-2-HAM	1.87	LST	0.00	316	1.78E-01	1.01E-01
Transition	MPI-ESM1-2-HR	0.94	LST	0.00	449	8.63E-01	8.14E-01
Transition	UKESM1-0-LL	1.25	LST	0.00	215	3.93E-01	1.26E-01

Supplementary Table C.3. *Changes (value) in model simulated precipitation (P), reported alongside number of data points in each category and statistical significance (p values from both Student's t-test and Wilcoxon test). Values shown for each season, resolution (latitudinal degrees) and model.*

Season	Model	Resolution	Variable	Value	# data points	p-value (t-test)	p-value (wilcoxon)
Annual	ACCESS-ESM1-5	1.25	P	0.49	133	2.64E-01	1.55E-01
Annual	AWI-ESM-1-1-LR	1.87	P	-0.32	224	1.45E-01	1.67E-02
Annual	CanESM5	2.79	P	0.00	101	5.91E-01	2.32E-01
Annual	CanESM5-CanOE	2.79	P	1.49	101	8.60E-01	5.61E-01
Annual	CESM2	0.94	P	-0.26	335	5.24E-01	3.16E-01
Annual	CESM2-FV2	1.89	P	0.07	101	6.20E-01	1.34E-01
Annual	CESM2-WACCM	0.94	P	0.13	335	6.96E-01	5.53E-01
Annual	CESM2-WACCM-FV2	1.89	P	-0.24	101	5.36E-01	2.94E-01
Annual	CMCC-CM2-SR5	0.94	P	-0.14	351	9.00E-01	4.92E-01
Annual	CMCC-ESM2	0.94	P	0.55	351	1.53E-01	6.62E-04
Annual	CNRM-ESM2-1	1.40	P	1.83	46	5.59E-01	5.96E-01
Annual	EC-Earth3-CC	0.70	P	0.03	733	2.75E-01	8.50E-01
Annual	EC-Earth3-Veg	0.70	P	-0.02	714	1.32E-04	1.05E-03
Annual	EC-Earth3-Veg-LR	1.12	P	-0.04	365	9.31E-01	6.37E-01
Annual	GISS-E2-1-G	2.00	P	-0.26	86	6.83E-01	6.28E-01
Annual	HadGEM3-GC31-LL	1.25	P	0.08	72	7.61E-01	8.75E-01
Annual	HadGEM3-GC31-MM	0.56	P	-0.07	464	3.16E-01	9.75E-02

Annual	INM-CM4-8	1.50	P	-0.15	20	9.51E-01	8.12E-01
Annual	INM-CM5-0	1.50	P	-0.16	105	8.58E-01	6.60E-01
Annual	IPSL-CM5A2-INCA	1.89	P	-0.13	66	4.12E-01	3.80E-01
Annual	IPSL-CM6A-LR	1.27	P	-0.08	145	6.14E-01	8.89E-01
Annual	MPI-ESM-1-2-HAM	1.87	P	-0.05	316	6.79E-01	9.74E-01
Annual	MPI-ESM1-2-HR	0.94	P	-0.14	449	8.28E-01	3.17E-01
Annual	UKESM1-0-LL	1.25	P	0.04	215	7.14E-01	2.84E-01
Dry	ACCESS-ESM1-5	1.25	P	0.25	133	8.77E-01	6.19E-01
Dry	AWI-ESM-1-1-LR	1.87	P	0.00	224	8.17E-01	6.53E-01
Dry	CanESM5	2.79	P	0.01	101	6.37E-01	7.41E-01
Dry	CanESM5-CanOE	2.79	P	-0.06	101	2.82E-01	5.41E-01
Dry	CESM2	0.94	P	-0.08	335	8.52E-01	9.73E-01
Dry	CESM2-FV2	1.89	P	-0.07	101	9.23E-01	5.57E-01
Dry	CESM2-WACCM	0.94	P	-0.01	335	8.82E-01	8.01E-01
Dry	CESM2-WACCM-FV2	1.89	P	-0.02	101	8.98E-01	8.46E-01
Dry	CMCC-CM2-SR5	0.94	P	0.20	351	2.18E-01	3.35E-02
Dry	CMCC-ESM2	0.94	P	-0.11	351	8.84E-01	9.70E-01
Dry	CNRM-ESM2-1	1.40	P	-0.17	46	8.66E-01	7.05E-01
Dry	EC-Earth3-CC	0.70	P	-0.10	733	5.22E-30	4.39E-39
Dry	EC-Earth3-Veg	0.70	P	-0.07	714	1.58E-21	2.50E-29
Dry	EC-Earth3-Veg-LR	1.12	P	-0.07	365	3.25E-08	4.38E-12
Dry	GISS-E2-1-G	2.00	P	0.15	86	9.18E-01	5.28E-01
Dry	HadGEM3-GC31-LL	1.25	P	0.32	72	2.99E-01	5.63E-01

Dry	HadGEM3-GC31-MM	0.56	P	-0.08	464	6.39E-01	3.71E-01
Dry	INM-CM4-8	1.50	P	-0.48	20	7.94E-01	8.41E-01
Dry	INM-CM5-0	1.50	P	-0.71	105	3.45E-03	2.14E-05
Dry	IPSL-CM5A2-INCA	1.89	P	-0.17	66	1.35E-01	4.62E-01
Dry	IPSL-CM6A-LR	1.27	P	-0.15	145	2.02E-01	8.67E-02
Dry	MPI-ESM-1-2-HAM	1.87	P	0.00	316	8.09E-01	5.09E-01
Dry	MPI-ESM1-2-HR	0.94	P	-0.03	449	7.03E-01	7.78E-01
Dry	UKESM1-0-LL	1.25	P	-0.02	215	6.67E-01	3.62E-01
Wet	ACCESS-ESM1-5	1.25	P	2.92	133	1.89E-02	7.81E-03
Wet	AWI-ESM-1-1-LR	1.87	P	-0.21	224	6.47E-01	4.24E-01
Wet	CanESM5	2.79	P	-1.64	101	7.86E-01	5.73E-01
Wet	CanESM5-CanOE	2.79	P	4.17	101	5.17E-01	1.79E-01
Wet	CESM2	0.94	P	1.01	335	8.20E-01	6.59E-01
Wet	CESM2-FV2	1.89	P	-0.88	101	1.03E-01	2.44E-02
Wet	CESM2-WACCM	0.94	P	-0.39	335	5.30E-01	1.37E-01
Wet	CESM2-WACCM-FV2	1.89	P	0.49	101	8.42E-01	5.87E-01
Wet	CMCC-CM2-SR5	0.94	P	0.26	351	3.99E-01	1.74E-01
Wet	CMCC-ESM2	0.94	P	-3.11	351	2.13E-02	4.93E-03
Wet	CNRM-ESM2-1	1.40	P	2.89	46	3.30E-01	2.68E-01
Wet	EC-Earth3-CC	0.70	P	0.08	733	9.04E-01	6.68E-01
Wet	EC-Earth3-Veg	0.70	P	-0.05	714	2.68E-03	6.43E-03
Wet	EC-Earth3-Veg-LR	1.12	P	0.06	365	3.68E-01	5.29E-02

Wet	GISS-E2-1-G	2.00	P	-0.22	86	1.74E-01	9.54E-01
Wet	HadGEM3-GC31-LL	1.25	P	-1.30	72	8.58E-01	9.60E-01
Wet	HadGEM3-GC31-MM	0.56	P	-0.42	464	2.84E-01	5.15E-02
Wet	INM-CM4-8	1.50	P	-0.48	20	6.79E-01	4.98E-01
Wet	INM-CM5-0	1.50	P	-0.41	105	2.12E-02	4.19E-05
Wet	IPSL-CM5A2-INCA	1.89	P	-0.70	66	5.02E-01	4.57E-01
Wet	IPSL-CM6A-LR	1.27	P	-0.61	145	9.51E-01	9.25E-01
Wet	MPI-ESM-1-2-HAM	1.87	P	0.42	316	4.98E-01	3.85E-01
Wet	MPI-ESM1-2-HR	0.94	P	-0.62	449	4.28E-01	4.74E-01
Wet	UKESM1-0-LL	1.25	P	1.47	215	5.63E-01	4.41E-01
Transition	ACCESS-ESM1-5	1.25	P	0.36	133	7.20E-01	3.99E-01
Transition	AWI-ESM-1-1-LR	1.87	P	-0.52	224	1.99E-02	1.02E-03
Transition	CanESM5	2.79	P	0.01	101	4.58E-01	1.42E-01
Transition	CanESM5-CanOE	2.79	P	1.85	101	5.29E-01	2.91E-01
Transition	CESM2	0.94	P	-0.39	335	9.51E-01	9.91E-01
Transition	CESM2-FV2	1.89	P	0.81	101	9.29E-01	4.57E-01
Transition	CESM2-WACCM	0.94	P	0.35	335	7.31E-01	6.67E-01
Transition	CESM2-WACCM-FV2	1.89	P	-0.12	101	9.51E-01	6.03E-01
Transition	CMCC-CM2-SR5	0.94	P	-0.46	351	2.36E-01	3.81E-02
Transition	CMCC-ESM2	0.94	P	-0.22	351	9.62E-01	7.16E-01
Transition	CNRM-ESM2-1	1.40	P	0.21	46	6.71E-01	2.77E-01
Transition	EC-Earth3-CC	0.70	P	0.02	733	3.90E-01	5.91E-01

Transition	EC-Earth3-Veg	0.70	P	-0.03	714	2.08E-03	6.00E-03
Transition	EC-Earth3-Veg-LR	1.12	P	-0.04	365	7.08E-01	7.89E-01
Transition	GISS-E2-1-G	2.00	P	0.10	86	4.74E-01	4.15E-01
Transition	HadGEM3-GC31-LL	1.25	P	-0.72	72	3.63E-01	2.84E-01
Transition	HadGEM3-GC31-MM	0.56	P	-0.13	464	5.72E-01	3.65E-01
Transition	INM-CM4-8	1.50	P	-0.18	20	3.85E-01	4.30E-01
Transition	INM-CM5-0	1.50	P	0.26	105	2.75E-01	2.77E-02
Transition	IPSL-CM5A2-INCA	1.89	P	-0.28	66	9.41E-01	7.81E-01
Transition	IPSL-CM6A-LR	1.27	P	-0.61	145	7.34E-01	3.05E-01
Transition	MPI-ESM-1-2-HAM	1.87	P	0.08	316	4.70E-01	6.39E-01
Transition	MPI-ESM1-2-HR	0.94	P	-0.16	449	4.47E-01	4.51E-01
Transition	UKESM1-0-LL	1.25	P	-0.24	215	1.93E-01	4.43E-02

Figures

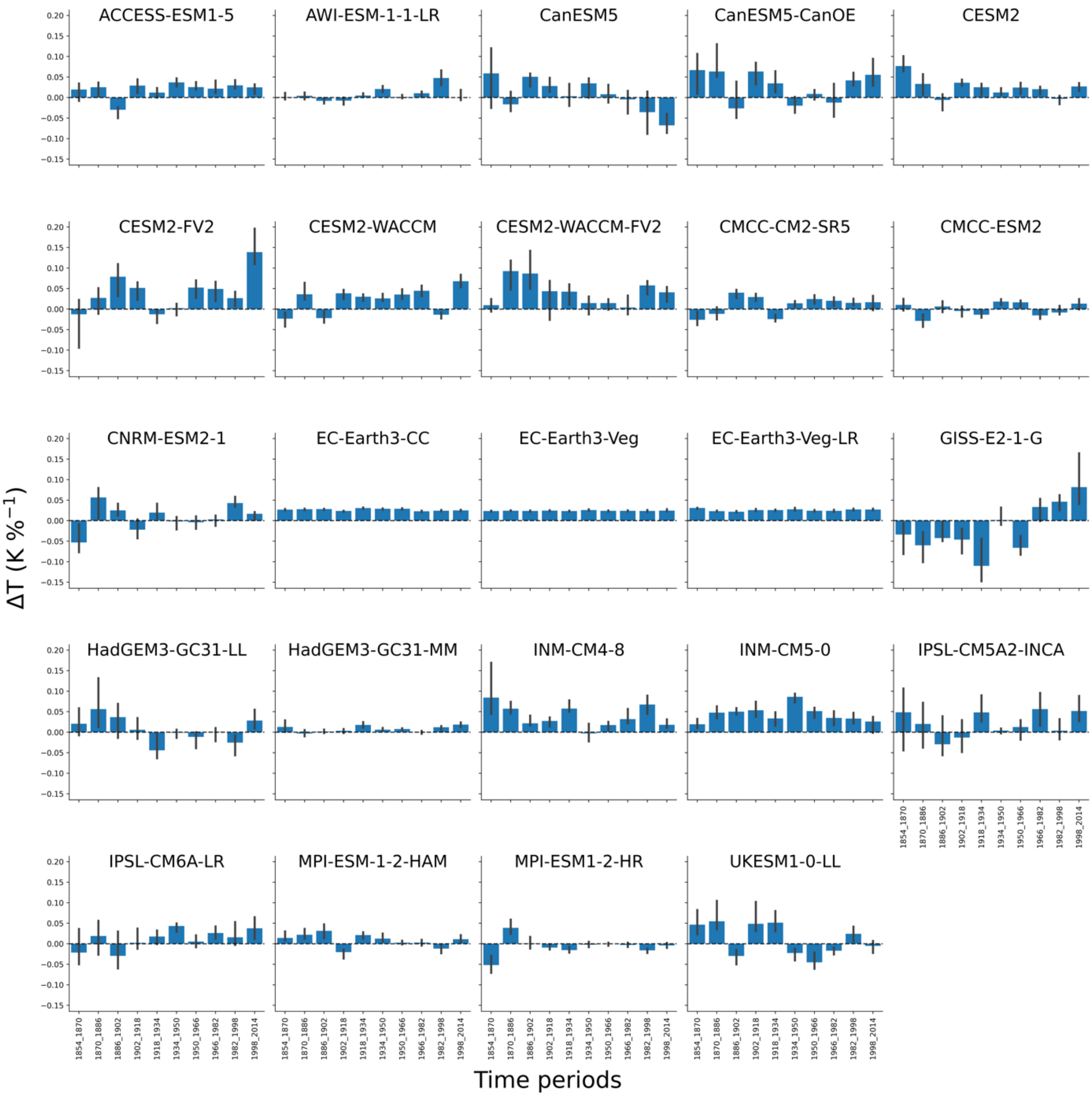

Supplementary Figure C.1. *Median change in simulated dry season local surface temperature due to forest loss (ΔT, K %$^{-1}$). Results are shown for each model and each of the ten 16-year time periods, from 1854-2014 (datasets listed in Table C.1). Model results are shown for areas where initial forest cover exceeds 70%. Error bars show the standard error of the mean for each model and time period.*

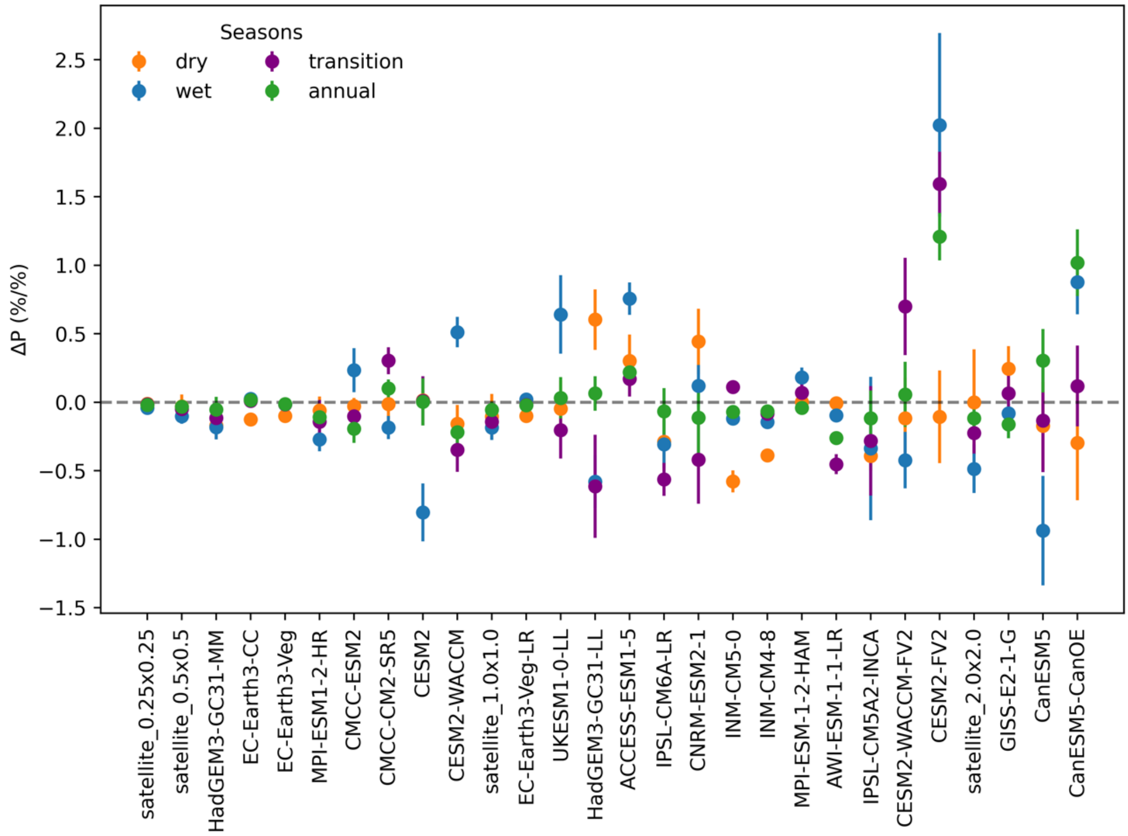

Supplementary Figure C.2. *Relative change in precipitation due to forest loss (ΔP, %/%), for each model and satellite and for each season. Results are calculated as the change in monthly precipitation divided by the mean monthly precipitation for each model and satellite dataset. The point represents the median of the pixels for each season, with the error bars showing the standard error of the mean.*

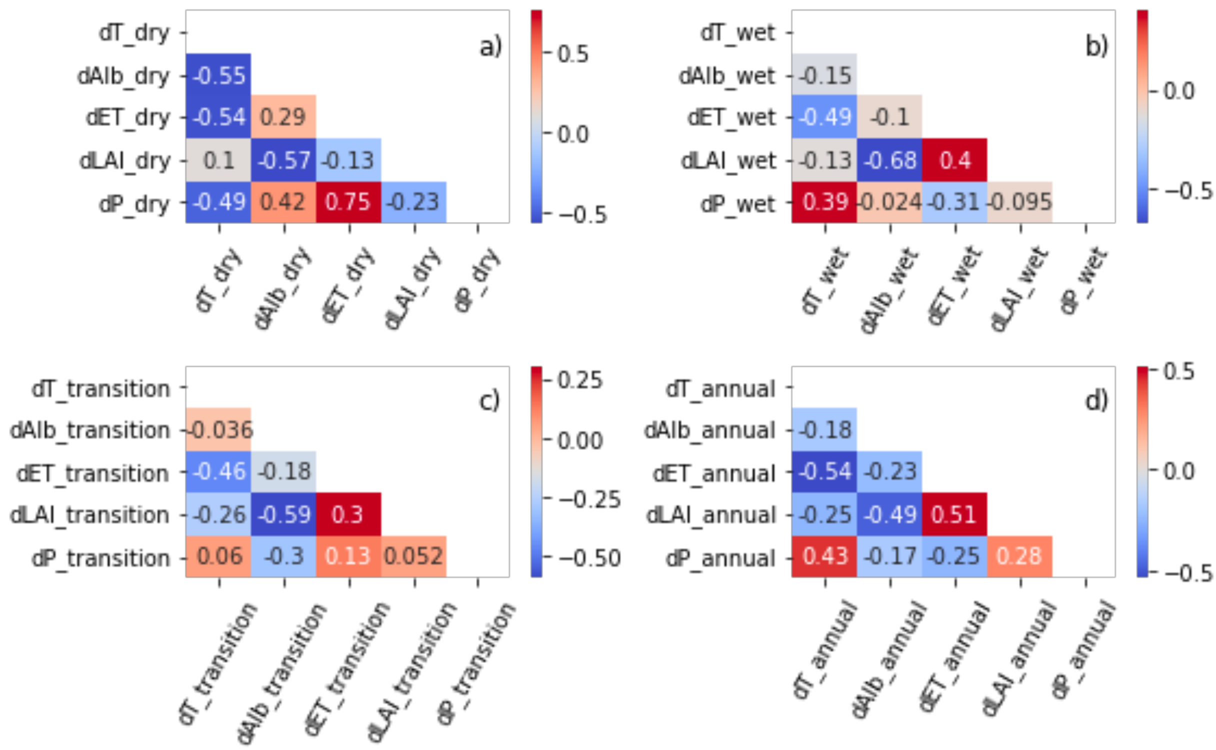

Supplementary Figure C.3. *Correlation matrix showing the relationships between each model variable for each season (dry a), wet b), transition c) and annual d)). Results show the Pearson correlation coefficient (Pearson's r) value with colouring indicating a positive (red) or negative (blue) relationship.*